Aalborg Universitet

AALBORG UNIVERSITY
DENMARK

Estimation of Extreme Responses and Failure Probability of Wind Turbines under Normal Operation by Controlled Monte Carlo Simulation

Sichani, Mahdi Teimouri

Publication date:
2011

Document Version
Publisher's PDF, also known as Version of record

Link to publication from Aalborg University

Citation for published version (APA):
Sichani, M. T. (2011). *Estimation of Extreme Responses and Failure Probability of Wind Turbines under Normal Operation by Controlled Monte Carlo Simulation*. Department of Civil Engineering, Aalborg University. DCE Thesis No. 31

General rights
Copyright and moral rights for the publications made accessible in the public portal are retained by the authors and/or other copyright owners and it is a condition of accessing publications that users recognise and abide by the legal requirements associated with these rights.

- Users may download and print one copy of any publication from the public portal for the purpose of private study or research.
- You may not further distribute the material or use it for any profit-making activity or commercial gain
- You may freely distribute the URL identifying the publication in the public portal -

Take down policy
If you believe that this document breaches copyright please contact us at vbn@aub.aau.dk providing details, and we will remove access to the work immediately and investigate your claim.

Downloaded from vbn.aau.dk on: May 05, 2023

Aalborg University
Department of Civil Engineering

DCE Thesis No. 31

Estimation of Extreme Responses and Failure Probability of Wind Turbines under Normal Operation by Controlled Monte Carlo Simulation

by

Mahdi Teimouri Sichani

October 2011

© Aalborg University

ISSN 1901-7294
DCE Thesis No. 31

Scientific Publications at the Department of Civil Engineering

Technical Reports are published for timely dissemination of research results and scientific work carried out at the Department of Civil Engineering (DCE) at Aalborg University. This medium allows publication of more detailed explanations and results than typically allowed in scientific journals.

Technical Memoranda are produced to enable the preliminary dissemination of scientific work by the personnel of the DCE where such release is deemed to be appropriate. Documents of this kind may be incomplete or temporary versions of papers—or part of continuing work. This should be kept in mind when references are given to publications of this kind.

Contract Reports are produced to report scientific work carried out under contract. Publications of this kind contain confidential matter and are reserved for the sponsors and the DCE. Therefore, Contract Reports are generally not available for public circulation.

Lecture Notes contain material produced by the lecturers at the DCE for educational purposes. This may be scientific notes, lecture books, example problems or manuals for laboratory work, or computer programs developed at the DCE.

Theses are monograms or collections of papers published to report the scientific work carried out at the DCE to obtain a degree as either PhD or Doctor of Technology. The thesis is publicly available after the defence of the degree.

Latest News is published to enable rapid communication of information about scientific work carried out at the DCE. This includes the status of research projects, developments in the laboratories, information about collaborative work and recent research results.

Published 2011 by
Aalborg University
Department of Civil Engineering
Sohngaardsholmsvej 57,
DK-9000 Aalborg, Denmark

Printed in Aalborg at Aalborg University

ISSN 1901-7294
DCE Thesis No. 31

Preface

The present thesis “Estimation of Extreme Responses and Failure Probability of Wind Turbines under Normal Operation by Controlled Monte Carlo Simulation” is the outcome of the research of a PhD study within the period October 2008 to October 2011 at the department of Civil Engineering, Aalborg university, Aalborg, Denmark. The thesis is presented as a collection of peer-reviewed articles published within this period in a number of journals and conferences.

I would like to thank my supervisor Prof.Dr.Techn. Søren R.K. Nielsen for his enthusiast and perseverance in this project. I would like to greatly appreciate his guidance and support, both technically and spiritually, which empowered me to move along this long road. Special thanks should be directed to Prof.Dr.Techn. Christian Bucher of Technical University of Vienna (TUWien) who hosted me in his institute for four months. I would like to appreciate Prof.Bucher for always giving me motivation toward my research and providing me with numerous technical discussions during my stay in Vienna. The friendly environment of the Center of Mechanics and Structural Dynamics (CMSC) of the Technical University of Vienna can not be forgotten. I would like to appreciate Prof.Dr.Techn. Arvid Naess of the Centre for Ships and Ocean Structures (CeSOS) of Norwegian University of Science and Technology (NTNU) for being so open and friendly in sharing their research works and ideas with me during my visit to their institute.

The Danish Energy Authority is acknowledged for support under the grant EFP07-II that made this research possible. I would like to thank my colleagues and friends for fruitful discussions, moral support and helpfulness during the course of the project.

Finally, I would like to thank my parents and my sister for their everlasting support they never refrained me during this time. Their impact on my work is not possible to be overestimated.

Aalborg, October 2011 Mahdi Teimouri Sichani

Summary in English

Extreme value predictions for application in wind turbine design are often based on asymptotic results. Assuming that the extreme values of a wind turbine responses, i.e. maximum values of the mud-line moment or blades' root stress, follow a certain but unknown probability density (mass) distribution, we are interested in estimating this distribution accurately far in its tail(s). This is typically done by assuming the epochal extremes in a 10 minute interval are distributed according to some asymptotic extreme value distribution with unknown parameters to be estimated based on simulated low order statistical moments. The results obtained by extrapolation of the extreme values to the stipulated design period of the wind turbine depend strongly on the relevance of these adopted extreme value distributions.

The problem is that this relevance cannot be decided from the data obtained by the indicated so-called crude Monte Carlo method. With failure probabilities of the magnitude 10^{-7} during a 10 min. sampling interval the tails of the distributions are never encountered during normal operations. To circumvent this problem the application of variance reduction Monte Carlo methods i.e. importance sampling (IS) might be considered. This suffers from strict requirement on the so called sampling density for a high dimensional parameter vector.

Newly developed advanced (controlled) Monte Carlo methods propose alternative solutions to this problem. Splitting methods such as Double & Clump (D&C), Russian Roulette & Splitting (RR&S) and finally distance controlled Monte Carlo (DCMC) are one class of these methods. The idea behind these methods is to artificially enforce "rare events" to happen more frequently. This can be done by distributing the statistical wight of the samples such that it is an estimate of their true probability density. Introducing sample weights allows increasing the number of samples which carry low statistical weights, i.e. low probability of occurrence, by further lowering their weights. This enables more accurate analysis of their behavior in the vicinity of the failure surface i.e. estimation of the probability of failure.

Another approach to this problem is to condition the Monte Carlo simulations using the so-called Markov Chain Monte Carlo (MCMC) technique. The standard method in this direction is the *subset simulation* (SS). Here the idea is to start by a standard Monte Carlo simulation with very low number of samples, compared to the true number required for estimation of the required probability. The next generation of samples are then simulated *conditioned* on those samples which have the least probability of occurrence in previous simulation.

Yet an alternative approach for estimation of the first excursion probability of any system is based on calculating the evolution of the Probability Density Function (PDF) of the process and integrating it on the specified domain. Clearly this provides the most accurate results among the three classes of the methods. The solution of the Fokker-Planck-Kolmogorov (FPK) equation for systems governed by a stochastic differential equation driven by Gaussian white noise will give the sought time variation of the probability density function. However the analytical solution of the FPK is available for only a few dynamic systems and the numerical solution is difficult for dynamic problem of more than 2-3 degrees of freedom. This confines the applicability of the FPK to a very narrow range of problems. On the other hand the recently introduced Generalized Density Evolution Method (GDEM), has opened a new way toward realization of the evolution of the PDF of a stochastic process; hence an alternative to the FPK. The considerable advantage of the introduced method over FPK is that its solution does not require high computational cost which extends its range of applicability to high order structural dynamic problems. The problem with method is that the number of basic random variables is rather limited.

Summary in Danish

Bestemmelsen af ekstremværdier for vindmølle design foretages i regelen ved hjælp af asymptotiske metoder. Antages ekstremværdien af en givet responsstørrelse, f.eks. maximalværdien af tårnmomentet ved fundamentet eller bladspændingerne ved roden, at følge en given, men ukendt sandsynlighedstæthed, er problemet at estimere enderne af denne tæthedsfunktion. Dette foretages typisk ved at antage at ekstremværdien i en periode af 10 minutters varighed er fordelt efter en antaget ekstremværdi fordeling med ukendte parametre, der estimeres efter givne atatistiske momenter af lav orden for den underliggende fordeling. Det opnåede resultat af ekstraåpolationen af ekstremværdien til den stipulerede design periode of vindmøllen afhænger i væsentlig grad af den valgte ekstremværdifordeling.

Problemet er, at gyldigheden af den benyttede fremgangsmåde kan ikke veficeres ved såkaldt crude Monte Carlo simulering. Med svigtsamdsynligheder af størrelsen 10^{-7} i et samplingsinterval af 10 min. vil enderne af fordelingen sjældent eller aldrig nås under normale driftbetingelser. En måde at omgå dette problem er anvendelsen af såkaldte variansreducerende Monte Carlo metoder, som importance sampling (IS). Denne metode har dog problemr ved fastlæggelsen samplingstæthedsfunktionen for parameter vektorer af høj dimensionalitet.

Som alternative løsningsalgoritmer er der i de senere år er udviklet såkaldte controlled Monte Carlo metoder til løsning af det beskrevne problem. En klasse af disse metoder udgøres af Double & Clump (D&C), Russian Roulette & Splitting (RR&S) og distance controlled Monte Carlo (DCMC). Ideen bag disse metoder er kunsigt af fremtvinge at "ekstrem hændelser" sker med højere frekvens. Dette kan foretages ved at fordele den statiske vægt of de simulerede tidsserier på en såden måde, at et estimat af deres virkelige sandsynlighedstæthedsfunktion opnås. Det er åbenmbart that introduktionen af vægte i løbet af simuleringen muliggør, at antallet af tidsserier med lav statistik vægt, dvs, med lav sandsynlighed, kan øges ved yderligere at reducere deres vægt. Ved at øge antallet af disse tidsserier opnås en mere præcis estimering af deres opførsel i omegnen af svigtfladen, herunder fastlæggelsen af svigtsandsynligheden.

En anden fremgangsmåde er anvendelsen af betingede Monte Carlo simularingsmetoder, kendt som Markov Chain Monte Carlo (MCMC) metoder. Standard metoden er *subset simulation* (SS). Ideen er her at starte simuleringen med en standard Monte Carlo simulering med et stærkt. Den næste generation af simuleringer startes dernæst *betinget* af de tidsserier, der i den foregående simulering havde den laveste sandsynlihed for at forekomme.

Endnu en alternativ fremsgansmåde til fastlæggelse af første udkrydsningssandsynligheder er baseret på bestemmelsen af sandsynlighedstæthedsfunktionen af processen som funktion af tiden, og integrere denne over det relevante område. Det er åbenbart, at denne fremgangsmåder vil give de mest nøjagtige resultater blandt de nævnte tre metoder. Løsningen Fokker-Planck-Kolmogorov (FPK) ligningen for systemer styret af en tilstandsdiffrential ligning påvirket af Gaussisk hvid støj vil give den søgte tidsvariation af tæthedsfunktionen. Imidlertid kendes der kun ganske få analytiske løsninger FPK ligningen, og numeriske løsning er vanskelig for dynamiske problemer af mere end 2-3 frihedsgrader. Dette begrænser anvendelsen af FPK ligningen til et meget begrænset antal problemer. For nyligt er den såkaldte Generalized Density Evolution Method (GDEM) blevet foreslået som en måde at omgå det bskrevne dimensionsproblem. I denne metode bestemmes udviklingen af sandsynlighedstæthedsfunktionen, som det sker ved FPK metoden, men der er ingen begrænsninger på antallet af frihedsgrader. Problemet ved metoden er at antallet af basisvarible, der fastlægger lastprocesserne, må være relativt begrænset.

Contents

List of Figures

List of Tables

CHAPTER 1
Introduction

In this chapter the statement of the problem in dynamic reliability of the wind turbines is presented. The route map of the thesis is addressed in this chapter and the relationship of the represented publications to the direction of the study is pointed out. The main focus of the thesis has been on applying VRMC methods on a wind turbine model. The primary requirement for this is a wind turbine model in a correlated wind field. The primary works consist of developing a wind field generator and a wind turbine model. Among all the VRMC method the following have been considered for application on the wind turbine: *Importance Sampling, Distance Control Monte Carlo, Asymptotic Sampling, Subset Simulation, Subset Simulation with Reduced Chain Correlation, Subset Simulation with Delayed Rejection, Horseracing Simulation* and the method of the *Average Conditional Exceedance Rates*. A short summary of the methods used in the thesis with their way of tackling the problem is provided. Other methods such as Line Sampling, Directional Sampling, Adaptive Sampling etc. have only been studied but not considered in detail.

1.1 Wind turbine failures

Wind turbines have a growing rate of use due to the considerations for renewable energy production. The development of these machines and their implementation have been changed from their early designs which shows positive attitude and benefit in them. There exist two major types of wind turbines e.g. the Horizontal Axis Wind Turbines (HAWT) and the Vertical Axis Wind Turbines (VAWT); only the HAWT will be considered in this thesis. The development of the wind turbines has led to setting up wind farms, a grid of wind turbines, designed for harvesting maximum wind power c.f. figure 1.1.a. More innovative ideas are toward installing them on towers and sky scrapers. Figure 1.1.b shows the three wind turbines installed on Bahrain world trade center and turned on for the first time on August 8, 2008. Each of these turbines is capable of generating 225KW energy which altogether provide about 10%-15% of the towers' total power consumption. Creation of such innovative ideas requires designing safe wind turbines with low probability of failure according to the safety regulations.

A wind turbine during its typical 20 or 50 years operation will face some very extreme conditions. Equipment problem such as gearbox failure or other unplanned events may happen during this period of time. Other sources of defects or malfunctioning in a wind turbine may rise within installation process. In modern wind turbines the blades and the nacelle need to be installed about hundred meters above the ground which needs plenty of crane work. The potential equipment and installation imperfections are detected by component condition monitoring of the turbine. This is the key toward optimized lifetime and capacity besides the profitability

a) b)

Figure 1.1 Different wind turbines installations; a) The 20 x 2 MW wind turbines provide 40 MW of clean power for the city of Copenhagen, b) Wind turbines on Bahrain world trade center. The two towers are linked via three skybridges, each holding a 3 x 225KW wind turbine providing 675kW of wind power production

of the wind turbine. The maintenance sections is in charge of treating these potential failure spots. Nevertheless a wind turbine, just like any mechanical system, is always subject to failure during its operation. This could be due to extreme weather condition or other reasons - such as emergency shut downs - during operation which enforces extreme working conditions on the turbine. Such circumstances may lead into catastrophe which threads both human being and the turbine life. Examples of such failures are the Searsburg Vermont catastrophic turbine failure on September 15, 2008. Turbine No.10 of the 11 turbine Searsburg wind facility collapsed on September 15 in high wind conditions. One of the turbine blades hit the base causing the tower to buckle and the nacelle and rotor assembly to crash to the ground c.f. figure 1.2.a. On October 24, 2008 a Suzlon wind turbine in Waynet Illinoise had one of its 140 foot long blades break off. A failure in the design procedure has been mentioned as the main reason for this failure. In February 2008 a Vestas wind turbine in Vig, Denmark had a dramatic self-destruction. The controller of the wind turbine did not function and the rotor started spinning out of control. One of the blades hits the tower cutting it to half and its debris hits other blades crushing them to parts as well c.f. 1.2.b. In order to decrease the possibility of these failures the codes of practice recommend safety factors of for the wind turbine parts. Definition of these safety factors is based on the designated probability of failure of the wind turbine. This necessitates estimation of the failure probability of the wind turbines down to probabilities of order 10^{-7}. The factors associated to these probabilities are the so-called *return periods* of the wind turbines. These return periods may be calculated on the basis of either 20 or 50 years of working condition called the *50-year* or *20-year* return periods respectively.

1.2 Statement of the problem

According to the IEC61400-1 standard (IEC 2005a; IEC 2005b), the design value r of a stochastic response { R(t) , t∈[0,∞[}(bending moment, stress, deformation, etc.) is obtained by extrapolation of the failure probability of the design value r under normal operation in a referential epoche T, e.g. a realization of length T of the process $R(t)$, to a given recurrence time (expected

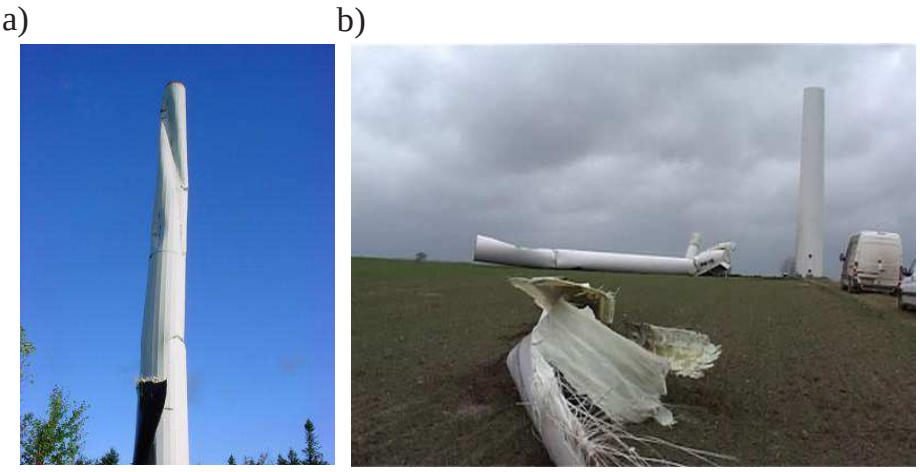

Figure 1.2 Examples of the failures of the wind turbines. a) Searsburg Vermont turbine, b) The Danish wind turbine

first-passage time) T_r. Presuming independent failure events in adjacent referential epoches the exceedance probability of the design value is given as

$$P\Big(R_{max}(T_r) > r\Big) = 1 - \Big(1 - P(R_{max}(T) > r)\Big)^{T_r/T} \simeq \frac{T_r}{T} P\Big(R_{max}(T) > r\Big) \tag{1.1}$$

$R_{max}(T) = \max\{R(t) : 0 \leq t \leq T\}$ and $R_{max}(T_r) = \max\{R(t) : 0 \leq t \leq T_r\}$. The failure probability in the referential epoche is given as

$$P\Big(R_{max}(T_r) > r\Big) = \int_{V_i}^{V_o} P\Big(R_{max}(T_r) > r|v\Big) f_V(v) dv \simeq \frac{T_r}{T} P\left(R_{max}(T) > r\right) \tag{1.2}$$

where $f_V(v)$ is the pdf of the mean wind velocity and $P\Big(R_{max}(T_r) > r|v\Big)$ is the failure probability on condition of $V = v$. V_i and V_o are the cut-in and cut-out wind speeds of the rotor. Since, T_r is the expected first-passage time, it follows that $P\Big(R_{max}(T_r) > r|v\Big) \lesssim 1$. With $T_r = 50$ year and $T = 600s$, (1.1) provides the relation

$$P\Big(R_{max}(T) > r\Big) \lesssim \frac{T}{T_r} = 3.8 \times 10^{-7} \tag{1.3}$$

The design value r is obtained as the solution to (1.3). It is out of question to determine this by conventional (crude) Monte Carlo simulation due to the indicated low failure probability. The suggested approach in the IEC61400-1 standard is to use a Weibull or a Gumbel distribution as the distribution function $F_{R_{max}(T)} = 1 - P\Big(R_{max}(T) > r\Big)$ for R_{max}

$$\left.\begin{aligned} F_{R_{max}(T)} &= 1 - \exp\left(-(\frac{r - r_o}{r_1})^{r_2}\right) \\ F_{R_{max}(T)} &= \exp\left(-\exp\left(\frac{r - r_o}{r_1}\right)\right) \end{aligned}\right\} \tag{1.4}$$

where r_o, r_1 and $r_2 > 0$ are locations, scale and shape parameters, which are estimated from the available samples. The results obtained by an extrapolation of the extreme values to the stipulated design period of the wind turbine depend strongly on the relevance of these adopted extreme value distributions combined with additional assumptions such as the choice of threshold level for considered peak. The problem is that the relevance of these assumptions cannot be decided from the data obtained by standard (so-called crude) Monte Carlo (SMC) method. With failure probabilities of the magnitude 10^{-7} during a 10 min. sampling interval the tails of the distributions are very seldom encountered during normal operations. To circumvent this problem the time-efficient, so-called Controlled Monte Carlo (CMC) simulation techniques need to be taken into account. In the present work the failure probability $P\Big(R_{max}(T) > r\Big)$ will be determined directly by means of a variance reducing Monte Carlo simulation method.

1.3 An overview into the problem

The problem of dynamic reliability analysis of the wind turbines falls into the category of high dimensional nonlinear first passage probability estimation. The term *high dimension* here refers to the number of the *basic random variables* of the problem i.e. white noise realizations which enter the turbulence filter. This should not be misinterpreted as the number of degrees of freedom of the structural system as is normally the case in structural dynamic problems. Typically the *dimension* here can be calculated as the number of the system excitations multiplied by the number of points in their temporal discretization.

Classical reliability methods, such as importance sampling, estimate the failure probability of a predefined barrier level. This is sufficient in reliability assessment problems but not in design problems; where the barrier level of a predefined failure probability, e.g. the value of "r" in Eq.(1.3), is required to be estimated. Nevertheless these methods are still applicable conditioned on coupling them with an additional optimization. The optimization scenario would be to estimate the barrier level by interpolation(extrapolation) from the obtained probabilities of some trial barrier levels.

The drawback of this approach is that it requires estimation of failure probability for several barrier levels which urges repetition of the major parts of the estimation procedure. Examples are re-calculation of the control functions (critical excitations) in IS (Macke and Bucher 2003) or important directions in LS (Schuëller 2008). This necessitates repetition of the majority of the computation procedures and causes significant reduction of efficiency of the method. Based on the mentioned discussions it is concluded that a high computational load will be demanded in such cases, especially for nonlinear systems, which de-motivates use of these methods. Therefore a proper method for our aim should have the following characteristics

1. Capability of estimating the barrier level for a given probability
2. Needless of significant a-priori system information i.e. a *black-box* method
3. Applicable on high dimensional problems without significant drop on efficiency
4. Low demands on the memory (memory overflow can be expected)

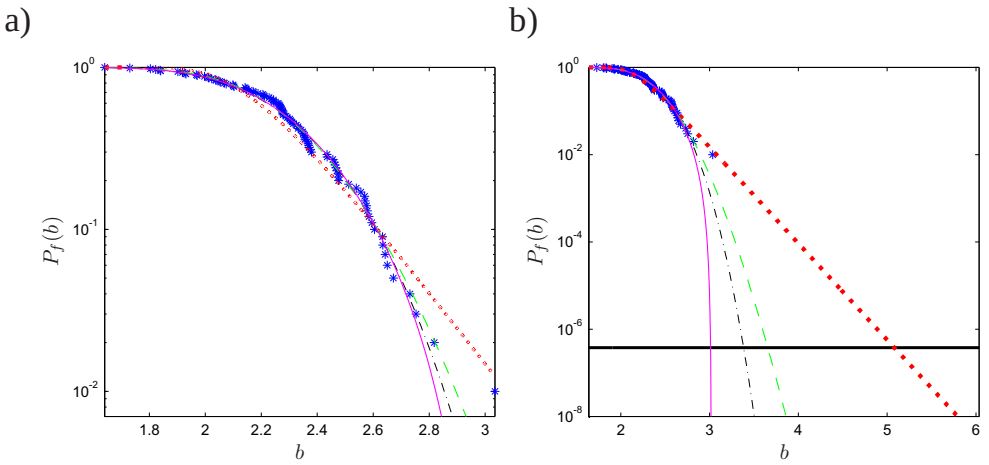

Figure 1.3 Extreme values of the response of the fixed speed wind turbine; a) Fitted distributions within the range of samples, b) Extrapolation of the fits to the 50 year return period; —: 50 year return period, -.-: 3 parameter Weibull, · · · : Gumbel, - - -: 3 parameter Lognormal, —: Generalized Extreme Value

1.4 Curve fitting approach

The simplest approach to obtain such information is the so-called "curve fitting" approach in which an extreme value distribution with unknown parameters will be fitted to the available samples of the process (Caires and Sterl 2005; Mackay *et al.* 2010). The distribution can be of any type i.e. Weibull, Gumbel, Lognormal, Generalized Extreme Value (GEV) etc. Here it is implicitly assumed that the parent distribution of the process belongs to the domain of attraction of one of the extreme value distributions; therefore the excess values above a given threshold follow a Generalized Pareto (GP) distribution (Naess and Clausen 2001). The required failure probability will be extrapolated from the fitted distribution. The data might be taken either from measured responses of a real wind turbine or from epoches of the response simulated by computer.

Additionally some sample refinement methods such as epochal method or the Peaks Over Threshold (POT) can be combined in order to obtain more convenient results. The POT method has been used frequently in the wind engineering industry for estimation of the extreme conditions of wind turbines i.e. extreme wind load. It can be shown that if the parent distribution of the outcrossing event belongs to one of the extreme value distributions then outcrossing above a sufficiently large level follows a Generalized Pareto (GP) distribution, (Naess and Clausen 2001). The most controversial part of the method is the type of distribution which should be fitted to the data. The type of probability distribution has high impact on the further analysis which is to be made based on such extrapolations. For instance it is reported by some authors that incorporation of the Gumbel distribution results in very low safety levels for structures subjected to wind load than to gravity load, (Minciarelli *et al.* 2001; Simiu and Heckert 1996). The extrapolations based on Weibull distribution will always lead to lower values for design loads, (Harris 2005); hence Weibull distribution might be used instead. From practical point of view Gumbel distribution is among the most popular distributions for the wind speed, (Ellingwood *et al.* 1980; Cook 1982). Nevertheless the use of POT and Monte Carlo simulation is more in favor of the reverse Weibull distribution, (Simiu and Heckert 1996). Simiu et al. (Simiu *et al.* 2001) analyzed 100 wind

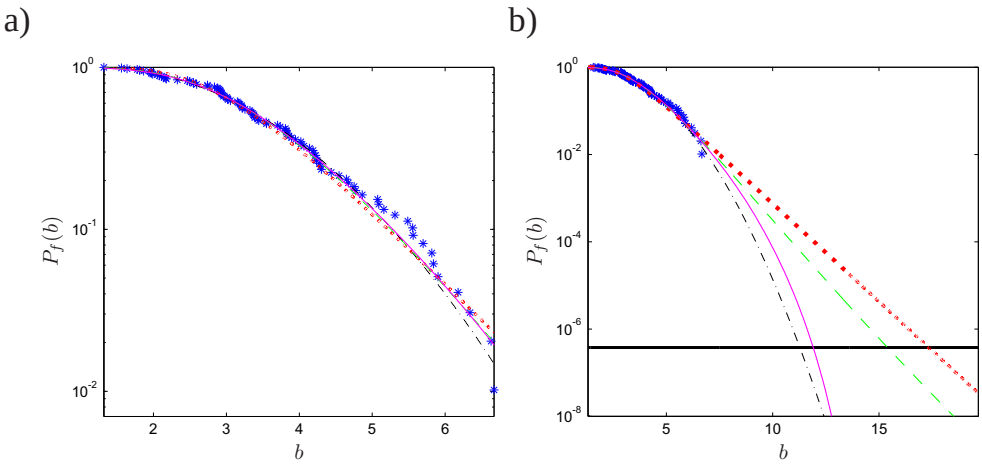

Figure 1.4 Extreme values of the response of the variable speed wind turbine; a) Fitted distributions within the range of samples, b) Extrapolation of the fits to the 50 year return period; —: 50 year return period, -.-: 3 parameter Weibull, · · · : Gumbel, - - -: 3 parameter Lognormal, —: Generalized Extreme Value

records from different stations and fitted the distribution to the dynamic wind pressure, as an alternative to the wind speed, and concluded that Weibull distribution fits better than the Gumbel distribution to the dynamic pressure of the wind. From the physical point of view assuming the Weibull distribution for the maxima of the annual epochs of the wind speed makes sense since Weibull distribution has limited upper tails which means that in reality an upper limit for the wind speed exists; while Gumbel distribution assumes no upper bound for the extreme value i.e. wind speed, (Simiu and Heckert 1996). Although theoretically speaking, if it is assumed that the wind speed is Weibull distributed, the parent distribution of maxima, then its maximas should be Gumbel distributed, (Harris 2005; Harris 2004; Cook and Harris 2004). Clearly it can not be said for sure which distribution should be used since Weibull, Gumbel, Log-normal have all been used by different authors, (Freudenreich and Argyriadis 2007; Naess and Gaidai 2009).

The advantage of this approach is its simplicity (the computational task is confined to find the distribution's parameters through fitting) and applicability to both *measurement and simulations*. Another advantage is that it can be applied to *low number of samples*. The disadvantage of this approach is that due to the inherent uncertainties in the fitting type, these methods do not yield accurate estimates of the low failure probabilities, i.e. it is not clear which extreme value distribution should be used in different situations. In order to illustrate the uncertainty in these extrapolation procedures four different extreme value distributions have been fitted to maxima of 100 epoches of the wind turbine model of chapter 3. In the fixed speed model it is assumed that the turbine is rotating with constant rotational speed equal to the rotor's nominal speed. In the variable speed model the blade pitch controller is in charge of keeping the rotational speed of the rotor constant around its nominal value. The simulated values of the maxima (barrier levels) are normalized by the mean value and standard deviation of the time history of all responses. The results of fits for fixed and variable speed models are shown in figures 1.3 and 1.4 respectively. It is seen from the figures that in both cases the extrapolation of different fits results in significantly different values for the 50 year return period hence indicating high uncertainty in the estimates.

1.5 Sampling approach

The other approach to the problem is sampling. This approach has strict requirement that a mathematical model of the system, which can be solved numerically by computer, is available. Next the population space of the problem can be simulated by taking random samples (realizations) of the process under consideration i.e. responses of the wind turbine. As the number of realizations increases toward infinity the distribution of the process will converge to its true distribution. This procedure is the basis of the so-called Standard Monte Carlo (SMC). The drawback of this approach is that it has very high computational demand for estimation of the low probability events. Therefore the variance reduction methods are proposed which try to cross over this computational demand by controlling the sample generation procedure.

1.5.1 Standard v.s. Variance Reduction Monte Carlo

Standard Monte Carlo

The subject of SMC is estimation of (1.5) by sampling. Here $f(\mathbf{X})$ denotes the joint PDF of the stochastic variable $\mathbf{X}$ and $\tilde{G}(\mathbf{X}) < 0$ is the Limit State Function (LSF) of the problem. The simplest way to approximate this integral is to take samples of $\mathbf{X}$ and examine if they are in the *failure domain*, $\mathfrak{F} = \{\mathbf{X}|\tilde{G}(\mathbf{X}) < 0\}$, or the *safe domain*, $\mathfrak{S} = \{\mathbf{X}|\tilde{G}(\mathbf{X}) > 0\}$.

$$P_f = \int \cdots \int_{\tilde{G}(\mathbf{X})<0} f(\mathbf{X})d\mathbf{X} = \int \cdots \int_{G(\boldsymbol{\Xi})<0} \varphi(\boldsymbol{\Xi})d\boldsymbol{\Xi} \tag{1.5}$$

where $G(\boldsymbol{\Xi}) \equiv \tilde{G}(\mathbf{X})$ is the LSF when its variables $\mathbf{X} = \{X_1, \cdots, X_n\}$ are transformed into normalized iid Gaussian variables $\boldsymbol{\Xi} = \{\Xi_1, \cdots, \Xi_n\}$ using i.e. Rosenblatt transformation. $\varphi(.)$ denotes the standard normal density function. The transformation is necessary in order to guarantee invariance of the solution toward definition of the LSF function (Madsen *et al.* 2006). Introducing the indicator function $I[.]$ defined as (1.6) allows changing the boundaries of the integrals in (1.5) into the domain of normal random variables as shown in (1.7).

$$I[G(\boldsymbol{\Xi})] = \begin{cases} 1 & G(\boldsymbol{\Xi}) \geq 0 \\ 0 & G(\boldsymbol{\Xi}) < 0 \end{cases} \tag{1.6}$$

$$P_f = \int \cdots \int_{G(\boldsymbol{\Xi})<0} \varphi(\boldsymbol{\Xi})d\boldsymbol{\Xi} = \int_{-\infty}^{\infty} \cdots \int_{-\infty}^{\infty} I[\boldsymbol{\Xi}]\varphi(\boldsymbol{\Xi})d\boldsymbol{\Xi} \tag{1.7}$$

The procedure of SMC consists of simulating the space of the process $\boldsymbol{\Xi}$ by generating random samples from $\varphi(\boldsymbol{\Xi})$. At this point the drawback of this approach becomes clear; which is, excessive number of samples should be generated for accurate estimation of the low probability events. Next, it is possible to choose those realizations which have any specific characteristics according to the specifications of the LSF $G(\mathbf{X})$. The LSF in structural dynamic is typically defined as exceedance of one(some) of the components of the process from a certain level, called the "barrier level" (or alternatively called "threshold level") b, within a prescribed time frame. The mean value and the standard deviation of the probability of occurrence of the event can then be estimated by simple counting rules as indicated in (1.8).

$$\hat{P}_f = \frac{1}{N}\sum_{n=1}^{N} I[G(\boldsymbol{\xi}_i)] \quad , \quad \sigma^2_{\hat{P}_f} = \frac{\hat{P}_f(1-\hat{P}_f)}{N} \tag{1.8}$$

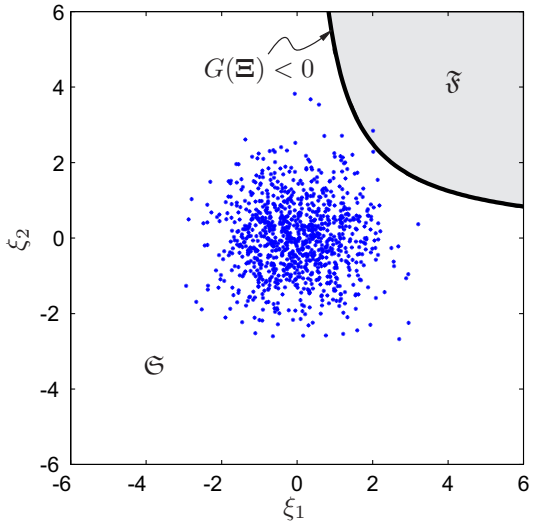

Figure 1.5 Schematic view of the Standard Monte Carlo

where $\boldsymbol{\xi}_i$ denotes a realization of the stochastic variable $\boldsymbol{\Xi}$. The variance of the SMC estimate, c.f. (1.8), proposes that if probability of $P_f = 10^{-5}$ is to be estimated with standard deviation of the estimation, $\sigma_{\hat{P}_f}$, of about 0.3, $N \approx 10^6$ samples should be generated. As a rule of thumb the sample generation is continued until at least 10 samples of the required event occur i.e. ten samples fall within the failure region. This guarantees that the coefficient of variation of the estimate is less than or equal to 0.3 indicating good accuracy in results. It is obvious that events with low probability of occurrence need more simulation (more samples) to let them happen. Figure 1.5 shows a schematic view of the samples of a normal Gaussian stochastic process composed of two iid random variables $\xi_1 \sim \mathcal{N}(0,1)$ and $\xi_2 \sim \mathcal{N}(0,1)$. Here the set of dots shows the so-called *sampling density* of the SMC concentrated around the origin of the space and the solid line indicates the LSF. The failure domain, i.e. domain of occurrence of the considered event, is shown by $\mathfrak{F}$ in grey. It can be seen that only one dot(sample) falls within this domain while many others are in the so-called *safe domain*, hence a rare event.

Variance Reduction Monte Carlo

The idea of the Variance Reduction Monte Carlo (VRMC) methods is to estimate the required probability with lower variance of the estimation compared to the variance of the estimations of the SMC, $\sigma^2_{\hat{P}_f}$ in (1.8) c.f. (1.9) where $\tilde{I}[\cdot,\cdot]$ denotes a *modified* indicator function consistent with the changes proposed by the method.

$$\tilde{P}_f = \sum_{n=1}^{N} \tilde{I}[G(\boldsymbol{\xi}_i), N] = \hat{P}_f \quad , \quad \sigma^2_{\tilde{P}_f} < \frac{\tilde{P}_f(1-\tilde{P}_f)}{N} = \sigma^2_{\hat{P}_f} \tag{1.9}$$

Therefore with the same number of samples higher accuracy in the simulation is achievable. Among the available VRMC methods four methods are considered in this work e.g. Importance Sampling (IS), Distance Controlled Monte Carlo (DCMC), Asymptotic Sampling (AS) and Sub-

set Simulation (SS). The "importance sampling" and the "distance controlled Monte Carlo" are described in detail in the abstract of the thesis. The detailed description of the "asymptotic sampling" and "subset simulation" and their application on the developed wind turbine model are provided within the papers in the appendix.

1.5.2 Importance Sampling

One of the most well-known methods for this purpose is the Importance Sampling(IS) based on the Girsanov theorem (Newton 1994; Tanaka 1998). The method shifts the sampling density of the simulation to the boundaries of the failure domain. Therefore more samples in the failure domain will be produced, c.f. figure 1.6. This shift is done in the multi-normal integral of (1.5) by changing the density as shown in (1.10). The red dots in figure 1.6 are the samples generated by the shifted sampling density $\phi(\boldsymbol{\Xi})$ in (1.10). However now it is obvious that the probability mass that is carried by each red sample is not equal to the probability mass of its counterpart within blue samples. More precisely the probability mass of the samples of the SMC, blue samples, is equal to one while for IS samples, red samples, it is equal to $h(\boldsymbol{\Xi})$.

$$P_f = \int \cdots \int_{G(\boldsymbol{\Xi})<0} \frac{\varphi(\boldsymbol{\Xi})}{\phi(\boldsymbol{\Xi})}\phi(\boldsymbol{\Xi})d\boldsymbol{\Xi} = \int \cdots \int_{G(\boldsymbol{\Xi})<0} h(\boldsymbol{\Xi})\phi(\boldsymbol{\Xi})d\boldsymbol{\Xi} \tag{1.10}$$

As can be seen from figure 1.6 this action located many more realizations in the failure domain hence allows a more accurate estimate of the event. The shift from the SMC sampling density to the IS sampling density takes place by introducing a set of the so-called control functions. These will be added to the system excitation as deterministic drifts. This scheme has been reported successful in some simple Stochastic Differential Equations (SDE) such as a Brownian motion, (Tanaka 1998; Naess and Skaug 1999a; Olsen and Naess 2006), or a crack growth model, (Tanaka 1999). Success of this scheme for non-oscillatory systems is also witnessed by other researchers and with somewhat different approach, (Dahl 2002). Nevertheless the introduced original scheme is incapable of satisfactory estimation of low probability events for high dimensional oscillatory systems, (Naess and Skaug 1999b). This urges changing the control functions which are depend more on the system behavior (Bucher 2000). The extension to nonlinear problems was studied by Au and Beck, (Au and Beck 2001b), and separately by Macke and Bucher, (Macke and Bucher 2003). Since the failure region for the oscillatory systems is relatively large, it is not efficient to produce samples in the region with the largest probability of failure. To overcome this problem the so-called multi modal sampling density might be used which generates the samples around a number of points in the failure domain. The sample generation process is emphasized around each point relative to the PDF at that point, (Karamchandani 1990). Such approach is considered in (Macke and Bucher 2003), i.e. the multi-modal sampling, and is shown that the method has a very satisfactory performance on linear and non-linear structural dynamic systems. The concept of design points from the reliability point of view and the method to choose them using FORM is discussed by Koo et. al, (Koo *et al.* 2005). They have mentioned an alternative way of designing the control functions based on the free vibration analysis and have compared their results with the exact design points, calculated using optimization methods, for both linear and non-linear structural systems which is in very good agreement with previous literature. Other possibilities for determination of the design points are optimization methods such as Genetic Algorithm (GA), (Obadage and Harnpornchai 2006). A modified version of the procedure proposed in previous literature with an iterative scheme is proposed and is shown that is capable of approximating low

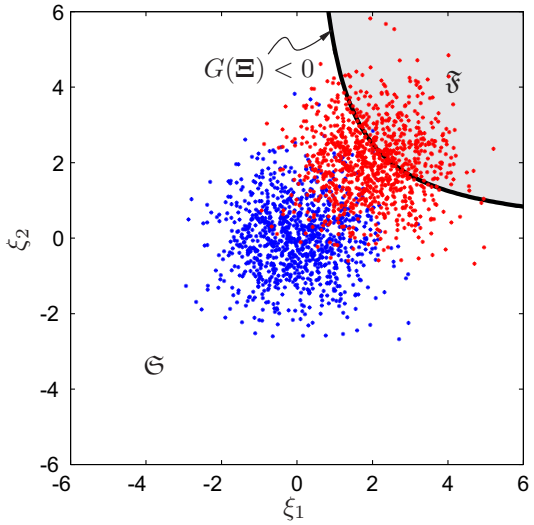

Figure 1.6 Schematic view of the importance sampling

failure probabilities for non-linear SDOF systems such as Duffing and Van der Pol oscillators (Olsen and Naess 2007; Naess and Gaidai 2008). In case of continuous Gaussian excitation it is necessary to introduce a rational shaping filter at the expense of increasing the dimensions of the dynamic state vector, (Ogawa and Tanaka 2009). This problem has been considered by some authors, (Koo *et al.* 2005; Olsen and Naess 2007), and a rigorous study on this subject is specifically performed by Ogawa and Tanaka, (Ogawa and Tanaka 2009), where they have used the Ornstein-Uhlenbeck process to construct a stochastic excitation having a specified power spectrum.

1.5.3 Distance Controlled Monte Carlo

The strategy of the splitting methods such as the Double & Clump (D&C) or the Distance Controlled Monte Carlo (DCMC) is to increase the number of realizations in the tails of the distribution function by splitting those closer to the indicated rare event. Figure 1.7 shows a schematic view of the DCMC approach which is the counterpart of the figure 1.5 in section 1.5.1. These methods categorize the importance of the realizations based on their closeness to the failure region, whereby the samples in the low probability regions, i.e. tails of the PDF, are considered important while the rest are considered unimportant. The important samples are then Doubled while the unimportant ones are Clumped together, (Pradlwarter *et al.* 1994; Pradlwarter *et al.* 1998). Russian Roulette & Splitting (RR&S) is a special variation of D&C in which the clumping unimportant realizations is replaced by Russian Roulette, (Pradlwarter and Schuëller 1997). It is also shown that as a penalty of numerical simplification, the variance of the failure estimate of the RR&S is larger than the D&C due to the unbalance of the statistical moments it urges during the killing process. An important issue in the RR&S procedure being the definition of the important from unimportant processes is addressed by introduction of the Distance Control (DC) in (Pradlwarter and Schuëller 1999); nevertheless the RR&S-DC may be favorable compared to the D&C since its proof for unbiasedness can be done rather easily and it does not suffer from

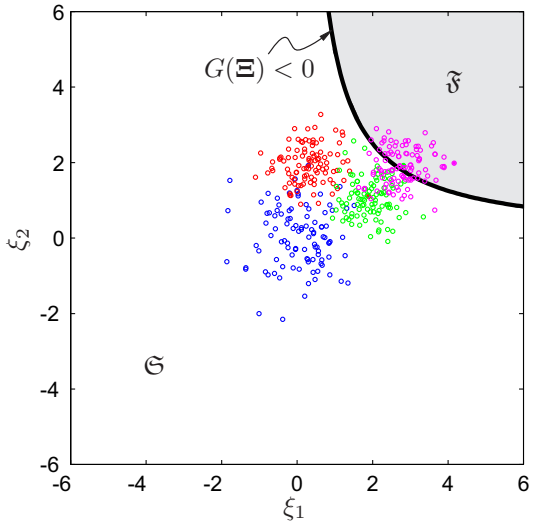

Figure 1.7 Schematic view of the distance controlled Monte Carlo

the artificial spatial dislocation as is the case for D&C. Therefore in the Distance Controlled Monte Carlo (DCMC) the distance measure is used to define the importance of each realization. Furthermore in order to avoid monotone increase of the number of samples sue to the splitting the RR&S is used to kill some unimportant processes.

1.5.4 Asymptotic Sampling

The fundamental problem of the reliability is defined as the solution of the (multi-normal) probability integral (1.11) i.e. an alternative way of representing (1.5)

$$P_f(\Xi) = \int\limits_{G(\Xi)<0} \prod_{i=1}^{N} \varphi\Big(-\frac{1}{2}\Xi_i^2\Big) d\Xi \tag{1.11}$$

$\varphi(.)$ denotes the standard normal density function. There exist a point with highest influence on the solution to this integral called the *design point*, $\boldsymbol{\xi}^*$. The characteristic of this point is that it is the point on the Limit State Function (LSF) with minimum distance to the origin in the space of the transformed variables Ξ. The primary approximation of this integral consists of fitting a (hyper)surface to the LSF at the design point and estimating (1.11) by this approximation; this is the idea of the so-called the First Order Reliability Method (FORM). A more accurate approximation of the LSF at the design point can however be obtained by fitting a paraboloid to it which is the basis of the Second Order Reliability Methods (SORM). Breitung (Breitung 1984) showed that the effect of the shape of the integral domain is projected into (1.11) through the principal curvatures of the LSF i.e. the eigenvalues of its Hessian matrix. Later the asymptotic approximation of this integral, as is expressed in (1.12), in the standard normal random space was obtained by Kiureghian et al. (Kiureghian *et al.* 1987) and in the space of the random variables

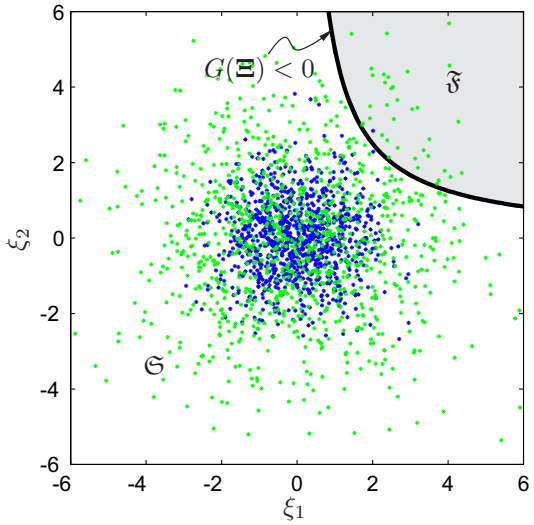

Figure 1.8 Schematic view of the asymptotic sampling

using the Laplace's integrals and Mill's ratio by Breitung (Breitung 1989).

$$P_f = (\beta; \Xi) = \int\limits_{G(\beta^{-1}\Xi)<0} \prod_{i=1}^{N} \varphi\Big(-\frac{1}{2}\Xi_i^2\Big) d\Xi \tag{1.12}$$

β in the parentheses on the left hand side denotes scaling of the variables in the LSF. The boundaries of the integral in (1.12) can be changed to unscaled LSF which reads

$$p(\beta; \Xi) = \beta^N \int\limits_{G(\Xi)<0} \prod_{i=1}^{N} \varphi\Big(-\frac{\beta^2}{2}\Xi_i^2\Big) d\Xi \tag{1.13}$$

Since then several methods are proposed for the SORM approximations of the (1.11) (Tvedt 1983; Tvedt 1990; Köylüoğlu and Nielsen 1994). The key difference between FORM and SORM approximations is played by the curvatures of the LSF as shown primarily in (Breitung 1984). Nevertheless calculation of the curvatures of the LSF at the design point is not an easy task for high dimensional problems. The numerical estimation of these curvatures can be performed using a *Gradient Projection* (GP) optimization algorithm (Kiureghian and Stefano 1991). Still the gradient of the LSF is required which is computationally demanding. The mentioned methods did not propose any sampling scheme which takes the advantage of asymptotic estimation of the failure probabilities. Bucher (Bucher 2009a) introduced such a sampling scheme and called it the Asymptotic Sampling (AS). The idea of this sampling is to scale up the random variables of the problem, $\boldsymbol{\xi}$, in order to get more samples in the failure domain c.f. figure 1.8. A primary discussion on the applicability of the method on design of earthquake elements was reported in (Bucher 2009b). Sichani et al. (Sichani *et al.* 2011a) showed the application of the method for the reliability of several linear and nonlinear structural systems. The applicability of the method for efficient estimation of the first passage probability of a wind turbines and a new scheme for fine tuning the estimation parameters is discussed in (Sichani *et al.* 2011b).

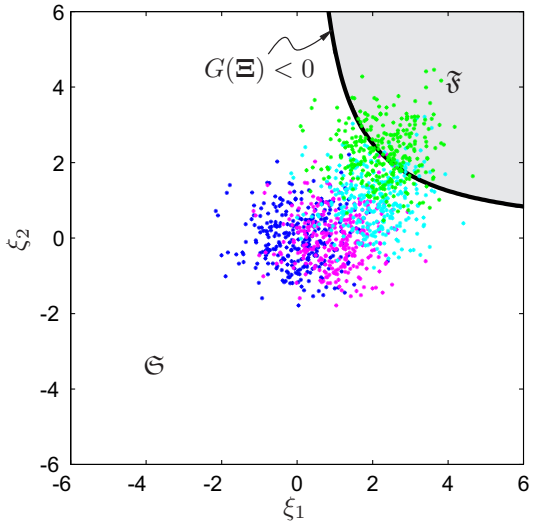

Figure 1.9 Schematic view of the subset simulation

1.5.5 Subset simulation

Another approach is the Subset Simulation (SS) (Au and Beck 2001a), which starts by taking a relatively wide superset of the intended failure region with a high probability of occurrence. This superset is chosen so that it includes the entire failure region as its subset. The Monte Carlo simulation is then used to generate some realizations in this superset. In the second step, the method incorporates a modified Metropolis algorithm (Metropolis *et al.* 1953) and takes advantage of the Markov property of the state vector, to evolve those realizations inside the superset. The first superset is taken as the whole probability region. The next superset is chosen as a subset of this superset with the same considerations as for the present superset. The second step is repeated *m* times, until the final failure region is completely attained. By this approach, a low probability is represented as multiplication of *m* high(-er) probabilities; the first superset represents a normal probability, and is estimated via Monte Carlo simulation, and the next supersets represent conditional probabilities, estimated by the Metropolis algorithm and the Markovian assumption.

Following the concept of the splitting, Ching et al. (Ching *et al.* 2005) introduced it into the original SS and later combined it into a hybrid subset simulation (Ching *et al.* 2005). The spherical subset simulation (S3) is introduced in (Katafygiotis and Cheung 2007) which transforms the excitations into a unit hyper sphere allowing to concentrate the sampling density of the simulation around the directions in which the so-called seeds or important directions for the Markov Chains are concentrated. A new scheme that combines the method with Importance Sampling (IS) and also the reliability sensitivity analysis with SS have been addressed in (Song *et al.* 2009). On the same bases of the subset simulation the horseracing simulation (Zuev and Katafygiotis 2011a; Zuev 2009) constructs the Conditional Cumulative Distribution Function (CCDF) as the simulations are running. This allows the method to recognize the most reliable realizations within simulation and use them for estimating the system's probability hence increases the rate at which lower barrier levels are achieved.

The recent proposals in this field have focused their attention on increasing efficiency of the method by modifying its sampling scheme. In this respect Santoso et al. (Santoso *et al.* 2011) proposed the modification which reduces the correlation of the Markov chains of the method. This should lead in reduced variance of the estimations of the method. They proposed to re-generate a new Markov chain whenever it is rejected by the Metropolis-Hastings accept\reject test. However for high dimensional problems, i.e. problems with thousands of basic random variables, this may not result in any improvement of the results. This is since the probability that the Markov chains move to the next state in the Metropolis-Hastings algorithms approaches to zero exponentially as the number of basic random variables of the problem increases. Another approach but in the similar concept is proposed in (Zuev and Katafygiotis 2011b) by delaying the rejection test of the algorithm. The main difference between this approach with previous one is that here the sample regeneration takes place whenever a candidate sample is rejected in the accept\reject by the dynamic analysis i.e. the candidate sample did not increase the barrier level.

1.5.6 Average Conditional Exceedance Rates (ACER)

The distribution of the extreme values of the stochastic process $X(t)$ over the time interval $t \in [0, T]$ under the Poisson assumption is given by (Naess 1984)

$$F_{M(t)}(b) = \text{Prob}\{M(t) \leq b\} = \exp\left(-\int_0^T \nu^+(b;t)\right) \tag{1.14}$$

where $\nu^+(b;t)$ denotes the mean up-crossing rate of the extreme values of the stochastic process $X(t)$ at time $t \in [0, T]$ from the barrier level b. It is clear that for a stationary stochastic process the mean up-crossing rate is independent of time thus can be written as

$$\nu^+(b) = \frac{1}{T}\int_0^T \nu^+(b;t)dt \tag{1.15}$$

Therefore if the mean up-crossing rate of the process is known, distribution of its extreme values can be calculated using (1.14). For this reason Rice's formula allows expressing the distribution of the mean up-crossing rate of the stochastic process $X(t)$ from the barrier level b, e.g. $F_{M(t)}(b)$, as (Soong and Grigoriu 1992)

$$\nu^+(b;t) = \int_0^\infty \dot{x} f_{X,\dot{X}}(b,\dot{x},t)d\dot{x} \tag{1.16}$$

where $f_{X,\dot{X}}(b,\dot{x},t)$ denotes the joint PDF of the $X(t)$ and $\dot{X}(t) = dX(t)/dt$. However this approach requires having the joint distribution of the process and its first time derivative $f_{X,\dot{X}}(b,\dot{x},t)$ which for most nonlinear processes can not be calculated even numerically. Another approach to this problem can be to introduce conditions in (1.16) which turns into (Naess and Gaidai 2008)

$$\nu^+(b;t) = \int_0^\infty \dot{x} f_{\dot{X}|X}(\dot{x}|b,t)d\dot{x} f_X(b) = E\{\dot{X}^+|X = b\}f_X(b) \tag{1.17}$$

where $\dot{X} = \max\{X(t); 0 \leq X \leq T\}$. For stationary processes it is proposed, based on (1.17), to assume the following mathematical format for the up-crossing rate of the process

$$\nu^+(b) = \tilde{\kappa}(b)\exp(-\alpha(b-\gamma)^\vartheta) \tag{1.18}$$

where $\tilde{\kappa}(b)$ will be a slowly varying function of the barrier level and will be approximately constant for high barrier levels that means $\lim_{b\to\infty} \tilde{\kappa}(b) \approx \kappa$. Therefore the methods ends up in estimating the parameters κ, α, γ and ϑ of (1.18). These parameters are estimated from the simulation time histories by some methods primarily developed by (Naess and Gaidai 2008). The method further elaborated regarding the statistical dependencies of the extreme value samples of the system response (Naess and Gaidai 2009). Here they introduced a numerically efficient way of estimating the Average Conditional Exceedance Rate (ACER) of the process which is assumed to have a similar mathematical closed form expression as proposed in (1.18). The advantage is that the ACER approach takes into account the statistical dependence of the samples of the process (Naess and Gaidai 2009; Naess *et al.* 2009). The latter approach is further elaborated as described in appendix G. It worth noting that the underlying assumption of these approaches is that the extreme values of the process are asymptotically Gumbel distributed c.f. (Naess and Gaidai 2008).

1.6 Probability density evolution approach

The evolution of the joint PDF of a process governed by a stochastic differential equation driven by Gaussian white noise is defined as the solution to the Fokker-Planck-Kolmogorov (FPK) equation. If this solution is available, it can be integrated on the specified domain to obtain the probability of failure. However the factor that makes this solution difficult is the dimensions of the problem. The recently introduced Generalized Density Evolution Method (GDEM), (Li and Chen 2004; Chen and Li 2009; Li and Chen 2009), has opened a new way toward realization of the evolution of the PDF of a stochastic process; hence an alternative to the FPK. The introduced method can handle high dimensional problems more easily however has some strict limitations on the number of basic random variables of the system. The idea is to obtain the evolution of the PDF of the process on the characteristic curves of the Liouville equations obtained for evolution of the PDF. However this approach has not been within the scope of this study, which has been the VRMC methods, it may be considered in future in case its applicability can be confirmed.

1.7 Chaotic motion of shallow cables

Wind turbine models include highly nonlinear structures. These nonlinearities stem from different sources such as structural nonlinearities due to large deformation and gyroscopic forces on the structural elements, loading nonlinearities due to aero-elastic load calculations and the time dependency of the system due to the wind turbine controller i.e. the pitch controller. All these elements may cause issues in stability or chaotic behavior of the system. A critical point on these problems is the whirling motion of the wind turbine rotor shaft which may cause instability or chaotic motion of the system. Obviously if the system behaves chaotic or runs into instability the reliability analysis of the system requires a more rigorous in detail study of the system. This is since the population of the system responses may change considerably. As in chaotic systems it is not only the loading which should be the basis of the analysis but also the initial conditions. In order to study these problems the flap-wise degrees of freedom (DOF) are not sufficient and the edgewise degrees of freedom should be included in the model. However developing such a model has been out of scope of this work as a warm start up the same analysis is performed

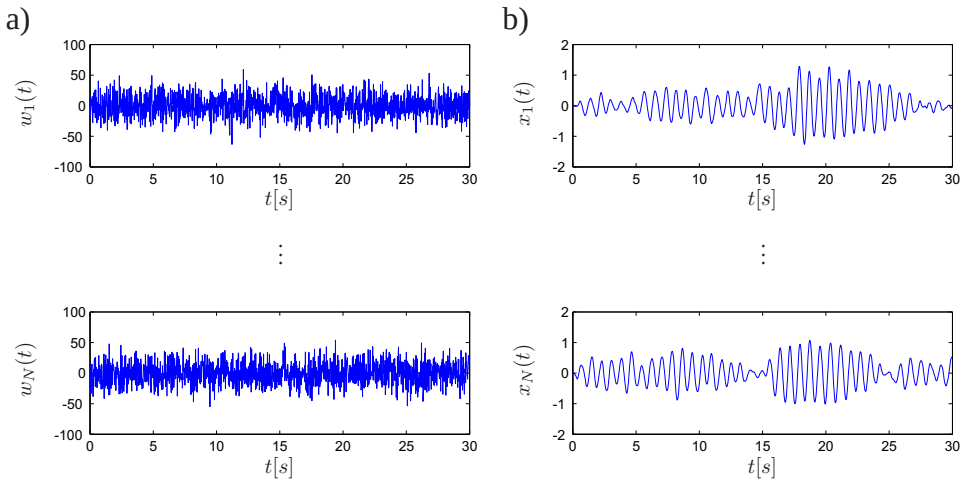

Figure 1.10 Different realizations of the benchmark problem; a) Excitation realizations, b) Response realizations

on the chaotic motion of a shallow cable (Nielsen and Sichani 2011). The cable model is also reduced to a two DOF model and then it is used for the chaotic analysis. This is done in order to decrease the computational cost of the analysis. This study can be followed by developing the nonlinear wind turbine model and applying similar analysis on it which is subject to future study.

1.8 Benchmark problem for VRMC methods

The relative performance of the variance reduction Monte Carlo methods is evaluated based on a single DOF linear oscillator (1.19), characterized by $\omega_n = 1s^{-1}$ and $\zeta_n = 0.01$

$$\ddot{x}(t) + 2\zeta_n\omega_n\dot{x}(t) + \omega_n^2 x(t) = w(t) \tag{1.19}$$

$w(t)$ is zero-mean Gaussian white noise with unit intensity. The barrier level is normalized with respect to the standard deviation of the response $\sigma_X = (4\zeta\omega^3)^{-1/2}$.

$$b_N = \frac{b}{\sigma_X} \tag{1.20}$$

For all methods in the benchmark examples 500 time series of the response to the excitation are simulated for analysis. Figure 1.10 shows some realizations of the system on the left column; realizations of the responses to these excitations are shown on the right column of the figure. In all numerical simulations performed in this study the limit state function is defined by the first passage outcrossing of the response from the given barrier level. In order to make maximum use of the simulation outcomes it is more convenient to choose the maximum of the absolute value of each simulated realization and sort them c.f. figure 1.11.a. This makes possibility of having the outcrossing from any certain barrier level b during the given time frame $t \in [0, T]$ c.f. figure 1.11.b.

For estimation of probability of failure in a long time interval, IS urges use of larger Δt for time integration than the DCMC. This comes from the point that all of the control functions

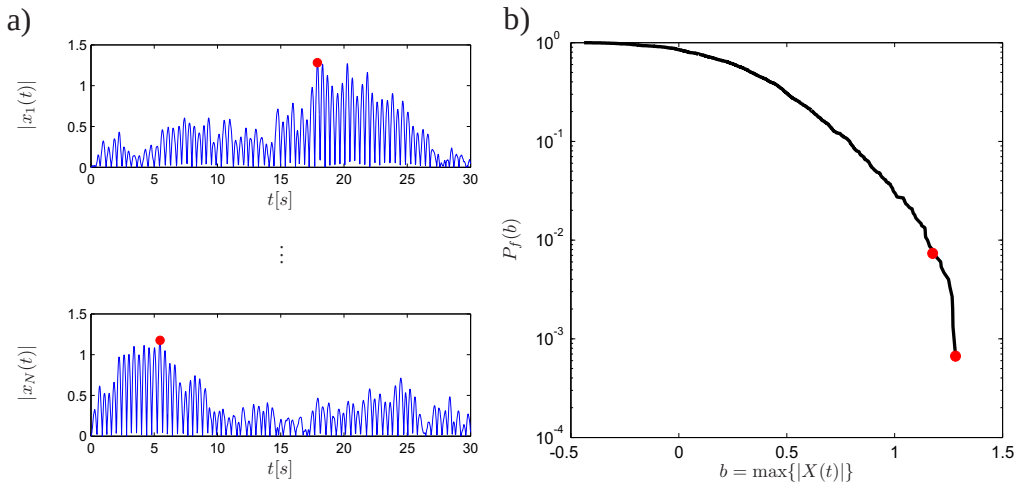

Figure 1.11 Transformation to the LSF and failure probability for the benchmark problem; a) Absolute values of the realizations of the response, b) Failure probability

which cause barrier crossing at each time instant in the whole time interval should be available for calculating the failure probability i.e. due to the requirement of the multi-modal sampling density. This requires either high memory to save total time history of all of the control functions or to compute all of the the control functions each time the simulation is performed, thus a dilemma between memory and speed. This is while in DCMC the opposite is actually preferred. This is since the more time points available within the same time frame, there exist more possibilities of pushing processes toward failure region by Russian Roulette and Splitting. Moreover the requirements of the DCMC on saving information is rather low hence no memory allocation problem will be encountered in this regard. However the numerical time integration should be repeated on more time points which clearly increases the demand on the computation cost.

Application of SS also needs saving some of the realizations of excitations of the previous simulations i.e. the so-called *seeds*, c.f. appendix F. The number of seeds is not constant and is related to both the *total number of realizations* and the *intermediate probability levels* of the simulations, i.e. p_0 in appendix F. These parameters together define the number of seeds needed to be stored in the memory. Nevertheless this is typically about 10% of all realizations which is still acceptable considering storage memory requirements.

Asymptotic sampling has no limitations or demands on either the time resolution of the numerical time integration or memory for storing the simulated data. Therefore the time resolution of the simulation could be set to the highest possible in order to save computation time. In the benchmark solution of all methods except DCMC $\Delta t = 0.02[s]$ and $t \in [0, 30]s$ has been used.

1.9 Layout of the thesis

The thesis is then written in the following chronological order:

Chapter 1 The overview on the problem of reliability of wind turbines is given in this chapter. The outline of the thesis and summary of the methods which are considered within this work are presented in this chapter.

Chapter 2 Describes the wind field generation based on stochastic subspace method. The method incorporates the Kalman filter to construct a so-called *forward innovation model* which is the final state space format that its parameters will be estimated. These parameters will then be estimated using a balanced realization method. A numerical example is presented which demonstrates use of the method.

Chapter 3 Describes the details of the reduced order model of the wind turbine model. The model is represented in its final form which integrates the collective pitch controller in it. The structural part is modeled based on the Finite Element (FE) method and a modal reduction is applied. Integration of the reduced order model with the state space wind generator results in a model with low computational demand - compared to the conventional wind turbine codes i.e. FAST, FLEX or BLADED - suitable for statistical analysis based on sampling i.e. Monte Carlo.

Chapter 4 Addresses the application of “importance sampling” for general oscillatory systems. The main part of this chapter deals with theory of importance sampling. A cook book for applying the method on any system is also presented in the chapter. Finally flaws of the method in application on the wind turbine are discussed in the chapter.

Chapter 5 Addresses application of the Distance Controlled Monte Carlo on the benchmark problem. Similar to chapter 4, the details of the steps taken in the method are described in detail and a cook book for application of the method is presented. The pros and cons of the method for application on the wind turbine are discussed at the end of the chapter.

Chapter 6 Provides an abstract conclusion achieved in this study.

Appendix A Provides a short derivation of the Kalman filter gain and Riccati equation used in the wind field generation.

Appendix B Describes details of the derivations of the importance sampling for Wind turbines.

Appendix C Discusses the application of the “asymptotic sampling” on general nonlinear high dimensional structural dynamic problems. The important factors which affect quality of the results when AS is applied to structural dynamic systems are addressed in the paper. An algorithm which increases efficiency of the method is also presented in the paper.

Appendix D Provides a quick overview on the four VRMC method e.g. IS, DCMC, AS and SS and their performance is compared on a common problem. Based on the results of this analysis and considerations of the wind turbine requirements on the failure probability estimations, conclusions are made on the applicability of the methods on the wind turbine model.

Appendix E Addresses a proper scheme for applying "asymptotic sampling" on the wind turbine model. The developed algorithm takes advantage of all simulation results for construction of the Cumulative Distribution Function (CDF) of the problem. This algorithm is then applied for failure estimation of the wind turbine model.

Appendix F incorporates the PID pitch controller in the wind turbine model. The failure probability of the pitch regulated model is then estimated by the standard "subset simulation" and two of its most recent modifications e.g. the "reduced chain correlation" and the "delayed rejection" algorithms. The results of the three methods have been compared together on the wind turbine model.

Appendix G Presents an enhancement on the estimation of the Average Conditional Exceedance Rates (ACER) of stochastic processes. Here the way the confidence bounds of the method are being estimated and estimation of the fitting parameters using an optimization algorithm are enhanced. This results in more robust estimation of the fit to the ACER functions. Finally the failure probability of the pitch regulated wind turbine using this method is carried out.

Appendix H addresses analysis of the chaotic motion of the shallow cables. In the paper the chaotic motion of cables with small sag in its sub and super harmonic frequencies are considered. The Lyapunov exponents are used to identify the range on which the systems behaves in a chaotic regime.

Note: The details of the "importance sampling" and "distance contol Monte Carlo", as they have been applied on the benchmarks problem, have been described in the abstract of the thesis. However due to difficulties in application on the wind turbine model only the "asymptotic sampling", "subset simulation" (the original method and the recent developments with two new sampling schemes) and the "ACER method" have been applied on the wind turbine model. The "horseracing simulation" has also been applied on the benchmark problem which showed bias in its estimates, therefore was not considered further for application on the wind turbine model.

CHAPTER 2
Correlated wind field generation

Turbulence of the incoming wind field is of paramount importance to the dynamic response of wind turbines. Hence reliable stochastic models of the turbulence should be available from which time series can be generated for dynamic response and structural safety analysis. In the paper an empirical cross spectral density function for the along-wind turbulence component over the rotor plane is taken as the starting point. The spectrum is spatially discretized in terms of a Hermitian cross-spectral density matrix for the turbulence state vector which turns out not to be positive definite. Since the succeeding state space and ARMA modeling of the turbulence rely on the positive definiteness of the cross-spectral density matrix, the problem with the non-positive definiteness of such matrices is at first addressed and suitable treatments regarding it are proposed. From the adjusted positive definite cross-spectral density matrix a frequency response matrix is constructed which determines the turbulence vector as a linear filtration of Gaussian white noise. Finally, an accurate state space modeling method is proposed which allows selection of an appropriate model order, and estimation of a state space model for the vector turbulence process incorporating its phase spectrum in one stage, and its results are compared with a conventional ARMA modeling method.

2.1 Introduction

Modern wind turbine wings are flexible and hence sensible to dynamic loads such as gusts caused by turbulence of the wind field impinging on the rotor disk. The dynamic response may lead to both fatigue failure and collapse due to the yielding bending stresses or collision between the deflected blade and the tower. It follows that turbulence must be taken into consideration at the design of wind turbines. In the IEC 61400-1, Ed. 3.0 design code of practice for large wind turbine, (IEC 2005a), the applied turbulence field is prescribed in terms of a frozen, homogeneous, non-isotropic turbulence field, which is convected into the rotor according to Taylor's hypothesis. Veers (Veers 1988) has suggested the use of empirical cross-spectral density functions for the time-stationary turbulence components between two points in the rotor plane, as has a long time been the practice in civil engineering, (Shiotani and Iwayani 1971). The presented spectra presume stochastic independence among the three turbulence components, with the consequence that the well-known negative correlation between the along wind and vertical components in turbulence boundary layer is not modeled. Further, the influence of the phase spectrum is ignored, rendering the coherence functions and hence the cross-spectral densities real. During past decades people have tried various modeling methods to simulate a turbulent wind field such as Fourier Analysis, ARMA modeling, Artificial neural network etc. (Solari and Tubino 2002; Kareem 2008). Among the proposed methods, ARMA models have received

considerable attention specifically due to their short memory requirement. These models are especially advantageous in controlled Monte Carlo simulations for low failure probability estimation, where it is very advantageous that turbulence is represented as a filtration of white noise processes. ARMA models are reported to be quite successful in modeling wind field as long as the coherence function between discretized nodal points on the rotor plane is assumed to be real, (Kareem 2008; Chen and Kareem 2001). However, their capability for modeling stochastic wind field with complex coherence function, which is the aim of this investigation, has not yet been demonstrated. The basic assumption in what follows is that the cross-spectral density function of the along wind turbulence component is available over the rotor plane. Further, the turbulence field is assumed to be spatial homogeneous and stationary in time. Next, the turbulence field is discretized in a number of nodal points as shown in Figure 2.1a. The approach is illustrated with an empirical cross-spectral density function, where the auto-spectral density function is given by Kaimal power spectrum and the complex coherence function is taken from Shiotani and Iwayani (Shiotani and Iwayani 1971). An important issue is the lack of positive definiteness of the cross-spectral density matrix of the turbulence vector at low angular frequencies. Positive definiteness is required to achieve numerical stability of the suggested models. Therefore, two modification schemes are proposed to guarantee positive definiteness of the modified cross spectral density matrix. The modified cross-spectral density matrix is then used to estimate an impulse response matrix which provides the turbulence vector by a convolution with a Gaussian white noise with independent unit intensity component processes. The indicated impulse response matrix is not causal, which is of great conceptual importance, since it shows that the ARMA model and the state space models, which make implicit use of causality of the process, approximate the original acausal process with a causal equivalent. Eventually a state space modeling (SSM) method is applied. The method takes advantage of singular value decomposition as a numerical tool to estimate both the optimum model order, and the state space model in one stage. Two numerical simulations are carried out to study the accuracy of the SSM method. It is concluded that the suggested state space modeling provides substantial improvements in simulating multivariable wind fields.

2.2 Turbulence model

The mean wind and the turbulence field are described in the $(z_1, z_2, z_3)-$ coordinate system with origin at the hub. The z_1-axis is horizontal, orthogonal to the rotor plane, and oriented towards the nacelle. The, z_3-axis is vertical, and oriented in the upwards direction, see Figure 2.1. The mean wind velocity V is assumed to be co-directional to the z_1-axis, and is considered constant over the rotor area $A = \pi R^2$, where R is the length of the blades. In what follows we shall only consider the turbulence component $v(\mathbf{z}, t)$ in the z_1-direction in neutral atmospheric turbulence at positions $\mathbf{z} = [z_1, z_2, z_3]$ in the rotor plane and at arbitrary times t. The turbulence field in the rotor plane will be modelled as a zero-mean, Gaussian time-stationary process $\{v(\mathbf{z}, t),\ (\mathbf{z}, t) \in R^3 \times R\}$. Then, the turbulence process is completely determined by its cross-covariance function defined as, (Papoulis 1991)

$$\kappa_{vv}(\mathbf{z}_1, t_1; \mathbf{z}_2, t_2) = E\big[v(\mathbf{z}_1, t_1)v(\mathbf{z}_2, t_2)\big] = \kappa_{vv}(\mathbf{r}, \tau) \tag{2.1}$$

$$\mathbf{r} = \mathbf{z}_2 - \mathbf{z}_1 \quad , \quad \tau = t_2 - t_1 \tag{2.2}$$

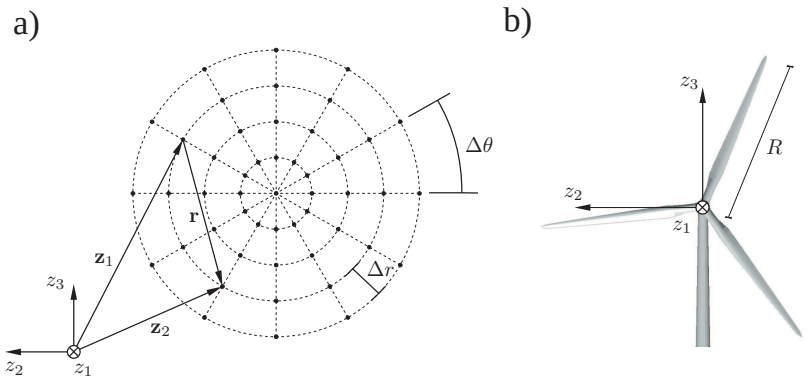

Figure 2.1 a) Discretization of rotor area. b) Three-bladed rotor.

where $E[\cdot]$ is the expectation operator, and $\mathbf{z}_1$ and $\mathbf{z}_2$ are the position vectors to two points in the rotor plane, see Figure 2.1. Alternatively, the correlation structure can be defined by the double-sided cross-spectral density function via the Wiener-Khintchine relation, (Papoulis 1991)

$$S_{vv}(\mathbf{z}_1, \mathbf{z}_2; \omega) = \frac{1}{2\pi} \int_{-\infty}^{\infty} \mathrm{e}^{-i\omega t}\, \kappa_{vv}(\mathbf{z}_1, \mathbf{z}_2; \tau)\, d\tau \tag{2.3}$$

$S_{vv}(\mathbf{z}_1, \mathbf{z}_2; \omega)$ may be written on the form

$$S_{vv}(\mathbf{z}_1, \mathbf{z}_2; \omega) = \gamma_{vv}(\mathbf{z}_1, \mathbf{z}_2; \omega) S_{vv}^{\frac{1}{2}}(\mathbf{z}_1; \omega) S_{vv}^{\frac{1}{2}}(\mathbf{z}_2; \omega) \tag{2.4}$$

where $\gamma_{vv}(\mathbf{z}_1, \mathbf{z}_2; \omega)$ is the so-called coherence function and $S_{vv}(\mathbf{z}; \omega)$ is the double-sided auto-spectral density of the turbulence. Due to the assumed homogeneity of the field over the rotor area the former depends on $\mathbf{z}_1$ and $\mathbf{z}_2$ via the difference $\mathbf{r} = \mathbf{z}_2 - \mathbf{z}_1$, and the latter is independent of the position vector $\mathbf{z}$. In the inertial sub-range of equilibrium range the double-sided auto-spectral density function may be given by the following empirical expression

$$\left.\begin{aligned} S_{vv}(\mathbf{r}; \omega) &= \frac{1}{V} F\left(\frac{\omega}{V}\right) \\ F(k) &= \frac{\sigma_v^2}{\gamma} \frac{L}{\left(1 + |Lk|\right)^{5/3}} \end{aligned}\right\} \tag{2.5}$$

V is the mean wind velocity at the hub, which is assumed to be constant over the rotor. σ_v is the standard deviation of the turbulence, L is the correlation length, and γ is a normalization parameter given as

$$\left.\begin{aligned} \sigma_v &= 2.18\, V_* \\ L &= 5.25\, h \\ \gamma &= 3 \end{aligned}\right\} \tag{2.6}$$

V_* is the friction velocity given as $V_* = V_{10} k_t \kappa$, where V_{10} is the mean wind velocity at 10m, $k_t = 0.17$ is a friction coefficient, and $\kappa = 0.40$ is von Karman's constant. The cross-spectral

density function fulfils the symmetry properties, (Papoulis 1991)

$$S_{vv}(\mathbf{z}_1, \mathbf{z}_2; \omega) = S^*_{vv}(\mathbf{z}_2, \mathbf{z}_1; \omega) = S^*_{vv}(\mathbf{z}_1, \mathbf{z}_2; -\omega) \tag{2.7}$$

where $*$ denotes complex conjugation. Due to the homogeneity the coherence function merely depends on $\mathbf{z}_1$ and $\mathbf{z}_2$ via the difference vector $\mathbf{r} = \mathbf{z}_2 - \mathbf{z}_1$. Then due to (7), the coherence must fulfil the following asymptotic values and symmetry properties

$$\left.\begin{aligned} &\gamma(\mathbf{r};\omega) = 1 \quad , \quad \mathbf{r} = \mathbf{0} \\ &\gamma(\mathbf{r};\omega) = 0 \quad , \quad |\mathbf{r}| = \infty \\ &\gamma(\mathbf{r};\omega) = \gamma^*(-\mathbf{r};\omega) \\ &\gamma(\mathbf{r};\omega) = \gamma^*(\mathbf{r};-\omega) \end{aligned}\right\} \tag{2.8}$$

An empirical expression, which complies with the indicated requirements has been given by (Shiotani and Iwayani 1971)

$$\gamma(\mathbf{r};\omega) = \exp\left(-\frac{|\mathbf{r}||\omega|}{V} d_1\right) \exp\left(i \frac{\mathrm{s}(\mathbf{r})|\mathbf{r}|\,\omega}{V} d_2\right) \tag{2.9}$$

where the sign function is defined so that $\mathrm{s}(\mathbf{r}) = 1$ and $\mathrm{s}(-\mathbf{r}) = -1$. The non-dimensional parameters d_1 and d_2 are given as $d_1 \simeq 1.5$ and $d_2 \simeq 1.3$, (Shiotani and Iwayani 1971).

2.3 Discretization of the turbulence field

The rotor plane is divided by n angular segments of magnitude $\Delta\theta = \frac{2\pi}{n}$, see Figure 2.1. Along each side of a segment the radius R of the rotor plane is divided into m equidistant intervals of the length $\Delta r = \frac{R}{m}$, defining m nodes. The total number of nodes becomes $M = nm + 1$, where the first node refers to the hub. Then, the discretized field, representing the turbulence in the defined nodes may be represented by the stochastic vector

$$\mathbf{v}(t) = \begin{bmatrix} v(\mathbf{z}_1, t) \\ v(\mathbf{z}_2, t) \\ \vdots \\ v(\mathbf{z}_M, t) \end{bmatrix} = \begin{bmatrix} v_1(t) \\ v_2(t) \\ \vdots \\ v_M(t) \end{bmatrix} \tag{2.10}$$

The double-sided cross-spectral density matrix of the turbulence vector becomes

$$\mathbf{S_{vv}}(\omega) = \begin{bmatrix} S_{vv}(\mathbf{z}_1, \mathbf{z}_1; \omega) & \cdots & S_{vv}(\mathbf{z}_1, \mathbf{z}_M; \omega) \\ S_{vv}(\mathbf{z}_2, \mathbf{z}_1; \omega) & \cdots & S_{vv}(\mathbf{z}_2, \mathbf{z}_M; \omega) \\ \vdots & \ddots & \vdots \\ S_{vv}(\mathbf{z}_M, \mathbf{z}_1; \omega) & \cdots & S_{vv}(\mathbf{z}_M, \mathbf{z}_M; \omega) \end{bmatrix} \tag{2.11}$$

$\mathbf{S_{vv}}(\omega)$ is a Hermitian matrix fulfilling the symmetry properties

$$\mathbf{S_{vv}}(\omega) = \mathbf{S^{\mathrm{T}*}_{vv}}(\omega) = \mathbf{S^*_{vv}}(-\omega) \tag{2.12}$$

Using the symmetry property (2.12) the cross-covariance matrix of the turbulence vector may be obtained from the following Finite Fourier Transform

$$\mathbf{C_{vv}}(\tau) = \int_{-\infty}^{\infty} \mathrm{e}^{i\omega\tau}\, \mathbf{S_{vv}}(\omega)\, d\omega \Rightarrow \tag{2.13}$$

$$\mathbf{C_{vv}}(j) \simeq 2\Delta\omega \mathrm{Re}\left(\sum_{k=0}^{N-1} \exp\left(i2\pi \frac{jk}{N} \right) \mathbf{S_{vv}}(k) \right) \tag{2.14}$$

$j = 0, 1, \ldots, N-1$

where the abbreviated notations $\mathbf{C_{vv}}(j) = \mathbf{C_{vv}}(j\Delta\tau)$ and $\mathbf{S_{vv}}(k) = \mathbf{S_{vv}}(k\Delta\omega)$ have been introduced, and where the time and frequency increments are related as $\Delta\tau\Delta\omega = \frac{2\pi}{N}$. $\mathbf{S_{vv}}(\omega)$ may be Gauss factorized on the form

$$\mathbf{S_{vv}}(\omega) = \mathbf{L}^*(\omega)\, \mathbf{D}(\omega)\, \mathbf{L}^{\mathrm{T}}(\omega) \tag{2.15}$$

where $\mathbf{L}(\omega)$ is a lower triangular complex matrix with 1 in the main diagonal, and $\mathbf{D}(\omega)$ is a real diagonal matrix. Since, $\mathbf{S_{vv}}(\omega)$ is not necessarily positive definite the diagonal components need not be positive real. If not so, we may define an auxiliary diagonal matrix $\tilde{\mathbf{D}}(\omega)$, in which the negative components of $\mathbf{D}(\omega)$ are set to zero. Correspondingly, the following positive semi-definite cross-spectral density matrix may be constructed

$$\tilde{\mathbf{S}}_{\mathbf{vv}}(\omega) = \mathbf{L}^*(\omega)\, \tilde{\mathbf{D}}(\omega)\, \mathbf{L}^{\mathrm{T}}(\omega) \tag{2.16}$$

$\tilde{\mathbf{S}}_{\mathbf{vv}}(\omega)$ may be factorized on the form

$$\tilde{\mathbf{S}}_{\mathbf{vv}}(\omega) = \mathbf{H}_{\mathbf{v}}^*(\omega)\mathbf{H}_{\mathbf{v}}^{\mathrm{T}}(\omega) \tag{2.17}$$

where

$$\mathbf{H_v}(\omega) = \mathbf{L}^*(\omega)\tilde{\mathbf{D}}^{\frac{1}{2}}(\omega) \tag{2.18}$$

$\tilde{\mathbf{D}}^{\frac{1}{2}}(\omega)$ is a diagonal matrix with the square root of $\mathbf{D}^{\frac{1}{2}}(\omega)$ on the main diagonal. $\mathbf{H_v}(\omega)$ has the form of a lower complex triangular matrix

$$\mathbf{H}_{\mathbf{v}}(\omega) = \begin{bmatrix} H_{11}(\omega) & 0 & \cdots & 0 \\ H_{21}(\omega) & H_{22}(\omega) & \cdots & 0 \\ \vdots & \vdots & \ddots & \vdots \\ H_{M\,1}(\omega) & H_{M\,2}(\omega) & \ldots & H_{M\,M}(\omega) \end{bmatrix} \tag{2.19}$$

Obviously, the columns of $\mathbf{H_v}(\omega)$ corresponding to the elements in the diagonal of $\tilde{\mathbf{D}}^{\frac{1}{2}}(\omega)$ set to zero become zero as well. Alternatively, the following eigenvalue decomposition may be considered

$$\mathbf{S_{vv}}(\omega) = \mathbf{\Psi}(\omega)\, \mathbf{\Lambda}(\omega)\, \mathbf{\Psi}^{*\mathrm{T}}(\omega) \tag{2.20}$$

where $\mathbf{\Psi}(\omega)$ is a modal matrix storing the eigenvectors of $\mathbf{S_{vv}}(\omega)$ column wise, and $\mathbf{\Lambda}$ is a diagonal matrix storing the corresponding eigenvalues. Notice, the formulation (2.20) assumes

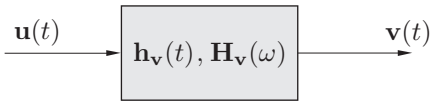

Figure 2.2 Turbulence vector **v**(t) as a linear filtration of a Gaussian white noise vector $\mathbf{u}(t)$.

that the eigenvectors have been normalized to unit length in which case $\mathbf{\Psi}^{-1}(\omega) = \mathbf{\Psi}^{*\mathrm{T}}(\omega)$. Next, the negative and zero eigenvalues in $\mathbf{\Lambda}(\omega)$ are set to a small positive number, e.g. $\varepsilon = 10^{-10}$, providing a modified eigenvalue matrix $\tilde{\mathbf{\Lambda}}(\omega)$, from which the following positive definite cross-spectral density matrix may be constructed

$$\tilde{\mathbf{S}}_{\mathbf{vv}}(\omega) = \mathbf{\Psi}(\omega)\,\tilde{\mathbf{\Lambda}}(\omega)\,\mathbf{\Psi}^{*\mathrm{T}}(\omega) \tag{2.21}$$

Finally, the lower triangular matrix $\mathbf{H}_{\mathbf{v}}(\omega)$ is obtained by a Cholesky decomposition of (2.21). The matrices $\mathbf{H}_{\mathbf{v}}(\omega)$ obtained by the two methods are not identical. The latter approach turns out to introduce smaller errors in the constructed positive definite cross-spectral density matrix compared to the target spectrum, as demonstrated in the numerical example. This improvement is obtained at the cost of a significant increase in the computational expenses. Notice, in both cases $\mathbf{S}_{\mathbf{vv}}(\omega)$ and $\tilde{\mathbf{S}}_{\mathbf{vv}}(\omega)$ only differ at angular frequencies, where the former is not positive definite. The symmetry property $\mathbf{S}_{\mathbf{vv}}(\omega) = \mathbf{S}^{*}_{\mathbf{vv}}(-\omega)$ implies that the following symmetry property prevails for $\mathbf{H}_{\mathbf{v}}(\omega)$

$$\mathbf{H}_{\mathbf{v}}(\omega) = \mathbf{H}^{*}_{\mathbf{v}}(-\omega) \tag{2.22}$$

Let $\{\mathbf{u}(t),\ t \in R\}$ denote an M-dimensional white vector noise process with the double-sided cross-spectral density and cross-covariance matrices given as

$$\mathbf{S}_{\mathbf{uu}}(\omega) = \mathbf{I} \tag{2.23}$$

$$\mathbf{C}_{\mathbf{uu}}(\tau) = 2\pi\delta(\tau)\,\mathbf{I} \tag{2.24}$$

where $\delta(\tau)$ is the Dirac delta function. Then, it follows from (2.17) that $\{\mathbf{v}(t),\ t \in R\}$ may be obtained by filtering $\{\mathbf{u}(t),\ t \in R\}$ through a linear filter with the frequency response matrix $\mathbf{H}_{\mathbf{v}}(\omega)$. The related impulse response matrix $\mathbf{h}_{\mathbf{v}}(t)$ is the inverse Fourier transform of $\mathbf{H}_{\mathbf{v}}(\omega)$. Using the symmetry property (2.22) $\mathbf{h}_{\mathbf{v}}(t)$ may be determined by the following Finite Fourier Transform

$$\mathbf{h}_{\mathbf{v}}(t) = \frac{1}{2\pi}\int_{-\infty}^{\infty} \mathrm{e}^{i\omega t}\,\mathbf{H}_{\mathbf{v}}(\omega)\,d\omega \Rightarrow \tag{2.25}$$

$$\mathbf{h}_{\mathbf{v}}(j) = \frac{\Delta\omega}{\pi}\mathrm{Re}\left(\sum_{k=0}^{N-1}\exp\left(i2\pi\frac{jk}{N}\right)\,\mathbf{H}_{\mathbf{v}}(k)\right) \tag{2.26}$$

$j = 0, 1, \ldots, N-1$

$\mathbf{h}_{\mathbf{v}}(t)$ becomes a lower triangular matrix similar to $\mathbf{H}_{\mathbf{v}}(\omega)$. The causality condition is generally not fulfilled, i.e. $\mathbf{h}_{\mathbf{v}}(t) \neq \mathbf{0},\ t < 0$. Notice that $\mathbf{h}_{\mathbf{v}}(-j) = \mathbf{h}_{\mathbf{v}}(N-j)$, and hence is available from (2.25) up to the Nyquist frequency $N/2$. Hence the turbulence vector process can be

obtained from the stochastic convolution integral

$$\mathbf{v}(t) = \int_{-\infty}^{\infty} \mathbf{h}_{\mathbf{v}}(t-\tau)\,\mathbf{u}(\tau)\,d\tau \tag{2.27}$$

which is approximated by the following Riemann sum

$$\mathbf{v}(j) = \sum_{l=-N/2}^{N/2} \mathbf{h}_{\mathbf{v}}(l)\mathbf{w}(j-l) \quad , \quad j = 0, 1, \ldots, N-1 \tag{2.28}$$

In (2.28) $\mathbf{w}(j)$ denotes an $M \times 1$ dimensional zero mean normal vector with mutually independent, identically distributed random variables with the variance $2\pi\Delta t$, where Δt denotes the time step in the discretization of the convolution integral. Then the cross-covariance function of the stationary stochastic sequence is given as

$$\mathbf{C}_{\mathbf{ww}}(k-j) = E\big[\mathbf{w}(j)\mathbf{w}^{\mathrm{T}}(k)\big] = \begin{cases} \mathbf{0} & , \quad j \neq k \\ 2\pi\Delta t\,\mathbf{I} & , \quad j = k \end{cases} \tag{2.29}$$

The cross-covariance matrix based on the filter method (2.28) becomes

$$\tilde{\mathbf{C}}_{\mathbf{vv}}(j) = 2\pi\Delta t \sum_{k=k_{\min}}^{k_{\max}} \mathbf{h}_{\mathbf{v}}(k)\mathbf{h}_{\mathbf{v}}^{\mathrm{T}}(k+j) \tag{2.30}$$

where

$$\begin{aligned} k_{\min} &= \max\left(-\tfrac{N}{2}, -\tfrac{N}{2} - j\right) \\ k_{\max} &= \min\left(\tfrac{N}{2}, \tfrac{N}{2} - j\right) \end{aligned} \tag{2.31}$$

2.4 ARMA modeling

In principle, simulation of the turbulence vector may be based on (2.28). However, $\mathbf{h}_{\mathbf{v}}(l)$ converges to zero very slowly with l as seen in Figure 2.5. This truncation error together with numerical integration error introduced by (2.25) in estimation of $\mathbf{h}_{\mathbf{v}}(l)$, cause discrepancy of the variance function of $\mathbf{h}_{\mathbf{v}}(l)$ with (2.13) as seen in Figure 2.11. Hence N should be very large to keep Δt at an acceptable level. To circumvent this problem an equivalent ARMA vector model with finite lengths p and q of the auto-regressive and moving average parts might be applied corresponding to the model

$$\mathbf{v}(k) + \sum_{l=1}^{p} \mathbf{A}_l \mathbf{v}(k-l) = \sum_{l=0}^{q} \mathbf{B}_l \mathbf{w}(k-l) \tag{2.32}$$

where $\mathbf{A}_l$ and $\mathbf{B}_l$ are real matrices of dimension $M \times M$. Following the suggestion of Samaras et al.(Samaras *et al.* 1985) the Two Stage Least Square (2SLS) method will at first be used to estimate $\mathbf{A}_l$ and $\mathbf{B}_l$ of (2.32). The algorithm consists of two major steps; in the first step an AR model of sufficiently high order $\acute{p}$ is calibrated for the process, and in the second step the obtained AR model is approximated by a shorter ARMA(p,q) model. To guarantee sufficient accuracy of

the modelling, Samaras et.al.(Samaras *et al.* 1985) proposed to choose $\acute{p} \geq p+q+2$, whereas Li and Kareem (Li and Kareem 1990) proposed the empirical relation $\acute{p} \geq 3(p+q)$

$$\mathbf{v}(k) + \sum_{l=1}^{\acute{p}} \tilde{\mathbf{A}}_l \mathbf{v}(k-l) = \mathbf{B}_0 \mathbf{w}(k) \tag{2.33}$$

To calibrate $\tilde{\mathbf{A}}_l$ coefficients, (2.33) is post multiplied by $\mathbf{v}^{\mathrm{T}}(k-j), k = 1, 2, \cdots$ and its expectation is taken which yields in (2.34)

$$\mathbf{C}^{\mathrm{T}}_{\mathbf{vv}}(j) + \sum_{l=1}^{\acute{p}} \tilde{\mathbf{A}}_l \mathbf{C}^{\mathrm{T}}_{\mathbf{vv}}(j-l) = \mathbf{0} \quad , \quad j = 1, 2, \cdots \tag{2.34}$$

where $\mathbf{C}_{\mathbf{vv}}(j) = \mathbf{C}^{\mathrm{T}}_{\mathbf{vv}}(-j)$ is used. Also $E[\mathbf{w}(j)\mathbf{v}^{\mathrm{T}}(j-k)] = \mathbf{0}$ for $k > 0$ according to the causality of the model. Evaluating (2.34) for $j = 1, \cdots, \acute{p}$ allows calibration of $\tilde{\mathbf{A}}_l$ in a least square sense. Next, post multiplying (2.33) by $\mathbf{w}^{\mathrm{T}}(k)$ and taking its expectation results in

$$\mathbf{C}_{\mathbf{vw}}(0) = 2\pi\Delta t \mathbf{B}_0 \tag{2.35}$$

Post multiplying (2.33) by $\mathbf{v}^{\mathrm{T}}(k)$ and taking its expectation together with using (2.35) derives (2.36) that will be used to estimate $\mathbf{B}_0\mathbf{B}_0^{\mathrm{T}}$

$$\mathbf{C}^{\mathrm{T}}_{\mathbf{vv}}(0) + \sum_{l=1}^{\acute{p}} \tilde{\mathbf{A}}_l \mathbf{C}^{\mathrm{T}}_{\mathbf{vv}}(-l) = 2\pi\Delta t \mathbf{B}_0 \mathbf{B}_0^{\mathrm{T}} \tag{2.36}$$

(2.36) is used for the estimation of $\mathbf{B}_0$ by performing Cholesky decomposition of $\mathbf{B}_0\mathbf{B}_0^{\mathrm{T}}$. The next step of the method is to calibrate an ARMA(p,q) model that fits at best to the estimated high order AR model. Therefore, the second least square is merely for shortening the memory of the model. Consequently the high order AR model is the more accurate of the two. This is the reason why the high order AR model of the 2SLS method is compared with the estimated model of the state space method in simulations. In the simulations, the covariance function of the 2SLS method is calculated recursively using equation (2.34).

Clearly accuracy of the model in capturing second order moments of the process increases as the model order increases. It is not only the higher accuracy that makes high order ARMA models more elegant but in modeling stochastic fields typically high orders for models are required for correct estimation of the second order statistical moments of the field. However a well-known problem which defines the upper bounds on the model order is the vulnerability of this type of models to stability (Soderstrom and Stoica 1981). ARMA models soon become unstable as the model order increases. This makes practical limitations on simulating stochastic fields i.e. vector (multi-variable) ARMA models. The reason is that unlike in the simulation of the scalar stochastic process, the energy of vector processes is *not* concentrated along only a few principal directions, e.g. the singular vectors of the Hankel matrix defined from (2.36) for estimation of the coefficients of the AR model. This is the key factor which defined the relationship of the model order and its energy harvesting ratio e.g. the amount of energy of the process captured by the model. Therefore systems which have more significant (non-zero) principal values (singular values) require higher model orders to capture the same amount of the energy of the process.

Recently a low order ARMA modeling technique is introduced which allows calibration of a low order ARMA model suitable for simulating stochastic fields, c.f. (Krenk 2011) . A multi-variable AR model with order one, e.g. $\acute{p} = 1$ in (2.33), is proposed to be used here. For an order one AR model the Yule-Walker equation (2.35) matches the covariance function at zero and first separation times e.g. $\mathbf{C}^{\mathrm{T}}_{\mathbf{vv}}(0)$ and $\mathbf{C}^{\mathrm{T}}_{\mathbf{vv}}(1)$ respectively. In (Krenk 2011) it is proposed to match the covariance function at zero separation time and k^{th} separation time instead e.g. $\mathbf{C}^{\mathrm{T}}_{\mathbf{vv}}(0)$ and $\mathbf{C}^{\mathrm{T}}_{\mathbf{vv}}(k)$ respectively. The direct outcome of the least square solution in this case will be the $\tilde{\mathbf{A}}^k_1$, then its k^{th} root will be calculated which results in the $\tilde{\mathbf{A}}_1$. The method is stated to provide very close estimations of the covariance function at all separation times for stochastic field simulation without critical stability problems.

2.5 State Space Modeling

In this section, a modified outline of the State Space Modelling (SSM) method are given to fit into the present framework. The method starts by the state space representation of the ARMA model shown in (2.37), (Overschee and Moor 1996; Markovsky *et al.* 2006)

$$\begin{array}{rcl} \mathbf{x}(j+1) & = & \mathbf{A}\mathbf{x}(j) + \mathbf{\Theta}(j) \\ \mathbf{v}(j) & = & \mathbf{C}\mathbf{x}(j) + \mathbf{\Phi}(j) \end{array} \tag{2.37}$$

where the auxiliary state vector $\mathbf{x}(j)$ is of dimension $L \times 1$, and $\mathbf{\Theta}(j)$ and $\mathbf{\Phi}(j)$ are stationary Gaussian white noise vector processes of the dimension $L \times 1$ and $M \times 1$, respectively. $\mathbf{A}$ is a system matrix of the dimension $L \times L$ and $\mathbf{C}$ is an observation matrix of the dimension $M \times L$. The cross-covariance matrices of the stochastic sequences $\{\mathbf{\Theta}(j)\}$ and $\{\mathbf{\Phi}(j)\}$ are given as

$$E\left[\begin{bmatrix} \mathbf{\Theta}(j) \\ \mathbf{\Phi}(j) \end{bmatrix} \begin{bmatrix} \mathbf{\Theta}^{\mathrm{T}}(k) & \mathbf{\Phi}^{\mathrm{T}}(k) \end{bmatrix}\right] = \begin{bmatrix} \mathbf{Q} & \mathbf{S} \\ \mathbf{S}^{\mathrm{T}} & \mathbf{R} \end{bmatrix} \delta_{jk} \tag{2.38}$$

where δ_{jk} is the Kronecker delta. The idea of the state space modelling is to estimate the matrices $\mathbf{Q}$ of dimension $L \times L$, $\mathbf{R}$ of dimension $M \times M$ and $\mathbf{S}$ of dimension $M \times L$ are noise covariance matrices, which are to be estimated along with $\mathbf{A}$ of dimension $L \times L$, $\mathbf{C}$ of dimension $M \times L$, so the output process $\mathbf{v}(j)$ satisfies a given target cross-covariance matrix $\mathbf{C}_{\mathbf{vv}}(j)$. At first, an equivalent Kalman filter model is formulated which provides a relation between $\mathbf{A}$ and $\mathbf{C}$ and some auxiliary matrices (Kalman gain $\mathbf{K}$, cross-covariance matrix of the Kalman state vector $\bar{\mathbf{\Sigma}}$, and the covariance matrix between the next state vector and the present output vector for the forward innovation model $\bar{\mathbf{G}}^{\mathrm{T}}$). Next, the system realization theorem is applied, which provides the estimation results for $\mathbf{A}$, $\mathbf{C}$ and $\bar{\mathbf{G}}^{\mathrm{T}}$. Starting from (2.38), the state vector process $\{\mathbf{x}(j)\}$ is a zero mean stationary Gaussian process fulfilling the properties

$$E[\mathbf{x}(j)] = \mathbf{0} \tag{2.39}$$

$$E[\mathbf{x}(j)\mathbf{x}^{\mathrm{T}}(j)] = \mathbf{\Sigma} \tag{2.40}$$

$$E[\mathbf{x}(j)\mathbf{\Theta}^{\mathrm{T}}(j)] = \mathbf{0} \tag{2.41}$$

$$E[\mathbf{x}(j)\mathbf{\Phi}^{\mathrm{T}}(j)] = \mathbf{0} \tag{2.42}$$

(2.41) follows from (2.38) and the resulting mutual stochastic independence of $\mathbf{x}(j)$ and $\mathbf{\Theta}(j)$. From (2.37) and (2.41) the following Lyapunov equation for the covariance matrix may be derived

$$\mathbf{\Sigma} = \mathbf{A}\mathbf{\Sigma}\mathbf{A}^{\mathrm{T}} + \mathbf{Q} \tag{2.43}$$

Similarly, the following relations for the output covariance matrix $\mathbf{C}^{\mathrm{T}}_{\mathbf{vv}}(i) = E[\mathbf{v}(j+i)\mathbf{v}^{\mathrm{T}}(j)]$ and the covariance matrix in the stationary state, $\mathbf{G}^{\mathrm{T}} = E[\mathbf{x}(j+1)\mathbf{v}^{\mathrm{T}}(j)]$, may be achieved

$$\begin{array}{rcl} \mathbf{G}^{\mathrm{T}} & = & \mathbf{A}\mathbf{\Sigma}\mathbf{C}^{\mathrm{T}} + \mathbf{S} \\ \mathbf{C}^{\mathrm{T}}_{\mathbf{vv}}(0) & = & \mathbf{C}\mathbf{\Sigma}\mathbf{C}^{\mathrm{T}} + \mathbf{R} \\ \mathbf{C}^{\mathrm{T}}_{\mathbf{vv}}(i) & = & \mathbf{C}\mathbf{A}^{i-1}\mathbf{G}^{\mathrm{T}} \end{array} \tag{2.44}$$

Accuracy of the modeling requires that the states of the model are estimated with the least possible error compared to the true states of the system. The state space model (2.37) might be transformed to the following so-called forward innovation model admitting the standard form of a Kalman filter, (Katayama 2005; Verhaegen and Verdult 2007)

$$\begin{array}{rcl} \bar{\mathbf{x}}(j+1) & = & \mathbf{A}\bar{\mathbf{x}}(j) + \mathbf{K}(j)\mathbf{e}(j) \\ \mathbf{v}(j) & = & \mathbf{C}\bar{\mathbf{x}}(j) + \mathbf{e}(j) \end{array} \tag{2.45}$$

where $\mathbf{K}(j)$ is a set of non-steady state Kalman filter gain matrices, and $\{\mathbf{e}(j)\}$ is a zero-mean Gaussian white noise vector sequence. Notice that whereas the state vector and the noise processes are affected by the transformation, the output vector $\{\mathbf{v}(j)\}$ is not changed. Accordingly, the covariance matrix between the next state vector and the present output vector for the model (3.36) is given by $\bar{\mathbf{G}}^{\mathrm{T}}(j) = E[\bar{\mathbf{x}}(j+1)\mathbf{v}^{\mathrm{T}}(j)]$. Let $\{\hat{\bar{\mathbf{x}}}(j)\}$ denotes the forward Kalman filter estimate of the process $\{\bar{\mathbf{x}}(j)\}$ which is related with deterministic initial value $\hat{\bar{\mathbf{x}}}(0) = \mathbf{0}$. Then equation (2.46) shows the development of the state estimation via the Kalman filter

$$\hat{\bar{\mathbf{x}}}(j+1) = \mathbf{A}\hat{\bar{\mathbf{x}}}(j) + \mathbf{K}(j)\left(\mathbf{v}(j) - \mathbf{C}\hat{\bar{\mathbf{x}}}(j)\right) \tag{2.46}$$

The second equation of (3.36) estimates the noise cross-covariance matrix, $E[\mathbf{e}(j)\mathbf{e}^{\mathrm{T}}(j)]$, as

$$E[\mathbf{e}(j)\mathbf{e}^{\mathrm{T}}(j)] = \mathbf{C}^{\mathrm{T}}_{\mathbf{vv}}(0) - \mathbf{C}\bar{\mathbf{\Sigma}}(j)\mathbf{C}^{\mathrm{T}} \tag{2.47}$$

From (2.44), (3.36) and (2.47) the following forward discrete algebraic Riccati equation can be derived and solved for the development of $\bar{\mathbf{\Sigma}}$. The Riccati equation (2.48) is time dependent in general, (Simon 2006), while as $j \to \infty$, the cross-covariance matrix approaches a constant value $\bar{\mathbf{\Sigma}} = \bar{\mathbf{\Sigma}}(\infty)$. Similarly the covariance matrix $\bar{\mathbf{G}}^{\mathrm{T}}(j)$ and the Kalman gain matrix $\mathbf{K}(j)$ approach constant values, i.e. $\bar{\mathbf{G}}^{\mathrm{T}} = \bar{\mathbf{G}}^{\mathrm{T}}(\infty)$ and $\mathbf{K} = \mathbf{K}(\infty)$, respectively.

$$\begin{array}{rcl} \bar{\mathbf{\Sigma}} & = & \mathbf{A}\bar{\mathbf{\Sigma}}\mathbf{A}^{\mathrm{T}} + (\bar{\mathbf{G}}^{\mathrm{T}} - \mathbf{A}\bar{\mathbf{\Sigma}}\mathbf{C}^{\mathrm{T}}) \\ & & \times(\mathbf{C}^{\mathrm{T}}_{\mathbf{vv}}(0) - \mathbf{C}\bar{\mathbf{\Sigma}}\mathbf{C}^{\mathrm{T}})^{-1}(\bar{\mathbf{G}}^{\mathrm{T}} - \mathbf{A}\bar{\mathbf{\Sigma}}\mathbf{C}^{\mathrm{T}})^{\mathrm{T}} \end{array} \tag{2.48}$$

Therefore, if $\{\mathbf{A}, \mathbf{C}, \bar{\mathbf{G}}^{\mathrm{T}}\}$ are available, it is required to solve (2.48) only once to obtain $\bar{\mathbf{\Sigma}}$. There exist various methods for solving the indicated Riccati equation; among them the eigenvalue method is employed in the current work. The idea is to introduce the factorization $\bar{\mathbf{\Sigma}} =$

$\mathbf{W}_1\mathbf{W}_2^{-1}$. Next, the matrices $\mathbf{W}_1$ and $\mathbf{W}_2$ of the dimension $L \times L$ are obtained from the generalized eigenvalue problem of dimension $2L$.

$$\begin{bmatrix} \mathbf{A}^{\mathrm{T}} - \mathbf{C}^{\mathrm{T}}\mathbf{C}_{\mathbf{vv}}^{-\mathrm{T}}(0)\bar{\mathbf{G}} & \mathbf{0} \\ -\bar{\mathbf{G}}^{\mathrm{T}}\mathbf{C}_{\mathbf{vv}}^{-\mathrm{T}}(0)\bar{\mathbf{G}} & \mathbf{I} \end{bmatrix} \begin{bmatrix} \mathbf{W}_1 \\ \mathbf{W}_2 \end{bmatrix} = \begin{bmatrix} \mathbf{I} & -\mathbf{C}^{\mathrm{T}}\mathbf{C}_{\mathbf{vv}}^{-\mathrm{T}}(0)\mathbf{C} \\ \mathbf{0} & \mathbf{A} - \bar{\mathbf{G}}^{\mathrm{T}}\mathbf{C}_{\mathbf{vv}}^{-\mathrm{T}}(0)\mathbf{C} \end{bmatrix} \begin{bmatrix} \mathbf{W}_1 \\ \mathbf{W}_2 \end{bmatrix} \mathbf{\Lambda} \tag{2.49}$$

where $\mathbf{I}$ is the square identity matrix of dimension $L \times L$. $\mathbf{\Lambda}$ contains L stable eigenvalues of the generalized eigenvalue pencil i.e. inside unit circle. Then, the stationary Kalman gain matrix $\mathbf{K}$ is estimated from

$$\mathbf{K} = (\bar{\mathbf{G}}^{\mathrm{T}} - \mathbf{A}\bar{\mathbf{\Sigma}}\mathbf{C}^{\mathrm{T}})(\mathbf{C}_{\mathbf{vv}}^{\mathrm{T}}(0) - \mathbf{C}\bar{\mathbf{\Sigma}}\mathbf{C}^{\mathrm{T}})^{-1} \tag{2.50}$$

Knowledge of the quadruple $\{\mathbf{A}, \mathbf{C}, \bar{\mathbf{\Sigma}}, \mathbf{K}\}$ is sufficient for constructing a state space model in the form of (3.36) capable of generating a stochastic process with any specified covariance function.

2.5.1 System realization theory

Next, the so-called realization algorithm, (Katayama 2005), is used as the starting point to estimate the triplet $\{\mathbf{A}, \mathbf{C}, \bar{\mathbf{G}}^{\mathrm{T}}\}$ which are then used to estimate $\bar{\mathbf{\Sigma}}$ and $\mathbf{K}$. In what follows, the hat sign over matrixes shows that they are estimation of the original matrix. At first the block Toeplitz matrix $\mathbf{T}$ of the cross-covariance matrices of the outputs, of dimension $Mi \times Mi$ is constructed

$$\mathbf{T} = \begin{bmatrix} \mathbf{C}_{\mathbf{vv}}^{\mathrm{T}}(i) & \mathbf{C}_{\mathbf{vv}}^{\mathrm{T}}(i-1) & \cdots & \mathbf{C}_{\mathbf{vv}}^{\mathrm{T}}(1) \\ \mathbf{C}_{\mathbf{vv}}^{\mathrm{T}}(i+1) & \mathbf{C}_{\mathbf{vv}}^{\mathrm{T}}(i) & \cdots & \mathbf{C}_{\mathbf{vv}}^{\mathrm{T}}(2) \\ \vdots & \vdots & \ddots & \vdots \\ \mathbf{C}_{\mathbf{vv}}^{\mathrm{T}}(2i-1) & \mathbf{C}_{\mathbf{vv}}^{\mathrm{T}}(2i-2) & \cdots & \mathbf{C}_{\mathbf{vv}}^{\mathrm{T}}(i) \end{bmatrix} \tag{2.51}$$

Referring to (2.44) it is clear that $\mathbf{T}$ can be constructed by multiplication of extended observability matrix $\mathbf{O}$, of dimension $Mi \times L$, and the reversed extended stochastic controllability matrix $\mathbf{P}$ of dimension $L \times Mi$ defined below

$$\mathbf{T} = \mathbf{O}\,\mathbf{P} = \begin{bmatrix} \mathbf{C} \\ \mathbf{CA} \\ \vdots \\ \mathbf{CA}^{i-1} \end{bmatrix} \begin{bmatrix} \mathbf{A}^{i-1}\bar{\mathbf{G}}^{\mathrm{T}} & \cdots & \mathbf{A}\bar{\mathbf{G}}^{\mathrm{T}} & \bar{\mathbf{G}}^{\mathrm{T}} \end{bmatrix} \tag{2.52}$$

The phrase extended observability matrix is used, since in general the number of block rows of the matrix is longer than the number of system states, i.e. $i > L$. The same explanation holds for the reversed extended stochastic controllability matrix. The strategy to estimate $\mathbf{O}$ and $\mathbf{P}$ in the next step is to decompose $\mathbf{T}$ into its singular values, sorted in a monotone non-increasing manner, and their corresponding singular vectors in the following way

$$\mathbf{T} = \begin{bmatrix} \mathbf{U}_1 & \mathbf{U}_2 \end{bmatrix} \begin{bmatrix} \mathbf{S}_1 & \mathbf{0} \\ \mathbf{0} & \mathbf{S}_2 \end{bmatrix} \begin{bmatrix} \mathbf{V}_1^{\mathrm{T}} \\ \mathbf{V}_2^{\mathrm{T}} \end{bmatrix} \tag{2.53}$$

$\mathbf{S}_1$ of dimension $r \times r$ is a diagonal matrix consisting of the first *r* singular values, $\mathbf{U}_1$ of dimension $Mi \times r$ is the block of the left singular vectors corresponding to $\mathbf{S}_1$ and $\mathbf{V}_1^{\mathrm{T}}$, of dimension $r \times Mi$, is the corresponding block of right singular vectors. On the condition that system is stable - all of the eigenvalues of the matrix $\mathbf{A}$ are inside unit circle - and the system is excited by white noise, $\mathbf{T}$ will have just *r* non-zero singular values which equals the system order. In such circumstances $\mathbf{S}_2 = \mathbf{0}$ is a square matrix of dimension $(Mi-r) \times (Mi-r)$, and L can be chosen as $L = r$. A proper model order is then proposed by the number of non-zero singular values of the $\mathbf{T}$ matrix. In practice, for instance in vector turbulence modeling, singular values of the $\mathbf{T}$ matrix decrease to zero gradually. This behavior, makes the task of selecting the non-zero singular values not so straight forward, see Figure 2.12. In such circumstances, the optimum model order is usually chosen i, for which $s_i \gg s_{i+1}$, where s_i is the i^{th} singular value. The extended observability and the reversed extended stochastic controllability matrices are then estimated as

$$\hat{\mathbf{O}} = \mathbf{U}_1 \mathbf{S}_1^{1/2} \quad , \quad \hat{\mathbf{P}} = \mathbf{S}_1^{1/2} \mathbf{V}_1^{\mathrm{T}} \tag{2.54}$$

Although it is possible to use different fractions of the singular values for estimation of $\mathbf{O}$ and $\mathbf{P}$, the benefit of the proposed decomposition is that it causes controllability and observability of the estimated system to be balanced. Balancing here means that the number of controllable and observable states of the system are equal. $\hat{\mathbf{C}}$ and $\hat{\tilde{\mathbf{G}}}^{\mathrm{T}}$ might be estimated as the first M rows of $\hat{\mathbf{O}}$ and the last M columns of $\hat{\mathbf{P}}$ respectively. Defining the following weights

$$\left.\begin{aligned} \mathbf{W}_C &= \begin{bmatrix} \mathbf{I}_{M\times M} & \mathbf{0}_{M\times(M-1)i} \end{bmatrix} \\ \mathbf{W}_G &= \begin{bmatrix} \mathbf{0}_{(M-1)i\times M} \\ \mathbf{I}_{M\times M} \end{bmatrix} \\ \mathbf{W}_{A_1} &= \begin{bmatrix} \mathbf{I}_{(M-1)i\times(M-1)i} & \mathbf{0}_{(M-1)i\times M} \end{bmatrix} \\ \mathbf{W}_{A_2} &= \begin{bmatrix} \mathbf{0}_{(M-1)i\times M} & \mathbf{I}_{(M-1)i\times(M-1)i} \end{bmatrix} \end{aligned}\right\} \tag{2.55}$$

$\hat{\mathbf{C}}, \hat{\tilde{\mathbf{G}}}^{\mathrm{T}}$ and $\hat{\mathbf{A}}$ are then be estimated as

$$\left.\begin{aligned} \hat{\mathbf{C}} &= \mathbf{W}_C \hat{\mathbf{O}} \\ \hat{\tilde{\mathbf{G}}}^{\mathrm{T}} &= \hat{\mathbf{P}} \mathbf{W}_G \\ \hat{\mathbf{A}} &= \left(\mathbf{W}_{A_1} \hat{\mathbf{O}}\right)^{\dagger} \mathbf{W}_{A_2} \hat{\mathbf{O}} \end{aligned}\right\} \tag{2.56}$$

Here $()^{\dagger}$ denotes the pseudo inverse of the matrix. $\{\hat{\mathbf{A}}, \hat{\mathbf{C}}, \hat{\tilde{\mathbf{G}}}^{\mathrm{T}}\}$ are then used to calculate $\hat{\tilde{\mathbf{\Sigma}}}$ and $\hat{\mathbf{K}}$ from (2.48) and (2.50) , respectively. Cross-covariance matrices of the estimated state space model can then be calculated from equation (2.44). Although state space representation of the model is quite convenient for any purpose, by introducing the forward shift operator *z* so that $\mathbf{v}(j-1) = z^{-1}\mathbf{v}(j)$, transfer function of the state space model might be constructed as

$$\begin{aligned} \mathbf{v}(j) &= \mathbf{H}(z)\mathbf{e}(j) \\ \mathbf{H}(z) &= \mathbf{C}\left(z\mathbf{I} - \mathbf{A}\right)^{-1}\mathbf{K} + \mathbf{I} \end{aligned} \tag{2.57}$$

2.5.2 Remarks on the algorithm

In order to guarantee feasibility of the state space model, two conditions should be fulfilled. First, the model must be stable, therefore all of the eigenvalues of $\hat{\mathbf{A}}$ must be located inside the

unit circle in the complex plane. Second, estimated noise covariance matrix by (2.47) must be symmetric and positive definite. Furthermore, define a lower triangular matrix $\mathbf{\Gamma}$, obtained by Cholesky decomposition of the noise covariance matrix given by (2.47). Then the white noise vector sequence in (3.36) might be generated as $\mathbf{e}(j) = \mathbf{\Gamma}\mathbf{w}_{\mathrm{s}}(j)$

$$\mathbf{C}_{\mathbf{w}_{\mathrm{s}}\mathbf{w}_{\mathrm{s}}}(k-j) = E\big[\mathbf{w}_{\mathrm{s}}(j)\mathbf{w}_{\mathrm{s}}^{\mathrm{T}}(k)\big] = \begin{cases} \mathbf{0} & , \quad j \neq k \\ \mathbf{I} & , \quad j = k \end{cases} \tag{2.58}$$

where $\mathbf{w}_{\mathrm{s}}(j)$ is a zero mean stationary Gaussian white noise vector of dimension $M \times 1$ with mutually independent random variables and cross-covariance matrix indicated by (2.58).

2.6 Numerical simulation

The along-wind turbulence will be simulated in the 5 nodes indicated in figure 2.3, all placed in the same plane perpendicular to the wind direction. Node 1 refers to the hub of the rotor plane, where the mean wind velocity is given as $V = 15\,[\mathrm{m/s}]$. To investigate efficiency of the SSM method for vector turbulence modeling in the first case turbulence is simulated only on node 1 and in the second case on all five nodes shown in Figure 2.3. Simulation parameters for the filter model are chosen $N = 2048, \Delta t = 0.0488s$. Figure 2.4 illustrates the accuracy of the modified cross-spectral density matrix, for 5 nodes, $\tilde{\mathbf{S}}_{\mathbf{vv}}(\omega)$ defined by (2.16) and (2.21), respectively, in comparison to the corresponding unmodified matrix $\mathbf{S}_{\mathbf{vv}}(\omega)$. The figure shows the relative error of $\tilde{\mathbf{S}}_{\mathbf{vv}}(\omega)$ compared to $\mathbf{S}_{\mathbf{vv}}(\omega)$ as expressed by the fractions of Euclidean norms $\| \tilde{\mathbf{S}}_{\mathbf{vv}}(\omega) - \mathbf{S}_{\mathbf{vv}}(\omega) \| / \| \mathbf{S}_{\mathbf{vv}}(\omega) \|$ as a function of the angular frequency in the interval $\omega \in [0, 4s^{-1}]$, where non-positive definiteness of $\tilde{\mathbf{S}}_{\mathbf{vv}}(\omega)$ occurs. As seen, the normalized error related to the modification (2.16) may be up to 100% at some frequencies. In contrast the modification (2.21) is related to much smaller errors. Figure 2.5 shows the components of the impulse

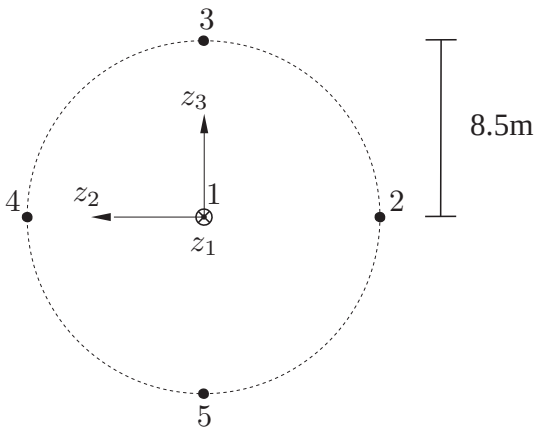

Figure 2.3 Definition of nodes in numerical example.

response matrix (2.25). Here and in the following the modified cross-spectral density matrix (2.21) is used. As seen, both $h_{11}(t)$ related to node 1, and the cross function $h_{21}(t)$ between nodes 2 and 1 are almost symmetric with time. In order to provide a common framework for

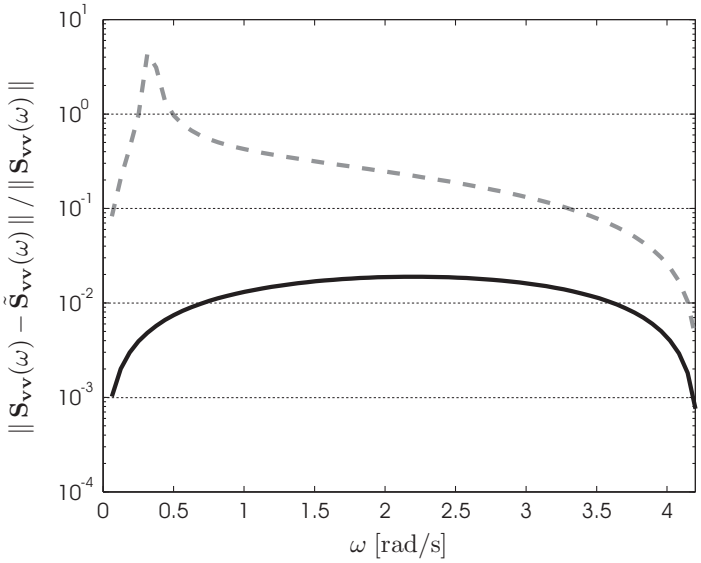

Figure 2.4 Relative error of Eucledian norm of modified cross-spectral density matrix. —:$\tilde{\mathbf{S}}_{\mathbf{vv}}(\omega)$ given by Eq. (2.21). − − −:$\tilde{\mathbf{S}}_{\mathbf{vv}}(\omega)$ given by Eq. (2.16).

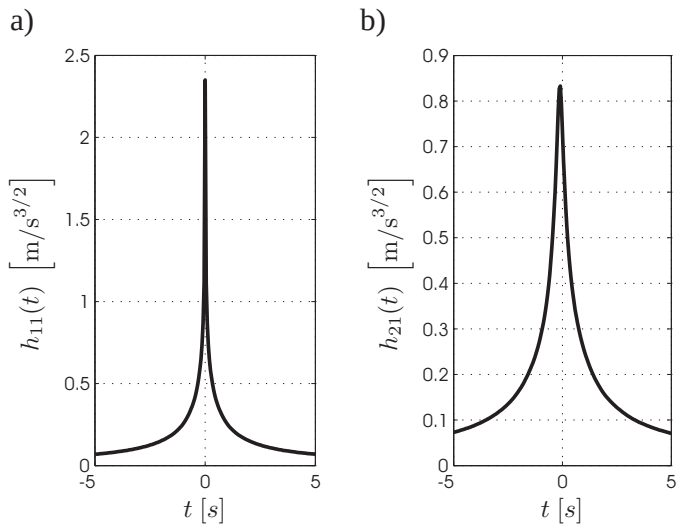

Figure 2.5 Components of the impulse response matrix. a) $h_{11}(t)$. b) $h_{21}(t)$.

comparing results of different methods, the same white noise realization is used for simulation of the time series of the turbulence process with all of the algorithms in this example. Figure 2.6 illustrates the quality of the time series based on (2.28). An AR model of order $\acute{p} = 30$

is calibrated with the 2SLS method and is used for simulating the turbulence at node 1. Figure 2.7 shows time series simulated using the calibrated AR model. Next the SSM method is

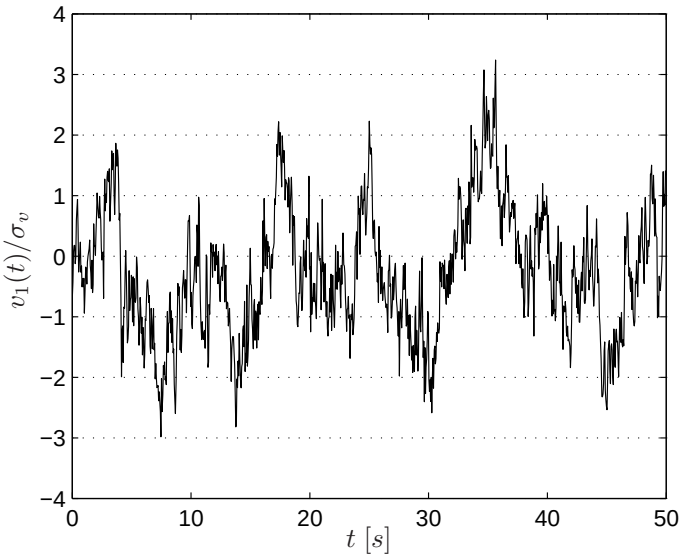

Figure 2.6 Numerical simulation of turbulence in node 1 based on Eq. (2.28).

used to estimate a state space model for the turbulence at node 1. Figure 2.8 shows $\ln(s_i + 1)$ versus singular value number, i, of the block Toeplits matrix $\mathbf{T}$, where s_i denotes i^{th} singular value. As can be seen the first five singular values are considerably larger than the others. This inculcates that the optimum model order is 5 in this case. Figure 2.9 shows the simulated time series of turbulence using a state space model of order 5. In what follows plots of auto- and cross-covariance functions are only indicated for positive time separation due to their symmetry property, $\mathbf{C_{vv}}(\tau) = \mathbf{C}^{\mathrm{T}}_{\mathbf{vv}}(-\tau)$. Figure 2.10 illustrates the relative performance of simulations obtained by the filter model with Eq.(2.28), the 2SLS method and the SSM method. In figure 2.10 the convergence of the standard deviation estimate $\hat{\sigma}_{v_1}$ by ergodic sampling is shown. Figure 2.11 shows the covariance function of the various models compared to the theoretic covariance function as given by Eq.(2.13) for the model orders 30 and 5 for 2SLS and SSM methods, respectively. As can be seen, second order statistics of the SSM are more akin to the original turbulence compared to the AR model calibrated by 2SLS method in both cases. From the presented example it can be concluded that variance estimations of all these models are of equal quality. However, the auto-covariance function estimate of the SSM method is much better than the estimates of the filter method and the 2SLS method. To investigate efficiency of the SSM method for vector turbulence modelling, in the next example rotor plane is discretized into five nodes shown in Figure 2.3. Figure 2.12 shows singular values of the block Toeplitz matrix used for SSM. As seen, there exist approximately 26 non-zero singular values which suggest a model order of 26 for this case. Furthermore, the 2SLS method is used to calibrate an AR model of order 60 which is compared to the SSM model. Figure 2.13 shows auto-covariance function of

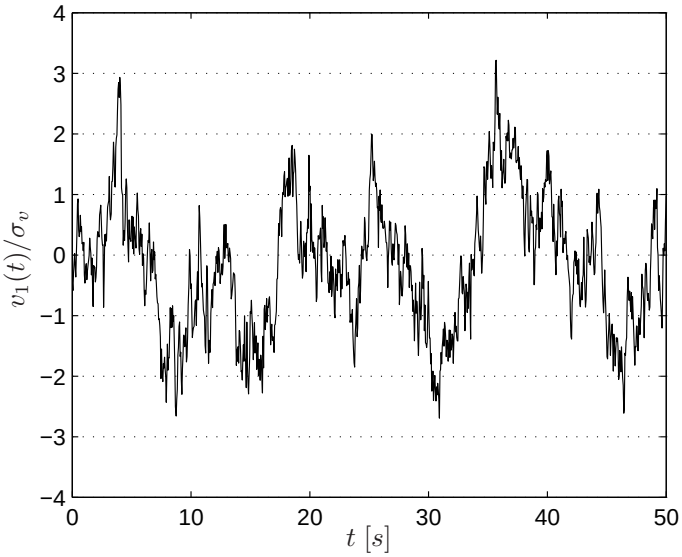

Figure 2.7 Numerical simulation of turbulence in node 1 based on AR(30) model, Eq. (2.33).

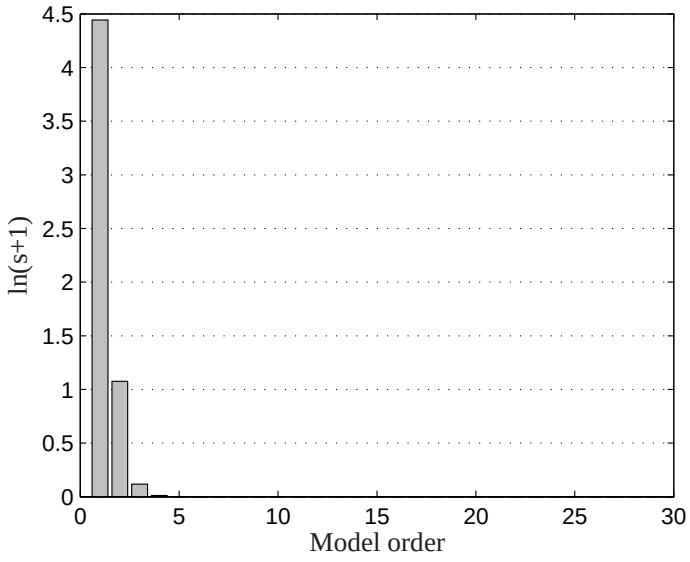

Figure 2.8 Singular values of the block Toeplits matrix of the cross-covariances used for model estimation in SSM.

the state space model of order 26 at node 1 and the AR model of order 60. Figure 2.14 shows

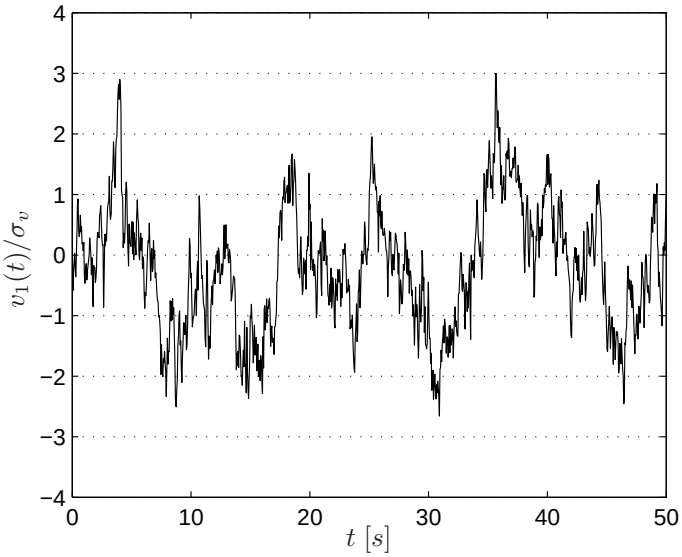

Figure 2.9 Numerical simulation of turbulence in node 1 based on SSM model of order 5, Eq. (3.36).

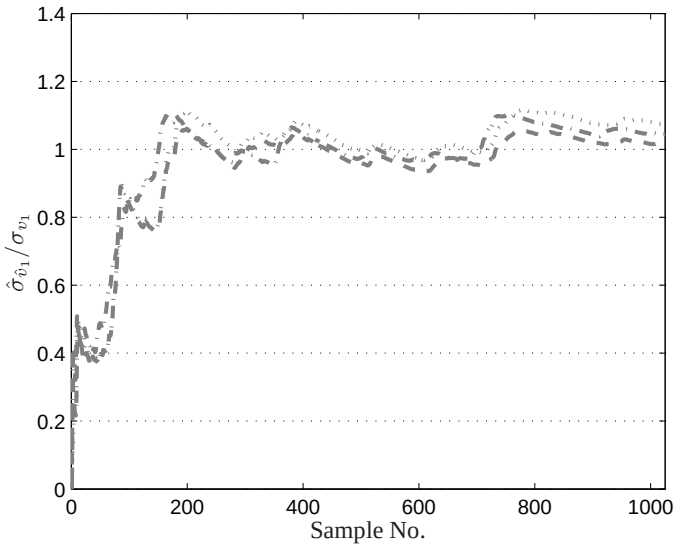

Figure 2.10 Convergence of standard deviation estimates for numerical simulation of turbulence in node 1. −. − .−: Filter model, Eq. (2.28). ….. : 2SLS, order 30. − − −: SSM, order 5.

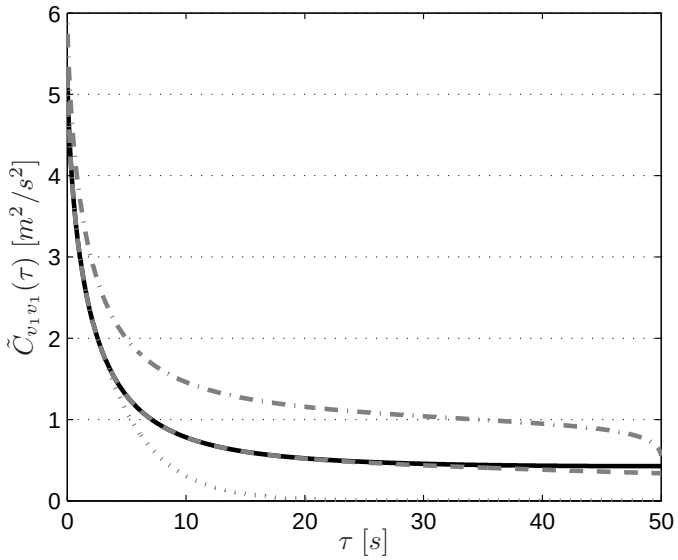

Figure 2.11 Auto covariance function of scalar model at node 1. ——: Covariance function, Eq. (2.13). −.−.−: Filter model, Eq. (2.28). ..... : 2SLS, order 60, Eq.(2.34). − − −: SSM, order 14, Eq.(2.44).

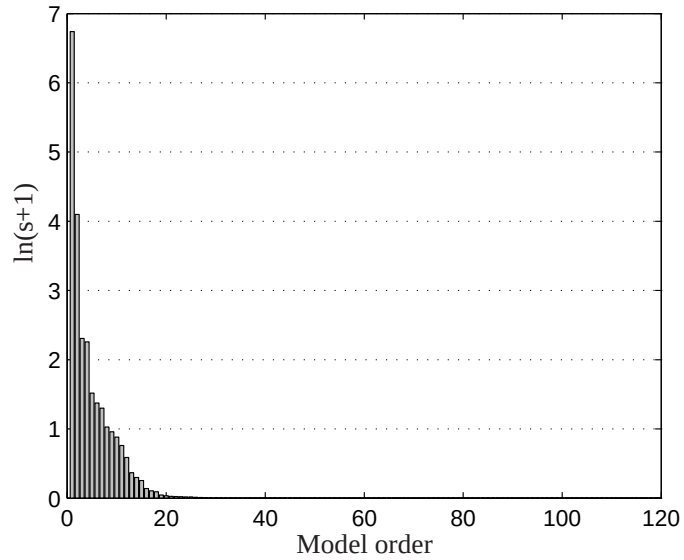

Figure 2.12 Singular values of the block Toeplits matrix of the cross-covariances used for model estimation in SSM.

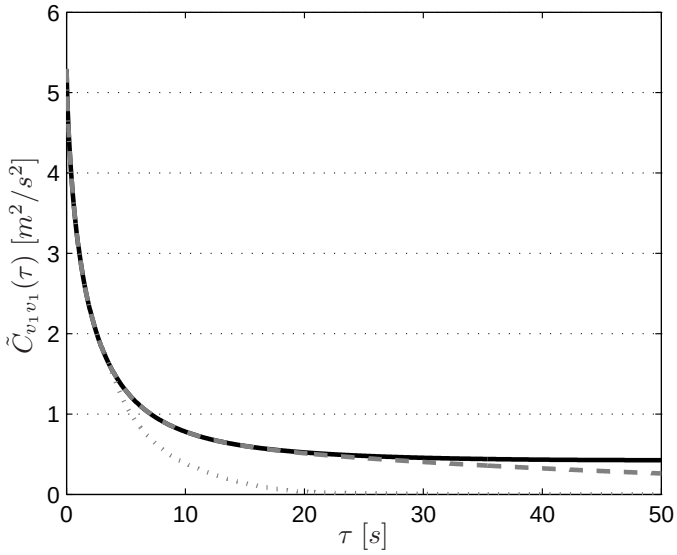

Figure 2.13 Auto-covariance function of the SSM model for vector turbulence at node 1. ——: Covariance matrix, Eq. (2.13). ..... : 2SLS, order 60, Eq.(2.34). – – –: SSM, order 26, Eq.(2.44).

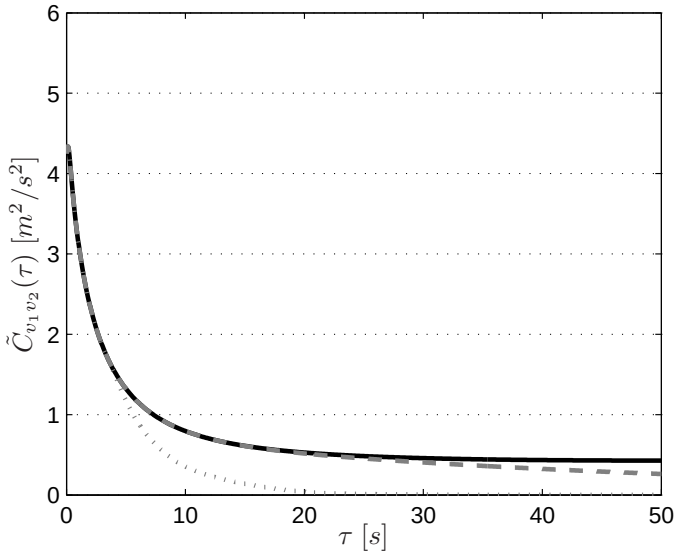

Figure 2.14 Cross-covariance function of the SSM model for vector turbulence between nodes 1 and 2. ——: Covariance matrix, Eq. (2.13). ..... : 2SLS, order 60, Eq.(2.34). – – –: SSM, order 26, Eq.(2.44).

cross-covariance function of the state space model between nodes 1 and 2 compared to the theoretical cross-covariance function. As seen the cross-covariance functions of the SSM are in very good agreement with the theoretical cross-covariance functions while the discrepancy of the AR model of the 2SLS is considerable. It should be noted that the order of the SSM model is considerably lower than the AR model of the 2SLS, nevertheless its covariance function is much more accurate.

CHAPTER 3
The Wind Turbine Model

A reduced order model of a wind turbine is developed in this study. The model specifications are adopted from the 5MW NREL Reference wind turbine. The model can be divided into four major parts (modules), the wind field simulator, the aerodynamic load calculation unit, the structural dynamic solver and the pitch controller. The structural model is based on a reduced order Finite Element (FE) model. The aerodynamic loads are calculated using the Blade Element Momentum theory (BEM) and the controller is a *Proportional-Integrator-Differentiator* (PID) collective blade pitch controller aiming at keeping the rotational speed of the rotor around its nominal value. However a brief description of the wind turbine model is already presented in some of the presented papers included in the thesis, this chapter is added in favor of providing an integrated detailed view into the wind turbine model used in the thesis.

3.1 Overview of the model

A general perspective of a wind turbine model is shown in figure 3.1. The modules within the grey area denotes the wind turbine model. The main parts of any wind turbine model are the *Wind field generator, Aerodynamic load calculation unit* and the *structural model solver*. Finally the *controller* module can also be considered as a subsection of the structural unit since the governing equations of the system can be combined with the controller and be solved simultaneously. The so-called *influence function* is the function responsible for determining the position of each blade, e.g. the azimuth angle of the rotor, hence determining the active nodes of the wind field at each instant of time. In the following sections each part of the model developed for this study will be described in detail.

3.2 Mechanical Model

The motions of the blades relative to the hub and the motion of the tower in the mean wind direction are modeled by single degree-of-freedom models. Only motions in the mean wind direction is considered for which reason no gyroscopic forces are present, save the centripetal forces. Let $y_i(x,t), i = 1,2,3$ denote the displacement fields of the blades relative to the hub, where $x \in [0, L]$ is measured from the hub and L is the length of the blades of figure 3.2. Further $y_4(x,t)$ denote the displacement of the tower in the same direction, where $x \in [0, h]$ is measured from the foundation and h is the height of the nacelle above the ground surface. Then, the indicated displacement fields may written

$$\left.\begin{array}{lcll} y_i(x,t) & \simeq & \Phi(x)q_i(t) & , \quad i = 1,2,3 \\ y_4(x,t) & \simeq & \Phi_0(x)q_4(t) & \end{array}\right\} \tag{3.1}$$

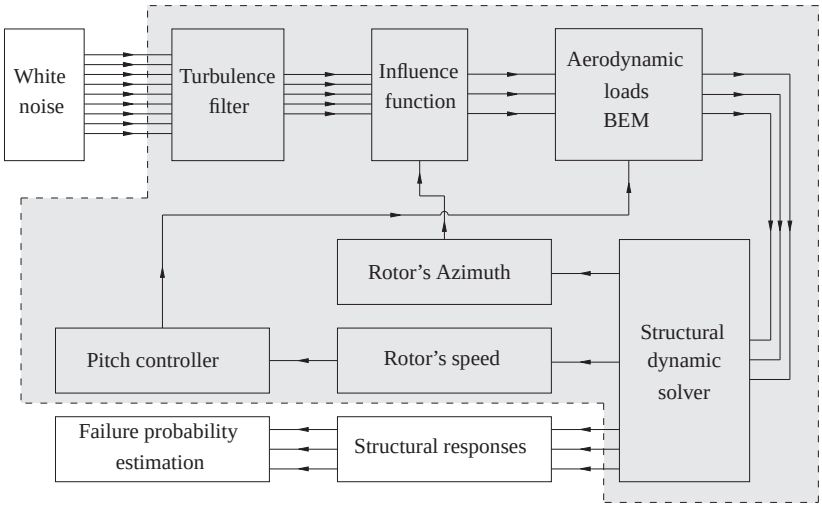

Figure 3.1 Flowchart of the wind turbine model

$\Phi_0(x)$ is the part of the fundamental eigenmode of the wind turbine belonging to the tower and $\Phi(x)$ is the fundamental fixed base mode shape of the blade. The mode shapes are normalized to one at the nacelle and the blade tip, respectively, so the generalized coordinates $q_1(t), q_2(t), q_3(t)$ may be interpreted as the tip displacement of the blades relative to the hub, and $q_4(t)$ is the displacement of the nacelle. Note that a quasi-static deformation of the nacelle due to the mean rotor thrust will only affect $q_4(t)$. The blades are modeled as Bernoulli-Euler beams with the bending stiffness $EI(x)$ around an axis orthogonal to the rotor plane, and the mass per unit length $\mu(x)$. Similarly, the tower is modeled as a Bernoulli-Euler beam with the bending stiffness $EI_0(x)$. The mass per unit length is formally written as

$$\bar{\mu}_0(x) = \mu_0(x) + M_0\delta(x-h) \tag{3.2}$$

$\mu_0(x)$ denotes the continuous mass distribution, M_0 is the mass of the nacelle and the hub; $\delta(\cdot)$ is Dirac's delta function. The dynamic load per unit length on the tower in the mean wind direction is denoted $p_4(x,t)$. Correspondingly, the load on the tree blades in the same direction are denoted $p_1(x,t), p_2(x,t)$ and $p_3(x,t)$. The rigid body motion of the drive train is modeled as a single rotational degree of freedom q_5 by assuming infinite stiff drive shafts and no elastic deformation in the gear, whereby the following kinematic relation emerge for the angular rotation of the rotor of the generator

$$q_g = Nq_5 \tag{3.3}$$

where N is the gear ratio, cf. figure 3.3. Furthermore, the mass moment of inertia of the gear wheels and the connected shafts are included into the mass moment of inertia J_r and J_g of the rotor and the generator rotor, respectively. The kinematic and potential energy of the system are

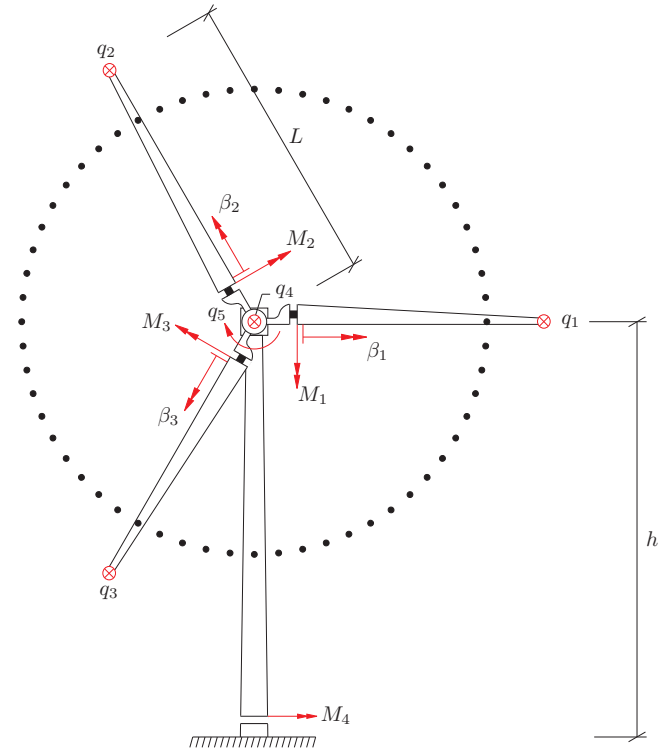

Figure 3.2 Definition of degrees of freedom section moments and pitch angles

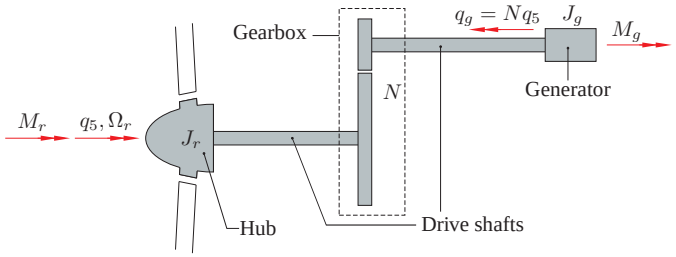

Figure 3.3 Single degree of freedom representation of drive train

calculated as

$$\mathcal{T} = \frac{1}{2}\int_0^h \bar{\mu}_0(x)\big(\Phi_0(x)\dot{q}_4(t)\big)^2 dx + \frac{1}{2}\sum_{i=1}^{3}\int_0^L \mu(x)\big(\Phi_0(h)\dot{q}_4(t) + \Phi(x)\dot{q}_i(t)\big)^2 dx + \frac{1}{2}J_r\big(\dot{q}_5(t)\big)^2 + \frac{1}{2}J_g\big(N\dot{q}_5\big)^2 \tag{3.4}$$

$$\begin{aligned}\mathcal{U} =&\frac{1}{2}\int_0^L EI_0(x)\left(\frac{d^2\Phi_0(x)}{dx^2}\right)^2 q_4^2(t)dx + \frac{1}{2}\sum_{i=1}^{3}\int_0^L EI(x)\left(\frac{d^2\Phi(x)}{dx^2}\right)^2 q_i^2(t)dx \\ &- \sum_{i=1}^{3}\int_0^L \big(\Phi_0(h)q_4(t) + \Phi(x)q_i(t)\big)p_i(x,t)dx - \int_0^h \Phi_0(x)q_4(t)p_4(x,t)dx \\ &- \big(M_r - (1+\eta)NM_g\big)q_5(t)\end{aligned} \tag{3.5}$$

Using Lagrange's equations (Meirovitch 2001),

$$\frac{d}{dt}\left(\frac{\partial \mathcal{T}}{\partial \dot{q}}\right) - \frac{\partial \mathcal{T}}{\partial q} + \frac{\partial \mathcal{U}}{\partial q} = \mathcal{F}_{nc} \tag{3.6}$$

where $\mathcal{F}_{nc}$ denotes the non-conservative forces. The following governing equations of the system may be obtained

$$\mathbf{m}\ddot{\mathbf{q}}(t) + \mathbf{c}\dot{\mathbf{q}}(t) + \mathbf{k}\mathbf{q}(t) = \mathbf{f}(t) \tag{3.7}$$

$$\mathbf{m} = \begin{bmatrix} m_1 & 0 & 0 & m_2 & 0 \\ 0 & m_1 & 0 & m_2 & 0 \\ 0 & 0 & m_1 & m_2 & 0 \\ m_2 & m_2 & m_2 & m_0 & 0 \\ 0 & 0 & 0 & 0 & J \end{bmatrix} \quad , \quad \mathbf{k} = \begin{bmatrix} k & 0 & 0 & 0 & 0 \\ 0 & k & 0 & 0 & 0 \\ 0 & 0 & k & 0 & 0 \\ 0 & 0 & 0 & k_0 & 0 \\ 0 & 0 & 0 & 0 & 0 \end{bmatrix} \tag{3.8}$$

$$\left.\begin{array}{lllllll} m &=& \int_0^L \mu(x)dx & , & m_4 &=& \int_0^L x\mu(x)\Phi(x)dx \\ m_1 &=& \int_0^L \mu(x)\Phi^2(x)dx & , & m_5 &=& \int_0^h x\mu_0(x)\Phi_0(x)dx \\ m_2 &=& \int_0^L \mu(x)\Phi(x)dx & , & m_0 &=& \int_0^h \mu_0(x)\Phi_0^2(x)dx + M_0 + 3m \\ m_3 &=& \int_0^L x\mu(x)dx & , & J_r &=& 3\int_0^L x^2\mu(x)dx \end{array}\right\} \tag{3.9}$$

m is the mass of the blade, m_0 and m_1 are the generalized masses related to the degrees of freedom $q_i(t), i = 1,\ldots,4$. m_2 is a coupling parameter in the mass matrix, and m_3, m_4 and m_5 will be used later at the calculation of the bending moments in the blade at the hub and in the lower foundation. J is the generalized mass moment of inertia related to the rigid body degree-of-freedom $q_5(t)$ given as

$$J = J_r + N^2 J_g \tag{3.10}$$

The damping matrix $\mathbf{c}$ merely includes structural damping. Aerodynamic damping is included later via the aerodynamic load. Then $\mathbf{c}$ may be written as

$$\mathbf{c} = \begin{bmatrix} 2\zeta\omega m_1 & 0 & 0 & 0 & 0 \\ 0 & 2\zeta\omega m_1 & 0 & 0 & 0 \\ 0 & 0 & 2\zeta\omega m_1 & 0 & 0 \\ 0 & 0 & 0 & 2\zeta_0\omega_0 m_0 & 0 \\ 0 & 0 & 0 & 0 & \eta M_{r,0}/\Omega_{r,0} \end{bmatrix} \tag{3.11}$$

$$\mathbf{q}(t) = \begin{bmatrix} q_1(t) \\ q_2(t) \\ q_3(t) \\ q_4(t) \\ q_5(t) \end{bmatrix} \quad , \quad \mathbf{f}(t) = \begin{bmatrix} f_1(t) \\ f_2(t) \\ f_3(t) \\ f_4(t) \\ f_5(t) \end{bmatrix} \tag{3.12}$$

where $\Omega_{r,0} = \dot{q}_{5,0}$ is the referential (nominal) rotational speed of the rotor. ω and ζ denote the eigenfrequency and damping ratio of the blades, when fixed to the hub. Correspondingly, ω_0 and ζ_0 denote the eigenfrequency and damping ratio of the lowest mode of the tower, which are assumed to be known. η is the loss factor of the transmission system due to friction in gears and bearings, which typically is a few percent and $M_{r,0} = P/\Omega_{r,0}$ is the referential rotor torque for $P = 5\text{MW}$ nominal power output. The generalized stiffness coefficients of the blades and the tower are given as

$$\left.\begin{aligned} k &= \int_0^L EI(x)\left(\frac{d^2\Phi(x)}{dx^2}\right)dx = \omega^2 m_1 \\ k_0 &= \int_0^h EI_0(x)\left(\frac{d^2\Phi_0(x)}{dx^2}\right)dx = \omega_0^2 m_0 \end{aligned}\right\} \tag{3.13}$$

k_0 is determined, so the generalized eigenvalue problem defined from (3.8) provides the prescribed angular lower eigenfrequency ω_0. The generalized external dynamic loads become

$$\left.\begin{aligned} f_i(t) &= \textstyle\int_0^L \Phi(x)p_i(x,t)dx \quad , \quad i = 1,2,3 \\ f_4(t) &= \textstyle\int_0^h \Phi_0(x)p_4(x,t)dx + \sum_{i=1}^3 \int_0^L \Phi(x)p_i(x,t)dx \\ f_5(t) &= M_r - (1+\eta)NM_g \end{aligned}\right\} \tag{3.14}$$

where M_r and M_g are the instantaneous rotor and generator torques respectively and asynchronous slip variable generator is considered for which the generator torque under normal operation conditions is linearly dependent on the rotational speed $N\dot{q}_5(t)$. The relation may be given on the form

$$M_g(t) = M_{g,0}\frac{N\dot{q}_5(t) - \Omega_{g,00}}{\Omega_{g,0} - \Omega_{g,00}} \tag{3.15}$$

where $M_{g,0} = M_{r,0}/N$ is the nominal generator torque, $\Omega_{g,0} = N\Omega_{r,0}$ is the nominal generator rotational speed and $\Omega_{g,00}$ is the generator speed for the zero generator torque. Using d'Alembert's principle the bending moments $M_1(t), M_2(t), M_3(t)$ at the hub of the blades and $M_4(t)$ at the foundation of the tower are given by, see figure 3.2

$$\left.\begin{aligned} M_i(t) &= \textstyle\int_0^L xp_i(x,t)dx - m_3\ddot{q}_4(t) - m_4\ddot{q}_i(t) \quad , \quad i = 1,2,3 \\ M_4(t) &= \textstyle\int_0^h xp_4(x,t)dx - \Big(m_5 + \big(M_0 + 3m\big)h\Big)\ddot{q}_4(t) \\ &\qquad + h\sum_{j=1}^3 \Big(\int_0^L p_i(x,t)dx - m_2\ddot{q}_i(t)\Big) \end{aligned}\right\} \tag{3.16}$$

which may be assembled in the following matrix equation

$$\mathbf{M}(t) = \mathbf{M}_0(t) - \mathbf{M}_1\ddot{\mathbf{q}}(t) \tag{3.17}$$

$$\mathbf{M}(t) = \begin{bmatrix} M_1(t) \\ M_2(t) \\ M_3(t) \\ M_4(t) \end{bmatrix} \quad , \quad \mathbf{M}_0(t) = \begin{bmatrix} \int_0^L xp_1(x,t)dx \\ \int_0^L xp_2(x,t)dx \\ \int_0^L xp_3(x,t)dx \\ \int_0^h xp_4(x,t)dx + h\sum_{i=1}^3 \int_0^L p_i(x,t)dx \end{bmatrix} \tag{3.18}$$

$$\mathbf{M}_1 = \begin{bmatrix} m_4 & 0 & 0 & m_3 & 0 \\ 0 & m_4 & 0 & m_3 & 0 \\ 0 & 0 & m_4 & m_3 & 0 \\ m_2 h & m_2 h & m_2 h & m_5 + (M_0 + 3m)h & 0 \end{bmatrix} \tag{3.19}$$

$\mathbf{M}_0(t)$ specifies the bending moment from the external loads and $-\mathbf{M}_1\ddot{\mathbf{q}}(t)$ are the moment constraints from the inertial forces. $\beta_1(t), \beta_2(t)$ and $\beta_3(t)$ denote the pitch angles of the blades, see figure 3.2. These are controlled by the 1st order filter equations assembled in the vector relation

$$\dot{\boldsymbol{\beta}}(t) = -\frac{1}{\tau}\Big(\boldsymbol{\beta}(t) - \boldsymbol{\beta}_0(\mathbf{q}, \dot{\mathbf{q}}, t)\Big) \tag{3.20}$$

$$\boldsymbol{\beta}(t) = \begin{bmatrix} \beta_1(t) \\ \beta_2(t) \\ \beta_3(t) \end{bmatrix} \quad , \quad \boldsymbol{\beta}_0(\mathbf{q}, \dot{\mathbf{q}}, t) = \begin{bmatrix} \beta_{1,0}(\mathbf{q}, \dot{\mathbf{q}}, t) \\ \beta_{2,0}(\mathbf{q}, \dot{\mathbf{q}}, t) \\ \beta_{3,0}(\mathbf{q}, \dot{\mathbf{q}}, t) \end{bmatrix} \tag{3.21}$$

τ is a constant specifying the time-delay of the pitch actuators. $\beta_{j,0}(\mathbf{q}, \dot{\mathbf{q}}, t)$ denotes the pitch control demand. This might be designed via different techniques either to suppress the undesirable vibrations of the structure, or to control the rotational speed of the rotor. In the first case, $q_i\ ,\ i = 1, \ldots, 4$ will be incorporated into the controller, while in the second case, the controller acts only on q_5 and its derivative. Only the latter case will be considered. From various available techniques for controller design, the PID controller, due to its wide range of applications in industry and its simplicity, (Ogata 2009), is chosen in this work. The control command is then expressed as

$$\begin{aligned} \boldsymbol{\beta}_{j,0}(\mathbf{q}, \dot{\mathbf{q}}, t) &= G\bigg(e(t) + \frac{1}{\tau_i}\int_0^t e(t)d\tau + \tau_d \frac{d}{dt}e(t)\bigg) \\ &= G\bigg(\dot{q}_5(t) - \Omega_{r,0} + \frac{1}{\tau_i}\Big(q_5(t) - t\Omega_{r,0}\Big) + \\ &\qquad \frac{\tau_d}{J}\Big(f_5(t) - \eta\frac{M_{r,0}}{\Omega_{r,0}}\dot{q}_5(t)\Big)\bigg) \quad , \quad j = 1, 2, 3 \end{aligned} \tag{3.22}$$

where $e(t)$ is the error signal defined as

$$e(t) = \dot{q}_5(t) - \dot{q}_{5,0} \tag{3.23}$$

as seen the control demand is identical for all blades. G is the controller gain which is chosen inverse proportional to the partial derivative $\frac{\partial M_r}{\partial \boldsymbol{\beta}}$, τ_i is the integral control time constant and τ_d is the differentiator time constant which is chosen as a fraction of τ_i. There exist several techniques for designing the indicated controller i.e. by means of the Ziegler-Nichols empirical tuning formula, (Ogata 2009). In practice a pure differentiator is rarely used due to its noise amplification effect, therefore it is usually replaced by a first order low-pass filter, (Xue *et al.* 2008). In the present work the controller gains are tuned manually with the gains indicated in table 3.1. The equations of motion (3.7) and the control equations (3.20) may be combined into the state vector equations

$$\dot{\mathbf{z}}(t) = \mathbf{A}\mathbf{z}(t) + \mathbf{B}\mathbf{f}\big(\mathbf{v}(t), \mathbf{z}(t)\big) + \mathbf{B}_0(t) \tag{3.24}$$

$$\mathbf{z}(t) = \begin{bmatrix} \mathbf{q}(t) \\ \dot{\mathbf{q}}(t) \\ \boldsymbol{\beta}(t) \end{bmatrix} \quad , \quad \mathbf{A} = \begin{bmatrix} \mathbf{0} & \mathbf{I} & \mathbf{0} \\ -\mathbf{m}^{-1}\mathbf{k} & -\mathbf{m}^{-1}\mathbf{c} & \mathbf{0} \\ \frac{1}{\tau}\mathbf{b}_1 & \frac{1}{\tau}\mathbf{b}_2 & -\frac{1}{\tau}\mathbf{I} \end{bmatrix} \tag{3.25}$$

$$\mathbf{B} = \begin{bmatrix} \mathbf{0} \\ \mathbf{m}^{-1} \\ \mathbf{b}_3 \end{bmatrix} \quad , \quad \mathbf{B}_0(t) = \begin{bmatrix} \mathbf{0} \\ \mathbf{0} \\ \mathbf{b}_0(t) \end{bmatrix} \tag{3.26}$$

where $\mathbf{b}_0(t), \mathbf{b}_1, \mathbf{b}_2$ and $\mathbf{b}_3$ are given as

$$\mathbf{b}_0(t) = -\frac{G\,\Omega_{r,0}}{\tau}\left(1 + \frac{t}{\tau_i}\right)\begin{bmatrix} 1 \\ 1 \\ 1 \end{bmatrix} \tag{3.27}$$

$$\mathbf{b}_1 = \frac{G}{\tau_i}\begin{bmatrix} 0 & 0 & 0 & 0 & 1 \\ 0 & 0 & 0 & 0 & 1 \\ 0 & 0 & 0 & 0 & 1 \end{bmatrix} \quad , \quad \mathbf{b}_2 = \tau_i\Big(1 - \eta\frac{\tau_d}{J}\frac{M_{r,0}}{\Omega_{r,0}}\Big)\mathbf{b}_1 \quad , \quad \mathbf{b}_3 = \frac{\tau_d}{J}\mathbf{b}_2$$

3.3 Aerodynamic load modeling

Only the aerodynamic load on the blades is considered, i.e. wind load on the tower is ignored; $p_4(x,t) = 0$. Aerodynamic damping is included via a quasi-static effective angle of attack $\alpha(x,t)$ so changes of the angle of attack is instantly felt in the aerodynamic loads. This means that the time scale for adjustment of the non-stationary flow is assumed to be small compared to the fundamental eigenperiod of the blade. The wind loads are calculated by the BEM method, (Hansen 2007). In this respect the following parameters are defined

$$\begin{aligned} V_r(x,t) &= \sqrt{(V + v - \dot{q}_4 - \dot{y}_i)^2(1-a)^2 + \dot{q}_5^2 r^2 (1+a')^2} \\ \phi(x,t) &= \arctan\left(\frac{(1-a)(V + v - \dot{q}_4 - \dot{y}_i)}{(1+a')\dot{q}_5 r}\right) \\ \alpha(x,t) &= \phi(x,t) - \beta_i(t) - \kappa(x) \end{aligned} \tag{3.28}$$

V_r is the relative wind speed c.f. figure 3.4. V denotes the mean wind speed and v is the turbulence contribution to the wind speed. The turbulence with a prescribed correlation structure is generated in 30 points on a circle with radius $0.8L$ as seen in figure 3.2. Next, the turbulence on a given blade is obtained by linear interpolation between the given points. The interpolated turbulence value is assumed common to all points on the blade. The mean wind speed V is assumed constant over the rotor area. a and a' are the axial and the tangential induction factors respectively, which are calculated below by means of the BEM method, and $\dot{q}_4 + \dot{y}_i(x,t)$, where $\dot{y}_i(x,t) = \Phi(x)\dot{q}_i(t)$, indicates the velocity of the cross-section of the abscissa x in the direction of the mean wind. This term is responsible for the aerodynamic damping of the blades and the turbine as a whole. ϕ is the so-called flow angle and $\kappa = \kappa(x)$ denotes the pre-twist of the blade. The lift and drag force per unit of the blade $p_L(x,t)$ and $p_D(x,t)$ are given as

$$\left.\begin{aligned} p_L(x,t) &= \tfrac{1}{2}\rho {V_r}^2(x,t) C_L(\alpha) c(x) \\ p_D(x,t) &= \tfrac{1}{2}\rho {V_r}^2(x,t) C_D(\alpha) c(x) \end{aligned}\right\} \tag{3.29}$$

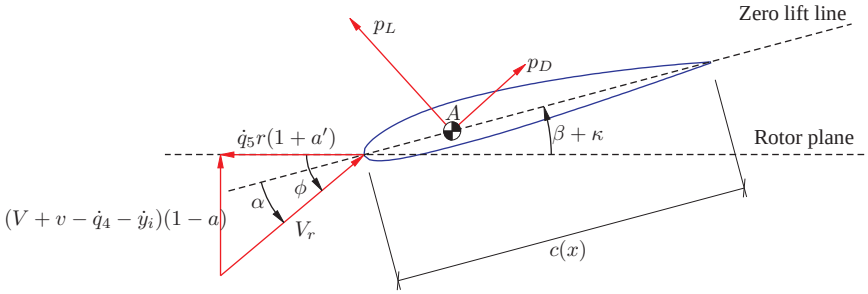

Figure 3.4 Blade profile definition of velocities and forces.

where ρ is the density of air, $c(x)$ is the chord length and $C_L(\alpha)$ and $C_D(\alpha)$ are the lift and drag coefficients. The load in the normal direction of the plane become

$$p_i(x,t) = \frac{1}{2}\rho {V_r}^2(x,t) C_N(\alpha) c(x) \tag{3.30}$$

where $C_N(\alpha)$ is the normal coefficient. $C_N(\alpha)$ and the corresponding tangential coefficient $C_T(\alpha)$ for the determination of the rotor torque are obtained from, see figure 3.4

$$\begin{bmatrix} C_N \\ C_T \end{bmatrix} = \begin{bmatrix} \cos\phi & \sin\phi \\ \sin\phi & -\cos\phi \end{bmatrix} \begin{bmatrix} C_L \\ C_D \end{bmatrix} \tag{3.31}$$

a and a' are then obtained as

$$a = \frac{1}{1+\dfrac{4F\sin^2\phi}{\sigma C_N}} \quad , \quad a' = \frac{1}{1+\dfrac{4F\sin\phi\cos\phi}{\sigma C_T}} \tag{3.32}$$

where F is the Prandtl's tip loss factor given as

$$F = \frac{2}{\pi}\cos^{-1}\left(\exp\left(-\frac{B}{2}\frac{L-x}{x\sin\phi}\right)\right) \tag{3.33}$$

where $B = 3$ is the number of blades. The above procedure needs to be iterated until convergence of the induction factors have been achieved. Figure 3.5 shows variation of the aerodynamic load versus wind speed at two diffenet locations on the blade of the 5MW reference wind turbine calculated using BEM method described above.

3.3.1 Wind modeling

Various wind speed distribution functions are used in simulation of wind loads i.e. Log-normal, Gumbel, etc. nevertheless the IEC standard (IEC 2005a) recommends that the mean wind speed over a time period of 10 min at the hub height is Rayleigh distributed with the following PDF

$$f_V(\mathrm{V_h}) = \frac{\pi \mathrm{V_h}}{2\mathrm{V_a^2}} \exp\left[-\pi\left(\frac{\mathrm{V_h}}{2\mathrm{V_a}}\right)^2\right] \tag{3.34}$$

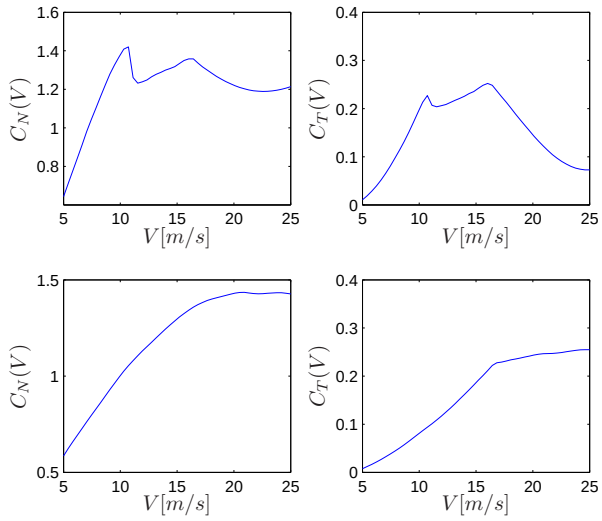

Figure 3.5 Aerodynamic load coefficient of the 5MW wind turbine blade for $\alpha = \kappa = \upsilon = 0$ and $\dot{q}_5 = \omega_{r,0}$; a) Normal load coefficient at 30m distance from blade's root, b) Tangential load coefficient at 30m distance from blade's root, c) Normal load coefficient at 60m distance from blade's root, d) Tangential load coefficient at 60m distance from blade's root

where $\mathrm{V_a} = 0.2\mathrm{V_{10}}$ and $\mathrm{V_h}$ is the wind speed at the hub height. Next, it is assumed that the mean wind speed in terms of height obeys the following power profile where υ is given in table 3.1

$$\mathrm{V(z)} = \mathrm{V_h}\left(\frac{\mathrm{z}}{\mathrm{h}}\right)^{\upsilon} \tag{3.35}$$

In this work it is assumed that the mean wind velocity V is constant over the rotor area. Following the requirements of the RR&S on the load vector, c.f. section 5.1, it is required that turbulence - the stochastic part of the wind load - is modeled as a process with short memory. ARMA models and state space models both satisfy this requirement. The governing equations of the system and the controller are usually represented in the state space form so it is advantageous if the load is represented in the same form. A calibrated ARMA model might be represented in the state space format, (Akaike 1974), alternatively a state space model for turbulence might be calibrated directly using the SSM method represented in chapter 2 which discards this transformation. The SSM method is even more attractive since its model seems to be more accurate, stable and with shorter memory (lower model order) than an ARMA model, (Sichani *et al.* 2010). Accordingly, in this work this approach is used to calibrate a state space model for the turbulence. The method is used to construct a state space model of the form (3.36); in which $\mathbf{x}(j+1)$ is an internal state vector at each discrete time step, $\mathbf{A}_T$ and $\mathbf{C}_T$ are system matrices and , $\mathbf{K}_T$ is the steady state Kalman gain matrix. $\mathbf{e}(j)$ is a random excitation vector characterized with its covariance matrix, $E[\mathbf{e}(j)\mathbf{e}^T(j)] = \mathbf{R}_T$, and $\mathbf{v}(j)$ is the q-dimensional vector of turbulence realizations on the discretized nodes of the rotor plane.

$$\begin{aligned} \mathbf{x}(j+1) &= \mathbf{A}_T\mathbf{x}(j) + \mathbf{K}_T\mathbf{e}(j) \\ \mathbf{v}(j) &= \mathbf{C}_T\mathbf{x}(j) + \mathbf{e}(j) \end{aligned} \tag{3.36}$$

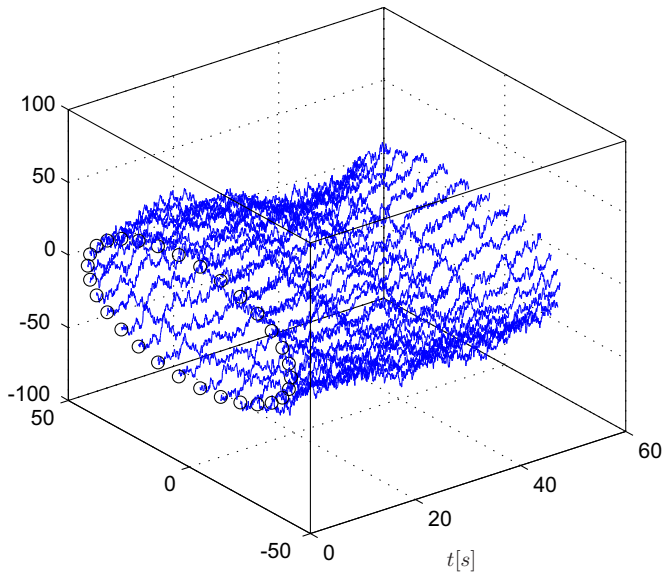

Figure 3.6 Realization of the turbulent wind field

The role of SSM is to calibrate the quadruple $(\mathbf{A}_T, \mathbf{K}_T, \mathbf{C}_T, \mathbf{R}_T)$ in a way that cross-covariance function of (3.36) matches best to the cross-covariance function of the turbulence. If it is preferred to have the turbulence directly based on mutually independent unit intensity Gaussian white noise variables i.e. $\mathbf{\Xi}(j) \sim N(0, \mathbf{I})$, (3.36) can be written in the form of (3.37) in which , $\mathbf{\Phi}_T$ is the square matrix which satisfies $\mathbf{e}(j) = \mathbf{\Phi}_T \mathbf{\Xi}(j)$. $\mathbf{\Phi}_T$ can be obtained by any decomposition of the covariance matrix of the noise such that $\mathbf{R}_T = \mathbf{\Phi}_T \mathbf{\Phi}_T^T$ i.e. Cholesky decomposition. Then $\mathbf{B}_T = \mathbf{K}_T \mathbf{\Phi}_T$ and $\mathbf{D}_T = \mathbf{\Phi}_T$

$$\begin{aligned} \mathbf{x}(j+1) &= \mathbf{A}_T \mathbf{x}(j) + \mathbf{B}_T \mathbf{\Xi}(j) \\ \mathbf{v}(j) &= \mathbf{C}_T \mathbf{x}(j) + \mathbf{D}_T \mathbf{\Xi}(j) \end{aligned} \tag{3.37}$$

A realization of the generated wind field on the perimeter of the rotor is shown in figure The presented approach for turbulence modeling does not take into account the rotational sampling effect of the turbulence process. Therefore it is needed to make an interpolation as the blades pass through different turbulence nodes in between two nodes. At a certain instant of time the portion of a given blade is defined by the center angle $q_5(t)$ placed in the sector delimited by the center angles θ_i and θ_{i+1} representing the turbulence components $v_i(t)$ and $v_{i+1}(t)$. Then, the turbulence $v(t)$ on the blade is obtained by linear interpolation as follow

$$v(t) = v_i(t) + \frac{v_{i+1}(t) - v_i(t)}{\theta_{i+1} - \theta_i}(q_5(t) - \theta_i) \tag{3.38}$$

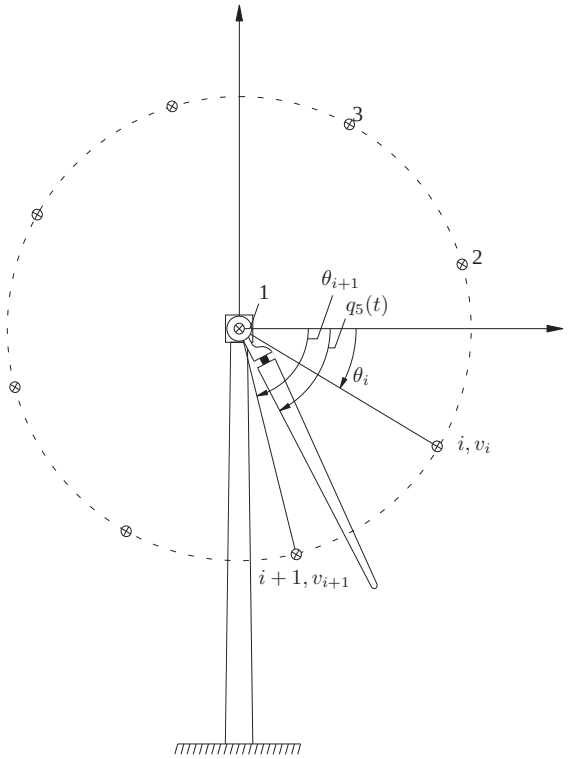

Figure 3.7 Interpolation of turbulence.

3.4 Model specifications

Structural properties of the tower and the blades are adopted from the definitions of the NREL 5MW wind turbine (Jonkman *et al.* 2009; Kooijman *et al.* 2003), and have been indicated in Table 1 along which the derived parameters entering the reduced model and the control parameters. The fundamental undamped fixed bay angular eigenfrequency, ω, and eigenmode, $\Phi(x)$, of the blades are determined by FE analysis where the blade is discretized in 49 Bernoulli-Euler beam elements with piecewise constant bending stiffness EI and mass per unit length μ. The variation of EI and μ has been shown in figure 3.8. The blade has 7 different airfoil profiles from stem to tip, (Jonkman *et al.* 2009), nevertheless in figure 3.8, the lift and drag coefficients of only the tip profile are shown as a sample. The lift and drag coefficients for each profile are interpolated with two piecewise polynomials, each of order 9, in two different intervals of α. The two fitting intervals for lift and drag coefficients are chosen so to allow best overall fit i.e. the least Sum of Squared Error (SSE) for all data points. Similarly, the eigenmode $\Phi_0(x)$ of the tower is determined by FE analysis, where the tower is discretized in 10 Bernoulli-Euler beam elements, with piecewise constant bending stiffness and mass per unit length. The mass of the nacelle and the blades $M_0 + 3m$ is attached as a point mass at the free end. The variation of the bending stiffness and the mass per unit length has been shown in figure 3.8.

Table 3.1 Structural and control parameters of the wind turbine model.

h	87.6 m	N	97	ω	4.2 rad/s
L	61.5 m	M_0	296780 kg	ω_0	2.0 rad/s
m	17415 kg	k	14120 N/m	τ	0.2 s
m_0	404520 kg	k_0	1667914 N/m	τ_i	5 s
m_1	791 kg	ζ	0.005	τ_d	0 s
m_2	1893 kg	ζ_0	0.01	G	0.1 rad
m_3	359304 kg m	η	0.05	υ	0.2
m_4	83228 kg m	ρ	1.25 kg/m^3	V_o	25 m/s
m_5	6100058 kg m	$\Omega_{r,0}$	1.27 rad/s	V_i	5 m/s
J_r	35337324 kg m^2	$\Omega_{g,00}$	73.7 rad/s	V_h	15 m/s
J_g	535 kg m^2	$M_{r,0}$	3946018 N m	V_r	15 m/s

Table 3.2 Blade aerodynamic properties.

Node[-]	Location	Element length [m]	Airfoil
1	2.8667	2.7333	Cylinder
2	5.6000	2.7333	Cylinder
3	8.3333	2.7333	Cylinder
4	11.7500	4.1000	DU40A17
5	15.8500	4.1000	DU35A17
6	19.9500	4.1000	DU35A17
7	24.0500	4.1000	DU30A17
8	28.1500	4.1000	DU25A17
9	32.2500	4.1000	DU25A17
10	36.3500	4.1000	DU21A17
11	40.4500	4.1000	DU21A17
12	44.5500	4.1000	NACA64A17
13	48.6500	4.1000	NACA64A17
14	52.7500	4.1000	NACA64A17
15	56.1667	2.7333	NACA64A17
16	58.9000	2.7333	NACA64A17
17	61.6333	2.7333	NACA64A17

The rated wind speed of the model i.e. the wind speed at which the nominal power is produced is $V_r = 10.72\mathrm{m/s}$ as indicated in table 3.1. For values higher than this value the pitch controller is turned on which decreases the rotor speed to its nominal value. The turbulence is generated in 31 nodes on the rotor plane as shown in figure 3.2. One node on the hub and 30 nodes on the perimeter of rotor plane on 0.8L distance from hub. The turbulence value between the nodes are interpolated from these nodes. The decrement of the loads and responses as well are the effect of the controller which tries to adjust the loads in a way that brings the rotational speed to its nominal value. The rated rotor speed in which the nominal power is generated is approximately 10m/s for this model. Accordingly it is expected that the controller increases the

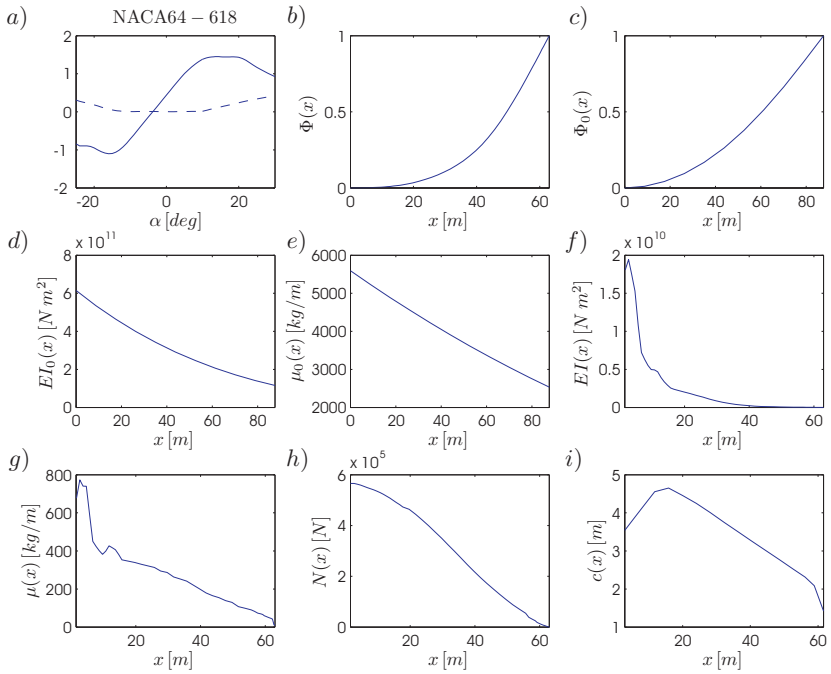

Figure 3.8 Structural properties of the NREL 5MW wind turbine. a) —: Lift coefficient of the NACA64-618, $-\,-\,-$: Drag coefficient of the NACA64-618, b) Blade's mode shape , c) Tower's mode shape , d) Bending stiffness of the tower , e) Mass per unit length of the tower , f) Bending stiffness of the blade , g) Blade's mass per unit length , h) Blade's inertial load , i) Blade's cord length.

pitch in extreme wind conditions, i.e. $V_h \in [15, 25]\,\mathrm{m/s}$, to decrease the rotational speed to its nominal value.

3.5 Effect of the pitch controller

Simulations show that the controller changes the system behavior significantly. Therefore a more detailed study with the aim of analyzing controller's effect is performed in this section. The two cases of operation referred to as *fixed speed* and *variable speed* will be considered. In the first case the rotational speed of the rotor is set to the nominal rotor speed $\Omega_{r,0}$ while in the second case the controller is in charge of keeping the speed around the nominal speed. According to the coupling between the rotor torque and the normal load, presence of the the pitch controller will affect the vibration level of the wind turbine. For further illustration a simulation of the wind turbine is carried out within 600 seconds. The same wind field realization is used for both fixed and variable speed models. As seen in Fig. 3.10 the vibration amplitude of the variable speed case during normal operation is lower than the fixed speed case. However this is not guaranteed and the opposite also happens. As a counter example the responses to a specific realization of the wind field - the realization at hub hight is shown in Fig. 3.9 - are shown in Fig. 3.11. As seen in this figure, in extreme conditions, i.e. $t \in [100, 200]s$, the vibration level of the variable

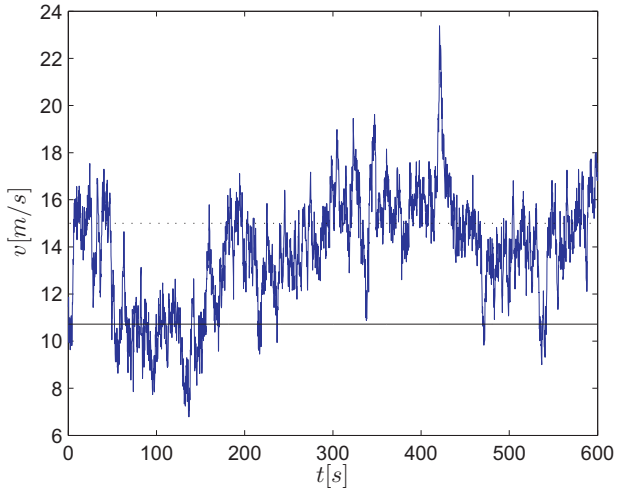

Figure 3.9 Turbulent wind realization at the hub hight. ...: Mean wind speed; —: rated rotor speed

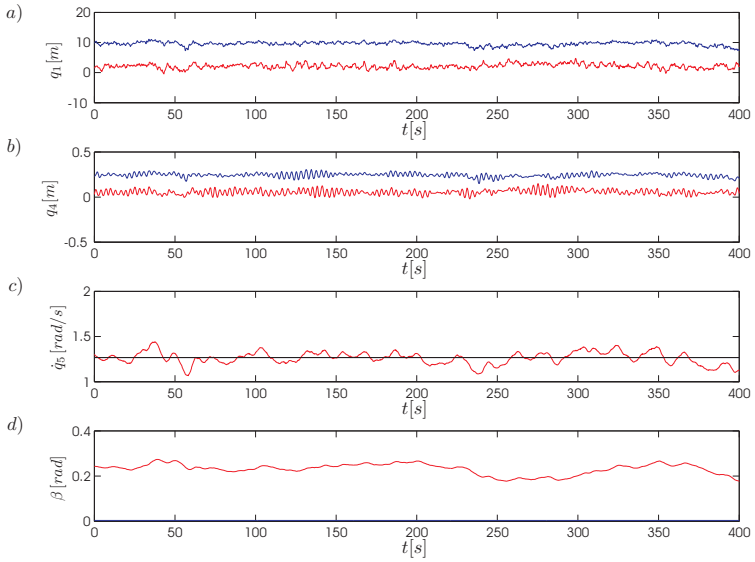

Figure 3.10 Modal responses of the wind turbine under normal operational condition. blue: fixed speed; red: variable speed

speed model exceeds its value for the fixed speed model. Results of this study show that this case is dominant in the extreme conditions. This analysis is provided in order to illustrate the effect of the pitch controller which may be either increment or decrement of the safety margin of the system in extreme conditions.

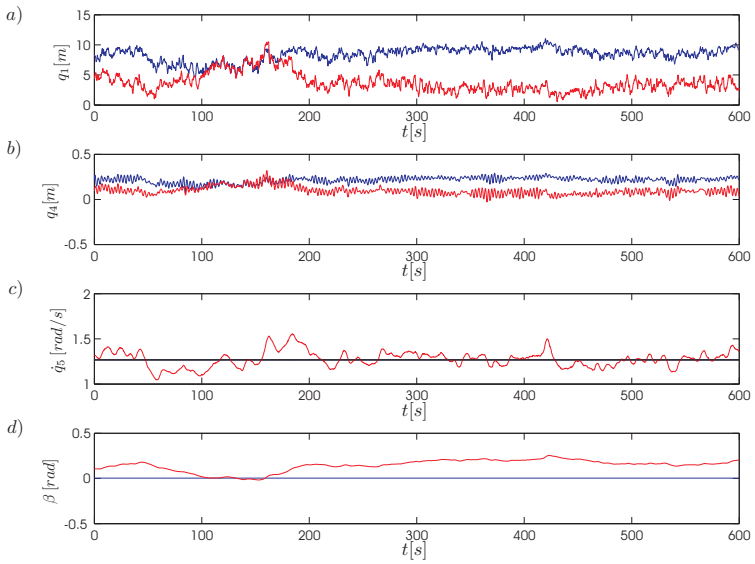

Figure 3.11 Modal responses of the wind turbine under extreme operational condition. blue: fixed speed; red: variable speed

CHAPTER 4
Importance Sampling

The basics of the importance sampling goes back to the Itô stochastic differential equations. Therefore the dynamic system should be represented in this form if not primarily done so. The main role in this method is actually played by the theory according to Girsanov which states that a Wiener process under a certain probability measure remains Wiener after adding a deterministic drift to it on the condition that the probability measure takes into account the effect of this additional drift term. This permits use of the so-called control functions which brings the system state to the boundaries of the failure region.

4.1 Itô Stochastic Differential Equations

Suppose the system is described by the Itô Stochastic Differential Equations (SDE) (4.1)

$$\left.\begin{array}{l} dX_i(t) = \mu_i(t,\mathbf{X})dt + \sum_{j=1}^{q} \sigma_{ij}(t,\mathbf{X})d\mathbf{W}_j(t) \\ X_i(s) \;\; = x_i \quad , \quad i = 1,\cdots,p \end{array}\right\} \tag{4.1}$$

where $X_i(t), i = 1,\cdots,p$ are p-dimensional system responses subjected to the initial conditions $X_i(s) = x_i$ for any $0 \le s \le T$ and $W_j(t), j = 1,\cdots,q$ are q-dimensional unit Wiener processes. Given that the failure domain boundary is specified by the failure surface $g\big(\mathbf{X}(t,\mathbf{W})\big) = 0$ such that

$$\mathcal{F} = \Big\{ \mathbf{X} \,|\, g\big(\mathbf{X}\big) > 0 \Big\} \tag{4.2}$$

using (4.1), (4.2) can be written in the terms of the Wiener excitation i.e. $\mathcal{F} = \Big\{ \mathbf{W} \,|\, g\big(\mathbf{W}\big) > 0 \Big\}$ the failure probability can be defined as

$$P_f = \int_{\mathcal{F}} dP_{\mathbf{W}}(\mathbf{w}) = \int_{\mathbf{R}^q} I\Big[g\big(\mathbf{X}(t,\mathbf{W})\big)\Big] dP_{\mathbf{W}}(\mathbf{w}) = E_{\mathbf{w}}\Big[I\big[g(\mathbf{X})\big]\Big] \tag{4.3}$$

where $I[.]$ is an indicator function which is equal to 1 if the process has outcrossed to the failure domain and else is zero. The probability measure $P_{\mathbf{w}}(\mathcal{B})$ relates a probability to any sub-domain $\mathcal{B} \in \mathbf{R}^q$ i.e. a differential volume around a sample point $\mathbf{w}$ can be written as $dP(\mathbf{W}) = f_{\mathbf{W}}(\mathbf{w})d\mathbf{w}$. $E_{\mathbf{w}}$ signifies the expectation operator under the probability measure

$f_{\mathbf{W}}(\mathbf{w})$. Based on (4.3) Monte Carlo simulation estimates the failure probability of the system by (4.4); where N is the number of Monte Carlo simulations.

$$\hat{P}_f = \frac{1}{N}\sum_{n=1}^{N} I\big[g(\mathbf{X}^{(n)})\big] \tag{4.4}$$

4.2 Girsanov Transformation

The idea of the IS based on the Girsanov theorem is to introduce a square integrable drift $\mathbf{u}_j^{(\tau)}(t)$ - i.e. $\sum_j^p \int_0^T \big(u_j^{(\tau)}(\gamma)\big)^2 d\gamma < \infty$ - to the excitation, (4.5), which brings the systems response to the failure region at the specific time instant $\tau \in [0, T]$.

$$d\tilde{\mathbf{W}}(t) = \mathbf{u}^{(\tau)}(t)dt + d\mathbf{W}(t) \tag{4.5}$$

The Itô SDE (4.1) can then be written as

$$\left.\begin{aligned} dX_i(t) &= \mu_i(t,\mathbf{X})dt - \sum_{j=1}^{q}\sigma_{ij}(t,\mathbf{X})\mathbf{u}_j^{(\tau)}(t)dt + \sum_{j=1}^{q}\sigma_{ij}(t,\mathbf{X})d\tilde{\mathbf{W}}_j(t) \\ X_i(s) &= x_i \quad , \quad i = 1,\cdots,p \end{aligned}\right\} \tag{4.6}$$

The Girsanov theorem then states that the process $\tilde{\mathbf{W}}$ is a Wiener process under the probability measure $P_{\tilde{\mathbf{W}}}$. Therefore generating samples of $\tilde{\mathbf{W}}$ under the probability measure $P_{\mathbf{W}}$ corresponds to generating samples of $\mathbf{W}$ under the probability measure $P_{\tilde{\mathbf{W}}}$. This is useful since then the drift of the excitation might be designed in any sense that brings the system to the failure at the desired time instance. Next, the probability measure should be changed properly to take into account the effect of this transformation. The probability measure of equation (4.3) can be changed in the following way

$$\left.\begin{aligned} P_f &= \int_{\mathbf{R}^q} I\Big[g\big(\mathbf{X}(t,\mathbf{W})\big)\Big]\frac{f_{\mathbf{W}}(\mathbf{w})}{f_{\tilde{\mathbf{W}}}(\mathbf{w})}f_{\tilde{\mathbf{W}}}(\mathbf{w})d\mathbf{w} \\ &= \int_{\mathbf{R}^q} I\Big[g\big(\mathbf{X}(t,\mathbf{W})\big)\Big]\frac{dP_{\mathbf{W}}(\mathbf{w})}{dP_{\tilde{\mathbf{W}}}(\mathbf{w})}f_{\tilde{\mathbf{W}}}(\mathbf{w})d\mathbf{w} \\ &= E_{\tilde{\mathbf{w}}}\left[I\big[g(\mathbf{X})\big]\frac{dP_{\mathbf{W}}(\mathbf{w})}{dP_{\tilde{\mathbf{W}}}(\mathbf{w})}\right] \end{aligned}\right\} \tag{4.7}$$

where $g(\mathbf{X}) = g\big(\mathbf{X}(t,\mathbf{W})\big)$ and the ratio $dP_{\mathbf{W}}(\mathbf{w})/dP_{\tilde{\mathbf{W}}}(\mathbf{w})$ is the well-known Radon-Nikodym derivative of the probability measure $dP_{\mathbf{W}}(\mathbf{w})$ with respect to the measure $dP_{\tilde{\mathbf{W}}}(\mathbf{w})$. $E_{\tilde{\mathbf{w}}}$ signifies the expectation operator under the probability measure $f_{\tilde{\mathbf{W}}}(\mathbf{w})$. Upon the Girsanov theorem the probability measure of (4.7) changes to $f_{\tilde{\mathbf{W}}}(\mathbf{w})$ hence (4.8)

$$P_f = E_{\mathbf{w}}\left[I\big[g(\tilde{\mathbf{X}})\big]\frac{dP_{\mathbf{W}}(\tilde{\mathbf{w}})}{dP_{\tilde{\mathbf{W}}}(\tilde{\mathbf{w}})}\right] \tag{4.8}$$

where $g(\tilde{\mathbf{X}}) = g\big(\mathbf{X}(t,\tilde{\mathbf{W}})\big)$. The significance of equation (4.7) is that the probability measure can be changed so that the process $\tilde{\mathbf{W}}$ can be used instead of the original process $\mathbf{W}$ to estimate

the failure probability of a system provided that the Radon-Nikodym derivative is taken into account. Based on (4.7), the failure probability of the system can be estimated using (4.9)

$$\hat{P}_f = \frac{1}{N}\sum_{n=1}^{N} I\left[g(\tilde{\mathbf{X}}^{(n)})\right]\left(\frac{dP_{\mathbf{W}}(\tilde{\mathbf{w}}^{(n)})}{dP_{\tilde{\mathbf{W}}}(\tilde{\mathbf{w}}^{(n)})}\right) \tag{4.9}$$

4.3 Radon-Nikodym derivative

Suppose the simulation is carried out within the time frame $t \in [0, T]$ with the time resolution is $\Delta T = T/N_t$ where N_t is the number of time samepls. Discretizing (4.5) results in

$$\Delta\tilde{W}_{j,k} = u_{j,k}^{(\tau)}\Delta t + \Delta W_{j,k} \tag{4.10}$$

where

$$\Delta W_{j,k} = W_j(k\Delta t) - W_j\big((k-1)\Delta t\big) \tag{4.11}$$

Hereafter for all of the introduced parameters except time i.e. $W_{j,k}$ and $X_{j,k}$ the index(es) before comma refer(s) to the spatial degrees of freedom and the index after comma refers to the time sample. $u_{j,k}^{(\tau)}$ is the so-called control function(s) (Macke and Bucher 2003) which brings responses of the system, i.e. displacement, velocity, stress etc., to the barrier level $\mathbf{x}_i^b$ at the time $t_k = k\Delta t$. Therefore $\Delta\tilde{W}_{j,k} \sim \mathcal{N}(u_{j,k}^{(\tau)}\Delta t, \sqrt{\Delta t})$. The increments of the Wiener process can be transformed to normal space

$$\Delta W_{j,k} = \Xi_{j,k}\sqrt{\Delta t} \tag{4.12}$$

where the following properties are satisfied

$$\left.\begin{array}{lcl} W_j(0) & = & 0 \\ \mathrm{E}\{W_j(t)\} & = & 0 \\ \mathrm{E}\{W_j(t_1)W_j(t_2)\} & = & \min(t_1, t_2) \end{array}\right\} \tag{4.13}$$

and $\boldsymbol{\Xi}_j$, $j = 1, \cdots, q$ are vectors with identically distributed Gaussian random numbers, with zero mean and unit standard deviation, components. This transformation is required in order to express the random variables of the problem in the normalized U-space. Therefore the reliability index β is independent of the definition of the limit state function $g(\Xi_{1,k}, \cdots, \Xi_{N_t,q})$, (Madsen *et al.* 2006). Next the following relations hold

$$\left.\begin{aligned} f_{\Delta W_{j,k}}(\Delta\tilde{w}_{j,k}) &= \frac{1}{(2\Delta t)^{1/2}}\exp\left(-\frac{(\Delta\tilde{w}_{j,k})^2}{2\Delta t}\right) \\ f_{\Delta\mathbf{W}}(\Delta\tilde{\mathbf{w}}) &= \prod_{j=1}^{q}\frac{1}{(2\Delta t)^{N_t/2}}\exp\left(-\frac{1}{2\Delta t}\sum_{k=1}^{N_t}\Delta\tilde{w}_{j,k}\right) \end{aligned}\right\} \tag{4.14}$$

The probability density $f_{\Delta\tilde{\mathbf{W}}}(\Delta\tilde{\mathbf{w}})$ is written

$$\left.\begin{aligned} f_{\Delta\tilde{W}_{j,k}}(\Delta\tilde{w}_{j,k}) &= \frac{1}{(2\Delta t)^{1/2}}\exp\left(-\frac{(\Delta\tilde{w}_{j,k} - u_{j,k}^{(\tau)}\Delta t)^2}{2\Delta t}\right) \\ f_{\Delta\tilde{\mathbf{W}}}(\Delta\tilde{\mathbf{w}}) &= \prod_{j=1}^{q}\frac{1}{(2\Delta t)^{N_t/2}}\exp\left(-\frac{1}{2\Delta t}\sum_{k=1}^{N_t}\left(\Delta\tilde{w}_{j,k} - u_{j,k}^{(\tau)}\Delta t\right)^2\right) \end{aligned}\right\} \tag{4.15}$$

Then the Radon-Nikodym derivative is

$$\frac{dP_{\Delta\mathbf{W}}(\Delta\tilde{\mathbf{w}})}{dP_{\Delta\tilde{\mathbf{W}}}(\Delta\tilde{\mathbf{w}})} = \frac{f_{\Delta\mathbf{W}}(\Delta\tilde{\mathbf{w}})}{f_{\Delta\tilde{\mathbf{W}}}(\Delta\tilde{\mathbf{w}})} = \exp\left(-\sum_{j=1}^{q}\sum_{k=1}^{N_t} u_{j,k}^{(\tau)}\Delta w_{j,k} - \frac{\Delta t}{2}\sum_{j=1}^{q}\sum_{k=1}^{N_t}\left(u_{j,k}^{(\tau)}\right)^2\right) \tag{4.16}$$

Which is continuous space can be expressed as, (Macke and Bucher 2003; Olsen and Naess 2006),

$$\begin{aligned}\mathcal{R}^{(\tau)} &= \frac{dP_{d\mathbf{W}}(d\tilde{\mathbf{w}})}{dP_{d\tilde{\mathbf{W}}}(d\tilde{\mathbf{w}})} = \\ &= \frac{f_{d\mathbf{W}}(d\tilde{\mathbf{w}})}{f_{d\tilde{\mathbf{W}}}(d\tilde{\mathbf{w}})} = \exp\left(-\sum_{j=1}^{q}\int_0^T u_j^{(\tau)}(t)dw_j - \frac{1}{2}\sum_{j=1}^{q}\int_0^T\left(u_j^{(\tau)}(t)\right)^2 dt\right)\end{aligned} \tag{4.17}$$

4.4 Control functions

Lets assume the i^{th} component of the process $\mathbf{X}(t)$ of (4.1) has reached the required barrier level $\mathbf{x}_i^b$ at time $\tau = N_\tau\Delta t$ i.e. $\mathbf{X}_i(\tau) = \mathbf{x}_i^b$. The barrier level is a known value for which the probability of outcrossing is to be estimated i.e. $\mathbf{x}_i^b = \mu_{\mathbf{X}_i(t)} + 3\sigma_{\mathbf{X}_i(t)}$ where $\mu_{\mathbf{X}_i(t)}$ and $\sigma_{\mathbf{X}_i(t)}$ are the mean value and the standard deviation of the process. Representing (4.1) in its discrete form follows

$$X_{i,k} = X_{i,k-1} + \mu_i(t_{k-1}, \mathbf{X}_{,k-1})\Delta t + \sum_{j=1}^{q}\sigma_{ij}(t_{k-1}, \mathbf{X}_{,k-1})\Delta\mathbf{W}_{j,k-1} \tag{4.18}$$

Considering (4.12) and (4.18) the *limit state function* is then defined as

$$g(\Xi_{1,1}, \cdots, \Xi_{q,N_t}) = \mathbf{X}_{i,N_\tau}(\Xi_{1,1}, \cdots, \Xi_{q,N_t}) - \mathbf{x}_i^b \tag{4.19}$$

The *design point* $\boldsymbol{\xi}^{(\tau)} = (\xi_{1,1}^{(\tau)}, \cdots, \xi_{p,N_t}^{(\tau)})$ is the point in the U-space, e.g. $\boldsymbol{\Xi}$, which has two important properties. First, it brings the system to the barrier level $\mathbf{x}_i^b$ at the design time τ. Second, it has the minimum distance from the origin. The distance from the origin to the design point for reaching the barrier level at time τ is written as

$$\beta^{(\tau)} = \left[\sum_{j=1}^{q}\sum_{k=1}^{N_t}\left(\xi_{j,k}^{(\tau)}\right)^2\right]^{1/2} \tag{4.20}$$

Therefore design point excitation for outcrossing at time instant τ can be defined as the solution to the following minimization problem

$$\boldsymbol{\xi}^{(\tau)} = \min_{\boldsymbol{\Xi}}\left(\left[\sum_{j=1}^{q}\sum_{k=1}^{N_t}\left(\Xi_{j,k}\right)^2\right]^{1/2}\right) \qquad s.t. \qquad \mathbf{X}_{i,N_\tau}(\Xi_{1,1}, \cdots, \Xi_{q,N_t}) = \mathbf{x}_i^b \tag{4.21}$$

The control functionfor arriving at the barrier level $x^b = 25$ at time $\tau = 40[s]$ for the single DOF linear oscillator of section 1.8 and its response are shown in figure 4.1.a and figure 4.1.b

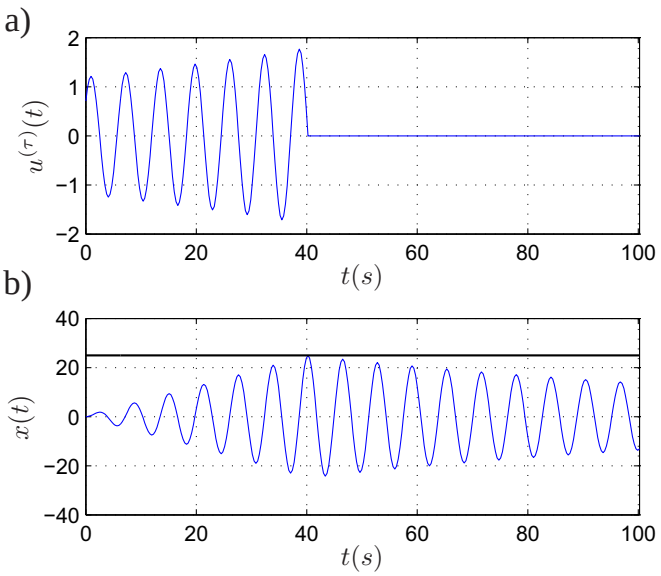

Figure 4.1 SDOF linear oscillator. a) Control function $u^{(\tau)}(t)$ for outcrossing at $\tau = 40[s]$, b) Response $x(t)$ to $u^{(\tau)}(t)$

respectively. According to the Girsanov theorem the process $\tilde{\mathbf{W}}$ is Wiener under probability measure $P_{\tilde{\mathbf{W}}}$ therefore is zero mean under this measure therefore

$$\mathrm{E}_{P_{\tilde{\mathbf{W}}}}\{\Delta\tilde{W}_{j,k}^{(\tau)}\} = \mathrm{E}_{P_{\tilde{\mathbf{W}}}}\{u_{j,k}^{(\tau)}\Delta t + \Delta W_{j,k}\} = 0 \quad \Rightarrow \quad \mathrm{E}_{P_{\tilde{\mathbf{W}}}}\{\Delta W_{j,k}\} = -u_{j,k}^{(\tau)}\Delta t \tag{4.22}$$

where $\tilde{\mathbf{W}}$ is replaced with (4.10). Introducing (4.12) into (4.22) allows obtaining the control functions in terms of the normally distributed iid variables $\Xi_{j,k}$ as

$$\mathrm{E}_{P_{\tilde{\mathbf{W}}}}\{\Xi_{j,k}\} = \xi_{j,k} = -u_{j,k}^{(\tau)}\sqrt{\Delta t} \tag{4.23}$$

It worth noting that (4.23) is valid for outcrossing barrier level at any time instant i.e. $\xi_{j,k} = \xi_{j,k}^{(\tau)}$, $\tau = 1, \cdots, N_t$. The design point can be transformed into continuous space by inserting (4.23) in (4.20) and taking the limit as $\Delta t \to 0$

$$\beta^{(\tau)} = \left[\sum_{j=1}^{q}\int_0^T \left(u_j^{(\tau)}(t)\right)^2 dt\right]^{1/2} \tag{4.24}$$

Comparison of the system response to $dW(t)$ and $d\tilde{W}(t)$ for the SDOF linear oscillator is shown in figure 4.2.a. The reliability index for the same oscillator versus time is shown in 4.2.b.

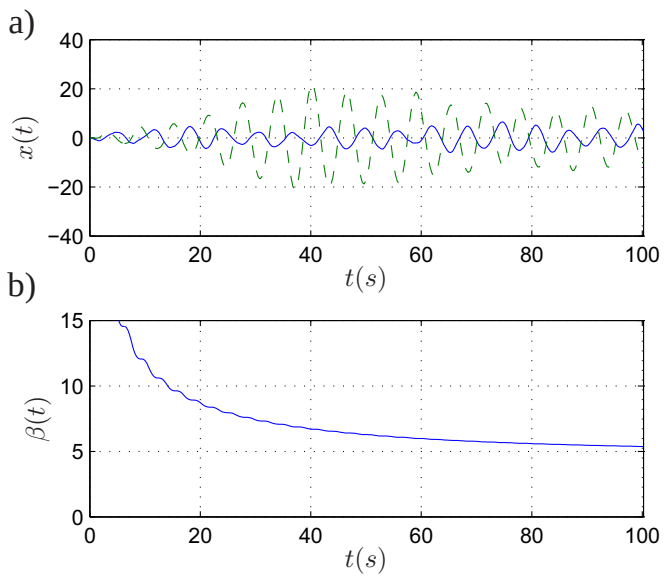

Figure 4.2 SDOF linear oscillator, $\tau = 40[s]$. a) —: Response to $dW(t)$, $--$: Response to $d\tilde{W}(t)$, b) Reliability index $\beta(t)$ for all time instants

4.5 Multi-modal sampling

The statement of the problem for importance sampling is: "*Estimate the probability that the system response exceeds the given barrier level (i.e. state of failure), x_i^b, within the time frame* $t \in [0, T]$". In crack growth problems the failure always occurs at the end of the simulation, e.g. $t = T$. Therefore it is requited to calculate only one control function $u_j^{(T)}(t)$ and do the calculations c.f. figure 4.3.a. However for oscillatory systems a considerable under estimation of the first passage probability is reported in the literature, (Naess and Skaug 1999b; Bucher 2000). This is since in oscillatory systems the failure can happen at any time within $t \in [0, T]$ c.f. figure 4.3.b. Indeed here the control functions of failure at different time instants interact with each other, (Macke and Bucher 2003). This suggests that first passage at time τ_1 (or outcrossing) from a barrier level $\mathbf{x}_i^b$ could possibly happen at time τ_2 with a certain probability. Therefore there should exist a correct scenario for choosing the failure time τ for oscillatory systems. Bucher (Bucher 2000) suggested construction of the failure times' probability density function using the distance of their control functions from origin i.e. *multi-modal sampling density*

$$\mathcal{W}(t) = \frac{\Phi\left(-\beta(t)\right)}{\int_0^T \Phi\left(-\beta(\gamma)\right) d\gamma} \tag{4.25}$$

where $\Phi(.)$ denotes the cumulative standard Gaussian distribution function and $\beta(t)$ is the distance defined in (4.24). For consistency of integration we have introduced $\beta(t) \equiv \beta^{(\tau)}, \tau = t$ here. Therefore the failure time instant in each simulation should be chosen (sampled) from this distribution. The multi-modal sampling probability density function $\mathcal{W}(t)$ is shown in figure 4.4

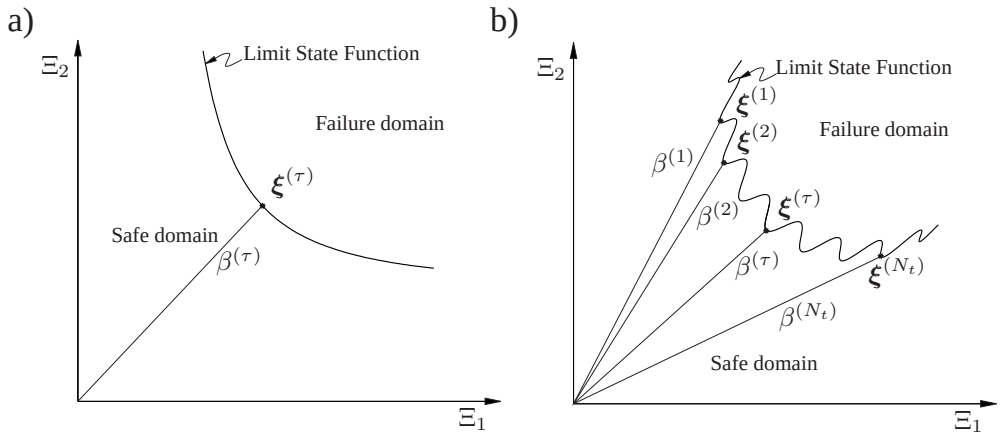

Figure 4.3 Limit state function for different problems; a) Non-oscillatory systems i.e. crack growth problems, b) Oscillatory systems

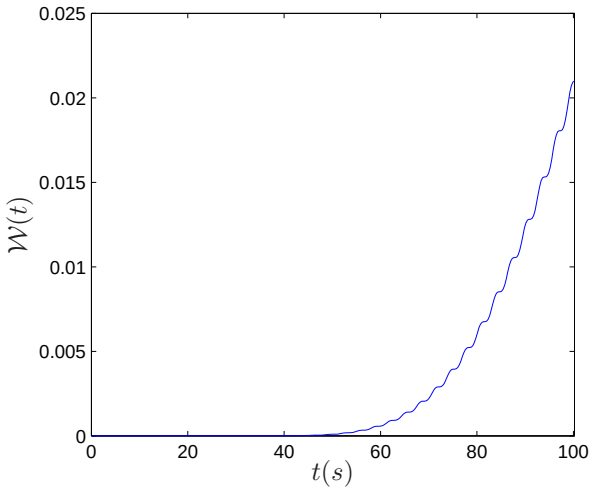

Figure 4.4 Multi-modal sampling density function for the SDOF linear oscillator

for the SDOF linear oscillator. Second, the Radon-Nikodym derivative (4.17) for all time instants in $t \in [0, T]$ should be calculated, i.e. failure could happen at arbitrary time l utilizing the control function $\mathbf{u}^{(l)}(t)$ and the Wiener process $d\overline{\mathbf{W}}(t)$

$$\left.\begin{aligned} d\tilde{W}_j(t) &= u_j^{(\tau)}(t)dt + dW_j(t) \\ d\tilde{W}_j(t) &= u_j^{(l)}(t)dt + d\overline{W}_j(t) \end{aligned}\right\} \Rightarrow d\overline{W}_j(t) = \left(u_j^{(\tau)}(t) - u_j^{(l)}(t)\right)dt + dW_j(t) \tag{4.26}$$

According to (Macke and Bucher 2003) the likelihood that the path generated by $u_j^{(\tau)}(t)$ and $dW_j(t)$ was generated by $u_j^{(l)}(t)$ and $d\overline{W}_j(t)$ is given by

$$\overline{\mathcal{R}}^{(\tau)}(l) = \exp\left(-\sum_{j=1}^{q} \int_0^T \left(u_j^{(\tau)}(t) - u_j^{(l)}(t) \right) dw_j - \frac{1}{2} \sum_{j=1}^{q} \int_0^T \left(u_j^{(\tau)}(t) - u_j^{(l)}(t) \right)^2 dt \right) \tag{4.27}$$

and the multi-modal derivative which takes into account the interactions first passage at different time instants is given as the ratio of (4.17) by (4.27)

$$\mathcal{R}_m^{(\tau)}(l) = \frac{\mathcal{R}^{(\tau)}}{\overline{\mathcal{R}}^{(\tau)}(l)} = \exp\left(-\sum_{j=1}^{q} \int_0^T u_j^{(l)}(t) dw_j(t) - \frac{1}{2} \sum_{j=1}^{q} \int_0^T \left(2u_j^{(l)}(t) - u_j^{(\tau)}(t) \right) u_j^{(l)}(t) dt \right) \tag{4.28}$$

and weighted with its associated probability

$$\mathcal{R}_{\mathcal{W}}^{(\tau)} = \int_0^T \frac{\mathcal{W}(\gamma)}{\mathcal{R}_m^{(\tau)}(\gamma)} d\gamma \tag{4.29}$$

where we have introduced $\mathcal{R}_m(\gamma) \equiv \mathcal{R}_m^{(\gamma)}, \gamma = \tau$ in (4.17) for consistency of integration. Finally (4.9) is re-written as (4.30)

$$\hat{P}_f = \frac{1}{N} \sum_{n=1}^{N} I\left[g(\tilde{\mathbf{X}}^{(\tau_n)}) \right] \mathcal{R}_{\mathcal{W}}^{(\tau_n)} \tag{4.30}$$

The final estimations of the "importance sampling" for the benchmark problem of chapter 1 is shown in figure 4.5

4.6 Applying importance sampling

The procedure of applying importance sampling based on the above description falls into the below steps

1. Find the set of control functions $u_j^{(\tau)}(t)$, $\tau = 1, \cdots, N_t$ according to (4.21)
2. Calculate $\beta^{(\tau)}$ for all control functions $\tau = 1, \cdots, N_t$ and
3. Calculate the multi-modal density function $\mathcal{W}(t)$ according to (4.25) and sample the failure time from it e.g. τ_j
4. Generate a set of $\Delta W_{j,k}$ according to (4.12)

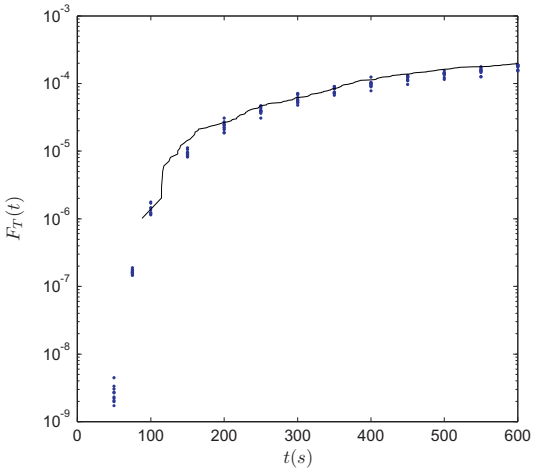

Figure 4.5 Estimations of the failure probability with IS; Solid line: SMC, dots : IS

5 Calculate the *drifted excitation* $d\tilde{\mathbf{W}}(t)$ according to (4.5)

6 Solve (4.1) with $d\tilde{\mathbf{W}}(t)$ as excitation

7 Calculate the Radon-Nikodym derivative $\mathcal{R}_{\mathcal{W}}^{(\tau)}$ using (4.28) and (4.29)

8 Repeat steps 3 to 7, N times and calculate $\hat{P}_f$ using (4.30)

Note: For finding the control functions, the first step above, for linear systems analytical relationships are available (Bucher 2000; Macke and Bucher 2003). It turns out to be the time reversed and scaled impulse response function (IRF) of the system.

Note: Finding the control functions for the Non-linear systems falls into a high dimensional optimization. Koo et al. (Koo *et al.* 2005) proposed, as a warm starting point, to solve the equations of system with initial conditions consistent with the barrier level, i.e. $x_i(0) = x_i^b$, $\dot{x}_i(0) = 0$, and then time reverse the corresponding excitation.

Note: Steps 1 and 7 above have very high demands on the computation cost specifically for nonlinear multi degree of freedom systems. This may render importance sampling (practically) inapplicable to such systems as the cost may be comparable to the standard Monte Carlo simulation.

4.7 IS for linear systems

In this section an abstract discussion on the calculation of the control functions for linear systems is presented. This is since for such systems there is no need for optimization and the control functions can be obtained analytically. More detailed discussions on obtaining control functions for nonlinear systems is available in (Olsen 2006). The LSF of the problem can be written as

The control functions for linear systems for failure at time instant τ, e.g. $u_j^{(\tau)}(t)$, can be obtained by

4.8 IS for wind turbines

There are several problems associated with the presented case of the wind turbine which demotivates use of IS. The most critical problems in this method are due to the nonlinearity of the loads and the high dimension of the system. It should be noted that dimension here refers to the number of *basic random variables* of the system i.e. white noise realizations which enter turbulence filter. Both complexity and memory requirements of the IS increases with system dimensions. For nonlinear systems there exist no analytical solution for finding design point excitations, hence using an optimization algorithm, which significantly decreases efficiency of the method, is inevitable.

Next, construction of the *multi-modal sampling density*, c.f. section 4.5, requires calculation of the control functions of the problem at any time instance within $t \in [0, 600]s$. This requires not only many optimization runs but also very high memory to save the designed control functions. Last but not least unlike SDOF problems or MDOF structural systems with only one stochastic excitation, i.e. a shear frame exposed to earthquake, the wind turbines is related to many stochastic processes used as excitations. This requires very lengthy computation for the IS procedure.

The problems that appear due to dimensionality, nonlinearity and non-whiteness of the excitations pose serious critics to the applications of the IS. These problems have also been noticed by other researchers who have tried different methods to overcome them. Nevertheless to the best knowledge of authors the cases are confined to the nonlinear SDOF systems excited by non-white noise having a specified filter equation, (Olsen and Naess 2007; Naess and Gaidai 2008), linear SDOF systems excited by white noise having a specified power spectrum, (Ogawa and Tanaka 2009), or linear MDOF systems with only one stochastic excitation process (Jensen and Valdebenito 2007). The above reasons conclude that using IS on the wind turbine model seems not to be applicable.

CHAPTER 5
Distance Controlled Monte Carlo

The idea of the Distance Controlled Monte Carlo (DCMC) is that the realizations in a simulation can be weighted, such as the Radon-Nikodym derivative in importance sampling, while the sum of weights of all realizations estimates the desired probability. Therefore the density of the realizations can be increase α times if weight $1/\alpha$ is given to each realization. However the main concern of the method is to achieve a high density of rare events by splitting them, in the same time the Russian Roulette game is played to kill randomly some unimportant realizations to keep the number of samples constant.

5.1 Distance Control & Russian Roulette

The difference between the SMC and the DCMC methods is that the former distributes the samples with uniform statistical weights within the sample space, c.f. figure 5.1; whereas the latter distributes the sample space with a density proportional to the joint probability density function (JPDF) of the process, figure 5.2. Therefore more samples appear at the tails in DCMC. The method starts by simulating all realizations simultaneously with equal weights i.e. $1/N$ where N is the number of realizations. The method encompassed two components "Distance Control"

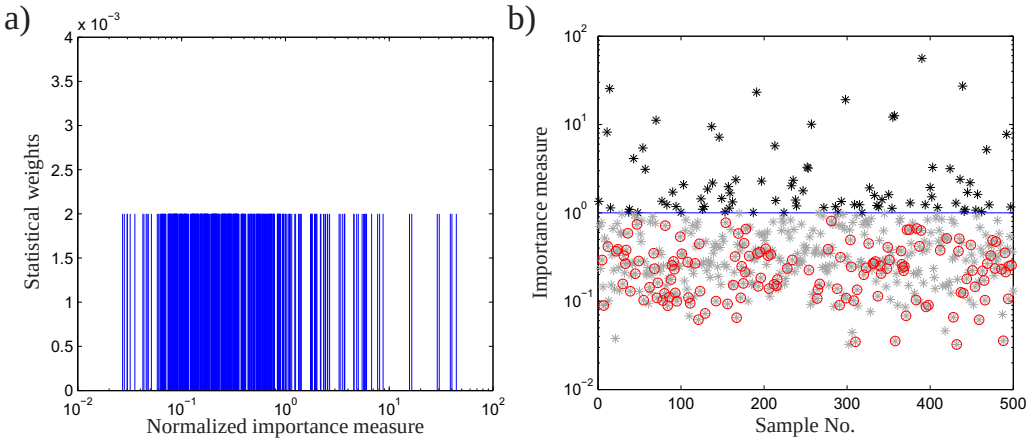

Figure 5.1 The standard Monte Carlo simulation a) Statistical weights of the samples versus normalized importance measure b)Distribution of the importance measure versus sample (realization) no. of each realization —: Importance margin, * (black): Important processes, * (grey): Unimportant processes, o (red): Killed processes

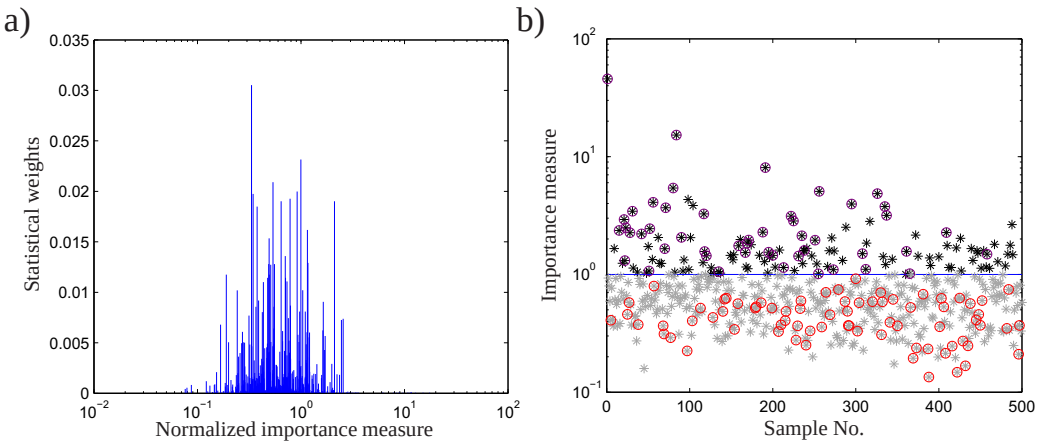

Figure 5.2 The distance controlled Monte Carlo simulation a) Statistical weights of the samples versus normalized importance measure b)Distribution of the importance measure versus sample (realization) no. of each realization — : Importance margin, * (black): Important processes, * (grey): Unimportant processes, o (red): Killed processes o (purple): Not-splittable

(DC), which determines the importance of the realizations with the aim of obtaining a uniform distribution of samples within the safe domain. The second component is the "Russian Roulette and Splitting" (RR&S), which replaces some "unimportant" realizations with the splitted "important" realizations. This aims in increasing the density of the realizartions in the important region i.e. closer to the barrier level. The action of killing, done within the game of Russian Roulette, is

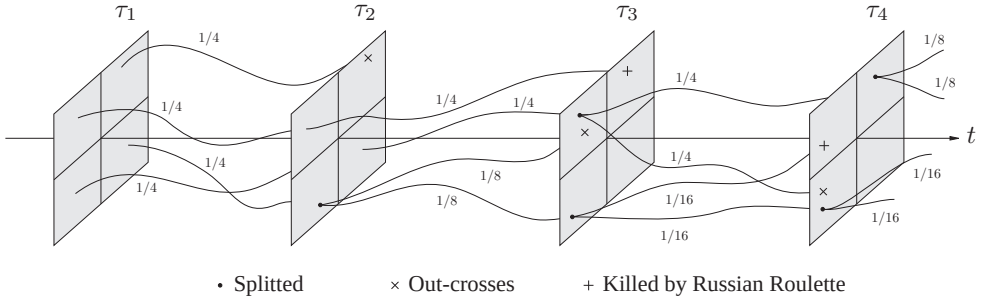

Figure 5.3 Development of processes in DCMC

only to keep the number of samples constant or in other words to avoid an ever increasing sample number. The candidates for killing are chosen from the unimportant processes, e.g. processes with low probability of outcrossing the barrier level. Next, the empty spaces of these unimportant processes will be substituted by the splitted important processes e.g. processes with high probability of outcrossing the barrier level. The splitting might be readily done by duplicating some of the important processes. The statistical weights of the important processes should be controlled such that the statistics of the simulation is not changed after splitting c.f. figure 5.1.

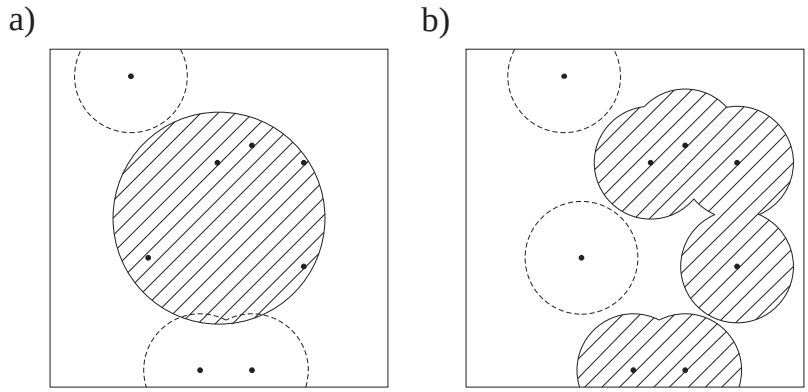

Figure 5.4 Absolute versus relative distance measures; ·: process, Hatch: Safe domain, Dashed circle: Important realizations, a) Absolute distance measure, b) Relative distance measure

5.2 Splitting

In general a process with weight 1 can be splitted to α identical processes with weights $1/\alpha$ on each. Here whenever a process is splitted to α processes the state of the realization will be exactly copied α times while the weight of each new process will be $1/\alpha$ times the weight of the original process. In case the process evolves as Markovian e.g. has independent increments, each of the duplicated states will evolve independently. Figure 5.1 shows development of four realizations of a stochastic process in DCMC simulation. Each curve represents a realization and the number next to it shows its statistical weight e.g. probability of the process being in that state. The RR&S takes place at each time τ_s , $s = 1, 2, 3, \cdots$ which kills some unimportant realizations and duplicates some of the important ones. It should be noted that the probability of each realization after duplication is set to half of the probability of the original process so the splitting does not change the probability mass of the simulation.

5.3 Distance measures

The importance of the distance measure is that it defines which samples should survive and which should splitted to form new ones. It can be defined as a function of the *absolute* distance between the processes and the barrier level. This forms the so-called “absolute distance measure” i.e. mechanical energy of the system c.f. figure 5.4.a. Alternatively it can be defined as a function of the *relative* distance between realizations i.e. “relative distance measure” i.e. the distance measure proposed by Pradlwarter and Schuëller (Pradlwarter and Schuëller 1999) c.f. figure 5.4.b. Both of these distance measures have been implemented on the benchmark example. It is seen that the relative distance measure performes better than the absolute distance measure i.e. less coefficient of variation in the estimates are obtained c.f. figure 5.6.

5.3.1 A Relative distance measure

A given realization $x_i^{(n)}(t)$ of the i^{th} component of the state vector $\mathbf{X}(t)$ at time $t = \tau$ is associated with the statistical weights $w_{i,\tau}^{(n)}$. For example in the standard Monte Carlo simulation with N samples the weights at each time instant are given $w_{i,\tau}^{(n)} = 1/N \;\; r = 1, \cdots, N$. During the simulation whenever a realization is killed its weight will be deleted from the total probability mass and whenever a process is splitted, its weight will be divided between its splits. Next, each realization is associated with the normalized vector with non-dimensional components $l_n = l\big(x_i^{(n)}(\tau)\big)$. Here, the components of l_n are given as

$$l_n = l\big(x_i^{(n)}(\tau)\big) = \frac{x_i(\tau) - \mu_{X_i}(\tau)}{\sigma_{X_i}(\tau)} \quad , \quad n = 1, \cdots, N \tag{5.1}$$

where $\mu_{X_i}(\tau)$ and $\sigma_{X_i}(\tau)$ denotes sample mean value and sample standard deviation of the simulated processes

$$\mu_{X_i}(\tau) = \frac{1}{N}\sum_{n=1}^{N} x_i^{(n)}(\tau) \quad , \quad \sigma_{X_i}(\tau) = \frac{1}{N}\sum_{n=1}^{N}\big(x_i^{(n)}(\tau) - \mu_{X_i}(\tau)\big)^2 \tag{5.2}$$

The distance measure is used to distribute the samples in the state space. Pradlwarter and Schuëller (Pradlwarter and Schuëller 1999) defines the distance measure $d\left(\mathbf{x}(t)\right)$ related to the realization in the following way

$$d\big(x_i^{(n)}(\tau)\big) = \sum_{r=1}^{R} a_r || \, l\left(x_{i_r|i}^{(n)}(\tau)\right) - l\big(x_i^{(n)}(\tau)\big) \, || \quad , \quad a_1 > a_2 > \cdots > a_R \tag{5.3}$$

where $x_{i_r|i}^{(n)}(\tau)$ denotes the r^{th} closest realization to $x_i^{(n)}(\tau)$ and $||.||$ is the Eucledian norm. The closest realization with the weight a_1 is weighted highest. The weights were chosen as

$$a_r = 2^{1-r} \tag{5.4}$$

5.3.2 An Absolute distance measure

For a SDOF oscillator subjected to Gaussian white noise $||\mathbf{l}(\mathbf{z})||$ with $\mathbf{l}(\mathbf{z}(t))$ defined by (5.1) is proportional to the mechanical energy of the oscillator. On figure 5.5 is shown two trajectories A and B with the same mechanical energy. If the external loads and damping forces are small these should be considered equally important, since they will approach the boundary in the same distance with a phase lag. The mechanical energy, itself could alternatively be used as a distance measure. This property carries over to multi-degrees of freedom. However, (5.1) does not represent the mechanical energy in any other case than the indicated. Instead, (5.3) is replaced with

$$d\big(x_i^{(n)}(t)\big) = \sum_{k=1}^{K} a_k E_m\big(x_{i_k|i}(t) - x_i(t)\big) \tag{5.5}$$

where the mechanical energy is given as

$$E_m\big(\mathbf{z}(t)\big) = \frac{1}{2}\dot{\mathbf{q}}^T(t)\mathbf{M}\dot{\mathbf{q}}(t) + \frac{1}{2}\big(\mathbf{q}(t) - E[\mathbf{q}(t)]\big)^T\mathbf{K}\big(\mathbf{q}(t) - E[\mathbf{q}(t)]\big) \tag{5.6}$$

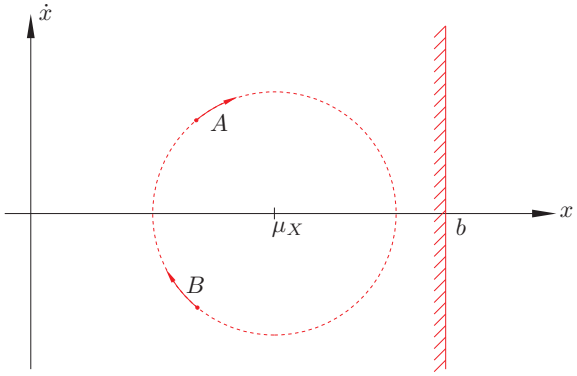

Figure 5.5 Mechanical energy of a SDOF oscillator; μ_X: Mean value of the process, b: Barrier level

where $\mathbf{M}$ and $\mathbf{K}$ denotes the mass matrix and the stiffness matrix and the vector $\mathbf{q}(t)$ stores the generalized degrees of freedom. This possibility is also examined by the authors though no better results than the weighting proposed by (5.3) is observed which has already been reported in literature (Pradlwarter and Schuëller 1997; Pradlwarter *et al.* 1998).

5.4 Importance measure

The importance measure is used to segregate the important realizations from unimportant ones. This parameter is defined as

$$c_\tau^{(n)} = \frac{d\big(x_i^{(n)}(\tau)\big)}{1 + \Big(\ln v\big(x_i^{(n)}(\tau)\big)\Big)^\beta} \tag{5.7}$$

where β is a real valued parameter which controls the level at which small weighted realizations are suppressed and the *weight measure* $v\big(x_i(\tau)\big)$ is defined as

$$v\big(x_i^{(n)}(\tau)\big) = 1 + \frac{1}{w_{i,\tau}^{(n)}} \sum_{r=1}^{R} a_k w_{i,\tau}^{(r|n)} \tag{5.8}$$

where $w_{i,\tau}^{(r|n)}$ are the weights associated to the samepls $x_{i_r|i}^{(n)}(\tau)$. The importance measure is normalized with its mean value. Therefore those realizations with their importance measure higher than the mean value will be assumed important ones and those with importance measure less than this mean are assumed to be unimportant (less important). This mean value is shown by the solid black line as the importance border in figures 5.1 and figure 5.2. Finally the probability of survival of the less important processes is defined as a function of their importance measure

$$p_s^{(n)} = 1 - p_0(1 - \hat{c}_\tau^{(n)}) \tag{5.9}$$

with assigned as a real number such that $p_0 \in (0,1]$ i.e. the probability of kill. Here $\hat{c}_\tau^{(n)}$ denotes the normalized importance measure by its mean e.g.

$$\hat{c}_\tau^{(n)} = \frac{c_\tau^{(n)}}{\bar{c}_\tau^{(n)}} \tag{5.10}$$

where $\bar{c}_\tau^{(n)} = 1/N \sum_{n=1}^{N} c_\tau^{(n)}$. In order to keep the method an unbiased estimator of the probability, the weight of the survived processes should be modified after the killing - note that the weight of the killed processes is zero afterwards - takes place (Pradlwarter and Schuëller 1999) as

$$\tilde{w}_{i,\tau}^{(n)} = \frac{w_{i,\tau}^{(n)}}{p_s^{(n)}} \tag{5.11}$$

Finally a minimum weight for splittable processes is defined to avoid high variance of the reliability estimates (Pradlwarter and Schuëller 1999). A reasonable choice for such weight is proposed $w_{min} = P_f/50$. This acts as the lower bound for the splittable processes meaning that any process having its statistical weight lower that w_{min} is not allowed to be splitted during simulation. The probability for a given barrier (threshold level) will then be estimated as

$$\hat{P}_f = \frac{1}{N} \sum_{n=1}^{N} I\left[g(x_i^{(n)}(t))\right] w_{i,t}^{(n)} \tag{5.12}$$

It is clear that (5.12) is very similar to (4.30) in the sense that the weights are only defined in two different manners i.e. $\mathcal{R}_{\mathcal{W}}^{(\tau_n)}$ in (4.30) is replaced with $w_{i,t}^{(n)}$ in (5.12).

5.5 Applying Distance Controlled Monte Carlo

The procedure of applying DCMC is as follows

1 Decide about the simulation parameters $x_i^b, \tau, K, \beta, p_0, w_{min}$

2 Generate N realizations of the system simultaneously with weights $w_{i,0}^{(n)} = 1/N$, $n = 1, \cdots, N$

3 Evolve all realizations until the next time $t = \tau_s$, $s = 1, 2, 3, \cdots$ being the times at which the RR&S-DC takes place

4 Find the processes that have outcrossed the boundaries of the safe domain and subtract their statistical weight from the total statistical weight of the simulation

5 Construct the *distance measure* $d\big(x_i^{(n)}(\tau)\big)$ for all N realizations according to either (5.3) or (5.5)

6 Calculate the *weight measure* $v\big(x_i^{(n)}(\tau)\big)$ for all processes (5.8)

7 Calculate the *importance measure* $c_\tau^{(n)}$ for all processes (5.7) using the calculated $d\big(x_i^{(n)}(\tau)\big)$ and $v\big(x_i^{(n)}(\tau)\big)$

8 Normalize the importance measure according to (5.10)

9 For the less important and splittable realizations $\mathcal{N} = \{n|\hat{c}_{\tau}^{(n)} < 1 \cap w_{i,\tau}^{(n)} > w_{min}\}$ calculate the probability of survival (5.9)

10 Kill some unimportant processes by playing the Russian Roulette on the members of the set $\mathcal{N}$. This is done by drawing a random number $\Xi \in [0, 1]$ for each member of the set, if the number is higher that the survival probability of it the realization will be killed, else it will be kept in the simulation

11 modify the weights of the survived processes according to (5.11)

12 Replace the killed processes and their weights by splitting some of the important processes

13 Stop the simulation if $t = T$ else go to step 3 above

Note: The main assumption of the method is that the system states evolve as Markove processes with independent increments.

Note: Estimation of w_{min} is based on the *unknown* P_f which is to be estimated. Therefore a reasonable guess for the probability which is to be estimated should be at hand.

Note: Simulation parameters $\tau, K, \beta, p_0, w_{min}$ can have considerable effect on the results.

Note: According to the procedure of the method, the finer the time resolution and larger the time frame of the simulation are, the more reliable the results are. However this increases the computational load.

In the simulation, time series are generated with $\Delta t = 0.041\text{s}$ and the DCMC is performed 147 times with $\Delta\tau = 0.041 \times 10^2\text{s}$. The distance measure is calculated as a weighted summation of six closest neighbor processes i.e. $K = 6$. The parameters of the DCMC are chosen $\beta = 0.8, p_0 = 0.5, w_{min} = 5 \times 10^{-5}$ and the results are shown in the figure 5.6. Figure 5.6 shows the DCMC results with two different distance measures. The results with the distance measure introduced by Pradlwarter et al. (Pradlwarter and Schuëller 1999), i.e. a relative distance measure, is shown in figure 5.6.a and the results wit the mechanical energy as the distance measure, i.e. an absolute distance measure, is shown in figure 5.6.b. Comparison of these figures show that the former distance measure shows better overall performance i.e. less coefficient of variation in the estimates.

5.6 DCMC for wind turbines

The advantage of the DCMC in application is that it does not require high amount of data to be kept in memory during simulation. Indeed the only data needed to be kept is the present state of each realization. However there exist some difficulties with its application which gives less motivation in using the method for the failure probability estimation of wind turbines. First, this method, like IS, provides failure probability of a(any) given threshold which is not encouraging since it decreases efficiency of the method in application c.f. section 1.3. Second, parameter

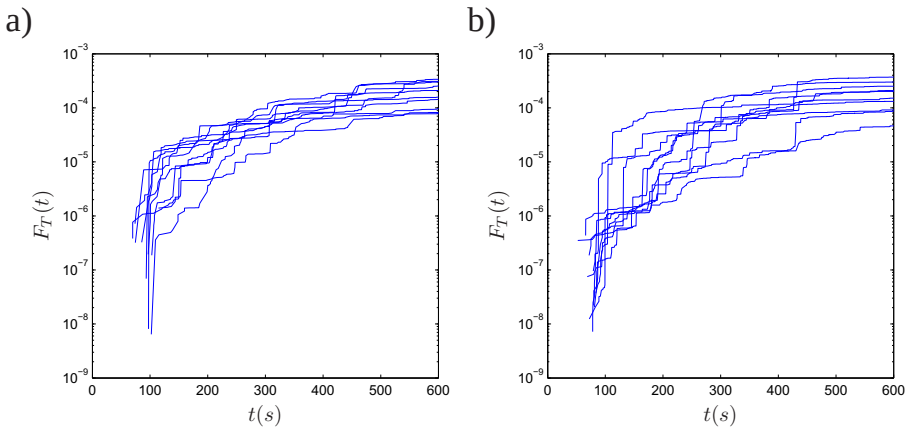

Figure 5.6 Ten estimations of first passage probability distribution for a single DOF oscillator using RR&S using 500 simulations; a) Pradlwarter's distance measure b)Mechanical energy distance measure

w_{min} defines the minimum weight of the processes which are allowed to be splitted during the RR&S. This is typically defined as a ratio of the final probability which is aimed to be estimated. Therefore an approximation of this probability should be available before the simulation starts. The wind turbine model can not satisfy this requirement. Next, there exist no global suggestion when (how often) RR&S should be played as the process evolves. This is important since firstly the time delay between two RR&S takes place need to be large enough in order to allow independence of the samples. On the other hand for the best performance, the processes should be splitted as many times as possible. This makes a potential confusion to define the optimum number of time steps the samples should be allowed to evolve before the next splitting actions take place. Last but not least from the programming point of view, communication of the processes during evolution, e.g. exchanging states during RR&S should be done carefully when the method is to be applied on large dynamic systems. According to the mentioned reasons the DCMC method has not been applied on the wind turbine model presented in this thesis.

CHAPTER 6
Conclusions and Future directions

Following are the conclusions and proposals for the future works are deduced from the research done within this thesis.

The VRMC methods however provide very good estimates for the general structural dynamic problems, in case of variable speed wind turbines still more work is required to increase applicability of these methods. The major problems in these systems stem from their high dimensions coupled with nonlinearities in the system. It is seen that in the case of the fixed speed wind turbine the methods are more successful than the variable speed case which is due to the additional nonlinearities that the controller adds to the model. Therefore still a reliable method which can work based on low number of samples without breaking down could be of great interest in this type of problems.

Observation of the results of VRMC methods on the developed model shows that unlike the normal operating conditions, during which the pitch controller decreases the effective load of the wind turbine, in extreme conditions the controller may increase the possibility of failure. It is however understood that the conditions made on the type and the specifications of the controller have considerable effect on this phenomenon. Therefore more careful study is needed for more accurate judgement in this respect.

Computational efficiency and speed are two important issue which needs special attention when it comes to analysis of the statistical behavior of the wind turbines. Therefore development of a model which allows fast generation of samples of the time history of the wind turbine will contribute in this regard. Inclusion of detailed model specifications such as non-homogeneous wind field, probabilistic structural properties and incorporation of more structural modes in the dynamic model are interesting aspects of the model.

The possibility of realizing evolution of the probability density function of wind turbines would be a very powerful tool for the failure probability estimation of these systems. This offers many possibilities for future improvement of the machines in design process. However a strict requirement for this, in case of using PDEM, is to reduce the number of basic random variables of the model to as low as possible. The is possible by using i.e. Karhunen-Loève transformation. The power point of such approach is that nonlinearities in the model do not seem to pose critical difficulties toward application of the method.

Bibliography

Akaike, Hirotugu (1974). Markovian representation of stochastic processes and its application to the analysis of autoregressive moving average processes. *Annals of the Institute of Statistical Mathematics* **26**, 363–387. 10.1007/BF02479833.

Au, Siu-Kui and Beck, James L. (2001a). Estimation of small failure probabilities in high dimensions by subset simulation. *Probabilistic Engineering Mechanics* **16**(4), 263 – 277.

Au, S. K. and Beck, J. L. (2001b). First excursion probabilities for linear systems by very efficient importance sampling. *Probabilistic Engineering Mechanics* **16**(3), 193 – 207.

Breitung, Karl (1984). Asymptotic approximations for multinormal integrals. *Journal of Engineering Mechanics* **110**(3), 357–366.

Breitung, Karl (1989). Asymptotic approximations for probability integrals. *Probabilistic Engineering Mechanics* **4**(4), 187 – 190.

Bucher, C. (2000). An importance sampling technique for randomly excited systems discretized by finite elements. In Ko, J.M. and Xu, Y.L. (Eds.), *Advances in structural dynamics*, Volume 2 of *Amsterdam: Elsevier*.

Bucher, Christian (2009a). Asymptotic sampling for high-dimensional reliability analysis. *Probabilistic Engineering Mechanics* **24**(4), 504 – 510.

Bucher, Christian (2009b). Probability-based optimal design of friction-based seismic isolation devices. *Structural Safety* **31**(6), 500 – 507. Optimization under Uncertainty with Emphasis on Structural Applications - Special Issue: Optimization.

Caires, S. and Sterl, A. (2005). 100-year return value estimates for ocean wind speed and significant wave height from the era-40 data. *Journal of Climate* **18**(7), 1032–1048.

Chen, Jian-Bing and Li, Jie (2009). A note on the principle of preservation of probability and probability density evolution equation. *Probabilistic Engineering Mechanics* **24**(1), 51 – 59.

Chen, Xinzhong and Kareem, Ahsan (2001). Aeroelastic analysis of bridges under multicorrelated winds: Integrated state-space approach. *Journal of Engineering Mechanics* **127**(11), 1124–1134.

Ching, J., Au, S.K., and Beck, J.L. (2005). Reliability estimation for dynamical systems subject to stochastic excitation using subset simulation with splitting. *Computer Methods in Applied Mechanics and Engineering* **194**(12-16), 1557 – 1579. Special Issue on Computational Methods in Stochastic Mechanics and Reliability Analysis.

Ching, J., Beck, J.L., and Au, S.K. (2005). Hybrid subset simulation method for reliability estimation of dynamical systems subject to stochastic excitation. *Probabilistic Engineering Mechanics* **20**(3), 199 – 214.

Cook, N.J. (1982). Towards better estimation of extreme winds. *Journal of Wind Engineering and Industrial Aerodynamics* **9**(3), 295 – 323.

Cook, Nicholas J. and Harris, R. Ian (2004). Exact and general FT1 penultimate distributions of extreme wind speeds drawn from tail-equivalent Weibull parents. *Structural Safety* **26**(4), 391 – 420.

Dahl, Fredrik A. (2002). Variance reduction for simulated diffusions using control variates extracted from state space evaluations. *Applied Numerical Mathematics* **43**(4), 375 – 381.

Ellingwood, B.R., Galambos, T.V., MacGregor, J.G., and Cornell, C.A. (1980). *Development of a probability based load criterion for American National Standard A58*. Washington, DC: NIST Special Publication 577, National Bureau of Standards.

Freudenreich, K and Argyriadis, K (2007). The load level of modern wind turbines according to iec 61400-1. *Journal of Physics: Conference Series* **75**(1), 012075.

Hansen, M.L.O. (2007). *Aerodynamics of wind turbines*. Earthscan; 2nd edition.

Harris, Ian (2005). Generalised Pareto methods for wind extremes. Useful tool or mathematical mirage? *Journal of Wind Engineering and Industrial Aerodynamics* **93**(5), 341 – 360.

Harris, R. I. (2004). Extreme value analysis of epoch maxima–convergence, and choice of asymptote. *Journal of Wind Engineering and Industrial Aerodynamics* **92**(11), 897 – 918.

IEC (2005a). *Amendment to the IEC 61400-1:2005 standard*. International Electrotechnical Commission.

IEC (2005b). *IEC 61400-1 (2005) International Standard, Wind turbines - Part 1: Design requirements* (third ed.). International Electrotechnical Commission.

Jensen, Hector A. and Valdebenito, Marcos A. (2007). Reliability analysis of linear dynamical systems using approximate representations of performance functions. *Structural Safety* **29**(3), 222 – 237. A Benchmark Study on Reliability in High Dimensions.

Jonkman, J., Butterfield, S., Musial, W., and Scott, G. (2009). Definition of a 5-MW reference wind turbine for offshore system development. Technical Report NREL/TP-500-38060, National Renewable Energy Laboratory.

Karamchandani, A. (1990, May). *New Methods in Systems Reliability*. Ph. D. thesis, Stanford University.

Kareem, Ahsan (2008). Numerical simulation of wind effects: A probabilistic perspective. *Journal of Wind Engineering and Industrial Aerodynamics* **96**(10-11), 1472 – 1497. 4th International Symposium on Computational Wind Engineering (CWE2006).

Katafygiotis, L.S. and Cheung, S.H. (2007). Application of spherical subset simulation method and auxiliary domain method on a benchmark reliability study. *Structural Safety* **29**(3), 194 – 207. A Benchmark Study on Reliability in High Dimensions.

Katayama, T. (2005). *Subspace Methods for System Identification*. Springer; 1st edition (October 20).

Kiureghian, Armen Der, Lin, Hong-Zong, and Hwang, Shyh-Jiann (1987). Second-order reliability approximations. *Journal of Engineering Mechanics* **113**(8), 1208–1225.

Kiureghian, Armen Der and Stefano, Mario De (1991). Efficient algorithm for second-order reliability analysis. *Journal of Engineering Mechanics* **117**(12), 2904–2923.

Koo, Heonsang, Kiureghian, Armen Der, and Fujimura, Kazuya (2005). Design-point excitation for nonlinear random vibrations. *Probabilistic Engineering Mechanics* **20**(2), 136 – 147.

Kooijman, H.J.T., Lindenburg, C., Winkelaar, D., and van der Hooft, E.L. (2003). Aero-elastic modelling of the dowec 6 MW pre-design in PHATAS. Technical Report DOWEC 10046_009, ECN-CX–01-135, Energy research center of the Netherlands.

Köylüoğlu, Hasan Uğur and Nielsen, Søren R.K. (1994). New approximations for sorm integrals. *Structural Safety* **13**(4), 235 – 246.

Krenk, Steen (2011, 26-28 May). Explicit calibration and simulation of stochastic fields by low-order arma processes. In Papadrakakis, M., Lagaros, N.D., and Fragiadakis, M. (Eds.), *Computational Methods in Structural Dynamics and Earthquake Engineering (COMPDYN 2011)*.

Li, Jie and Chen, Jianbing (2009). *Stochastic Dynamics of Structures*. Wiley-Interscience.

Li, J. and Chen, J. B. (2004). Probability density evolution method for dynamic response analysis of structures with uncertain parameters. *Computational Mechanics* **34**, 400–409. 10.1007/s00466-004-0583-8.

Li, Yousun and Kareem, A. (1990). Arma systems in wind engineering. *Probabilistic Engineering Mechanics* **5**(2), 49 – 59.

Mackay, Edward B. L., Challenor, Peter G., and Bahaj, AbuBakr S. (2010). On the use of discrete seasonal and directional models for the estimation of extreme wave conditions. *Ocean Engineering* **37**(5-6), 425 – 442.

Macke, M. and Bucher, C. (2003). Importance sampling for randomly excited dynamical systems. *Journal of Sound and Vibration* **268**(2), 269 – 290.

Madsen, H.O., Krenk, S., and Lind, N.C. (2006). *Methods of Structural Safety*. Dover Publications; First Thus edition (February 24, 2006).

Markovsky, I., Willems, J.C., Huffel, S.V., and Moor, B. De (2006). *Exact and Approximate Modeling of Linear Systems: A Behavioral Approach*. SIAM (Philadelphia, US).

Meirovitch, L. (2001). *Fundamentals of Vibrations*. McGraw-Hill.

Metropolis, Nicholas, Rosenbluth, Arianna W., Rosenbluth, Marshall N., Teller, Augusta H., and Teller, Edward (1953). Equation of state calculations by fast computing machines. *The Journal of Chemical Physics* **21**(6), 1087–1092.

Minciarelli, Fabio, GioffrÃÍ, Massimiliano, Grigoriu, Mircea, and Simiu, Emil (2001). Estimates of extreme wind effects and wind load factors: influence of knowledge uncertainties. *Probabilistic Engineering Mechanics* **16**(4), 331 – 340.

Naess, Arvid (1984). Technical note: On the long-term statistics of extremes. *Applied Ocean Research* **6**(4), 227 – 228.

Naess, A. and Clausen, P.H. (2001). Combination of the peaks-over-threshold and bootstrapping methods for extreme value prediction. *Structural Safety* **23**(4), 315 – 330.

Naess, A. and Gaidai, O. (2008). Monte Carlo methods for estimating the extreme response of dynamical systems. *Engineering Mechanics ASCE* **134**(8), 628–636.

Naess, A. and Gaidai, O. (2009). Estimation of extreme values from sampled time series. *Structural Safety* **31**(4), 325 – 334.

Naess, A., Leira, B.J., and Batsevych, O. (2009). System reliability analysis by enhanced Monte Carlo simulation. *Structural Safety* **31**(5), 349 – 355.

Naess, A. and Skaug, C. (1999a). Estimates of failure probability by importance sampling for dynamic systems. *Structural dynamics* **1-2**, 277–282.

Naess, A. and Skaug, C. (1999b). Importance sampling for dynamical systems. In R.E. Melchers, M.G. Stewart (Ed.), *Proc. ICASP 8 Conference (eds) (Rotterdam: A A Balkema)*, Rotterdam: A A Balkema, pp. 749–755.

Newton, Nigel J. (1994). Variance reduction for simulated diffusions. *SIAM Journal on Applied Mathematics* **54**(6), 1780–1805.

Nielsen, S.R.K. and Sichani, M.T. (2011). Stochastic and chaotic sub- and superharmonic response of shallow cables due to chord elongations. *Probabilistic Engineering Mechanics* **26**(1), 44 – 53. Special Issue: Stochastic Methods in Mechanics – Status and Challenges.

Obadage, A.S. and Harnpornchai, N. (2006). Determination of point of maximum likelihood in failure domain using genetic algorithms. *International Journal of Pressure Vessels and Piping* **83**(4), 276 – 282. The 16th European Safety and Reliability Conference.

Ogata, K. (2009). *Modern Control Engineering* (5 ed.). Prentice Hall; 5 edition.

Ogawa, Jun and Tanaka, Hiroaki (2009). Importance sampling for stochastic systems under stationary noise having a specified power spectrum. *Probabilistic Engineering Mechanics* **24**(4), 537 – 544.

Olsen, Anna Ivanova (2006). *Time-variant reliability of dynamic systems by importance sampling and probabilistic analysis of ice loads*. Ph. D. thesis, Norwegian University of Science and Technology (NTNU).

Olsen, A. I. and Naess, A. (2006). Estimation of failure probabilities of linear dynamic systems by importance sampling. *Sadhana-academy Proceedings in Engineering Sciences* **31**, 429–443.

Olsen, A. Ivanova and Naess, A. (2007). An importance sampling procedure for estimating failure probabilities of non-linear dynamic systems subjected to random noise. *International Journal of Non-Linear Mechanics* **42**(6), 848 – 863.

Overschee, Peter Van and Moor, Bart De (1996). *Subspace Identification for Linear Systems: Theory - Implementation - Applications*. Springer; 1 edition (May 31).

Papoulis, A. (1991). *Probability, Random Variables and Stochastic Processes*. McGraw-Hill Companies.

Pradlwarter, H. J. and Schuëller, G. I. (1997). On advanced monte carlo simulation procedures in stochastic structural dynamics. *International Journal of Non-Linear Mechanics* **32**(4), 735 – 744. Third International Stochastic Structural Dynamics Conference.

Pradlwarter, H. J. and Schuëller, G. I. (1999). Assessment of low probability events of dynamical systems by controlled monte carlo simulation. *Probabilistic Engineering Mechanics* **14**(3), 213 – 227.

Pradlwarter, H. J., Schuëller, G. I., and Dorka, U. (1998). Reliability of mdof-systems with hysteretic devices. *Engineering Structures* **20**(8), 685 – 691.

Pradlwarter, H. J., Schuëller, G. I., and Melnik-Melnikov, P. G. (1994). Reliability of mdof-systems. *Probabilistic Engineering Mechanics* **9**(4), 235 – 243.

Samaras, Elias, Shinzuka, Masanobu, and Tsurui, Akira (1985). Arma representation of random processes. *Journal of Engineering Mechanics* **111**(3), 449–461.

Santoso, A.M., Phoon, K.K., and Quek, S.T. (2011). Modified metropolis-hastings algorithm with reduced chain correlation for efficient subset simulation. *Probabilistic Engineering Mechanics* **26**(2), 331 – 341.

Schuëller, G.I. (2008). *Computational stochastic dynamics - some lessons learned*, Chapter 1, pp. 3–20. Computational Structural Dynamics and Earthquake Engineering Vol.2, Structures & Infrastructures Series. Taylor & Francis.

Shiotani, M. and Iwayani, Y. (1971). Correlation of wind velocities in relation to the gust loadings. In *Proceedings of the 3rd Conference on Wind Effects on Buildings and Structures*.

Sichani, M.T., Nielsen, S.R.K., and Bucher, C. (2011a). Applications of asymptotic sampling on high dimensional structural dynamic problems. *Structural Safety* **33**(4-5), 305 – 316.

Sichani, M.T., Nielsen, S.R.K., and Bucher, C. (2011b). Efficient estimation of first passage probability of high-dimensional nonlinear systems. *Probabilistic Engineering Mechanics* **26**(4), 539 – 549.

Sichani, M.T., Pedersen, B.J., and Nielsen, S.R.K. (2010). Stochastic subspace modelling of turbulence. *World Academy of Science, Engineering and Technology* **58**, 1140–1148.

Simiu, E. and Heckert, N. A. (1996). Extreme wind distribution tails: A "peaks over threshold" approach. *Journal of Structural Engineering-asce* **122**.

Simiu, E., Heckert, N. A., Filliben, J. J., and Johnson, S. K. (2001). Extreme wind load estimates based on the Gumbel distribution of dynamic pressures: an assessment. *Structural Safety* **23**(3), 221 – 229.

Simon, D. (2006). *Optimal State Estimation: Kalman, H Infinity, and Nonlinear Approaches*. Wiley-Interscience.

Soderstrom, T. and Stoica, P. (1981, apr). On the stability of dynamic models obtained by least-squares identification. *Automatic Control, IEEE Transactions on* **26**(2), 575 – 577.

Solari, G. and Tubino, F. (2002). A turbulence model based on principal components. *Probabilistic Engineering Mechanics* **17**(4), 327 – 335.

Song, Shufang, Lu, Zhenzhou, and Qiao, Hongwei (2009). Subset simulation for structural reliability sensitivity analysis. *Reliability Engineering & System Safety* **94**(2), 658 – 665.

Soong, T. T. and Grigoriu, Mircea (1992). *Random Vibration of Mechanical and Structural Systems*. Prentice Hall.

Tanaka, H. (1998). Application of an importance sampling method to time-dependent system reliability analyses using the girsanov transformation. In *Structural safety and reliability (ICOSSAR 97)*, Volume 1-3, pp. 411–418.

Tanaka, H. (1999). Importance sampling simulation for a stochastic fatigue crack growth model. In *Proc. ICASP8*1999*, Volume 2, pp. 907–914.

Tvedt, Lars (1983). Two second-order approximations to the failure probability. Technical Report RDIV/20-004-83, Det norske Veritas.

Tvedt, Lars (1990). Distribution of quadratic forms in normal space—application to structural reliability. *Journal of Engineering Mechanics* **116**(6), 1183–1197.

Veers, Paul S. (1988). Three-dimensional wind simulation. Technical Report SAND88-0152 UC-261, Sandia National Laboratories, Albuquerque, NM 87185.

Verhaegen, M. and Verdult, V. (2007). *Filtering and System Identification: A Least Squares Approach*. Cambridge University Press; 1 edition (May 28).

Xue, D., Chen, Y.Q., and Atherton, D.P. (2008). *Linear Feedback Control: Analysis and Design with MATLAB*. Society for Industrial and Applied Mathematics (SIAM).

Zuev, Konstantin (2009). *Advanced stochastic simulation methods for solving high-dimensional reliability problems*. Ph. D. thesis, Hong Kong University of Science and Technology.

Zuev, K.M. and Katafygiotis, L.S. (2011a). The horseracing simulation algorithm for evaluation of small failure probabilities. *Probabilistic Engineering Mechanics* **26**(2), 157 – 164.

Zuev, K.M. and Katafygiotis, L.S. (2011b). Modified metropolis-hastings algorithm with delayed rejection. *Probabilistic Engineering Mechanics* **26**(3), 405 – 412.

APPENDIX A
Derivations of Kalman filter gain and Riccati equation

Detailed derivation of the Kalman filter gain (2.50) and the Riccati equation (2.48) are presented respectively. Kalman filter gain equation is derived as follows

$$\begin{aligned} \bar{\mathbf{G}}^{\mathrm{T}}(j) &= E[\bar{\mathbf{x}}(j+1)\mathbf{v}^{\mathrm{T}}(j)] \\ &= E\left[\Big(\mathbf{A}\bar{\mathbf{x}}(j)+\mathbf{K}(j)\left\{\mathbf{v}(j)-\mathbf{C}\bar{\mathbf{x}}(j)\right\}\Big)\mathbf{v}^{\mathrm{T}}(j)\right] \\ &= \mathbf{A}E[\bar{\mathbf{x}}(j)\mathbf{v}^{\mathrm{T}}(j)]+\mathbf{K}(j)\left(\mathbf{C}_{\mathbf{vv}}^{\mathrm{T}}(0)-\mathbf{C}E[\bar{\mathbf{x}}(j)\mathbf{v}^{\mathrm{T}}(j)]\right) \end{aligned} \tag{A-1}$$

Where $\mathbf{C}_{\mathbf{vv}}(0)=\mathbf{C}_{\mathbf{vv}}^{\mathrm{T}}(0)$ is used. Next

$$\begin{aligned} E[\bar{\mathbf{x}}(j)\mathbf{v}^{\mathrm{T}}(j)] &= E\left[\bar{\mathbf{x}}(j)\left(\bar{\mathbf{x}}^{\mathrm{T}}(j)\mathbf{C}^{\mathrm{T}}+\mathbf{e}^{\mathrm{T}}(j)\right)\right] \\ &= \bar{\mathbf{\Sigma}}(j)\mathbf{C}^{\mathrm{T}} \end{aligned} \tag{A-2}$$

Substituting (A-2) into (A-1) results in

$$\bar{\mathbf{G}}^{\mathrm{T}}(j)=\mathbf{A}\bar{\mathbf{\Sigma}}(j)\mathbf{C}^{\mathrm{T}}+\mathbf{K}(j)\left(\mathbf{C}_{\mathbf{vv}}^{\mathrm{T}}(0)-\mathbf{C}\bar{\mathbf{\Sigma}}(j)\mathbf{C}^{\mathrm{T}}\right) \tag{A-3}$$

That can be solved for $\mathbf{K}(j)$ which ends up in (2.50)

$$\mathbf{K}(j)=\left(\bar{\mathbf{G}}^{\mathrm{T}}(j)-\mathbf{A}\bar{\mathbf{\Sigma}}(j)\mathbf{C}^{\mathrm{T}}\right)\left(\mathbf{C}_{\mathbf{vv}}^{\mathrm{T}}(0)-\mathbf{C}\bar{\mathbf{\Sigma}}(j)\mathbf{C}^{\mathrm{T}}\right)^{-1} \tag{A-4}$$

The Riccati equation (2.48) is derived as follows

$$E[\bar{\mathbf{x}}(j+1)\bar{\mathbf{x}}^{\mathrm{T}}(j+1)]=E\left[\Big(\mathbf{A}\bar{\mathbf{x}}(j)+\mathbf{K}(j)\mathbf{e}(j)\Big)\Big(\mathbf{A}\bar{\mathbf{x}}(j)+\mathbf{K}(j)\mathbf{e}(j)\Big)^{\mathrm{T}}\right] \tag{A-5}$$

$$\bar{\mathbf{\Sigma}}(j+1)=\mathbf{A}\bar{\mathbf{\Sigma}}(j)\mathbf{A}^{\mathrm{T}}+\mathbf{K}(j)\left(\mathbf{C}_{\mathbf{vv}}^{\mathrm{T}}(0)-\mathbf{C}\bar{\mathbf{\Sigma}}(j)\mathbf{C}^{\mathrm{T}}\right)\mathbf{K}^{\mathrm{T}}(j) \tag{A-6}$$

Substituting Kalman gain from (A-4) results in

$$\begin{aligned} \bar{\mathbf{\Sigma}}(j+1) &= \mathbf{A}\bar{\mathbf{\Sigma}}(j)\mathbf{A}^{\mathrm{T}}+\left(\bar{\mathbf{G}}^{\mathrm{T}}(j)-\mathbf{A}\bar{\mathbf{\Sigma}}(j)\mathbf{C}^{\mathrm{T}}\right)\times \\ &\quad \left(\mathbf{C}_{\mathbf{vv}}^{\mathrm{T}}(0)-\mathbf{C}\bar{\mathbf{\Sigma}}(j)\mathbf{C}^{\mathrm{T}}\right)^{-1}\left(\bar{\mathbf{G}}^{\mathrm{T}}(j)-\mathbf{A}\bar{\mathbf{\Sigma}}(j)\mathbf{C}^{\mathrm{T}}\right)^{\mathrm{T}} \end{aligned} \tag{A-7}$$

APPENDIX B
Importance sampling for Wind turbines

B.1 Representation of the model in the Itô SDE form

To apply IS based on (Macke and Bucher 2003) it is necessary to have estimation of the system responses, i.e. displacements, at the failure time instance when it is excited by the increments of the Wiener process. This estimation is the base for constructing the so-called control functions. Their characteristic is: " if the system is excited with them the response will be at the failure state (boundary of the LSF) at failure time instance, i.e. $t_m = m\Delta t$ ". These deterministic drifts are then added to the Wiener increments and the result is used as the final system excitation. Starting by designing control functions, if excitations are not Wiener increments themselves, they should be represented in terms of them. The turbulence can be represented as filtered increments of the unit intensity Wiener process

$$\mathbf{v}(m) = \sum_{k=0}^{m-1} \mathbf{g}(m-k)\Delta\mathbf{W}(k) \tag{B-1}$$

$\Delta\mathbf{W}(k) \in \mathbf{R}^{q\times m}$ is a stochastic matrix containing identically distributed, mutually independent normal random variables

$$\Delta\mathbf{W}(k) \sim N\big(\mathbf{0}, \sqrt{\Delta t}\,\mathbf{I}\big) \tag{B-2}$$

$\mathbf{g}(k)$ is a time-invariant impulse response matrix function which is determined from (3.37) as follows

$$\mathbf{g}(k) = \begin{cases} \mathbf{D}_T & , \quad k = 0 \\ \mathbf{C}_T\mathbf{A}_T^{k-1}\mathbf{B}_T & , \quad k > 0 \end{cases} \tag{B-3}$$

(B-1) is a linear filter equivalent given the solution to $\{\,\mathbf{v}(t), t \in [t_0, \infty[\,\}$ at discrete instants of time. Alternatively, $\{\,\mathbf{v}(t), t \in [t_0, \infty[\,\}$ may be obtained as the solution to the linear Itô differential equation

$$\left.\begin{array}{rcl} d\mathbf{v}(t) & = & \mathbf{a}\mathbf{v}(t)dt + \mathbf{s}d\mathbf{W}(t) \\ \mathbf{v}(t_0) & = & \mathbf{0} \end{array}\right\} \tag{B-4}$$

the drift matrix $\mathbf{a}$ and the diffusion matrix $\mathbf{s}$ are yet unknown quadratic constant matrices of dimension $q \times q$, which may be specified as indicated below. $\{\, \mathbf{W}(t), t \in [t_0, \infty[\,\}$ is q-dimensional vector process of mutually independent unit intensity Wiener component process. The solution of (B-4) at the discrete instants of time is given as

$$\mathbf{v}(m) = e^{\mathbf{a}m\Delta t}\mathbf{v}(0) + \sum_{k=0}^{m-1} e^{\mathbf{a}(m-k)\Delta t}\mathbf{s}\Delta\mathbf{W}(k) \tag{B-5}$$

$e^{\mathbf{a}(m-k)\Delta t}$indicates the matrix exponential based on the matrix $\mathbf{a}$. Comparison of (B-1) and (B-5) provides the following relationship between $\mathbf{a}, \mathbf{s}$ and $\mathbf{g}(k)$

$$\mathbf{g}(k) = e^{\mathbf{a}k\Delta t}\mathbf{s} \tag{B-6}$$

$\mathbf{a}$ and $\mathbf{s}$ may be determined so (B-6) is fulfilled at best with $\mathbf{g}(k)$ given by (B-3). Notice that $\mathbf{a}$ and $\mathbf{s}$ are not needed in the method, which merely requests to solution given by (B-1). Since (B-3) is a linear differential equation in $\mathbf{z}(t)$, the solution of (3.24) at the discretized instant of time may be written as

$$\mathbf{z}(m) = \mathbf{z}_0(m) + \sum_{k=0}^{m-1} \mathbf{h}(m-k)\mathbf{f}\big(\mathbf{v}(k), \mathbf{z}(k)\big) \tag{B-7}$$

where the initial condition is given as

$$\begin{aligned}\mathbf{z}_0(m) &= e^{\mathbf{A}m\Delta t}\mathbf{z}_0(0) + \\ &+ \left(\left(\left(1 + \frac{t_0}{\tau_i}\right)\mathbf{A}^{-1} + \frac{1}{\tau_i}\mathbf{A}^{-2}\right)e^{\mathbf{A}m\Delta t} + \left(\left(1 + \frac{m\Delta t}{\tau_i}\right)\mathbf{A}^{-1} + \frac{1}{\tau_i}\mathbf{A}^{-2}\right)\right)\mathbf{B}_1\end{aligned} \tag{B-8}$$

$$\mathbf{B}_1 = -\frac{G\Omega_{r,0}}{\tau_i}\begin{bmatrix}\mathbf{0}\\ \mathbf{0}\\ 1\\ 1\\ 1\end{bmatrix} \tag{B-9}$$

where the impulse response function is given as

$$\mathbf{h}(k) = e^{\mathbf{A}k\Delta t}\mathbf{B}\Delta t \tag{B-10}$$

$e^{\mathbf{A}k\Delta t}\Delta t$ represents the matrix exponential function and $\mathbf{A}$ is the system matrix in (3.26). (3.26) and (3.27) have been used at the derivation of (B-8). The dependence of the load vector $\mathbf{f}$ on the state vector $\mathbf{z}(k)$ is via the azimuthal angle $q_5(k)$, its derivative $\dot{q}_5(k)$ and the pitch angles $\boldsymbol{\beta}(k)$. $\mathbf{h}(k)$ represents the impulse response matrix for the structural state variable. The solution to (B-1) and (B-7) form the solutions to an integrated continuous time vector process $\{\, \mathbf{X}(t), t \in [t_0, \infty[\,\}$ of dimension $(13+q) \times 1$ defined as

$$\mathbf{X}(t) = \begin{bmatrix}\mathbf{z}(t)\\ \mathbf{v}(t)\end{bmatrix} \tag{B-11}$$

Formally $\{\,\mathbf{X}(t), t \in [t_0, \infty[\,\}$ may be written as the solution to the Itô differential equation

$$\left.\begin{array}{rcl} d\mathbf{X}(t) & = & \left[\begin{array}{c} \mathbf{Az} + \mathbf{Bf}(\mathbf{v},\mathbf{z}) + \mathbf{B}_0(t) \\ \mathbf{av} \end{array}\right] dt + \left[\begin{array}{c} \mathbf{0} \\ \mathbf{s} \end{array}\right] d\mathbf{W}(t) \\ \mathbf{X}(0) & = & \left[\begin{array}{c} \mathbf{z}(0) \\ \mathbf{0} \end{array}\right] \end{array}\right\} \tag{B-12}$$

$\mathbf{X}(t)$ is a Markov diffusion process driven by the q-dimensional unit Wiener process. The drift vector and diffusion matrix may be determined based on the solution equation (B-1) and (B-7).

B.2 Control functions : Nonlinear model

Let $\mathbf{v}(k) \in \mathbf{R}^q$ denote the turbulence vector and $\mathbf{g}(k) \in \mathbf{R}^{q\times q}$ denote the IRF matrix of turbulence. It is obvious that the number of turbulence nodes is not equal to the number of structure's DOF in general, $q \neq p$. the so-called *influence functions* will assign the right turbulence node to each DOF. The vector of Wiener increments is defined as $\Delta\mathbf{W}(k) = \sqrt{\Delta t}\boldsymbol{\Xi}(k)$ where $\boldsymbol{\Xi}(k) \in \mathbf{R}^{q\times 1}$ are mutually independent standard Gaussian random numbers with $E[\boldsymbol{\Xi}(k)\boldsymbol{\Xi}^T(k)] = \mathbf{I}$. System response, e.g. displacement, of the aimed DOF at the failure time instance $t_m = m\Delta t$ is written as

$$z_i(m) = \Delta t \sum_{j=1}^{p}\sum_{k=0}^{m} h_{ij}(m-k) f\big(v_j(k)\big) \tag{B-13}$$

where p is the number of system DOFs, $f\big(v_j(k)\big) \in \mathbf{R}^{p\times 1}$ is the function that determines the aerodynamic loads in terms of turbulence. This function represents the iterative BEM method for the blades' DOFs and is zero for the other DOFs. $v_j(k), j = 1, \cdots, p$ are the components of the turbulence vector exciting each DOF at time $k\Delta t$. In order to define $v_j(k)$ provided that $\mathbf{v}(k)$ is available a function is required which determines the spatial subset of turbulence nodes that are exciting the blades at the specified time instance. This function is defined as $\mathbf{N}\big(\theta_i(k)\big) \in \mathbf{R}^{p\times q}$ and is multiplied by the turbulence vector, i.e. $v_j(k) = \mathbf{N}\big(\theta_i(k)\big)\mathbf{v}(k)$, which will be referred to as *influence function* hereafter. In the numerical case here $p = 5$; the 4^{th} row of $\mathbf{N}(\cdot)$ indicates the turbulence at the hub height and its last row can be set to zero since the rotational DOF is not affected by the turbulence directly. The elements of the first three rows of the influence function are defined as

$$N_{ij}\big(\theta_j(k)\big) = \left\{\begin{array}{lll} 1 & , & \theta_j(t) \in \big[\theta_l - \frac{\Delta\theta}{2}, \theta_l + \frac{\Delta\theta}{2}\big[\\ 0 & , & \text{otherwise} \end{array}\right. \quad , \quad j = 1,2,3 \tag{B-14}$$

where $\theta_j(k)$ defines the j^{th} blade position at time instance $k\Delta t$ and $\theta_l, l = 1, \cdots, q$ defines the angular positions of the turbulence nodes. $\Delta\theta = 2\pi/(q-1)$ indicates the angular distance between turbulence nodes. Incorporating this influence function in (B-13), the system responses is written as

$$\begin{array}{rcl} z_i(m) & = & \sum_{j=1}^{p}\sum_{k=0}^{m} h_{ij}(m-k) f\big(v_j(k)\big) \\ & = & \sum_{j=1}^{p}\sum_{k=0}^{m} h_{ij}(m-k) f\Big(\mathbf{N}\big(\theta_j(k)\big)\mathbf{v}(k)\Big) \\ & = & \sum_{j=1}^{p}\sum_{k=0}^{m} h_{ij}(m-k) f\Big(\mathbf{N}\big(\theta_j(k)\big)\sum_{r=0}^{k}\mathbf{g}(k-r)\Delta\mathbf{W}(r)\Big) \end{array} \tag{B-15}$$

In case that rotational speed of the rotor is assumed to be fixed equal to its nominal value, the position of the first blade is $\theta_1(k) = k\Delta t\Omega_{r,0}$ and the other two blades are $\theta_2(k) = \theta_1(k)+2\pi/3$ and $\theta_3(k) = \theta_1(k) + 4\pi/3$. In such case the influence function is predicted for any time as $\mathbf{N}\big(\theta_i(k)\big) \equiv \mathbf{N}(k)$; which can be replaced in (B-15). It is clear that (B-15) is a nonlinear equation with many basic random variables inside e.g. $\Delta\mathbf{W}(r)$. The control functions should then be obtained via optimization as described in section 4.4.

B.3 Control functions: Linear model

The nonlinearity in (B-15) comes from the aerodynamic load calculation function $f(\cdot)$. Therefore if a linearization is available for the model, the control functions can be designed in a more efficient way. This is possible by defining the virtual IRFs such as $\tilde{\mathbf{h}}(k) \in \mathbf{R}^{q\times q}$, i.e. a combination of the system IRFs and the excitation IRFs that relate system responses directly to the normal space in which excitations are $\boldsymbol{\Xi}(k)$. They may be represented in the following form

$$z_i(m) = \sum_{j=1}^{q}\sum_{r=0}^{m}\tilde{h}_{ij}(m-r)\Delta W_j(r) = \sqrt{\Delta t}\sum_{j=1}^{q}\sum_{r=0}^{m}\tilde{h}_{ij}(m-r)\Xi_j(r) \tag{B-16}$$

where $\Xi_j(r)$ is the j^{th} component of the vector $\boldsymbol{\Xi}(r)$. Thus the safety margin for the i^{th}DOF, reaching the margin of failure at m^{th} time instant is written

$$G = x_i^b - z_i(m) = x_i^b - \sqrt{\Delta t}\sum_{j=1}^{q}\sum_{r=0}^{m}\tilde{h}_{ij}(m-r)\Xi_j(r) \tag{B-17}$$

The mean value and the standard deviation of the process reads

$$\mu_G^{(m)} = x_i^b \quad , \quad \sigma_G^{(m)} = \left(\Delta t\sum_{j=1}^{q}\sum_{r=0}^{m}\tilde{h}_{ij}^2(m-r)\right)^{1/2} \quad , \tag{B-18}$$

the reliability index, $\beta_G^{(m)}$, can be estimated as

$$\beta_G^{(m)} = \frac{\mu_G^{(m)}}{\sigma_G^{(m)}} = \frac{x_i^b}{\sqrt{\Delta t\sum_{j=1}^{q}\sum_{r=0}^{m}\tilde{h}_{ij}^2(m-r)}} \tag{B-19}$$

the unit normal vector toward the design point is calculated as

$$\alpha_{ij}^{(m)}(r) = \frac{\partial G/\partial\Xi_j(r)}{|\partial G/\partial\Xi_j(r)|} = \frac{\tilde{h}_{ij}(m-r)}{\sqrt{\sum_{j=1}^{q}\sum_{r=0}^{m}\tilde{h}_{ij}^2(m-r)}} \tag{B-20}$$

whereby the desifn point becomes

$$\xi_{ij}^{(m)}(r) = \beta_G^{(m)}\,\alpha_{ij}^{(m)}(r) = \frac{x_i^b}{\sqrt{\Delta t}\sqrt{\sum_{j=1}^{q}\sum_{r=0}^{m}\tilde{h}_{ij}^2(m-r)}}\tilde{h}_{ij}(m-r) \tag{B-21}$$

and the control functions, $u_{ij}^{m}(r)$, which cause failure of the i^{th} DOF at the target failure time instance can be designed as

$$u_{ij}^{(m)}(r) = \frac{x_i^b}{\Delta t \sum_{j=1}^{q} \sum_{r=0}^{m} \tilde{h}_{ij}^2(m-r)} \tilde{h}_{ij}(m-r) \quad , \quad s = 1, \cdots, 5 \tag{B-22}$$

APPENDIX C
Applications of asymptotic sampling on high dimensional structural dynamic problems

The paper presented in this appendix is published in *Structural Safety*, Volume 33, Issues 4-5, July 2011, Pages 305-316.

Structural safety

Order detail ID:	56239216
Order License Id:	2742950603737
Article Title:	Applications of asymptotic sampling on high dimensional structural dynamic problems
Author(s):	Sichani, M.T.
DOI:	10.1016/J.STRUSAFE.2011.05.002
Date:	Jan 01, 2011
ISSN:	0167-4730
Publication Type:	Journal
Volume:	33
Issue:	4-5
Start page:	305
Publisher:	ELSEVIER BV

Permission Status: **Granted**

Permission type: Republish or display content
Type of use: reuse in a thesis/dissertation

View details

http://www.elsevier.com/copyright

Structural Safety 33 (2011) 305–316

Contents lists available at ScienceDirect

Structural Safety

journal homepage: www.elsevier.com/locate/strusafe

Applications of asymptotic sampling on high dimensional structural dynamic problems

M.T. Sichani [a,*], S.R.K. Nielsen [a], C. Bucher [b]

[a] Department of Civil Engineering, Aalborg University, 9000 Aalborg, Denmark
[b] Center of Mechanics and Structural Dynamics, Vienna University of Technology, Karlsplatz 13, Vienna, Austria

ARTICLE INFO

Article history:
Received 21 June 2010
Received in revised form 16 May 2011
Accepted 16 May 2011

Keywords:
Low failure probability
Asymptotic sampling
Oscillatory systems

ABSTRACT

The paper represents application of the asymptotic sampling on various structural models subjected to random excitations. A detailed study on the effect of different distributions of the so-called support points is performed. This study shows that the distribution of the support points has considerable effect on the final estimations of the method, in particular on the coefficient of variation of the estimated failure probability. Based on these observations, a simple optimization algorithm is proposed which distributes the support points so that the coefficient of variation of the method is minimized. Next, the method is applied on different cases of linear and nonlinear systems with a large number of random variables representing the dynamic excitation. The results show that asymptotic sampling is capable of providing good approximations of low failure probability events for very high dimensional reliability problems in structural dynamics.

© 2011 Elsevier Ltd. All rights reserved.

1. Introduction

Estimation of small failure probabilities and large safety indices of structures are important issues in which Monte Carlo simulation loses its efficiency due to the excessively high number of samples required to be simulated. Recently methods have been developed which allow efficient estimation of these low probability events. These methods tackle this problem from very different points of view i.e. importance sampling [1,2] moves the sampling density function to the boundaries of the failure domain, directional sampling [3] tries to find the boundaries of the limit state function $G(\mathbf{X})$ in different directions of the random variables within the U-space. Here primarily the original random variables of the limit state function, $\mathbf{X}$, with joint probability distribution function $F_{\mathbf{X}}(\mathbf{x})$ are transformed into the standard normally distributed random variables $\mathbf{U}$, the domain of which is called the U-space, using the Rosenblatt transformation T: $\mathbf{X} \rightarrow \mathbf{U}$ [3]. On the other hand the subset simulation methods [4–6] or the S3 method, [7] work on the basis of the Markov Chain Monte Carlo (MCMC) which is capable of generating samples of a conditional stochastic process. A comprehensive comparison of the performance of these methods can be found in [8]. Nevertheless the applicability of all the methods seems to have practical restrictions regarding both the temporal and spatial dimensions of the problem under consideration and also the presence of nonlinearity in the system, [9]. In [10] it is shown that importance sampling can lead to biased results for high dimensional problems on a linear Single Degree of Freedom (SDOF) oscillator. The paper indicates that very careful and detailed analysis of the system is required when using importance sampling in high dimensions to make sure that the results are unbiased. In [11] it is reported that the importance sampling loses its efficiency on a SDOF elasto-plastic oscillator. A geometrical explanation of the reason why importance sampling fails for high dimensional problems and also the difficulties concerning nonlinear problems is provided in [12]. On the other hand the subset simulation [4] which reportedly performs quite satisfactory on many systems might still fail for estimation of first passage excursion probability of order 10^{-5} of a SDOF Duffing oscillator, [9].

Considering a realistic engineering problem in which a Multi Degree of Freedom (MDOF) system with possibly strong nonlinearities is excited by multiple non-white stochastic excitations and the failure probability is to be estimated within a long time interval (thus defining a high dimensional reliability problem) applicability of most of these methods can not be guaranteed due to severe problems related to complexity, very high computation cost or excessively high memory requirements. A good example of such a case is a wind turbine in which a highly nonlinear MDOF system is excited by many stochastic processes, say 100, for which the failure probability is to be estimated within a time interval of 600 s. In such a case applicability of most of the available methods in the literature can be questioned.

Another important issue which is not considered in the previous studies is the cases of high dimensional multiple non-white stochastic excitations. In such cases, readily applicable methods are the ones

* Corresponding author. Tel.: +45 9940 8570; fax: +45 9814 8243.
E-mail addresses: mts@civil.aau.dk (M.T. Sichani), soren.nielsen@civil.aau.dk (S.R.K. Nielsen), christian.bucher@tuwien.ac.at (C. Bucher).

0167-4730/$ - see front matter © 2011 Elsevier Ltd. All rights reserved.
doi:10.1016/j.strusafe.2011.05.002

which best satisfy the following two conditions in essence. First, the method should not need the so-called tractable data of the system, i.e. the critical excitations in case of the importance sampling method, since nonlinearities and high dimension of the problem do not allow efficient calculation and tracing of such data. Second, for large systems the memory limits do not allow saving large amount of information from the pre-processing, time history of the previous simulations in terms of excitation or response. The first restriction proposes use of the so-called black box methods which do not incorporate any specific information of the model. The second limitation would restrict the available choices to those which do not have high demand on the data storage. Severity of these conditions varies considerably according to the specific case of the problem under consideration. This inculcates that choosing the proper method to solve a specific problem might not be a trivial task and requires a good insight into both the methods and the problem.

A method recently proposed and shown to be efficient for such cases is asymptotic sampling. The method is based on an asymptotic approximation of the failure probability, [13]. Due to its very low demand both on the memory requirement and also the a-priori knowledge of the system behavior, the method seems to have a wide range of applicability among practical problems which typically have high spatial as well as temporal dimensions in their excitations comprising some sort of nonlinearity. Nevertheless, accuracy of the method on such systems is not reported in the literature yet. In the present article application of the method on linear and nonlinear SDOF and MDOF systems exposed to different stochastic excitations has been studied. Calibration of support points and its effect on the estimations of the method is studied in detail and simulations are carried out to illustrate the discussions. Finally an optimization algorithm is proposed which locates the support points in the order which increases accuracy and precision of the method.

2. Asymptotic sampling

The idea in the Asymptotic Sampling (AS) is to change the excitation level to cause more Monte Carlo simulations to exit from the barrier and then adjust the estimated probabilities, [3,14]. In this regard the intensity of the white noise driving the system is increased artificially by the factor f^{-1} which causes more processes to outcross from the boundaries of the safe domain. It is shown, [13,14], that the reliability index asymptotically has a linear relation with f factor $\beta(f) = f\beta(1)$ which is utilized to estimate $\beta(1)$ by estimating $\beta(f)$ using standard Monte Carlo simulation. In this concept it is proposed to use the following function for the extrapolation.

$$\beta(f) = Af + \frac{B}{f} \tag{1}$$

The procedure then follows as the following steps

1. Transform the random variables of the problem into the U-space, e.g. $\boldsymbol{\Xi}$, using Rosenblatt transformation T: $\mathbf{X} \rightarrow \mathbf{U}$.
2. Choose an $f \in [0,1]$ and increase the standard deviation of $\boldsymbol{\Xi}$ to obtained scaled random variables $\boldsymbol{\Xi}_f = \boldsymbol{\Xi}/f$.
3. Perform the standard Monte Carlo simulation with $\boldsymbol{\Xi}_f$ and calculate the scaled failure probability $p_f(f)$
4. Estimate the scaled reliability index as $\beta(f) = \Phi^{-1}(1 - p_f(f))$.
5. Repeat the steps 2–4 for different values of "f" to construct a set of $(f, \beta(f))$ which will be referred as "support points" hereafter.
6. Estimate coefficients A and B of (1) using constructed set of $(f, \beta(f))$ by regression analysis. In order to put equal weights on all support points in regression analysis (2) may be used instead of (1)

$$\frac{\beta(f)}{f} = A + \frac{B}{f^2} \tag{2}$$

7. Estimate the un-scaled reliability index $\beta(1) = A + B$ and failure probability $p_f(1) = 1 - \Phi(\beta(1))$.

The method is examined on a simple problem for which limit state is defined as a multiplication of random variables as (3) where $X_1 \sim \ln N(38, 14.44)$ and $X_2 \sim N(54, 7.29)$. For this problem the exact results are $\beta = 5.151$ which is related to $p_f = 1.3 \times 10^{-7}$, [15]. It is seen that choosing the minimum and maximum limits for number of out-crossings are related to the nature of the problems and a general judgement can not be made in this state. Fig. 1 shows results of AS for the problem which its limit state function is defined as $g(X_1, X_2) < 0$ where $g(X_1, X_2)$ is defined in (3). Five different "f" values, hence five support points, have been chosen for each simulation case. 1000 Monte Carlo simulations, corresponding to the step 3 in the above procedure, are performed for each support point. $\beta(1)$ is estimated from these support points as described in steps 6 and 7 above. In order to obtain coefficient of variation of the estimated $\beta(1)$ values for each distribution type and range of support points, this procedure is repeated 100 times and the results are shown in Fig. 1. In order to demonstrate effect of the optimized range for distribution of the support points Fig. 1a shows the simulations results for $f \in [0.3, 0.5]$ while in Fig. 1b–d $f \in [0.0516, 0.3290]$. Distribution of the support points in each simulation is indicated in the caption of the figure. In what is referred as the exponential distribution, support points are concentrated around the maximum "f" value while in the logarithmic distribution, support points are concentrated around the minimum "f" value. The figure shows that both the range from which f factor is chosen and the way support points are distributed affect the final results. To find the optimum range of f, its minimum and maximum limits are chosen so that on the maximum at least 40% of the realizations cross out and in the minimum at most 20% of the realizations cross out. The percentage of error in the mean value of the estimated beta is shown by (4) in the figure.

$$g(X_1, X_2) = X_1 X_2 - 1140 \tag{3}$$

$$e(\bar{\beta}) = \left(\frac{\bar{\beta}}{\beta} - 1\right) \times 100 \tag{4}$$

where $\bar{\beta} = \mathrm{E}[\hat{\beta}]$.

3. Sampling methods

Together with the mentioned methods, low-discrepancy sequences of random numbers might be used instead of a standard pseudo random number generator. These methods generate quasi-random numbers which are less random than a set of pseudo random numbers but are more uniformly distributed therefore have a lower discrepancy. There exist different methods of low-discrepancy random number generation such as Latin Hypercube Sampling (LHS) [16], Good Lattice Point (GLP) [17], Hua–Wang point set (H–W) [18], Sobol sequences [19] etc. In [14] the application of LHS and Sobol algorithm are also considered for various problems and is reported that use of Sobol quasi-random numbers increases efficiency of AS up to 2 times compared to the use of pseudo random numbers. A recent study on the application and performance of utilizing these sampling methods with the standard Monte Carlo and also importance sampling can be found in [20,21]. Although it is stated that using low-discrepancy random sequences increases efficiency of the estimation techniques for low dimensional problems, it is mentioned that high dimensionality poses problems on the accuracy of the estimations which needs further considerations.

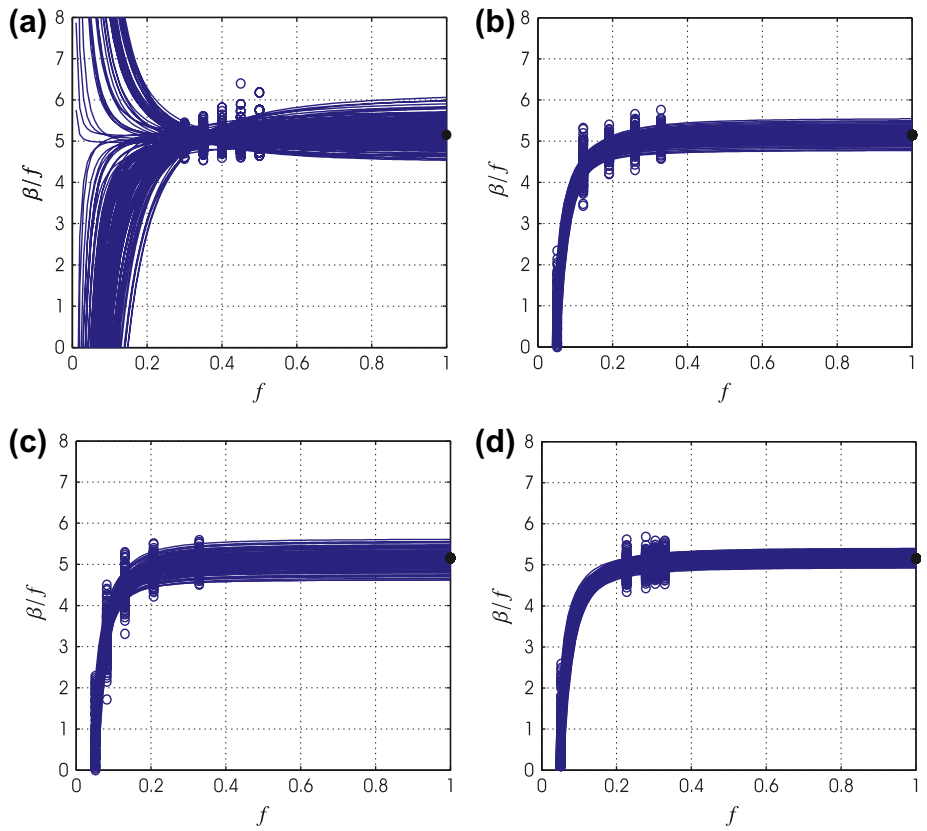

Fig. 1. 100 estimations of the reliability index with asymptotic sampling. (a) Uniformly distributed support points, $\mathrm{CoV}(P_f) = 1.7, \mathrm{e}(\bar{\beta}) = 1.72$. (b) Uniformly distributed support points, $\mathrm{CoV}(P_f) = 0.93, \mathrm{e}(\bar{\beta}) = 0.47$. (c) Exponentially distributed support points, $\mathrm{CoV}(P_f) = 1.25, \mathrm{e}(\bar{\beta}) = 0.52$. (d) Logarithmical distributed support points, $\mathrm{CoV}(P_f) = 0.56, \mathrm{e}(\bar{\beta}) = 0.14$.

4. Calibration of support points

It is seen (c.f. Fig. 1) that both location and distribution of the support points have considerable effect mainly on the precision of the method. So far, no method has been proposed to determine the range and the distribution of the support points in an optimal way. Therefore it is interesting to study the effect of these parameters on the performance of the method. Unfortunately the appropriate value of the scaling parameter f depends on the type of the problem i.e. the shape of its limit state function, the barrier level, etc. For example for high barrier levels elements of f should be distributed in a smaller range than the range for low barrier levels. Nevertheless the distribution of points seems to be quite problem independent. Based on these observations an optimization procedure is developed in this study which allows calibration of the support points' locations with rather low computation cost. Although this algorithm increases the computation cost of the method in the first step, this effort has justification due to the considerable beneficial effect it has on the accuracy and precision of the estimates. The significance of the optimization is that for different problems the suitable range in which support points should be distributed cannot be known in advance. Defining the support points' range as

$$\left.\begin{aligned} &\mathbf{f} \in [f_{min}, f_{max}] \\ &f_{min} = \{f \mid \sum_{i=1}^{N_{sim}} I(f, \Xi_i) = N_{oc}^{max}\} \\ &f_{max} = \{f \mid \sum_{i=1}^{N_{sim}} I(f, \Xi_i) = N_{oc}^{min}\} \end{aligned}\right\} \tag{5}$$

where $I(.)$ is the indicator function, i.e. $I(f,\Xi_i) = 1$ if $\{f,\Xi_i\} \in F$ and $I(f,\Xi_i) = 0$ else; where F indicates the failure domain and Ξ_i is the ith realization of the excitation process in the so-called U-space i.e. $\Xi \sim N(\mathbf{0},\mathbf{I})$ is Gaussian distributed random variables as defined in Sections 1 and 2. N_{oc}^{max} is the maximum outcrossing nomber of simulations expected to have when $f = f_{min}$. N_{oc}^{min} is the minimum outcrossing number expected to have when $f = f_{max}$. Simulations indicate that points close to f_{min} and f_{max} are both important and should be present in the support points if minimum Coefficient of Variation (CoV) of the estimated failure probability is desired. The maximum number of outcrossings obviously is limited by the number of simulations, but depending on the geometry of the actual limit state function it may be considerably smaller (e.g. $N_{oc}^{max} = N_{sim}/2$ for a linear limit state passing through the origin in U-space). In this study these parameters are set to $N_{oc}^{min} = 0.02N_{sim}$ and $N_{oc}^{max} = 0.98N_{sim}$; N_{sim} is the number of simulations for each support point.

4.1. Start point of the algorithm

Although in general the proposed optimization algorithm should be able to find the optimum values starting from any initial value, providing a good (close to optimum) initial point f_{init} increases efficiency of method by doing less iterations in the optimization loop. We start by discretizing the excitation process which is transformed to the U-space, $\mathbf{W}(k) = \mathbf{W}(t)|_{t=k\Delta t}$, and doing the same for the response process $\mathbf{X}(k) = \mathbf{X}(t)|_{t=k\Delta t}$ where $k = 0, \ldots, N-1$corresponds to the continuous time interval $t \in [0,T]$, i.e. $T = (N-1)\Delta t$. Assuming the following transformation from excitation to response

$$\mathbf{X}(k) = \mathbf{G}(\mathscr{W}(k)) \tag{6}$$

where $\mathscr{W}(k) = [\mathbf{W}(k), \ldots, \mathbf{W}(0)]$. Decomposing the transformation in (6) into its linear and nonlinear parts and substituting $\mathbf{W}(k) = f\widetilde{\mathbf{W}}(k)$ results in

$$\mathbf{X}(k) = \mathbf{X}_{Lin.}(k) + \mathbf{X}_{Nonlin.}(k) = f\mathbf{G}_{Lin.}(\widetilde{\mathscr{W}}(k)) + \mathbf{G}_{Nonlin.}(f\widetilde{\mathscr{W}}(k)) \tag{7}$$

where $\widetilde{\mathscr{W}}(k) = [\widetilde{\mathbf{W}}(k), \ldots, \widetilde{\mathbf{W}}(0)] = f^{-1}\mathscr{W}(k)$ is the scaled counterpart of $W(k)$ by f. The scaled response, $\widetilde{\mathbf{X}}(k) = \mathbf{G}(f\widetilde{\mathscr{W}}(k))$, can also be decomposed into

$$\widetilde{\mathbf{X}}(k) = \widetilde{\mathbf{X}}_{Lin.}(k) + \widetilde{\mathbf{X}}_{Nonlin.}(k) = \mathbf{G}_{Lin.}(\widetilde{\mathscr{W}}(k)) + \mathbf{G}_{Nonlin.}(\widetilde{\mathscr{W}}(k)) \tag{8}$$

(7) and (8) derive the following relation between normal and scaled responses

$$\widetilde{\mathbf{X}}(k) = \left(\frac{\mathbf{X}(k)}{f} + \mathbf{G}_{Nonlin.}(\widetilde{\mathscr{W}}(k)) - \frac{1}{f}\mathbf{G}_{Nonlin.}(f\widetilde{\mathscr{W}}(k))\right) \tag{9}$$

for the linear part of the transformation (9) the following applies

$$E[\widetilde{\mathbf{X}}_{Lin.}(k)] = \frac{1}{f}E[\mathbf{X}_{Lin.}(k)] \tag{10}$$

Eq. (10) means that for linear (part of) systems the factor f simply scales the response process. Therefore it is clear that the nth maximum of the stochastic response X sorted in descending order can be scaled up to the required barrier level where the scaling factor is defined as $f^{X_{BL}} = X^{(n)}_{max}/X_{BL}$. The schematic illustration of the effect of the f factor on the PDF of the response is shown in Fig. 2. This analysis provides a very simple yet efficient relationship for choosing the initial guess for f in the optimization algorithm as

$$\frac{1}{f^{X_{BL}}_{init}} \approx \frac{X_{BL}}{X^{(n)}_{max}(f=1)} \tag{11}$$

where X_{BL} is the required barrier level, $f^{X_{BL}}_{init}$ denotes the initial estimation for f_{min} for barrier level and $X^{(n)}_{max}(f=1)$ is the nth maximum of the stochastic response process $X(k)$, $k \in [0, N-1]$ to unscaled excitation, i.e. $f = 1$, sorted in descending order. The approximation used in (11) counts for the nonlinear part of the transformation which is not considered in the last parts of the derivation. n is the maximum outcrossing number therefore is equal to N^{max}_{oc} for estimating f_{min} and is equal to N^{min}_{oc} for estimating f_{max}. Eq. (11) generally provides a good approximation for nonlinear systems if accompanied by a Monte Carlo simulation with N_{sim} number of samples. In such case the PDF depicted in Fig. 2 represents the PDF of the maximas of the samples of the Monte Carlo simulation. Obviously N_{sim} for calibration of support points is not required to be equal to the number of simulations in asymptotic sampling i.e. in this study it is set to 100. In case of linear systems it is further possible to take advantage of the ergodicity of the response process and have a very efficient approximation of the above formula using only one realization of the response. In this sense $X^{(n)}_{max}(f=1)$ is the nth maximum of the time samples of a single realization of the response process sorted in descending order. Once the range of f is determined the parameters a, b and c of optimization, c.f. Fig. 4, can be calibrated adaptively to cover the required range in the least possible steps. Nevertheless these parameters do not change considerably therefore in this study for all examples they are set to $a = b = 1.5$ and $c = 0.5$. The values of f_{min} and f_{max} obtained using only one realization from (11) with ergodic sampling assumption, with 100 Monte Carlo simulations and their corresponding optimized values are mentioned in Table 1. The initial guess of Eq. (11) with ergodic sampling for the SDOF linear oscillator is very close to the optimum values and optimization does not seem to be necessary. On the other hand for nonlinear systems the difference between ergodic sampling's initial guess and the optimum values is considerable, therefore urging use of optimization. For convenience sorted maximum values of 500 samples of a standard Monte Carlo simulations are plotted together with the sorted absolute maximum values of one sample of dynamic analysis for the Duffing oscillator in Fig.9c. The figure indicates there is no considerable difference for the maximum values only in this case while for the other two cases the difference is considerable c.f. Table 1. In case of nonlinear systems it is beneficial to find the initial guess by performing some extra Monte Carlo simulations and then using the optimization to prevent unnecessary loops in the optimization algorithm.

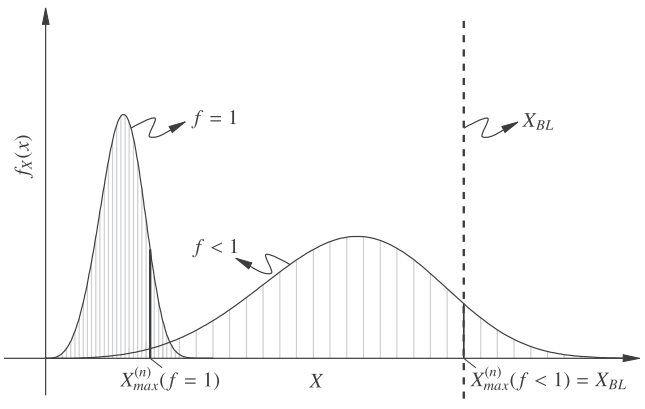

Fig. 2. The effect of f on scaling PDF of the (maximas of the) response.

4.2. Optimization algorithm

The optimization algorithm has two main stages. First to find the values of f_{min} at which maximum number of outcrossing from the barrier level takes place, e.g. N^{max}_{oc} and f_{max} at which minimum number of outcrossing from the barrier level, e.g. N^{min}_{oc} takes place. Second stage is to distribute the points as desired in the found range of $\mathbf{f} \in [f_{min}, f_{max}]$. The general perspective of the optimization algorithm is shown in Fig. 3 while the detailed procedure of each block of Fig. 3, indicated with block labels **A**-**G**, is represented in Fig. 4. Here we want to leave f_{min} as fast as possible and find more support points around f_{max}, however with some support points in between. The strategy is to start from a reasonably small "f" value, i.e. the initial guess of (11), and increase it until the number of outcrossed processes is close enough to the N^{max}_{oc}. Once the initial "f" value is found, next "f" value is approximated as $f(j) = f(j-1)^c$, c.f. Fig. 4, until we reach the N^{min}_{oc}. This type of function especially with $c \in (0,1]$ is favorable in our context since it leaves f_{min} very quickly and becomes more careful in increasing "f" values as the values approach f_{max}. Defining j as the counter of the loop for "f" values, N_f as the total number of elements of the vector $\mathbf{f}$ and N_{oc} as the number of outcrossed processes from the barrier level. Initially $\mathbf{f}$ is set to zeros, e.g. $\mathbf{f} = [0, \ldots, 0]_{1\times N_f}$.

f_{min} is defined as any value for "f" which results in $0.9N_{sim} < N_{oc} \leqslant N^{max}_{oc}$. If the initial candidate of the f_{min} causes too many outcrossing, e.g. $N_{oc} > N^{max}_{oc}$, we increase f_{min} by setting $f(j) = f(j)^c$ and then $f_{min} = f(j)$. This loop will continue until we find an "f" value which satisfies $0.9N_{sim} < N_{oc} \leqslant N^{max}_{oc}$. In case the candidate value does not satisfy $N_{oc} > 0.9N_{sim}$ the algorithm will decrease the candidate "f" according to $f(j) = \frac{1}{2}f(j)(1 + f(j)^a)$ and checks if the change made in the value is more than 50% of the initial guess, $f_{init.}$, far from it. This check is to avoid getting too close to the initial guess which decreases the convergence speed of the algorithm. If not too close, we choose this value as f_{min}, else we choose $f_{min} = \frac{3}{2}f(j)$ and do the checks to see if N_{oc} is in the expected range. This procedure is repeated until f_{min} is found accurately.

In the next step the middle points will be estimated. Since it is not known in advance when we are going to hit f_{max}- defined as any "f" value with the condition $N^{min}_{oc} \leqslant N_{oc} < 0.2N_{sim}$, care must be taken into account. If for the candidate "f" value $N_{oc} < N^{min}_{oc}$, which indicates that we are in the region close to f_{max}, we increase the number of out-crossings by decreasing "f" as $f(N_f) = f(j)^b$ and set $f_{max} = f(N_f)$. Next we take the average of $f(j-1)$ and $f(N_f)$as $f(j)$. If

Table 1
Values of f_{min} and f_{max} using (11) and the final values by optimization.

Case	Barrier level		f_{min}	f_{max}
SDOF oscillator	25	1 sample	0.392	0.676
		100 samples	0.393	0.767
		Optimum value	0.400	0.709
Duffing oscillator	0.55	1 sample	0.335	0.695
		100 samples	0.289	0.727
		Optimum value	0.210	0.557
Bouc-Wen oscillator	0.64	1 sample	0.017	0.215
		100 samples	0.164	0.603
		Optimum value	0.277	0.618
Linear MDOF oscillator	0.0115 (subcase.4)	1 sample	0.179	0.300
		100 samples	0.258	0.702
		Optimum value	0.277	0.618
Nonlinear MDOF oscillator	0.028 (subcase.4)	1 sample	0.098	0.220
		100 samples	0.113	0.465
		Optimum value	0.186	0.678

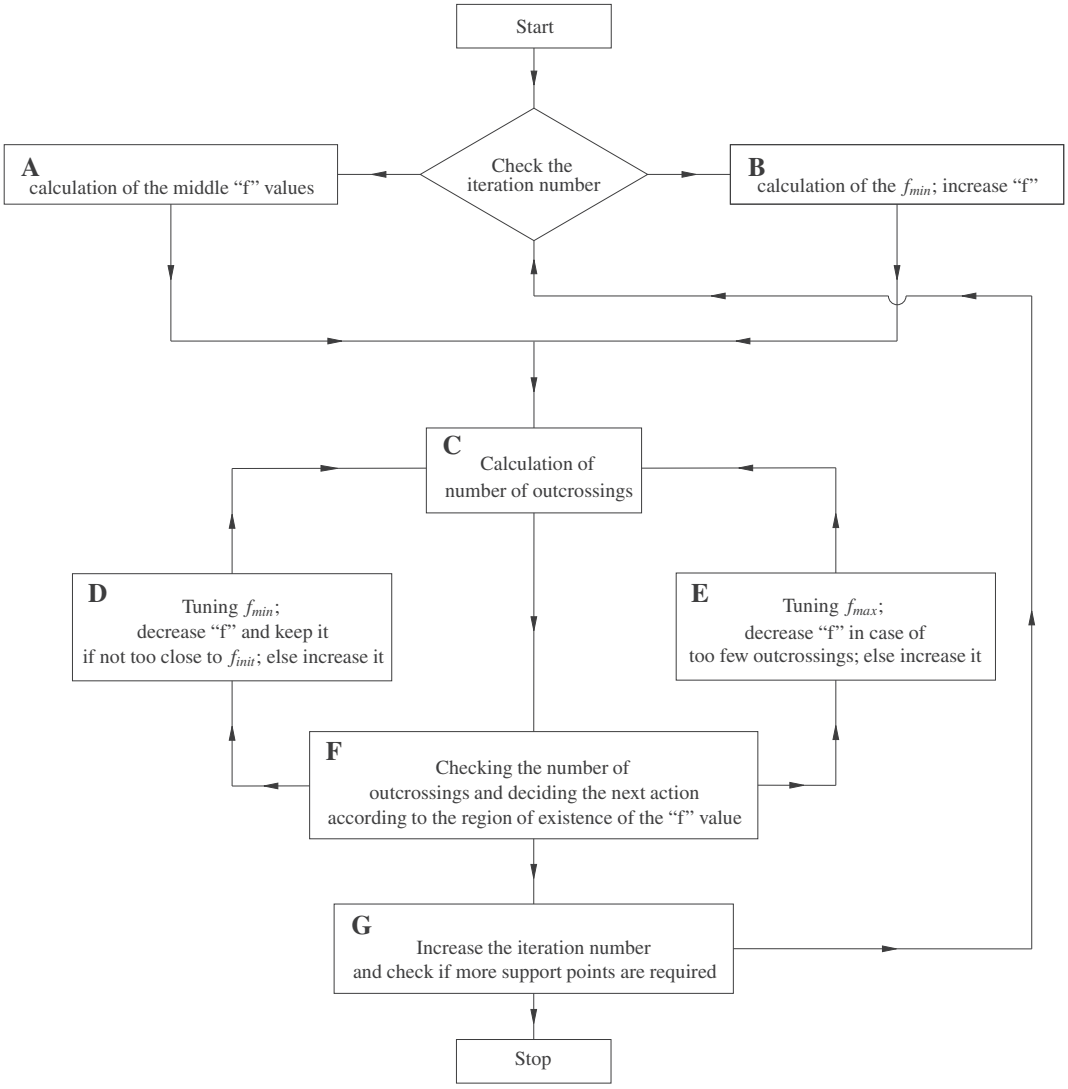

Fig. 3. The general view of the optimization scheme for calibration of support points' locations.

for the candidate "f" value $N_{oc} \geqslant N_{oc}^{min}$ one of the following may occur

$f(N_f) \neq 0$ and $N_{oc} \geqslant 0.2N_{sim}$ Which indicates that a good approximation for f_{max} has been found in previous steps and is placed at $f(N_f)$. It is advantageous to improve our estimate for the current candidate of "f" in order to get $N_{oc} < 0.2N_{sim}$. Here we increase "f" by setting $f(N_f) = f(j)^c$ – as a last chance to obtain a higher value for f_{max} – and take average of this value with $f(j-1)$. The average is taken in favor of the fact that in this

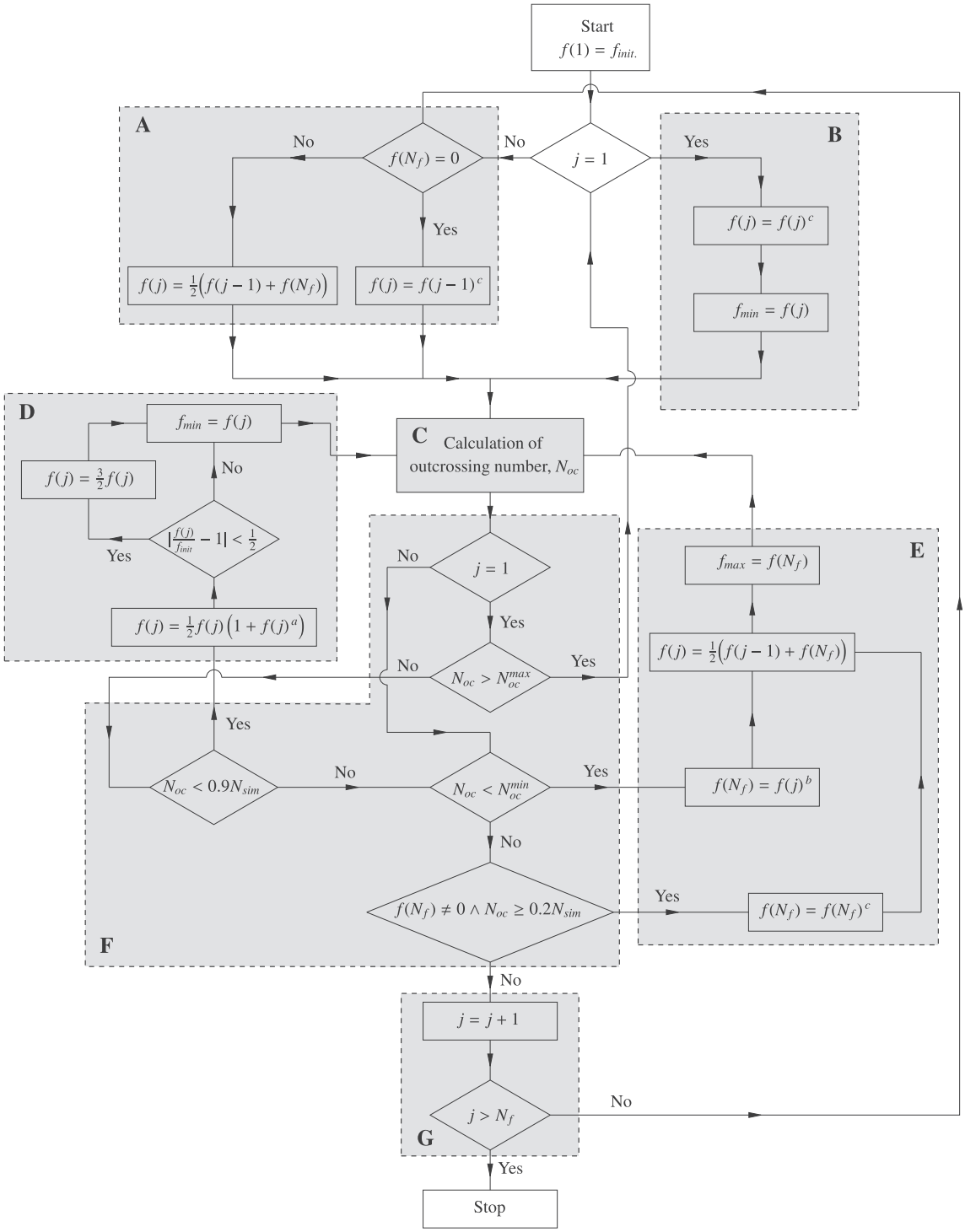

Fig. 4. The details of the optimization scheme for calibration of support points' locations. The block labels **A**–**G** refer to Fig. 3.

region we do not want to risk more simulation without new information in them i.e. simulation with too few out-crossings. $f(N_f) = 0$ or $N_{oc} < 0.2N_{sim}$ This means that a good candidate for f_{max} is not available or the candidate "f" value is already in the region close to f_{max}. Therefore we increase the candidate "f" value by $f(j) = f(j-1)^c$ and go to the next step

In practice the proposed algorithm is very general and typically only some of its blocks are used within a simulation. The simulations show that it is fast and robust in finding the support points' range $[f_{min}, f_{max}]$ and distributing them within this range. It worth mentioning here that it is desired that the algorithm satisfies $N_{oc} < N_{oc}^{min}$ at least once during simulation. This ensures that the region in which f_{max} exists has been found with good accuracy. It is seen that the proposed algorithm is successful in fulfilling this criterion in the numerical simulations.

4.3. Bias

Although obviously the asymptotic sampling method yields asymptotically unbiased results as the sample size approaches infinity (since in this case asymptotic sampling reduces to crude

Monte Carlo), there may be some bias at small sample sizes. This is inherently related to the location of support points as defined by the numerical values for the factor f discussed in the previous section. As mentioned in [14], the cases in which the failure domain form a closed region (i.e. an "island") are rather unsuitable for the application of asymptotic sampling as the general prerequisites of the asymptotics as described by Breitung [13] are not satisfied. In order to investigate the potential bias introduced by asymptotic sampling in such a case, consider a simple two-dimensional problem with an elliptical failure domain in standard Gaussian space as shown in Fig. 5. The failure domain is characterized by the lengths of the principal axes α and γ of the ellipse and by the distance β from the origin. This distance is equal to the reliability index as obtainable from the First Order Reliability Method (FORM). By adjusting the numerical values of α and γ, the failure domain can be made to approach various shapes from a hyperplane to an isolated point. Due to the rotational symmetry of the probability density function in standard Gaussian space it is sufficient to consider a special orientation of the failure domain such that the design point $\mathbf{u}^*$ lies on the u_2-axis as shown in Fig. 5. For a numerical study, the values $\beta = 4$ and $\gamma = 2$ are fixed and the value of α is varied from 0.2 to 5. Also, the magnitude of the factor f for support points is varied by choosing the intervals [0.3,0.6], [0.5,0.8], and [0.6,0.9], respectively. The results from asymptotic sampling are shown in Fig. 6 along with reference solutions from crude Monte Carlo (100 million samples). Fig. 6 shows that for the cases in which α is rather small (i.e. the island is small) there is a bias such that the probability of failure is overestimated. This bias is reduced as α increases. Also, the bias becomes significantly smaller if the support points for the extrapolation have f-factors closer to 1 (as is to be expected). It should be mentioned that similar behavior (in terms of the bias) can be expected from other standard reliability methods such as directional sampling [22] since in this method usually only the first intersection between the direction vector and the limit state surface is searched for, thus neglecting possible returns to the safe domain farther out along this direction. It should be noted that more complex situations are possible in the case of high-dimensional problems, but it may be anticipated that the reason for a possible bias still lies in such "islands" (or "bubbles") of failure.

5. Numerical case study

In the numerical case studies for all cases the failure probabilities are estimated 10 times with asymptotic sampling and their mean value is considered as the final failure probability; the related coefficient of variation of the estimates are represented in Table 2. The optimization parameters, c.f. Fig. 4, are set to $a = b = 1.5$ and $c = 0.5$ in all cases.

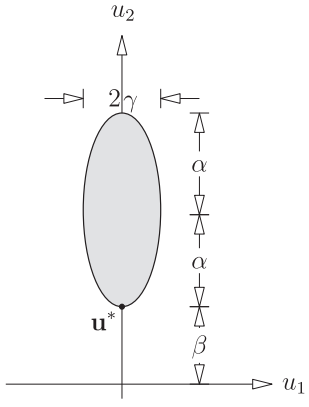

Fig. 5. Elliptical failure domain in standard Gaussian space.

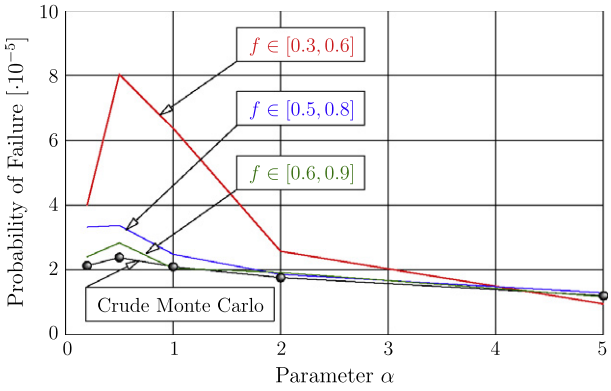

Fig. 6. Results from asymptotic sampling with elliptical failure domain.

5.1. Single DOF oscillator

The first simulation is based on a single DOF linear oscillator (12), characterized by $\omega_n = 1\ \mathrm{s}^{-1}$ and $\zeta_n = 0.01$

$$\ddot{x}(t) + 2\zeta_n\omega_n\dot{x}(t) + \omega_n^2 x(t) = w(t) \tag{12}$$

$w(t)$ is zero-mean Gaussian white noise with unit intensity. The barrier level is normalized with respect to the standard deviation of the response $\sigma_X = (4\zeta\omega^3)^{-1/2}$.

$$b_N = \frac{b}{\sigma_X} \tag{13}$$

The normalized barrier level is assumed to be $b_N = 5$ in simulations. Simulations are carried out with $\Delta t = 0.0614$ s and $t \in [0,600]$ s which involves 9772 samples to examine the performance of the method in high dimensions. For each barrier level 500 time series are simulated and five support points are chosen for curve fitting with different Δf and range of f. Fig. 7 illustrates the effect of distribution of support points. Clearly very small f values will cause all of the processes to cross out which does not give any information while choosing very large f values will cause few out crossings which increases the uncertainty of the estimation. To check the accuracy of the above statement, various Monte Carlo simulations are performed with different distributions of the support points. Results of this analysis are shown in Fig. 7. Exact failure probability and reliability index for the problem, calculated with standard Monte Carlo simulation with 2×10^6 samples, are $P_f = 2.07 \times 10^{-4}$ and $\beta = 3.5310$ respectively. The black dots on the right hand side of the figures show the exact value of the beta. It is seen that the maximum accuracy of the method, i.e. the least standard deviation of the estimate, is achieved in case support points are distributed in the region where 2–98% of the realizations crosses out c.f. Fig. 7d compared to Fig. 7a in which 2–50% of the realizations have crossed out. This interval can be found using any simple search algorithm or the proposed optimization algorithm. The simulations witness that coefficient of variation (CoV) of the failure probability estimation based on the estimated β is decreases by a factor of 6 if support points are chosen in the optimal way. Fig. 8 shows estimations of the failure probability for the same barrier level in different time instants. Fig. 8a shows results of estimation with a uniform distribution of support points and Fig. 8b shows the results with optimally distributed support points. Solid line in both figures shows the results of the standard Monte Carlo simulation. The results witness that optimally distributed support points have clearly higher precision at all instants of time.

Table 2
Estimated failure probabilities.

Simulation case	Barrier Level	Samples	P_f^{MCS}	P_f^{AS}	CoV^{AS}
Duffing oscillator	0.40	500	1.12×10^{-2}	1.13×10^{-2}	0.22
	0.45	500	1.00×10^{-3}	1.15×10^{-3}	0.37
	0.50	500	3.50×10^{-5}	4.96×10^{-5}	0.47
	0.55	500		1.47×10^{-6}	0.49
	0.60	500		1.24×10^{-8}	0.63
Bouc-Wen oscillator	0.4	500	5.28×10^{-3}	5.55×10^{-3}	0.14
	0.5	500	4.70×10^{-4}	4.90×10^{-4}	0.35
	0.6	500	4.20×10^{-5}	5.35×10^{-5}	0.39
	0.7	500		3.78×10^{-6}	0.52
	0.8	500		3.40×10^{-7}	0.66
Linear MDOF oscillator	0.0515	500	1.05×10^{-4}	1.78×10^{-4}	0.31
	0.0560	500	1.62×10^{-5}	2.80×10^{-5}	0.61
	0.0100	500	3.14×10^{-4}	3.15×10^{-4}	0.15
	0.0115	500	1.43×10^{-5}	1.59×10^{-5}	0.34
Nonlinear MDOF oscillator	0.047	500	1.46×10^{-4}	3.30×10^{-4}	0.32
		1000		2.97×10^{-4}	0.28
		5000		1.51×10^{-4}	0.17
	0.052	500	5.41×10^{-6}	1.54×10^{-5}	0.36
		1000		2.32×10^{-5}	0.28
		5000		2.31×10^{-5}	0.14
	0.024	500	4.63×10^{-5}	7.89×10^{-5}	0.39
		1000		7.41×10^{-5}	0.27
		5000		8.39×10^{-5}	0.18
	0.028	500	3.94×10^{-6}	1.35×10^{-5}	0.98
		1000		9.40×10^{-6}	0.42
		5000		9.51×10^{-6}	0.17

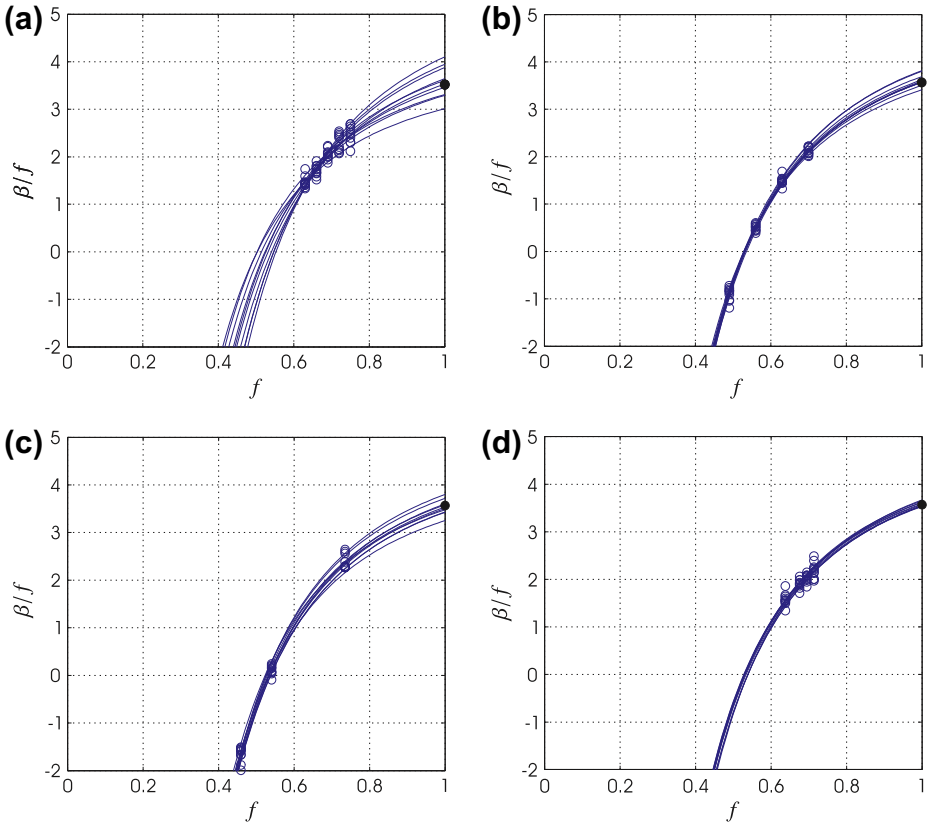

Fig. 7. Ten estimations of the reliability index β with asymptotic sampling for 600[s] for the single DOF oscillator using 500 simulations and five support points. (a) $f_{max} = 0.75$, $\Delta f = 0.03$, $CoV(P_f(600))=1.2$. (b) $f_{max} = 0.7$, $\Delta f = 0.07$, $CoV(P_f(600)) = 0.4$. (c) Exponentially distributed optimized support points, $CoV(P_f(600)) = 0.6$. (d) Logarithmical distributed optimized support points, $CoV(P_f(600)) = 0.2$.

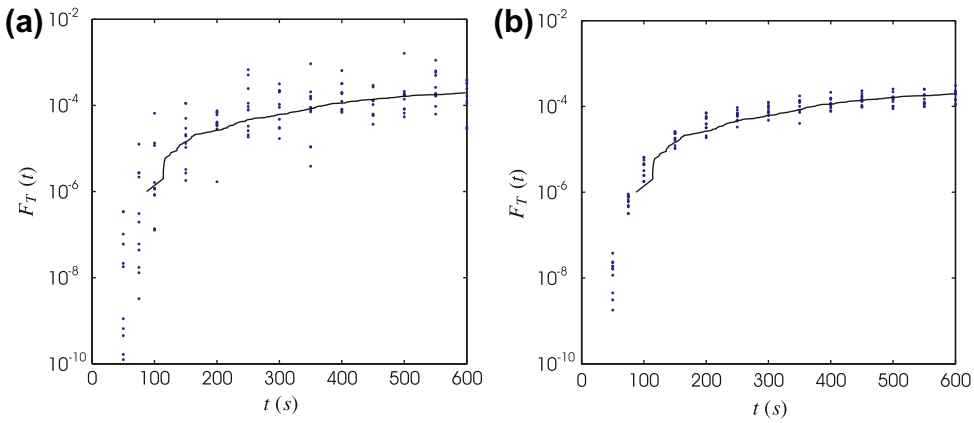

Fig. 8. Estimations of the failure probability $F_t(t)$ with Monte Carlo (solid line, 10^6 samples) and asymptotic sampling (dots, 500 samples). (a) Standard asymptotic sampling, CoV(P_f(600)) = 1.2. (b) Optimized support points, CoV(P_f(600)) = 0.35.

5.2. Nonlinear Duffing oscillator

Despite being a simple case of a nonlinear system, Duffing oscillator is interesting due to its wide range of applications. The parameters of the oscillator are chosen as $\bar{\omega}_n = 10\ \mathrm{s}^{-1}$ and $\zeta_n = 0.01$ and ϵ parameter which controls the intensity of the nonlinearity in the model is chosen $\epsilon = 10$. The equation of motion of the oscillator is written as

$$\ddot{x}(t) + 2\zeta_n\omega_n\dot{x}(t) + \omega_n^2(x(t))x(t) = w(t) \tag{14}$$

where

$$\omega_n^2(x(t)) = \bar{\omega}_n^2(1 + \epsilon x^2(t)) \tag{15}$$

where $w(t)$is the unit intensity Gaussian white noise i.e. $E[w(t)w(t+\tau)] = \delta(\tau)$. The failure probability is to be estimated within the time $t \in [0,15]$ s with $\Delta t = 0.01$ s for different barrier levels as mentioned in Table 2. 500 samples are used to calculate the failure probability with asymptotic sampling. Fig. 9a shows the results of 10^6 Monte Carlo simulation versus asymptotic sampling using 500 samples. Fig. 9b shows histogram of the sample generation of the asymptotic sampling with 10^4 samples. Fig. 9c indicates sorted maximum values of 500 samples of the Monte Carlo for this oscillator versus the first 500 time samples of just one dynamic sim-

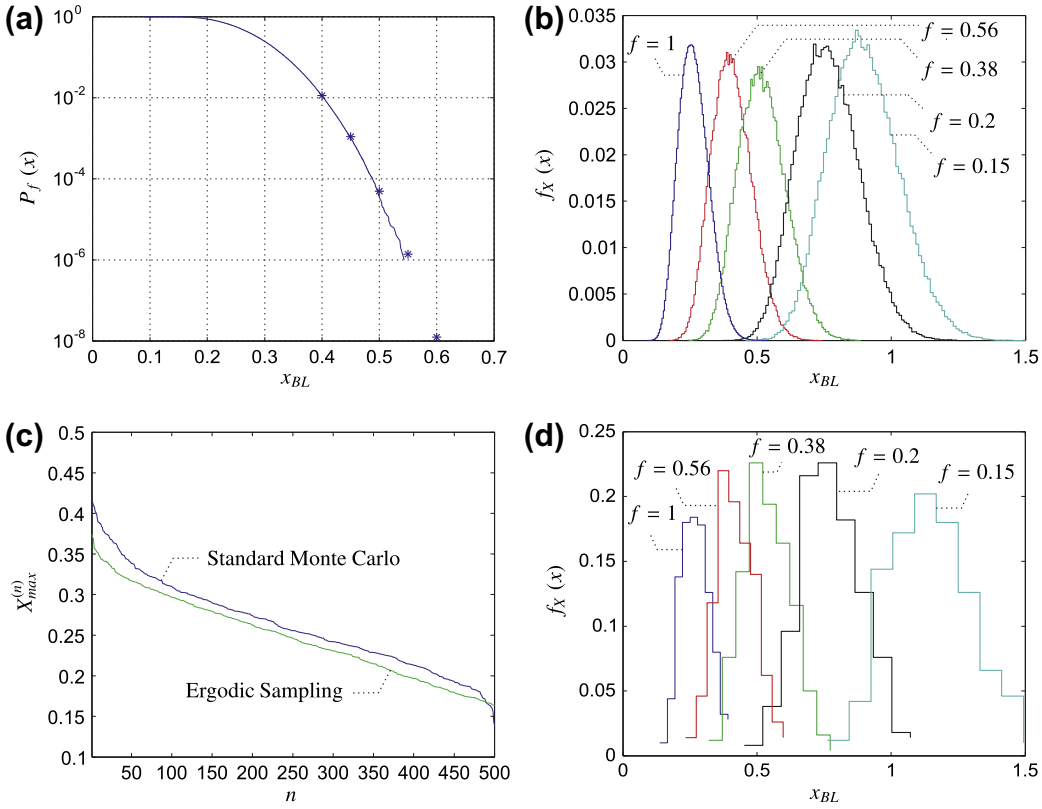

Fig. 9. Asymptotic sampling for Duffing oscillator, $t \in [0,15]$ s, $\Delta t = 0.01$ s, $\epsilon = 10$. (a) Estimation of failure probability by Monte Carlo (solid line, 10^6 samples) and Asymptotic sampling (asterisks, 500 samples). (b) Histograms of asymptotic sampling with 10^4 samples. (c) Sorted maximum values of the absolute response of the system; blue: Monte Carlo with 500 samples, green: Ergodic sampling with one sample. (d) Histograms of asymptotic sampling with 500 samples. (For interpretation of the references to colour in this figure legend, the reader is referred to the web version of this article.)

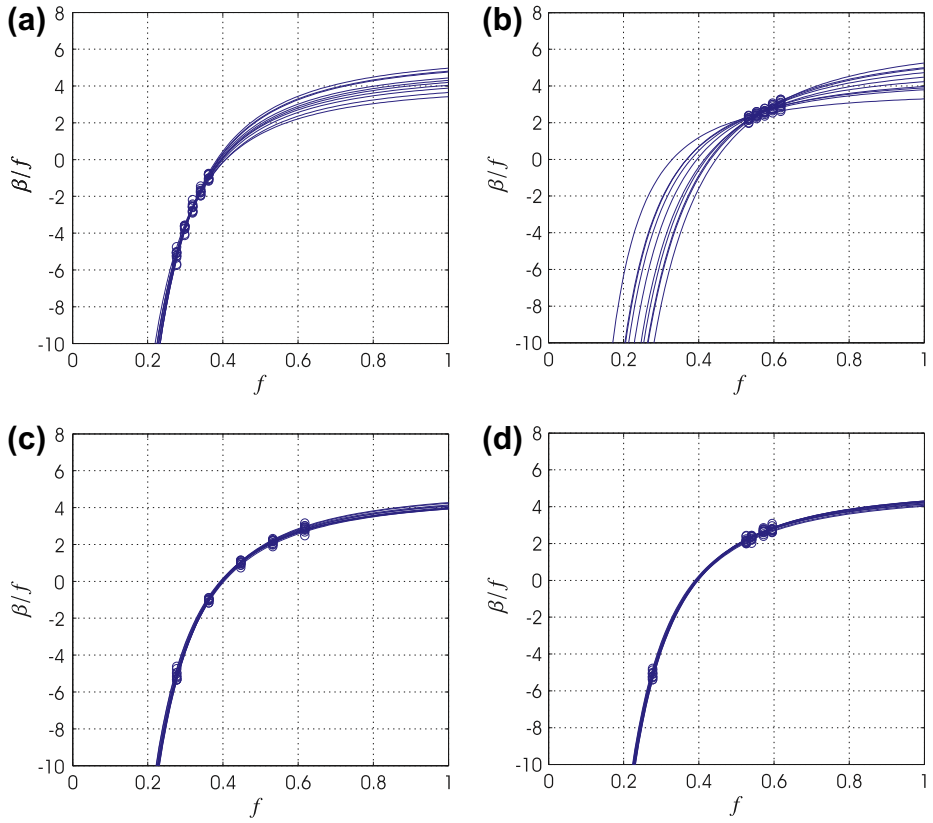

Fig. 10. Ten estimations of the reliability index β with asymptotic sampling for 20[s] for the Bouc-Wen oscillator using 500 simulations and five support points. (a) $f_{max} = 0.36$, $\Delta f = 0.02$, $\overline{P}_f = 5.52 \times 10^{-5}$, CoV($P_f(20)$) = 1.79. (b) $f_{max} = 0.618, \Delta f = 0.02, \overline{P}_f = 6.65 \times 10^{-5}$, CoV($P_f(20)$) = 2.27. (c) Exponentially distributed optimized support points, $\overline{P}_f = 2.74 \times 10^{-5}$, CoV($P_f(20)$) = 0.47. (d) Logarithmical distributed optimized support points, $\overline{P}_f = 1.44 \times 10^{-5}$, CoV($P_f(20)$) = 0.46.

ulation of the oscillator which is used for estimating the initial guess for the optimization algorithm using ergodic sampling assumption i.e. the linear part of the oscillator. Fig. 9d shows a histogram of the sample generation of the asymptotic sampling with 500 samples. Comparison of Fig. 5b and d show that the sampling density of the asymptotic sampling is not severely affected by changing the sample sizes. These simulations are also performed to illustrate the mechanism in which asymptotic sampling moves the PDF of the simulation.

5.3. Nonlinear Bouc-Wen oscillator exposed to non-stationary excitation

The Bouc-Wen oscillator is chosen as the next single DOF nonlinear case. This model simulates a single storey shear frame applied to non-stationary earthquake excitation which is modeled as a Kanai-Tajimi filtered modulated white noise. The systems equations of motion are written as

$$\begin{aligned} &m\ddot{x} + c\dot{x} + (1-\alpha)kz + \alpha kx = -ma(t) \\ &\dot{z} = A\dot{x} - \beta\dot{x}|z| - \gamma|\dot{x}|z \end{aligned} \tag{16}$$

where $a(t)$ is the ground acceleration given by

$$\begin{aligned} &\ddot{y} + 2\zeta\omega\dot{y} + \omega^2 y = e(t)w(t) \\ &a(t) = -(2\zeta\omega\dot{y} + \omega^2 y) \end{aligned} \tag{17}$$

where $e(t)$ is the envelop process modeled as

$$e(t) = 4(\exp(-0.25t) - \exp(-0.5t)) \tag{18}$$

$w(t)$ is Gaussian white noise process $E[w(t+\tau)w(t)] = Ie^2(t)\delta(\tau)$ where $I = 0.64\ \mathrm{m}^2/\mathrm{s}^4$ is the intensity of the white noise. Parameters of the model are chosen as the ones used in [3] i.e. $m = 40 \times 10^3$ kg, $k = 1 \times 10^6$ N/m, $c = 5 \times 10^3$ Ns/m, $\alpha = 0.603$, $\beta = -1.8548$, $\gamma = 39.36$, $A = 5.868$. The failure probability estimated using Monte Carlo simulation for barrier level $X_{BL} = 0.64$ within $t \in [0,20]$ s with 6×10^5 samples is $p_f = 1.3 \times 10^{-5}$. Fig. 10 shows estimations of $\beta(1)$ for different distributions of support points with 500 samples for this oscillator. Fig. 11a and b show the results of the AS compared to the standard Monte Carlo estimates and the histogram of the samples of the asymptotic sampling with 500 samples, respectively. The results indicate that the least coefficient of variation for estimated failure probability is obtained by the logarithmic distribution of support points, e.g. Fig. 10d, like the linear case and that the estimations of the model are in very good agreement with the standard Monte Carlo simulation.

5.4. Linear MDOF oscillator

The linear MDOF oscillator is simulated as a special case of the next example where $\epsilon = 0$. Standard Monte Carlo simulation is performed on this case with 1.05×10^6 samples and the results are compared with estimations of the asymptotic sampling.

5.5. Nonlinear MDOF oscillator

The Duffing type MDOF oscillator of the Benchmark problem according to [8] is adopted to investigate the performance of the asymptotic sampling on a common problem. The system consists of a 10DOF shear frame subject to the earthquake load. The earthquake excitation is simulated as a filtered modulated white noise as

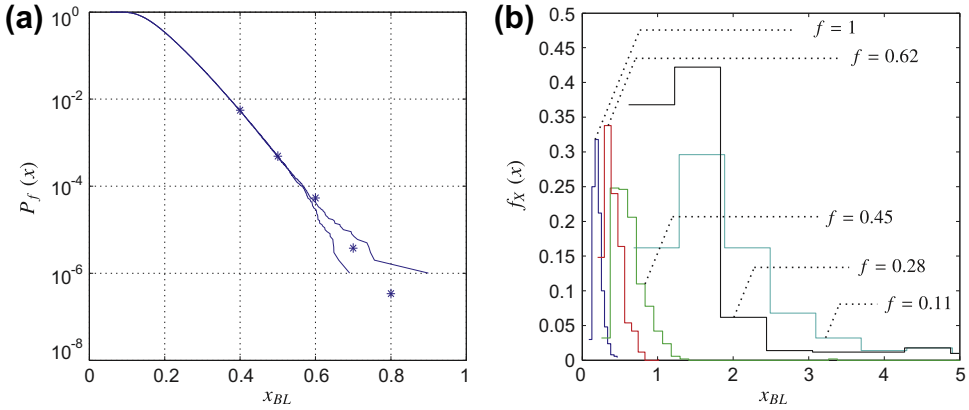

Fig. 11. Asymptotic sampling for Bouc-Wen oscillator, $t \in [0,20]$ s, $\Delta t = 0.02$ s. (a) Estimation of failure probability by Monte Carlo (solid lines, 10^6 samples each) and Asymptotic sampling (asterisks, 500 samples). (b) Histograms of asymptotic sampling with 500 samples.

$$\begin{aligned}\dot{\mathbf{X}}(t) &= \mathbf{A}_{EQ}\mathbf{X}(t) + \mathbf{B}_{EQ}w(t)\\ p(t) &= \mathbf{C}_{EQ}\mathbf{X}(t) + \mathbf{D}_{EQ}w(t)\end{aligned} \tag{19}$$

where

$$\mathbf{A}_{EQ} = \begin{bmatrix} 0 & 1 & 0 & 0 \\ -\Omega_{1g}^2 & -2\zeta_{1g}\Omega_{1g} & 0 & 0 \\ 0 & 0 & 0 & 1 \\ \Omega_{1g}^2 & 2\zeta_{1g}\Omega_{1g} & -\Omega_{2g}^2 & -2\zeta_{2g}\Omega_{2g} \end{bmatrix}, \quad \mathbf{B}_{EQ} = \begin{bmatrix} 0 \\ 1 \\ 0 \\ 0 \end{bmatrix} \tag{20}$$

$$\mathbf{C}_{EQ} = \begin{bmatrix} \Omega_{1g}^2 & 2\zeta_{1g}\Omega_{1g} & -\Omega_{2g}^2 & -2\zeta_{2g}\Omega_{2g} \end{bmatrix}, \quad \mathbf{D}_{EQ} = [0] \tag{21}$$

where $w(t)$ is the white noise i.e. $E[w(t)w(t+\tau)] = I\delta(\tau)$ with intensity $I = 0.08$ m^2/s^3 modulated by the function

$$h(t) = \begin{cases} t/2, & 0s \leqslant t \leqslant 2s \\ 1, & 2s \leqslant t \leqslant 10s \\ \exp(-0.1(t-10)), & t \geqslant 10s \end{cases} \tag{22}$$

where $\Omega_{1g} = 15$ rad/s, $\omega_{2g} = 0.3$ rad/s, $\zeta_{1g} = 0.8$and $\zeta_{2g} = 0.995$. The equations of motion for the system are

$$\mathbf{M}\ddot{\mathbf{u}}(t) + \mathbf{C}\dot{\mathbf{u}}(t) + \mathbf{K}(\mathbf{u}(t))\mathbf{u}(t) = \mathbf{F}(t) \tag{23}$$

$$\mathbf{M} = \begin{bmatrix} m_1 & 0 & 0 & \dots & 0 \\ 0 & m_2 & 0 & \dots & 0 \\ 0 & 0 & 0 & \dots & 0 \\ \vdots & \vdots & \ddots & \vdots & 0 \\ 0 & 0 & 0 & 0 & m_{10} \end{bmatrix}, \quad \mathbf{C} = \begin{bmatrix} c_1+c_2 & -c_2 & 0 & \dots & 0 \\ -c_2 & c_2+c_3 & -c_3 & \dots & 0 \\ 0 & -c_3 & c_3+c_4 & \dots & 0 \\ \vdots & \vdots & \ddots & \vdots & 0 \\ 0 & 0 & 0 & -c_{10} & c_{10} \end{bmatrix} \tag{24}$$

$$\mathbf{K} = \begin{bmatrix} \bar{k}_1+\bar{k}_2 & -\bar{k}_2 & 0 & \dots & 0 \\ -\bar{k}_2 & \bar{k}_2+\bar{k}_3 & -\bar{k}_3 & \dots & 0 \\ 0 & -\bar{k}_3 & \bar{k}_3+\bar{k}_4 & \dots & 0 \\ \vdots & \vdots & \ddots & \vdots & 0 \\ 0 & 0 & 0 & -\bar{k}_{10} & \bar{k}_{10} \end{bmatrix}, \quad \mathbf{1} = \begin{Bmatrix} 1 \\ 1 \\ \vdots \\ 1 \\ 1 \end{Bmatrix}_{10\times 1} \tag{25}$$

and

$$\bar{k}_i = k_i\left(1 + \epsilon\left(\frac{u_i(t) - u_{i-1}(t)}{\delta u_{ref}}\right)^2\right), \quad \text{for } i = 1,\dots,10 \tag{26}$$

where $\mathbf{F}(t) = -\mathbf{M}\{\mathbf{1}\}p(t)$, $\delta u_{ref} = 0.02$ m and $\epsilon = 0.1$. System parameters are assumed to be

$$\begin{aligned} m_1 = \dots = m_{10} &= 10\times 10^3 \text{ kg}, \quad k_1 = k_2 = k_3 = 40\times 10^6 \text{ N/m}, \quad k_4 \\ &= k_5 = k_6 = 36\times 10^6 \text{ N/m}, \quad k_7 = k_8 = k_9 = k_{10} \\ &= 32\times 10^6 \text{ N/m}, \quad c_i = 2\zeta_i\sqrt{m_i k_i} \end{aligned}$$

and $\zeta_i = 0.04$ for $i = 1, \dots, 10$. The results of failure probability estimation for different cases of barrier levels with asymptotic sampling with various number of samples are shown in Table 2. The time interval of the simulations in all subcases is $t \in [0,20]$ s with the resolution $\Delta t = 0.005$ s. In the first two subcases the failure event is defined as the displacement of the first storey exceeds 0.047 m and 0.052 m while the next two subcases are defined as when the relative displacement of the tenth storey exceeds 0.024 m and 0.028 m within the mentioned time interval. Results of the standard Monte Carlo simulations are as reported in [8]. The results show that asymptotic sampling overestimates the failure probability in this case. In order to study the reason for this overestimation, the number of samples is increased to 1000 and 5000. In all cases the method consistently over estimates the failure probability which indicates that there exist some bias on the estimations of the method.

6. Conclusions

The paper provides some practical guidelines for the application of the asymptotic sampling method to problems in structural dynamics involving a large number of random variables. This method is based on Monte Carlo simulation with artificially increased standard deviations of the basic random variables in standard Gaussian space and some asymptotic properties of the failure probability. Hence the application is basically straightforward. This study aimed at an optimal choice for the increased standard deviations with particular focus on the efficiency and accuracy of the method. For this purpose, a simple and effective optimization strategy was developed and implemented.

The numerical examples show that the asymptotic sampling method can handle complex stochastic dynamics problems reasonably well. As shown in this study, the choice of appropriate support points for the extrapolation of the safety index or failure probability has a significant effect on the estimation uncertainty. This pertains to both bias and sampling error. The method is not negatively affected by the dimensionality of the problem, i.e. several thousands of random variables do not pose any difficulties. The cases of nonlinear SDOF oscillators (Duffing, Bouc-Wen) show that accurate results down to probability levels of 10^{-8} can be achieved with less than 3000 simulations.

The case of a Duffing-type MDOF system indicates a bias in the estimated failure probabilities. This bias can be explained by isolated regions of failure in the space of random variables. A respective simple example shows that this bias can be removed by shifting the factors of support points for the probability extrapolation closer to unity. This step, however requires increased numerical effort since then the probabilities for the interpolation become smaller and more simulations are needed for reliable estimates.

It may be summarized that asymptotic sampling treats some well-known problems in structural dynamics reasonably well. While the method is certainly not most efficient and/or most accurate in all cases, it appears that due to its simplicity the method may be considered a very versatile tool for reasonably accurate estimation of failure probabilities, in particular for very high-dimensional problems.

Further studies will focus on the application of the concepts as developed here to practical cases such as the potential failure of wind turbines under the dynamic action of a turbulent and spatially correlated stochastic wind field.

Acknowledgement

The Danish Energy Authority is acknowledged for support under the Grant EFP07-II, Estimation of Extreme Responses and Failure Probability of Wind Turbines under Normal Operation by Controlled Monte Carlo Simulation.

References

[1] Macke M, Bucher C. Importance sampling for randomly excited dynamical systems. J Sound Vib 2003;268:269–90.
[2] Au SK, Beck JL. First excursion probabilities for linear systems by very efficient importance sampling. Probab Eng Mech 2001;16:193–207.
[3] Bucher C. Computational analysis of randomness in structural mechanics. 1 ed. CRC Press; 2009.
[4] Au SK, Beck JL. Estimation of small failure probability in high dimensions by subset simulation. Probab Eng Mech 2001;16:263–77.
[5] Ching J, Beck JL, Au SK. Hybrid subset simulation method for reliability estimation of dynamical systems subject to stochastic excitation. Probab Eng Mech 2005;20:199–214.
[6] Ching J, Au SK, Beck JL. Reliability estimation for dynamical systems subject to stochastic excitation using subset simulation with splitting. Comput Methods Appl Mech Eng. 2005;194:1557–79.
[7] Katafygiotis LS, Cheung SH. Application of spherical subset simulation method and auxiliary domain method on a benchmark reliability study. Struct Safety 2007;29:194–207.
[8] Schuëller GI, Pradlwarter HJ. Benchmark study on reliability estimation in higher dimensions of structural systems: an overview. Struct Safety 2007;29:167–82.
[9] Valdebenito MA, Pradlwarter HJ, Schuëller GI. The role of the design point for calculating failure probabilities in view of dimensionality and structural nonlinearities. Struct Safety 2010;32:101–11.
[10] Au SK, Beck JL. Important sampling in high dimensions. Struct Safety 2003;25:139–63.
[11] Au SK, Lam HF, Ng CT. Reliability analysis of single-degree-of-freedom elastoplastic systems. I: critical excitations. J Eng Mech 2007;133(10):1072–80.
[12] Katafygiotis LS, Zuev KM. Geometric insight into the challenges of solving high-dimensional reliability problems. Probab Eng Mech 2008;23:208218.
[13] Breitung KW. Asympotic approximations for multinormal integrals. J Eng Mech 1984;110(3):357366.
[14] Bucher C. Asymptotic sampling for high-dimensional reliability analysis. Probab Eng Mech 2009;24:504–10.
[15] Shinozuka M. Basic analysis of structural safety. J Struct Eng 1983;109(3):721–40.
[16] Olsson A, Sandberg G, Dahlblom O. On Latin hypercube sampling for structural reliability analysis. Struct Safety 2003;25(1):47–68.
[17] Fang KT, Wang Y. Number-theoretic methods in statistics. London: Chapman & Hall; 1994.
[18] Hua LK, Wang Y. Applications of number theory to numerical analysis. Berlin/Beijing: Springer/Science Press; 1981.
[19] Bratley P, Fox BL. Algorithm 659: implementing Sobols quasirandom sequence generator. ACM Trans Math Software 1988;14:88–100.
[20] Dai H, Wang W. Application of low-discrepancy sampling method in structural reliability analysis. Probab Eng Mech 2004;19:425–36.
[21] Niea J, Ellingwood BR. A new directional simulation method for system reliability. Part I: application of deterministic point sets. Struct Safety 2009;31:55–64.
[22] Bjerager P. Probability integration by directional simulation. J Eng Mech 1988;114:1285–302.

APPENDIX D
Variance reduction Monte Carlo methods for wind turbines

The paper presented in this appendix is published in *Proceedings of 11th International Conference on Applications of Statistics and Probability in Civil Engineering (ICASP11)*, August 2011.

Variance reduction Monte Carlo methods for wind turbines

M.T. Sichani & S.R.K.Nielsen & P.Thoft-Christensen
Department of Civil Engineering
Aalborg University, 9000 Aalborg, Denmark

ABSTRACT: Development of Variance Reduction Monte Carlo (VRMC) methods has proposed the possibility of estimation of rare events in structural dynamics. Efficiency of these methods in reducing variance of the failure estimations is a key parameter which allows efficient risk analysis, reliability assessment and rare event simulation of structural systems. Different methods have been proposed within the last ten years with the aim of estimating low failure probabilities especially for high dimensional problems. In this paper applicability of four of these methods i.e. Importance Sampling (IS), Distance Controlled Monte Carlo (DCMC), Asymptotic Sampling (AS) and Subset Simulation (SS) are compared to each other on a common problem. The aim of the study is to determine the most appropriate method for application on realistic systems, e.g. a wind turbine, which incorporate high dimensions and highly nonlinear structures.

1 INTRODUCTION

Assessment of reliability and design of highly nonlinear and high dimensional structures such as wind turbines require estimation of very low failure probabilities of the system. This task can be tackled from three different points of view. The first class of methods are the extreme value distribution fittings to the extracted data of a wind turbine (Caires & Sterl 2005, Mackay, Challenor, & Baha 2010). These data might be taken either from measured responses of a real wind turbine or from epoches of the response simulated by computer. This can be done in combination with some sampling methods such as the epochal method or the Peaks Over Threshold method (POT). It is implicitly assumed that the parent distribution belongs to the domain of attraction of one of the extreme value distributions; therefore the excess values above a given threshold follow a Generalized Pareto (GP) distribution (Naess & Clausen 2001). The required failure probability will be extrapolated from the fitted distribution.

On the other hand the so-called Variance Reduction Monte Carlo simulations (VRMC) might be used for estimating the failure probabilities (Sichani, Nielsen, & Bucher a). The applicability and efficiency of the VRMC methods on wind turbines is the subject of this study in order to understand advantages and limitations of VRMC methods within the framework of wind turbines. The VRMC methods enable efficient estimation of the first excursion of the wind turbines within reasonable computation charge. However, they do not provide any means of understanding the evolution of the PDF of the process within time. This is of great interest since it gives a good insight into the statistical characteristics of the system and effect of different components, i.e. controller, on it.

Another approach for estimation of the first excursion probability of any system is based on calculating the evolution of the Probability Density Function (PDF) of the process and integrating it on the specified domain. Clearly this provides the most accurate result among the three class of the methods. The Fokker-Planck-Kolmogorov (FPK) equation is a well-known tool for realizing the evolution of a stochastic process governed by a differential equation. Although solution of the FPK for even low order structural dynamic problems require excessive numerical computations. This confines the applicability of the FPK to a very narrow range of problems. On the other hand the recently introduced Generalized Density Evolution Method (GDEM), (Li & Chen 2009, Chen & Li 2009), has opened a new way toward realization of the evolution of the PDF of a stochastic process. It is an alternative to the FPK. The considerable advantage of the introduced method over FPK is that its solution does not require high computational cost which extends its range of applicability to high order structural dynamic problems.

2 ESTIMATION OF LOW FAILURE PROBABILITIES

Estimation of failure probabilities of a wind turbine model is not a trivial task since it incorporates a highly

nonlinear model for which the failure probability is to be estimated within a long time duration e.g. 600s. However on the structure part, the wind turbine consists of a simple linear model, nonlinearities in such models appear from loading. These stem from two origins namely the nonlinear aerodynamic loads and the presence of a controller. The aerodynamic loads are highly nonlinear functions of the instantaneous wind speed and the pitch angles of the blades which are calculated with different means e.g. Blade Element Momentum theory (BEM) in this study. The pitch-controller introduces additional nonlinearities to the model i.e. due to its saturation state. Next according to the design criterions the barrier level of a specified failure probability, e.g. 3.8×10^{-7}, is required to be defined. This can most efficiently be estimated if the Cumulative Density Function (CDF) of the failure probability can be derived down to low failure probabilities of the order 10^{-7}.

The focus of this paper is on the VRMC methods. Among the various available methods Importance Sampling (IS) (Bucher 2000, Au & Beck 2001, Macke & Bucher 2003) , Distance Controlled Monte Carlo (DCMC) (Pradlwarter, Schuëller, & Melnik-Melnikov 1994, Pradlwarter & Schuëller 1997, Pradlwarter & Schuëller 1999), Asymptotic Sampling (AS) (Bucher 2009, Sichani, Nielsen, & Bucher a, Sichani, Nielsen, & Bucher b), and Subset Simulation (SS) (Au & Beck 2001) are chosen primarily.

All of the methods aim at the same subject, i.e. estimation of the low failure probability events. However they tackle the problem from very different points of view. IS moves the so-called sampling density of the problem to the boundaries of the failure region hence generates more samples in this area. DCMC works more on a logical basis where the idea is to run all the simulation samples simultaneously and find those processes which are closer to the boundaries of the safe domain and increase the outcrossing events by putting more emphasis on these important events. The AS development is based on the asymptotic estimation of failure probabilities (Breitung 1989). Here the advantage of the linear relationship of the safety index for multi-normal probability integrals is considered to estimate low failure probabilities by proper scaling of the probability integral. AS forces more outcrossing by increasing the excitation power. SS takes its basis on the conditional probability estimation. It breaks the problem of a low failure probability estimation into estimation of a multiplication of some higher probabilities. Next a conditional sampler i.e. Modified Metropolis-Hastings algorithm is used to estimate the conditional probabilities.

Primarily introduced methods are used for failure probability estimation of a Single Degree of Freedom (SDOF) oscillator. Comparison is made on the results of the methods in terms of their accuracy, requirements and computational load. Standard Monte Carlo (SMC) simulation for the same system is performed for global comparison of accuracy of the methods.

This study prevails advantages and disadvantages of each of the methods in application on dynamic systems. Next, the method with highest merit is chosen and applied on a wind turbine model developed in previous study c.f. figure 7.

3 IMPORTANCE SAMPLING

3.1 *Introduction*

To apply IS (Macke & Bucher 2003) it is necessary to have estimation of the system responses at the failure time instance, i.e. displacements, when it is excited by the increments of the Wiener process. This estimation is the basis for constructing the so-called control functions which their characteristics are that they bring the system response to the failure state at failure time instance, i.e. $t_k = k\Delta t$, if the system is excited with them. Next, these deterministic drifts are added to the Wiener increments and the result is used as the final system excitation. Starting by designing control functions, if excitations are not Wiener increments themselves, they should be represented in terms of them. Suppose the system is described by the Itô SDE (1)

$$\left.\begin{aligned} d\mathbf{Z}(t) &= \boldsymbol{\mu}(t,\mathbf{Z})dt + \boldsymbol{\sigma}(t,\mathbf{Z})d\mathbf{W}(t) \\ \mathbf{Z}(s) &= \mathbf{z} \end{aligned}\right\} \tag{1}$$

where $\mathbf{Z}(t)$ is p-dimensional system response subjected to the initial conditions $\mathbf{Z}(s) = \mathbf{z}$ for any $0 \leq s \leq T$ and $\mathbf{W}(t)$ is the vector of q-dimensional unit Wiener processes. Given that the failure domain boundary is specified by the failure surface $g\big(\mathbf{Z}(t,\mathbf{W})\big) = 0$ such that

$$\mathcal{F} = \Big\{ \mathbf{Z} \,|\, g\big(\mathbf{Z}\big) > 0 \Big\} \tag{2}$$

using (1), (2) can be written in the terms of the Wiener excitation i.e. $\mathcal{F} = \Big\{ \mathbf{W} \,|\, g\big(\mathbf{W}\big) > 0 \Big\}$ the failure probability can be defined as

$$\begin{aligned} P_f &= \int_{\mathcal{F}} dP_{\mathbf{W}}(\mathbf{w}) \\ &= \int_{\mathbf{R}^q} I\Big[g\big(\mathbf{Z}(t,\mathbf{W})\big)\Big] dP_{\mathbf{W}}(\mathbf{w}) \\ &= E_{\mathbf{w}}\Big[I\big[g(\mathbf{Z})\big]\Big] \end{aligned} \tag{3}$$

where $I[.]$ is an indicator function which is equal to 1 if the process has outcrossed to the failure domain and else is zero. The probability measure $P_{\mathbf{w}}(\mathcal{B})$ relates a probability to any sub-domain $\mathcal{B} \in \mathbf{R}^q$, i.e. a differential volume around a sample point $\mathbf{w}$, and can be written as $dP(\mathbf{W}) = f_{\mathbf{W}}(\mathbf{w})d\mathbf{w}$. $E_{\mathbf{w}}$ signifies the expectation operator under the probability measure $f_{\mathbf{W}}(\mathbf{w})$.

Based on (3) SMC estimates the failure probability of the system by (4); where N_{sim} is the number of Monte Carlo samples.

$$\hat{P}_f = \frac{1}{N_{sim}} \sum_{j=1}^{N_{sim}} I\big[g(\mathbf{Z}^{(j)})\big] \tag{4}$$

3.2 *The Girsanov Transformation*

The idea of the IS based on the Girsanov theorem is to introduce a square integrable drift $\mathbf{u}(t)$ - i.e. $\sum_j^p \int_0^T \mathbf{u}_j^2(\tau)d\tau < \infty$ - into the excitation, which brings the systems response to the failure region at the desired time.

$$d\tilde{\mathbf{W}}(t) = \mathbf{u}(t)dt + d\mathbf{W}(t) \tag{5}$$

The Itô SDE (1) can then be written as

$$\left.\begin{aligned} d\mathbf{Z}(t) =& \boldsymbol{\mu}(t,\mathbf{Z})dt - \boldsymbol{\sigma}(t,\mathbf{Z})\mathbf{u}(t)dt \\ &+ \boldsymbol{\sigma}(t,\mathbf{Z})d\tilde{\mathbf{W}}(t) \\ \mathbf{Z}(s) =& \mathbf{z} \end{aligned}\right\} \tag{6}$$

The Girsanov theorem then states that the process $\tilde{\mathbf{W}}$ is a Wiener process under the probability measure $P_{\tilde{\mathbf{W}}}$. Therefore generating samples of $\tilde{\mathbf{W}}$ under the probability measure $P_{\mathbf{W}}$ corresponds to generating samples of $\mathbf{W}$ under the probability measure $P_{\tilde{\mathbf{W}}}$. This means that the drift of the excitation might be designed in any sense that brings the system to the failure at the desired time instance. Next, the probability measure should be changed properly to take into account the effect of this transformation which is done in the following way

$$\left.\begin{aligned} P_f &= \int_{\mathbf{R}^q} I\Big[g\big(\mathbf{Z}(t,\mathbf{W})\big)\Big] \frac{f_{\mathbf{W}}(\mathbf{w})}{f_{\tilde{\mathbf{W}}}(\mathbf{w})} f_{\tilde{\mathbf{W}}}(\mathbf{w})d\mathbf{w} \\ &= \int_{\mathbf{R}^q} I\Big[g\big(\mathbf{Z}(t,\mathbf{W})\big)\Big] \frac{dP_{\mathbf{W}}(\mathbf{w})}{dP_{\tilde{\mathbf{W}}}(\mathbf{w})} f_{\tilde{\mathbf{W}}}(\mathbf{w})d\mathbf{w} \\ &= E_{\tilde{\mathbf{w}}}\left[I\big[g(\mathbf{Z})\big] \frac{dP_{\mathbf{W}}(\mathbf{w})}{dP_{\tilde{\mathbf{W}}}(\mathbf{w})} \right] \end{aligned}\right\} \tag{7}$$

where $g(\mathbf{Z}) = g\big(\mathbf{Z}(t,\mathbf{W})\big)$ and the ratio $dP_{\mathbf{W}}(\mathbf{w})/dP_{\tilde{\mathbf{W}}}(\mathbf{w})$ is the well-known Radon-Nikodym derivative of the probability measure $dP_{\mathbf{W}}(\mathbf{w})$ with respect to the measure $dP_{\tilde{\mathbf{W}}}(\mathbf{w})$. $E_{\tilde{\mathbf{w}}}$ signifies the expectation operator under the probability measure $f_{\tilde{\mathbf{W}}}(\mathbf{w})$. Upon the Girsanov theorem the probability measure of (7) can be changed to $f_{\tilde{\mathbf{W}}}(\mathbf{w})$ hence (8)

$$P_f = E_{\mathbf{w}}\left[I\big[g(\tilde{\mathbf{X}})\big] \frac{dP_{\mathbf{W}}(\tilde{\mathbf{w}})}{dP_{\tilde{\mathbf{W}}}(\tilde{\mathbf{w}})} \right] \tag{8}$$

where $g(\tilde{\mathbf{Z}}) = g\big(\mathbf{Z}(t,\tilde{\mathbf{W}})\big)$. The significance of equation (7) is that the probability measure can be changed so that the process $\tilde{\mathbf{W}}$ can be used instead of the original process $\mathbf{W}$ to estimate the failure probability of a system provided that the Radon-Nikodym derivative is taken into account. Based on (7), the failure probability of the system can be estimated using (9)

$$\hat{P}_f = \frac{1}{N_{sim}} \sum_{j=1}^{N_{sim}} I\big[g(\tilde{\mathbf{Z}}^{(j)})\big] \left(\frac{dP_{\mathbf{W}}(\tilde{\mathbf{w}}^{(j)})}{dP_{\tilde{\mathbf{W}}}(\tilde{\mathbf{w}}^{(j)})} \right) \tag{9}$$

4 RUSSIAN ROULETTE & SPLITTING WITH DISTANCE CONTROL

The method encompassed two components “Russian Roulette and Splitting” (RRS), which replaces “unimportant” realizations with the “important” ones, and “Distance Control” (DC), which takes care of determining the importance of the realizations. The method substitutes the processes with low probability of causing failure, called the unimportant processes, by the so-called important processes i.e. processes with higher probability of failure. This substitution might be readily done by splitting(duplicating) some of the important processes with control over their statistical weights such that the statistics of the simulation is not changed after splitting. The distance measure is used to distribute the samples in the state space. Pradlwarter and Schuëller (Pradlwarter, Schuëller, & Melnik-Melnikov 1994) define this in the following way. A given realization $\mathbf{z}(t)$ of the p-dimensional state vector $\mathbf{Z}(t)$ is associated with a vector $\mathbf{l}\left(\mathbf{z}(t)\right)$ with non-dimensional components $l_i\left(\mathbf{z}(t)\right)$.

$$l_i\big(\mathbf{z}(t)\big) = \frac{z_i(t) - \mu_{Z_i}(t)}{\sigma_{Z_i}(t)} \quad , \quad i = 1, \cdots, p \tag{10}$$

where $\mu_{Z_i}(t)$ and $\sigma_{Z_i}(t)$ denotes the mean value and the standard deviation of the possible non-stationary process $\mathbf{Z}(t)$. In case these cannot be determined analytically a preliminary SMC is performed. The components $l_i\left(\mathbf{z}(t)\right)$ may otherwise be specified with arbitrarily selected relative weight. The distance measure $d\left(\mathbf{z}(t)\right)$ related to the realization is then defined as

$$\left.\begin{aligned} d\big(\mathbf{z}_j(t)\big) =& \sum_{k=1}^{K} a_j \left|\left| \mathbf{l}\left(\mathbf{z}_{j_k|j}(t)\right) - \mathbf{l}\left(\mathbf{z}_j(t)\right) \right|\right| \\ & a_1 > a_2 > \cdots > a_K \end{aligned}\right\} \tag{11}$$

where $\mathbf{z}_{j_k|j}(t)$ denote the k[th] closest realization to $\mathbf{z}_j(t)$ and $||.||$ is the Euclidian norm. The closest realization with the weight a_1 is weighted highest. The weights were chosen as

$$a_j = 2^{1-j} \tag{12}$$

For a SDOF oscillator subjected to Gaussian white noise $||\mathbf{l}(\mathbf{z})||$ with $\mathbf{l}(\mathbf{z}(t))$ defined by (10) is proportional to the mechanical energy of the oscillator. However, (10) does not represent the mechanical energy in any other case than the indicated. Instead, (11) can be replaced with

$$d\big(\mathbf{z}_j(t)\big) = \sum_{j=1}^{K} a_j E_m\big(\mathbf{z}_{j_k|j}(t) - \mathbf{z}_j(t)\big) \qquad (13)$$

where E_m is the mechanical energy of the system. The mechanical energy, itself could alternatively be used as a distance measure. This possibility is also examined by the authors though no improvement of the results compared to the weighting proposed by (11) is observed; which has already been reported in the literature (Pradlwarter, Schuëller, & Melnik-Melnikov 1994, Pradlwarter & Schuëller 1997).

5 SUBSET SIMULATION

The subset simulation strategy starts from the reachable barrier level(s) by a predefined low number of samples and increase the level gradually until the highest barrier level required. This can be done by defining intermediate probability levels $p_f = p_f^{(m)} < p_f^{(m-1)} < \cdots < p_f^{(1)}$ corresponding to the intermediate barrier levels $b = b_m > b_{m-1} > \cdots > b_1$. Using this property taken from the fact that failure probability can not increase as the barrier level increases, the required failure probability p_f is written as

$$p_f(b_2|b_1) = \frac{p_f(b_2 \bigcap b_1)}{p_f(b_1)} = \frac{p_f(b_2)}{p_f(b_1)} \qquad (14)$$

using (14) the final failure probability, i.e. the lowest failure probability required, is written as the following product

$$p_f(b) = p_f(b_1) \prod_{i=1}^{m-1} p_f(b_{i+1}|b_i) \qquad (15)$$

The method then follows with estimation of each of the m terms on the right hand side of (15) using some type of Monte Carlo simulation. Therefore it is beneficial to let the barrier level be chosen in an adaptive manner and fix the intermediate failure probabilities associated to them. All of the terms in the product are chosen large enough so that they can be estimated with low number of samples, i.e. $p_0 = 0.1$ in conjunction with (16).

$$\left.\begin{array}{rcll} p_f(b_1) & = & p_0 & \\ p_f(b_{i+1}|b_i) & = & p_0 \quad , & i = 1, \cdots m-1 \end{array}\right\} \qquad (16)$$

$p_f(b_1)$ can then be estimated efficiently by SMC with low number of samples i.e. $N_{sim} = 100$. However the conditional probability terms in (14) can not be estimated by SMC and need a technique which is capable of generating samples conditioned on the previous samples. Au and Beck (Au & Beck 2001) proposed using a Modified Metropolis-Hastings (MMH) algorithm for this purpose and called it the *subset simulation*. The method starts with a SMC with N_{sim} number of samples which allows accurate estimation for the first term on the right hand side of (15). The realizations of the excitations in the i^{th} level of the simulation, i.e. $\dot{\mathbf{W}}^{(i)} = \{\dot{\mathbf{w}}_1^{(i)}, \cdots, \dot{\mathbf{w}}_{N_{sim}}^{(i)}\}$ where $\dot{\mathbf{W}}^{(i)}$ denotes increments of the Wiener process, which their response corresponds to the barrier levels higher than the barrier level b_1. These realizations provide a set of the so-called seeds for generating the next generation of excitations. Candidates for next generation of excitations are generated using a conditional sampler , e.g. MMH, using these seeds. This step provides the estimation for the conditional terms in (15) and will be repeated m times , c.f. (15), to reach the required failure probability i.e. p_0^m provided (16).

$$p_f^i = \frac{p_f^{i-1}}{N_{sim}} \sum_{j=1}^{N_{sim}} I_{\mathfrak{F}^{(i)}}(\dot{\mathbf{w}}_j^{(i)}) \quad , \quad i = 1, \cdots, m \qquad (17)$$

where $p_f^0 = 1$; p_f^i represents the minimum failure probability calculated in the i^{th} step of the simulation. $\mathfrak{F}$ denotes the failure domain and $I_{\mathfrak{F}^{(i)}}(\dot{\mathbf{w}}_j^{(i)})$ is the indicator function which will be one if the response to $\dot{\mathbf{w}}_j^{(i)}$ lies in the i^{th} intermediate failure domain and is zero otherwise.

6 ASYMPTOTIC SAMPLING

The method is developed based on the asymptotic estimation of multi-normal integrals. The problem of approximating a multi-normal probability integral (18) on the scaled LSF which can be represented after proper transformation of random variables as

$$p(\beta; \boldsymbol{\xi}) = \int\limits_{g(\beta^{-1}\boldsymbol{\xi})<0} \prod_{i=1}^{N} \varphi\Big(-\frac{1}{2}\xi_i^2\Big) d\boldsymbol{\xi} \qquad (18)$$

where $\boldsymbol{\xi} = \{\xi_1, \cdots, \xi_N\}$ denotes the vector of standardized independent multi-normal random variables; LSF is defined as $g(\beta^{-1}\boldsymbol{\xi}) < 0$. The first parameter in the parentheses on the left hand side denotes scaling of the variables in the LSF. $\varphi(.)$ denotes the standard normal density function. The boundaries of the integral in (18) can be changed to unscaled LSF which reads

$$p(\beta; \boldsymbol{\xi}) = \beta^N \int\limits_{g(\boldsymbol{\xi})<0} \prod_{i=1}^{N} \varphi\Big(-\frac{\beta^2}{2}\xi_i^2\Big) d\boldsymbol{\xi} \qquad (19)$$

which is shown to be asymptotically equal to $\Phi(-\beta)|J|^{-1/2}$ as $\beta \to \infty$; where $|J|^{-1/2}$ is a parameter related to the first and second order derivatives of the LSF at the design point. (18) and (19) mean that the desired low probabilities can be approximated on a scaled failure domain and then transformed back into the unscaled domain. This idea forms the procedure of AS (Bucher 2009) which starts with a SMC on the scaled variables i.e. excitations with *artificially* increased standard deviation. The reliability index is primarily estimated based on the scaled failure probability, e.g. $\beta(f) = \Phi(1 - p^{scaled})$, and is then scaled back to the unscaled space, e.g. $\beta(1) = f^{-1}\beta(f)$. The desired probability is estimated as $\Phi^{-1}\big(\beta(1)\big)$ then. More details of the method and some practical aspects for improving its efficiency on dynamic problems are presented in (Sichani, Nielsen, & Bucher a, Sichani, Nielsen, & Bucher b).

7 NUMERICAL SIMULATION

7.1 *SDOF oscillator*

The first simulation is based on a single DOF linear oscillator (20), characterized by $\omega_n = 1s^{-1}$ and $\zeta_n = 0.01$

$$\ddot{x}(t) + 2\zeta_n\omega_n\dot{x}(t) + \omega_n^2 x(t) = w(t) \tag{20}$$

$w(t)$ is zero-mean Gaussian white noise with unit intensity. The barrier level is normalized with respect to the standard deviation of the response $\sigma_X = (4\zeta\omega^3)^{-1/2}$.

$$b_N = \frac{b}{\sigma_X} \tag{21}$$

The failure event is defined as the maximum of the absolute value of the response of the oscillator exceeds a certain threshold "b", i.e. $\Pr(|y(t)| > b)$ for $t \in [0, 600]$. The normalized barrier level is assumed to be $b_N = 5$ in simulations. Simulations are carried out with $\Delta t = 0.0614s$ and $t \in [0, 600]s$ which involves 9772 samples to examine the performance of the method in high dimensions. Exact failure probability and reliability index for the problem, calculated with standard Monte Carlo simulation with 2×10^6 samples, are $P_f(600) = 2.07 \times 10^{-4}$ and $\beta = 3.5310$ respectively.

7.1.1 *Importance sampling*

Figure 1.a shows one of the control functions of the SDOF oscillator. The response of the system to this excitation, i.e. deterministic drift, is shown in 1.b. Estimation of the failure probability for different time instances are shown in figure 2. As seen from this figure IS is very attractive in the first sight due to its high accuracy for failure levels. However its shortcomings in application to more complicated problems are also

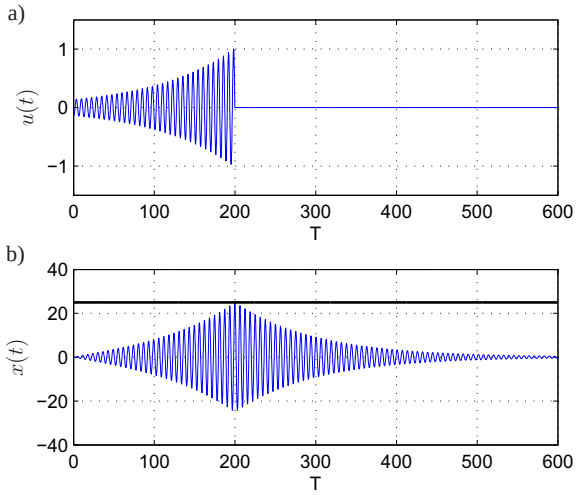

Figure 1: Control function and response of the SDOF oscillator; a) Control function, b) response.

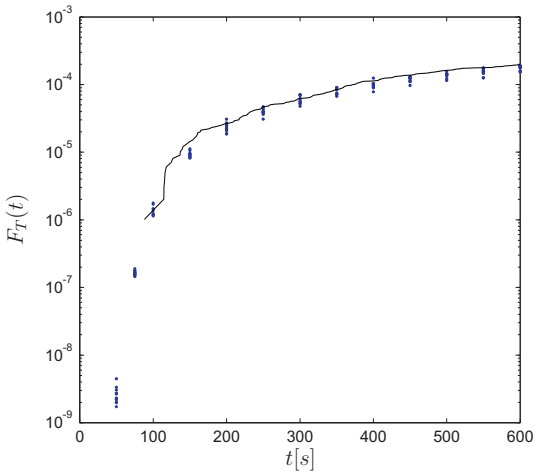

Figure 2: Estimations of the failure probability with IS; Solid line: SMC, dots : IS

considerable. Since failure may occure at any time instance within a distinguished time period $t \in [0, T]s$, IS requires that all of the control functions that cause failure during this time interval should be available to allow considering the interaction between different design point control functions. This requires heavy dynamic analysis in order to compute these control functions primarily and also high memory is required to save them. Unfortunately this requirement specifically for Multi Degree Of Freedom (MDOF) nonlinear systems poses severe difficulties as in such cases there exist no analytical solution for the design point excitations. In such cases a high dimensional optimization algorithm should be used to find the design points excitations, alternatively called control functions, which is very expensive, (Koo, Der Kiureghian, & Fujimura 2005).

These problems have also been noticed by other researchers however to the best knowledge of authors IS applications are very limited i.e. nonlinear SDOF systems, (Naess & Gaidai 2008), or linear MDOF systems with only one stochastic excitation process (Jensen & Valdebenito 2007). The above reasons conclude that using IS with presented scheme may not be

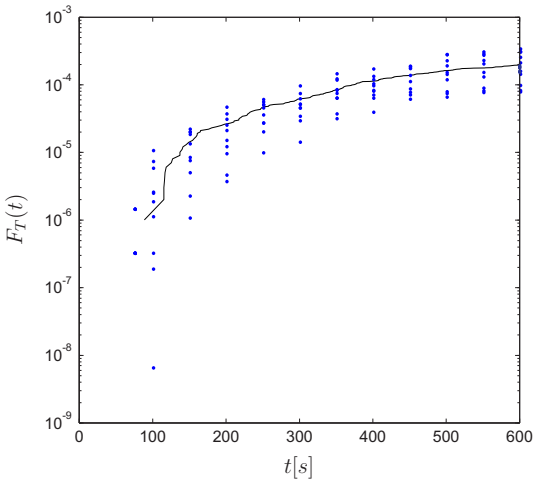

Figure 3: Estimations of the failure probability with DCMC; Solid line: SMC, dots: DCMC

considered a proper candidate for for application to wind turbine models.

7.1.2 *Russian roulette & splitting with distance control*

The DCMC with the distance measure considered as a weighted summation of six closest neighbor processes i.e. $K = 6$. The parameters of the DCMC are chosen $\beta = 0.8, p_0 = 0.5, w_{min} = 5 \times 10^{-5}$, (Pradlwarter & Schuëller 1999), and the results are shown in the figure 3. A unique feature of DCMC compared to the other algorithms implemented in this study is that it works directly on the responses and does not make any changes in the excitations. Advantages of DCMC are generality of application and low memory requirements and its capability in handling high dimensional problems. The method's shortcomings are the implementation of it which requires all of the samples to run in parallel i.e. all 500 simulations should evolve simultaneously to allow statistical weighting adjustment. This requires to change the states during the time integration of the governing equations. This may cause some practical issues during implementation of the algorithm on practical codes. Next, DCMC like IS is capable of estimating failure probability of a predefined threshold level. This is less motivating in wind turbine problems where the opposite is required i.e. the threshold for a given failure probability.

7.1.3 *Asymptotic sampling*

For each barrier level $N_{sim} = 500$ number of samples with 5 support points are used with different Δf and range of *f*. Figure 4 illustrates the effect of distribution of support points. Clearly too low values for *f* will cause all of the processes to cross out which does not give any information while choosing too large *f* will cause few out crossings which increases the uncertainty of the estimation. It is seen that the maximum accuracy of the method, i.e. the least standard deviation of the estimate, is achieved when the support points are distributed in the region where 2 to 98

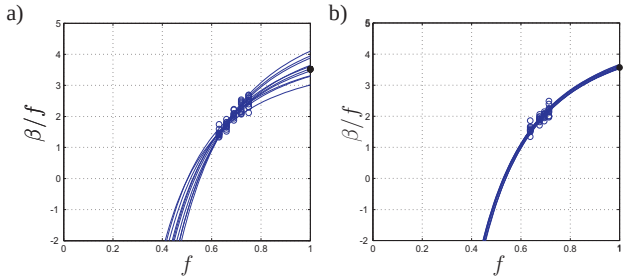

Figure 4: Sstimations of the reliability index β with asymptotic sampling for 600[s]; single DOF oscillator. a) Uniform distributed support points , CoV$\big(P_f(600)\big)$=1.2 b) Non-uniform distributed support points, CoV$\big(P_f(600)\big)$=0.2

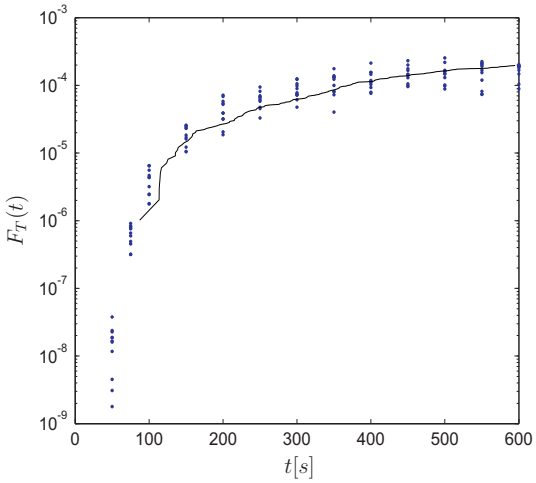

Figure 5: Estimations of the failure probability with AS; Solid line: SMC, dots: AS

percent of the realizations crosses out c.f. figure 4.b compared to figure 4.a in which 2 to 50 percent of the realizations have crossed out. The black dots on the right hand side of the figures show the exact value of the beta. Figure 5 shows estimations of the failure probability for the same barrier level in different time instants where solid line shows the SMC results.

7.1.4 *Subset simulation*

Results of SS applied on the oscillator for failure for different time instants within the time interval $t \in [0, 600]s$ are shown in figure 6 as counterpart of figures 2, 5 and 3. For estimation of failure probability in this figure 4 levels of MCMC is used only for $T = 400s, 450s, 600s$; for $T = 150s, 200s, 250, 300, 350s$ 5 MCMC levels are used and for $T = 100s, 75s, 50s$ respectively 6,7 and 8 MCMC levels with $p_0 = 0.1$ with $N_{sim} = 500$ samples in each step. The proposal distribution is assumed uniform with half spread equal to the standard deviation of the excitation seeds (Au, Cao, & Wang 2010).

The SS approach is based on changing the excitation realizations like IS and AS. The method is based on designing new excitations within a fixed time duration based on previous excitation realizations which have reached the highest barrier levels in previous simulations e.g. seeds. In this way it may be interpreted as a stochastic optimization procedure. The

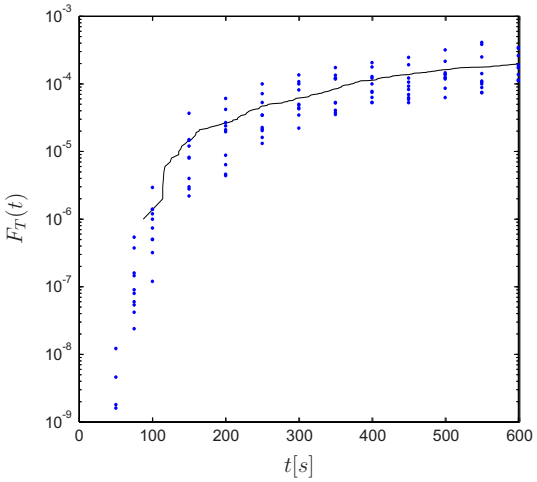

Figure 6: Estimations of the failure probability with SS; Solid line: SMC, dots: SS

method has several interesting features which is in line with requirements of the wind turbine design criteria. An advantage of SS is that it estimates the thresholds related to a given failure probability. This is what is required in wind turbine design codes, (IEC 2005), while the other three methods provide the failure probability given for a predefined threshold level. SS is a very accurate method for low failure probability estimation of high dimensional nonlinear systems (Au, Ching, & Beck 2007). However some practical procedures should be taken into account for very high number of basic variables which should be kept in memory during simulations e.g. random numbers required to generate the turbulent wind field. Nevertheless the method seems to propose a good candidate for application on the wind turbine model. Most favorably the method is a so-called acts as a black-box which means it does not require any a-priori knowledge of system which adds to its advantages.

7.2 *Wind turbine*

Design codes for wind turbines are based on a return period (expected first-passage time) of $T_r = 50$year, which itself requires design values related to the failure probability of the wind turbine models down to the order 10^{-7}. According to the IEC61400-1 standard (IEC 2005), the design value r of a stochastic response $\{$ R(t) , t$\in$[0,∞[$\}$(deformation, bending moment, stress, etc.) is obtained by extrapolation of the failure probability under normal operation of the design value r in a referential epoche T to T_r. Presuming independent failure events in adjacent referential epoches the exceedance probability of the design value is given as

$$P\Big(R_{max}(T_r) > r\Big) \simeq \frac{T_r}{T} P\Big(R_{max}(T) > r\Big) \quad (22)$$

$R_{max}(T)$ and $R_{max}(T_r)$ denote the maxima value in intervals T and T_r. With $T_r = 50$ year and $T = 600s$,

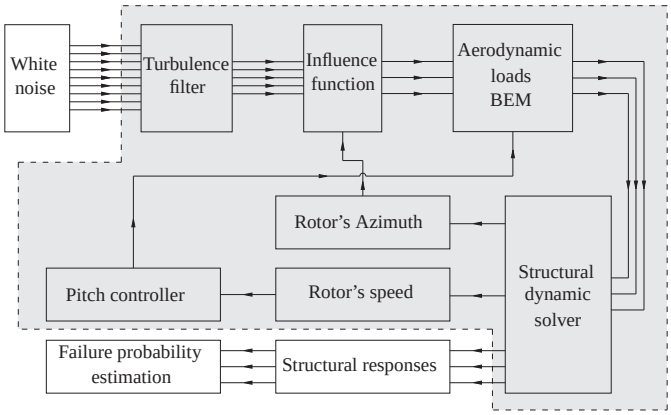

Figure 7: Flowchart of the wind turbine model.

(22) provides the relation

$$P\Big(R_{max}(T) > r\Big) \lesssim \frac{T}{T_r} = 3.8 \times 10^{-7} \quad (23)$$

The design value r is obtained as the solution of (23). It is out of question to determine this by SMC simulation due to the indicated low failure probability. The suggested approach in the IEC61400-1 standard is to use a Weibull or a Gumbel distribution as the distribution function $F_{R_{max}(T)} = 1 - P\Big(R_{max}(T) > r\Big)$. The locations, scale and shape parameters, which are estimated from the available sample. Applicability of the selected method on a reduced order model of a 5MW reference wind turbine developed in previous study c.f. figure 7, (Sichani, Nielsen, & Bucher b), is tested. Specifications of the wind turbine model are adopted from the NREL reference wind turbine (Jonkman, Butterfield, Musial, & Scott 2009). It is attempted to cover the principal behavior of a wind turbine.

The model consists of structural and aerodynamic loads but no controller, i.e. fixed rotational speed is assumed. The details of the model specifications are explained in (Sichani, Nielsen, & Bucher b). The wind field is simulated in 31 nodes on 50m distance from nacelle of the rotor with 63m blades using a state space model. Failure probabilities of the model are estimated with the AS as the primary candidate method. Figure 8 shows failure probability of the wind turbine model estimated with SMC with 4×10^5 samples, AS with 32×500 samples (Sichani, Nielsen, & Bucher b), Weibull and Gumbel fits with 500 simulations each. The results of AS estimations show good consistency with the SMC results. The AS method has the advantages of very low memory requirement and simplicity of application even for very high dimensional problems.

8 CONCLUSIONS

Among the methods considered in this paper IS shows the highest accuracy however faces serious difficulties

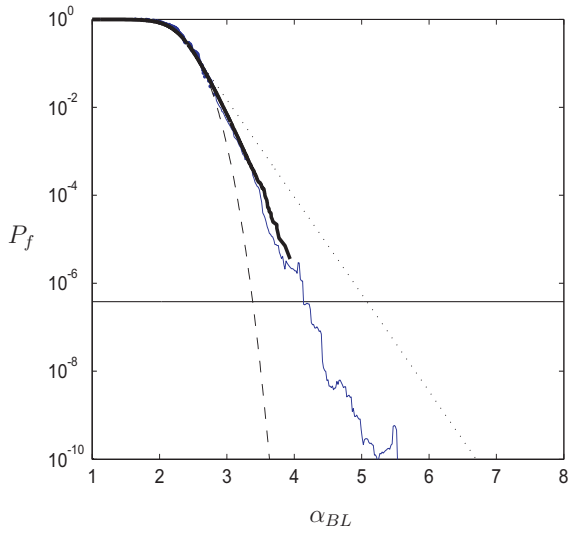

Figure 8: Estimated failure probability of the wind turbine for fixed speed wind turbine. —: 50 year recurrence period, bold black: SMC, − −: 3-parameter Weibull distribution, · · · : Gumbel distribution, blue: AS.

in application on wind turbine models due to excessively high number of dynamic analysis it requires for nonlinear systems. The DCMC method is applicable on such models however certain features, i.e. parallel running and communication of samples during solution, are required which may limit its applications on practical codes. The AS and SS methods seem the most suitable methods since they have similar characteristics regarding no a-priori knowledge about model as well as low memory requirements. The AS method is already applied on a wind turbine model and results show good agreement with the SMC with much higher efficiency.

It worth mentioning that total number of dynamic analysis required by all of the methods mentioned in the paper for accurate results may be considerably larger than the nominal number of samples, e.g. 500 in this paper, except the DCMC method.

REFERENCES

Au, S., Z. Cao, & Y. Wang (2010). Implementing advanced monte carlo simulation under spreadsheet environment. *Structural Safety 32*(5), 281 – 292. Probabilistic Methods for Modeling, Simulation and Optimization of Engineering Structures under Uncertainty in honor of Jim Beck's 60th Birthday.

Au, S., J. Ching, & J. Beck (2007). Application of subset simulation methods to reliability benchmark problems. *Structural Safety 29*(3), 183 – 193. A Benchmark Study on Reliability in High Dimensions.

Au, S. K. & J. L. Beck (2001). First excursion probabilities for linear systems by very efficient importance sampling. *Probabilistic Engineering Mechanics 16*, 193–207.

Breitung, K. (1989). Asymptotic approximations for probability integrals. *Probabilistic Engineering Mechanics 4(4)*, 187–190.

Bucher, C. (2000). *An importance sampling technique for randomly excited systems discretized by finite elements.*, Volume II. In: Ko J.M., Xu Y.L., editors, Advances in structural dynamics. Amsterdam: Elsevier.

Bucher, C. (2009). Asymptotic sampling for high-dimensional reliability analysis. *Probabilistic Engineering Mechanics 24*, 504–510.

Caires, S. & A. Sterl (2005). 100-year return value estimates for ocean wind speed and significant wave height from the era-40 data. *Journal of Climate 18(7)*, 1032–1048.

Chen, J. & J. Li (2009). A note on the principle of preservation of probability and probability density evolution equation. *Probabilistic Engineering Mechanics 24*, 51–59.

IEC (2005). Wind turbines – part 1: Design requirements. IEC International Standard 61400-1.

Jensen, H. & M. Valdebenito (2007). Reliability analysis of linear dynamical systems using approximate representations of performance functions. *Structural Safety 29*, 222–237.

Jonkman, J., S. Butterfield, W. Musial, & G. Scott (2009). Definition of a 5-mw reference wind turbine for offshore system development. *National Renewable Energy Laboratory 20*, 136–147.

Koo, H., A. Der Kiureghian, & K. Fujimura (2005). Design-point excitation for non-linear random vibrations. *Probabilistic Engineering Mechanics 20*, 136–147.

Li, J. & J. Chen (2009). *Stochastic Dynamics of Structures.* Wiley.

Mackay, E., P. Challenor, & A. Baha (2010). On the use of discrete seasonal and directional models for the estimation of extreme wave conditions. *Ocean Engineering 37*, 425–442.

Macke, M. & C. Bucher (2003). Importance sampling for randomly excited dynamical systems. *Journal of Sound and Vibration 268*, 269–290.

Naess, A. & P. Clausen (2001). Combination of the peaks-over-threshold and bootstrapping methods for extreme value prediction. *Structural Safety 23*, 315–330.

Naess, A. & O. Gaidai (2008). Monte carlo methods for estimating the extreme response of dynamical systems. *Journal of Engineering Mechanics 134(8)*, 628–636.

Pradlwarter, H. & G. Schuëller (1997). On advanced monte carlo simulation procedures in stochastic structural dynamics. *International Journal of Non-Linear Mechanics 32(4)*, 753–774(10).

Pradlwarter, H. & G. Schuëller (1999). Assesment of low probability events of dynamical systems by controlled monte carlo simulation. *Probabilistic Engineering Mechanics 14*, 213–227.

Pradlwarter, H., G. Schuëller, & P. Melnik-Melnikov (1994). Reliability of mdof systems. *Probabilistic Engineering Mechanics 9(4)*, 235–243.

Sichani, M., S. Nielsen, & C. Bucher (a). Applications of asymptotic sampling on high dimensional structural dynamic problems. *submitted to Structural Safety*.

Sichani, M., S. Nielsen, & C. Bucher (b). Efficient estimation of first passage probability of high dimensional non-linear systems. *submitted to Probabilistic Engineering Mechanics*.

APPENDIX E
Efficient estimation of first passage probability of high-dimensional nonlinear systems

The paper presented in this appendix is published in *Probabilistic Engineering Mechanics*, Volume 26, Issue 4, October 2011, Pages 539-549.

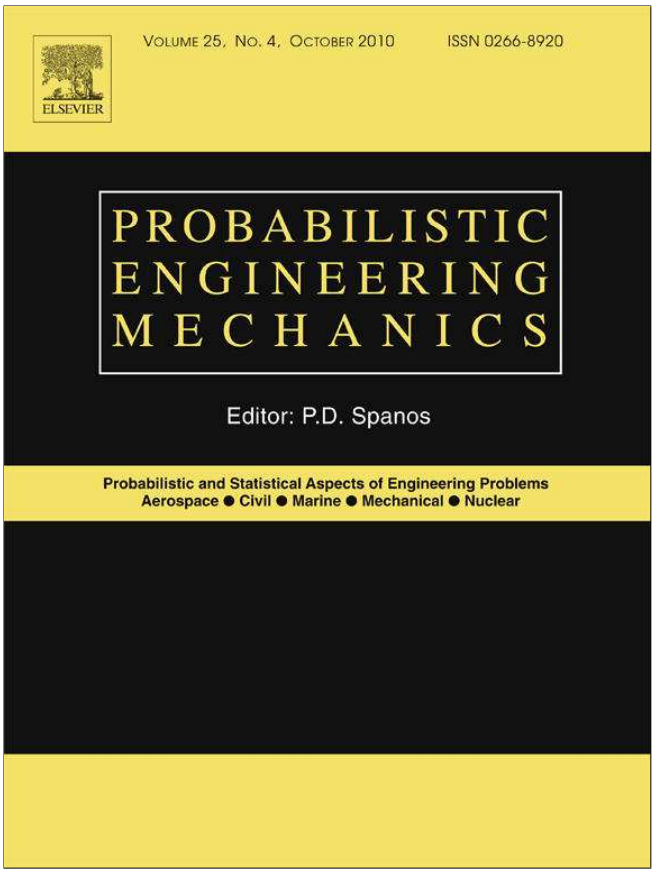

Probabilistic engineering mechanics

Order detail ID:	56242217
Order License Id:	2742980303640
Article Title:	Efficient estimation of first passage probability of high-dimensional nonlinear systems
Author(s):	Sichani, M.T.
DOI:	10.1016/J.PROBENGMECH.2011.05.01
Date:	Oct 01, 2011
ISSN:	0266-8920
Publication Type:	Journal
Volume:	26
Issue:	4
Start page:	539
Publisher:	ELSEVIER LTD.

Permission Status: Granted

Permission type: Republish or display content
Type of use: reuse in a thesis/dissertation

View details

http://www.elsevier.com/copyright

Probabilistic Engineering Mechanics 26 (2011) 539–549

Contents lists available at ScienceDirect

Probabilistic Engineering Mechanics

journal homepage: www.elsevier.com/locate/probengmech

Efficient estimation of first passage probability of high-dimensional nonlinear systems

M.T. Sichani [a,*], S.R.K. Nielsen [a], C. Bucher [b]

[a] Department of Civil Engineering, Aalborg University, 9000 Aalborg, Denmark

[b] Center of Mechanics and Structural Dynamics, Vienna University of Technology, Karlsplatz 13, Vienna, Austria

ARTICLE INFO

Article history:
Received 27 July 2010
Received in revised form
17 May 2011
Accepted 20 May 2011
Available online 27 May 2011

Keywords:
Variance reduction
Monte Carlo
High dimensions
Nonlinear systems
Wind turbine

ABSTRACT

An efficient method for estimating low first passage probabilities of high-dimensional nonlinear systems based on asymptotic estimation of low probabilities is presented. The method does not require any a priori knowledge of the system, i.e. it is a black-box method, and has very low requirements on the system memory. Consequently, high-dimensional problems can be handled, and nonlinearities in the model neither bring any difficulty in applying it nor lead to considerable reduction of its efficiency. These characteristics suggest that the method is a powerful candidate for complicated problems. First, the failure probabilities of three well-known nonlinear systems are estimated. Next, a reduced degree-of-freedom model of a wind turbine is developed and is exposed to a turbulent wind field. The model incorporates very high dimensions and strong nonlinearities simultaneously. The failure probability of the wind turbine model is estimated down to very low values; this demonstrates the efficiency and power of the method on a realistic high-dimensional highly nonlinear system.

© 2011 Elsevier Ltd. All rights reserved.

1. Introduction

Efficient estimation of the first excursion probability of complex structural systems such as wind turbines is a challenging task, since a wind turbine is governed by a highly nonlinear and high-dimensional model. However, the term "dimensionality" as used here mainly refers to the basic stochastic variables of the system, i.e. excitations or structural model uncertainties, rather than the dimensions of the structural system. There already exist a number of variance reduction Monte Carlo simulations which overcome the task of efficient estimation of low failure probabilities; see [1,2]. However, although efficient estimation of low failure probabilities for low-dimensional problems especially with linear characteristics has been shown to be possible by these methods, high-dimensional cases face serious problems; see [3,4]. These problems might be of either analytical or numerical nature; in each case they can easily render a method inapplicable; see [5–7]. One class of available methods is the black-box methods, i.e. methods which do not need any a priori knowledge of the system under consideration, sometimes called trackable data. The remaining methods might therefore be called grey-box methods, denoting the demand for some a priori knowledge of the system. This a priori knowledge traces back to the limit state function (LSF) of the problem. However, they might appear in different forms, such as critical design point excitations in importance sampling (IS) [8,9], the gradient of the limit state function, or important directions through the design point in line sampling (LS) [10,11]. The amount of a priori system information required by grey-box methods varies for different methods. An important problem that exists with respect to these data is that an efficient calculation of this a priori information is not always guaranteed. It may require complicated mathematical analysis of the system, which may not be possible for complex systems, or an excessive number of numerical dynamic analyses, which clearly decreases the efficiency of the method. Furthermore, as the complexity of the system increases, for example, due to the presence of nonlinearities, non-white excitations, or multiple excitation processes, calculation of these a priori data becomes more difficult. In such cases black-box methods, which do not have limitations regarding the parameters mentioned, are preferred. Examples of such methods can be found in the family of subset simulation techniques; see [12,13]. Another method has recently been introduced [14,15] with the ability of estimating very low failure probabilities of order 10^{-7} with considerably lower computation cost compared to standard Monte Carlo (MC) simulation. The method is conceptually based on asymptotic approximation of the probability integrals proposed by Breitung [16,17]. It has previously been shown that the method provides good estimations of the low failure probabilities with low sensitivity to the problem dimensions. Furthermore, according to the generality of the concept, which keeps quite close to standard Monte Carlo simulation, nonlinearities of any

* Corresponding author. Tel.: +45 9940 8570; fax: +45 9814 8243.
E-mail addresses: mts@civil.aau.dk (M.T. Sichani), soren.nielsen@civil.aau.dk (S.R.K. Nielsen), christian.bucher@tuwien.ac.at (C. Bucher).

0266-8920/$ – see front matter © 2011 Elsevier Ltd. All rights reserved.
doi:10.1016/j.probengmech.2011.05.013

kind do not increase its computational cost considerably. Other advantages of the method are its very low memory requirements and simplicity of implementation, which extend the range of the problems it is applicable to. In this paper, a very efficient scheme for analysis of high-dimensional systems with any type of nonlinearity is proposed. The proposed scheme allows calculation of the very low failure probabilities of the system needed in design problems. Three numerical examples are provided to illustrate the applications of the method on popular nonlinear systems. Further, a reduced-order model of a wind turbine is developed, and its failure probability is estimated with the proposed method. The wind turbine model is a very difficult example for which most of the variance reduction methods are not applicable. It is shown that the proposed scheme provides very good estimations of the failure probability of such a complicated case with a very low computation cost compared to Monte Carlo simulation.

2. Statement of the method

The basis of the proposed scheme is asymptotic sampling (AS), proposed by Bucher [15]. The proposed scheme consists of simulating N_{sim} simulations with the artificially increased intensity of the driving white noise of the excitation in the so-called U-space, which is done by the scaling factor f starting from 1. Note that, according to [15], f denotes an artificial increase of the standard deviation of the basic variables in standard Gaussian space by a factor of $1/f$. Some remarks about the underlying concept are given here. It relies on the asymptotic behavior of the failure probability in n-dimensional i.i.d. Gaussian space as the reliability index β tends to infinity (see [16]). This can equivalently be expressed by the limit that the standard deviation σ of the variables, and hence the failure probability p_f, approach zero. Breitung also states that the *generalized reliability index* β_G as defined by

$$\beta_G = -\Phi^{-1}(p_f) \tag{1}$$

is asymptotically equal to the linearized reliability index β as both tend to infinity. Consider a (possibly highly nonlinear) limit state function $g(\mathbf{X})$ in which $g < 0$ denotes failure. Let σ be the standard deviation of the i.i.d. Gaussian variables X_k, $k = 1 \ldots n$. We are going to determine the functional dependence of the generalized safety index β on the standard deviation σ by using an appropriate sampling technique. This is aided by some analytical considerations in which we study the case of a linear limit state function. Let this limit state function be defined as

$$g(\mathbf{X}) = -\sum_{i=1}^{n} \frac{x_i}{s_i} + 1. \tag{2}$$

If $\mathbf{X}$ is a vector of standardized Gaussian variables, then we have the reliability index $\beta(1)$ from (see, e.g., [15])

$$\frac{1}{\beta(1)^2} = \sum_{i=1}^{n} \frac{1}{s_i^2}. \tag{3}$$

If we now change the standard deviation from unity to a value of $\frac{1}{f}$ for all variables x_i, and keep the limit state function as it was, then we can relate this to standardized variables $U_i = fX_i$ such that

$$g(\mathbf{U}) = -\sum_{i=1}^{n} \frac{U_i}{fs_i} + 1, \tag{4}$$

and the reliability index is given by

$$\frac{1}{\beta(f)^2} = \sum_{i=1}^{n} \frac{1}{f^2 s_i^2} = \frac{1}{f^2 \beta(1)^2}. \tag{5}$$

Hence, we observe

$$\beta(f) = f \cdot \beta(1), \tag{6}$$

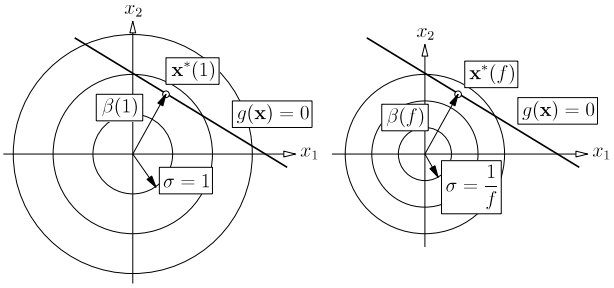

Fig. 1. Linear limit state under scaling of standard deviations.

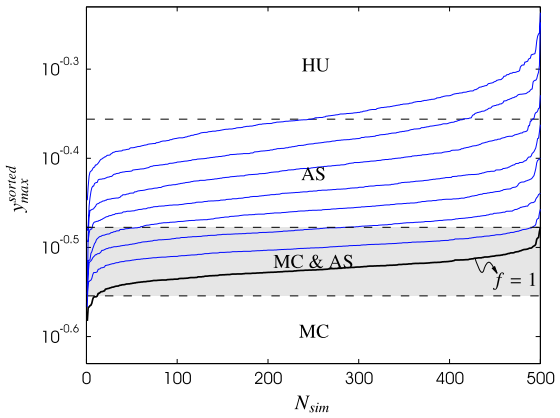

Fig. 2. Schematic plot of sorted maxima of a system for various f values. Black curve: $f = 1$, blue curves: $f < 1$, MC: standard Monte Carlo simulation, AS: asymptotic sampling, HU: high uncertainty. (For interpretation of the references to colour in this figure legend, the reader is referred to the web version of this article.)

in which $\beta(1)$ is the safety index evaluated for $f = 1$. This means that, in order to obtain a good estimate for $\beta(1)$, we can compute the safety index for a smaller value of the scale f using Monte Carlo simulation and then simply extrapolate by multiplying the obtained result by f. Further details are given in [14,15]. The geometric relations are shown in Fig. 1. While this result is exact for linear limit state functions, it holds only asymptotically as $\beta \to \infty$ for general nonlinear cases, as shown by Breitung [16]. Therefore, the concept of asymptotic sampling utilizes the asymptotic behavior of the safety index β by applying an extrapolation and regression technique.

In the first step, a Monte Carlo simulation corresponding to $f = 1$ with N_{sim} samples is performed. Next, the maximum of each realization is stored as $\mathbf{y}_{max}(i) = \max\{y^{(i)}(t)\}$, $t \in [0, T]$, $i = 1, \ldots, N_{sim}$, where $y^{(i)}(t)$ refers to the ith realization of the process. The maximum values of the realizations are then sorted in an incrementing manner denoted as $\mathbf{y}_{max}^{sorted}$. This procedure is then repeated for different values of f. The $\mathbf{y}_{max}^{sorted}$ for different f values are shown schematically in Fig. 2. In Fig. 2, the first region, denoted MC, refers to the standard Monte Carlo region defined as $\mathbf{y}_{max} \in [\min\{\mathbf{y}_{max}^{sorted}(f = 1)\}, \min\{\mathbf{y}_{max}^{sorted}(f < 1)\}[$. The second region, AS & MC, is defined as $y_{max} \in [\min\{\mathbf{y}_{max}^{sorted}(f < 1)\} \max\{\mathbf{y}_{max}^{sorted}(f = 1)\}]$. This region can be used as a check that AS estimates the correct values for $f = 1$. The whole region above, defined as $\mathbf{y}_{max} \in]\max\{\mathbf{y}_{max}^{sorted}(f = 1)\}, \max\{\mathbf{y}_{max}^{sorted}(f < 1)\}]$, is where only asymptotic estimation of failure probability is possible, where the uppermost part might not be used for anything due to the high level of uncertainty. For each barrier level, i.e. each horizontal line in Fig. 2, in the AS region, the sum of the points above the line divided by N_{sim} gives the scaled failure probability with the scaling factor f related to the curve. The reliability index of each barrier level is calculated as $\beta^{initial} = \Phi(1 - p_f^{initial})$. Finally, curve fitting to the obtained β values is performed and is used to obtain $\beta(1)$,

which is used to calculate the probability of exceeding the related barrier level.

2.1. Scale factor increments

The next issue to be dealt with is the way the f values are chosen. Noticing that the response of the system at each time instant is a transformation of the excitation variables, denoted $\mathbf{G}$, the excitation(s) and response processes can be discretized as $\mathbf{W}(k) = \mathbf{W}(t)|_{t=k\Delta t}$ and $\mathbf{X}(k) = \mathbf{X}(t)|_{t=k\Delta t}$, respectively. $k = 0, \ldots, N-1$ corresponds to the continuous time interval $t \in [0, T]$; i.e. $T = (N-1)\Delta t$. The following relationship between excitation and response holds:

$$\mathbf{X}(k) = \mathbf{G}(\boldsymbol{\mathcal{W}}(k)), \tag{7}$$

where $\boldsymbol{\mathcal{W}}(k) = [\mathbf{W}(k), \ldots, \mathbf{W}(0)]$. The transformation is then decomposed into its linear and nonlinear parts $\mathbf{W}(k) = f\tilde{\mathbf{W}}(k)$, which results in

$$\begin{aligned}\mathbf{X}(k) &= \mathbf{X}_{Lin.}(k) + \mathbf{X}_{Nonlin.}(k)\\ &= f\mathbf{G}_{Lin.}(\tilde{\boldsymbol{\mathcal{W}}}(k)) + \mathbf{G}_{Nonlin.}(f\tilde{\boldsymbol{\mathcal{W}}}(k)),\end{aligned} \tag{8}$$

where $\tilde{\boldsymbol{\mathcal{W}}}(k) = [\tilde{\mathbf{W}}(k), \ldots, \tilde{\mathbf{W}}(0)] = f^{-1}\boldsymbol{\mathcal{W}}(k)$ is the scaled counterpart of $\boldsymbol{\mathcal{W}}(k)$ by f. $\tilde{\mathbf{X}}(k) = \mathbf{G}(\tilde{\boldsymbol{\mathcal{W}}}(k))$ can also be decomposed into

$$\begin{aligned}\tilde{\mathbf{X}}(k) &= \tilde{\mathbf{X}}_{Lin.}(k) + \tilde{\mathbf{X}}_{Nonlin.}(k)\\ &= \mathbf{G}_{Lin.}(\tilde{\boldsymbol{\mathcal{W}}}(k)) + \mathbf{G}_{Nonlin.}(\tilde{\boldsymbol{\mathcal{W}}}(k)).\end{aligned} \tag{9}$$

(8) and (9) produce the following relation between normal and scaled responses:

$$f\tilde{\mathbf{X}}(k) = \mathbf{X}(k) + f\mathbf{G}_{Nonlin.}(\tilde{\boldsymbol{\mathcal{W}}}(k)) - \mathbf{G}_{Nonlin.}(f\tilde{\boldsymbol{\mathcal{W}}}(k)). \tag{10}$$

Assuming dominance of the linear part of (10), $\mathbf{X}(k)$, over the nonlinear terms, $f\mathbf{G}_{Nonlin.}(\tilde{\boldsymbol{\mathcal{W}}}(k)) - \mathbf{G}_{Nonlin.}(f\tilde{\boldsymbol{\mathcal{W}}}(k))$, the following applies:

$$E[\mathbf{X}_{Lin.}(k)] \approx fE[\tilde{\mathbf{X}}_{Lin.}(k)]. \tag{11}$$

Therefore, the nth maximum of the stochastic response X sorted in descending order can be scaled up to the required barrier level where the scaling factor is defined as $f^{X_{BL}} = X^{(n)}_{max}/X_{BL}$. However, while using only the linear part of (10) decreases the accuracy of the estimate in general, it does not pose a critical deficiency in the algorithm. This is since the exact "f" value is not necessary and a good estimate of it works as well. Indeed, the better the two nonlinear terms in (10) cancel out each other, i.e. the smaller the term $f\mathbf{G}_{Nonlin.}(\tilde{\boldsymbol{\mathcal{W}}}(k)) - \mathbf{G}_{Nonlin.}(f\tilde{\boldsymbol{\mathcal{W}}}(k))$, the sooner we obtain a certain X_{BL} as the nth maximum according to (11); nevertheless, this requirement will be satisfied anyway. Therefore, (11) is to be seen as a tool which allows finding only a *sensible estimate* of the "f" value which scales up the system responses such that X_{BL} is their nth maximum. The consequence is that some more simulations may be required to reach the required level. The simulations considered in this study witness that (11) works well in this respect. Next, in order to guarantee sufficient points for curve fitting, the domain in which the maxima of the simulations are spread is divided into the minimum desired number of support points in the curve fitting, N^{sp}_{min}, as

$$\frac{\Delta f}{f} = -\frac{2\sigma_f}{\mu_f N^{sp}_{min}}, \tag{12}$$

where $\mu_f = \mathrm{E}[y_{max}(f)]$ and $\sigma_f = \mathrm{E}[y^2_{max}(f) - \mu^2_f]$. The next f value is then calculated as $f + \Delta f$. (12) returns the values within $2\sigma_N$ spread around the mean value of the process. For Gaussian distributed samples, 2σ spread around th mean includes $\mathrm{erf}(1/\sqrt{2}) \times 100 \approx 68\%$ of the points; however, it is obvious that the maxima do not follow a Gaussian distribution but an unknown distribution which is to be estimated. Nevertheless, since only a rough estimate of the range in which the points are located is required, (12) provides a good estimate of the range of maxima. Alternatively,

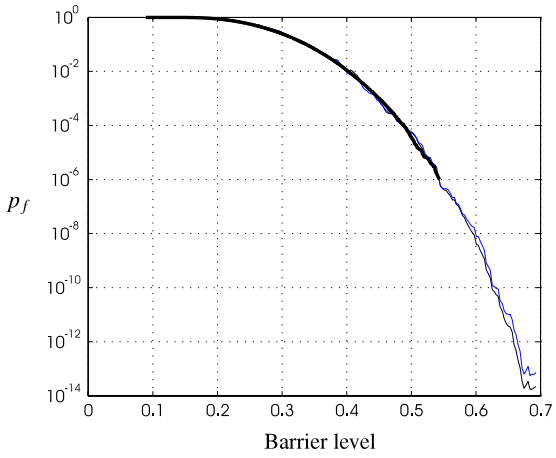

Fig. 3. Comparison of cumulative distribution functions (CDFs) of the Duffing oscillator. Bold black: Monte Carlo estimate, black: AS with $\beta = Af + B/f$, blue: AS with smoothed $\beta = Af + Bf^{-c}$. (For interpretation of the references to colour in this figure legend, the reader is referred to the web version of this article.)

$$\frac{\Delta f}{f} = \frac{\min\{\mathbf{y}^{sorted}_{max}\} - \max\{\mathbf{y}^{sorted}_{max}\}}{N^{sp}_{min}\mu_f + \delta_N\mu_f} \tag{13}$$

could be used instead of (12), where $\delta_N \in \mathbb{N}$ is to ensure the whole range will be covered with the required number of support points. Nevertheless, both (12) and (13) give similar results in this context. In the numerical examples in this paper, $N^{sp}_{min} = 5$ and (12) are used. A conventional choice for δ_N would be 3 if (13) is preferred.

2.2. Scale factor bounds

Next, it is beneficial to also consider a lower bound for f to avoid numerical difficulties, i.e. instability in numerical integration. Considering that 10^3 samples are used in each dynamic analysis, a failure probability of 10^{-2} can be obtained with a coefficient of variation(CoV) of about 0.3. This value for the failure probability gives the reliability index $\beta = \Phi^{-1}(1 - p_f) \approx 2$. The relationship $\beta(f) = f\beta(1)$ [15] shows that in the ideal case a probability of order 10^{-16} can be estimated with 1000 samples with $f \geq 0.2$. However, for real cases, and especially for nonlinear systems, this simple assumption might be used only to provide a practical expected range for f. Therefore, a reasonable range of scaling factor is proposed as $f \in [0.1, 1]$.

2.3. Curve fitting

Originally, it is proposed to use (14) with equal weights on all the points.

$$\beta(f) = Af + \frac{B}{f}. \tag{14}$$

As mentioned in the previous section, a criterion for checking the accuracy of the AS estimation is to predict the failure probability of the MC & AS region, see Fig. 2, by asymptotic sampling. This study shows that, although for most cases the proposed curve provides good estimations of the failure probability in this area (see Fig. 3), for more complicated cases, e.g. a wind turbine (see Fig. 16), the linear curve seems to have some errors in estimating the probability in this area i.e. the black curve shows a noticeable jump from the standard Monte Carlo curve around $p_f = 10^{-2}$. Therefore it is proposed to use a more general curve (15), which

includes (14) as a special case when $c = 1$:

$$\beta(f) = Af + Bf^{-c}, \quad c > 0. \tag{15}$$

It should be mentioned that the process of fitting (15) would be computationally more demanding than fitting (14), although not considerably. Another advantage of (15) is that it allows examining the validity of (14) by checking the values of the power c for different values of the failure probability. In order to check this, plots of c versus N_{points} denoting the number of barrier levels are provided in the paper for all the numerical examples. In almost all cases, clear growth of the power c is observed as the failure probability decreases. In order to make a smooth estimation of failure probabilities, a linear interpolation is then performed on the calculated powers and is used to obtain the failure probability.

3. General nonlinear systems

In all numerical simulations – including the wind turbine model of Section 4 – 500 realizations are simulated for each f value. In the case of the Duffing oscillator, Bouc–Wen oscillators and the wind turbine model, 30, 16, and 32 f values are used, respectively, within the range indicated in Section 2.2. The main computational cost of the algorithm is in dynamic analysis of the systems at hand, while the rest of the procedure, i.e. curve fitting and extrapolation of β values for each barrier level, has rather low computational cost, comparable to one dynamic analysis of the system.

3.1. Duffing oscillator

The first case represents failure probability estimation of a Duffing-type oscillator. The equation of motion of the oscillator is written as

$$\left.\begin{aligned} &\ddot{x}(t) + 2\zeta_n\omega_n\dot{x}(t) + \omega_n^2(x(t))x(t) = w(t) \\ &\omega_n^2(x(t)) = \bar{\omega}_n^2(1 + \epsilon x^2(t)) \end{aligned}\right\}. \tag{16}$$

The linear angular eigenfrequency and damping ratio of the oscillator are chosen as $\bar{\omega}_n = 10\ \mathrm{s}^{-1}$ and $\zeta_n = 0.01$, and the parameter which controls the intensity of the nonlinearity in the model is chosen as $\epsilon = 10$. $w(t)$ is the unit intensity Gaussian white noise with the auto-covariance function $E[w(t)w(t+\tau)] = \delta(\tau)$. The failure probability is to be estimated within the time $t \in [0, 15]$s with $\Delta t = 0.01$ s for different barrier levels. 500 samples are used to calculate the failure probability with the proposed scheme on asymptotic sampling. Fig. 3 shows a comparison of the estimated failure probability of the Duffing model with three different curves. The solid black curve shows the results of a standard Monte Carlo simulation with 10^6 samples. The thin black curve shows the fitting with the curve $\beta(f) = Af + B/f$ with A and B as parameters of the fit. The exponents c of the second fit are plotted for 100 points evaluated as the barrier levels of the model, and are shown in Fig. 4. The blue curve in Fig. 3 shows the results of the fit with the linear interpolated power of Fig. 4. The magnitude of the power in Fig. 4, $c \in [0.7, 1.4]$, suggests that $\beta(f) = Af + B/f$ with power fixed to $c = 1$ might be used as a good candidate for this model, and the predictions are reliable.

3.2. Bouc–Wen oscillator

The second simulation consists of a single-degree-of-freedom (SDOF) Bouc–Wen oscillator excited with non-stationary earthquake excitation modeled as a Kanai–Tajimi filtered modulated white noise. The system's equations of motion are written as

$$\begin{aligned} &m\ddot{x} + c_d\dot{x} + (1-\alpha)kz + \alpha kx = -ma(t) \\ &\dot{z} = A\dot{x} - \beta\dot{x}|z| - \gamma|\dot{x}|z, \end{aligned} \tag{17}$$

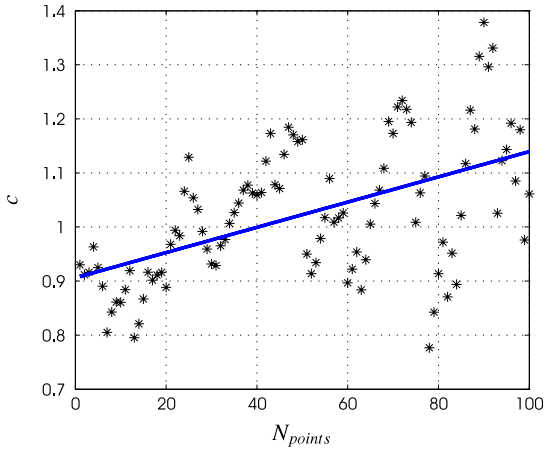

Fig. 4. Exponents c of $\beta(f) = Af + Bf^{-c}$ of the Duffing oscillator. Asterisk: exponents of the fit, line: line fitted to the exponents.

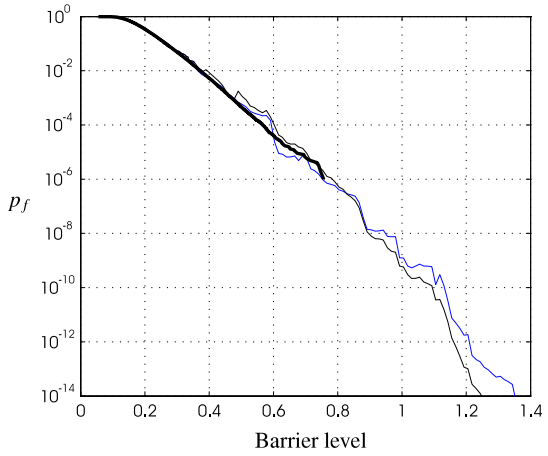

Fig. 5. Comparison of CDFs of the Bouc–Wen oscillator. Bold black: Monte Carlo estimate, black: AS with $\beta = Af + B/f$, blue: AS with smoothed $\beta = Af + Bf^{-c}$. (For interpretation of the references to colour in this figure legend, the reader is referred to the web version of this article.)

where $a(t)$ is the ground acceleration given by

$$\begin{aligned} &\ddot{y} + 2\zeta\omega\dot{y} + \omega^2 y = e(t)w(t) \\ &a(t) = -(2\zeta\omega\dot{y} + \omega^2 y), \end{aligned} \tag{18}$$

where $e(t)$ is the envelope process modeled as

$$e(t) = 4(\exp(-0.25t) - \exp(-0.5t)), \tag{19}$$

and $w(t)$ is a Gaussian white noise process $E[w(t+\tau)w(t)] = Ie^2(t)\delta(\tau)$, where $I = 0.64\ \mathrm{m}^2/\mathrm{s}^4$ is the intensity of the white noise. The parameters of the model are chosen as those used in [15], i.e. $m = 40 \times 10^3$ kg, $k = 1 \times 10^6$ N/m, $c_d = 5 \times 10^3$ N s/m, $\alpha = 0.603$, $\beta = -1.8548$, $\gamma = 39.36$, $A = 5.868$. The failure probability estimated using standard Monte Carlo simulation for barrier level $X_{BL} = 0.64$ with 6×10^5 samples is $p_f = 1.3 \times 10^{-5}$. Fig. 5 shows the failure probability estimation of the model for different barrier levels. Fig. 5 shows a comparison of the estimated failure probability of the Bouc–Wen model with three different curves with the same specifications as described for the Duffing model. The results show that the black curve generally performs well in this case, as well as the Duffing oscillator. Next, the powers of the second fit plotted versus the barrier levels of the model are shown in Fig. 6. The values of $c \in [0.5, 2]$ indicate that for this model the predictions of the original fit are also acceptable.

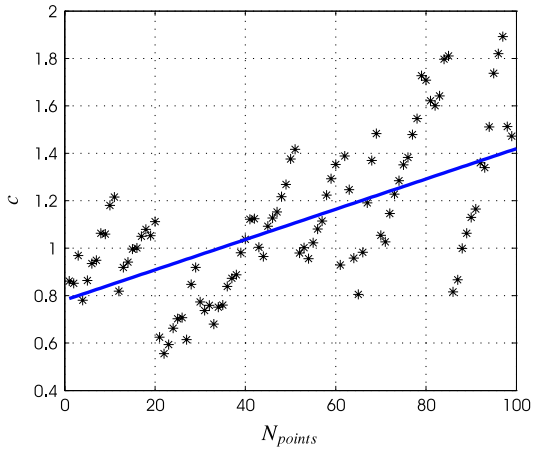

Fig. 6. Exponents "c" of $\beta(f) = Af + Bf^{-c}$ of the Bouc–Wen oscillator. Asterisk: exponents of the fit, line: line fitted to the exponents.

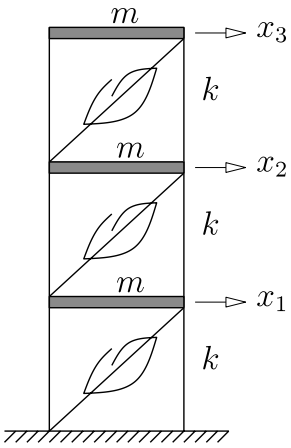

Fig. 7. Three-degree-of-freedom shear frame with Bouc–Wen-type nonlinearity.

3.3. Nonlinear shear frame

A shear-frame-type structure as shown in Fig. 7 subjected to a random ground acceleration $a(t)$ is investigated. The inter-story restoring force r_{ik} is given in terms of the relative displacement $x_{ik} = x_i - x_k$, the relative velocity $\dot{x}_{ik} = \dot{x}_i - \dot{x}_k$, and the internal plastic variables z_i as

$$r_{ik} = (1-\alpha)k(x_i - z_i) + \alpha k x_{ik} + c_d \dot{x}_{ik}. \tag{20}$$

This includes a viscous damper with damping constant c_d. The differential equations governing the state variables are

$$\begin{aligned} \dot{z}_i &= A\dot{x}_{ik} - \beta\dot{x}_{ik}|z_i - x_i| - \gamma|\dot{x}_{ik}|(z_i - x_i) \\ \ddot{x}_i &= -r_{ik}/m - a(t). \end{aligned} \tag{21}$$

The numerical values chosen for the example are the same as previously used in the SDOF Bouc–Wen example. The ground acceleration is a non-stationary Kanai–Tajimi-type random process. The Kanai–Tajimi (K–T) parameters are the same as before. The noise driving the K–T filter has an intensity of 0.0064, i.e. by a factor of 100 smaller than before.

3.3.1. Case 1: absolute displacement of the first story

Fig. 8 shows the cumulative distribution function (CDF) of the shear frame for two different curves fitted to the data of maxima. Fig. 9 shows the change of the power of the second fit, as shown for the previous model in Fig. 6.

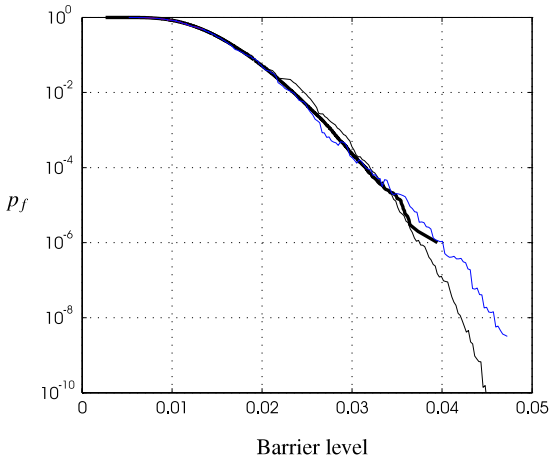

Fig. 8. Comparison of CDFs of the shear frame with Bouc–Wen nonlinearity, case 1. Bold black: Monte Carlo estimate, black: AS with $\beta = Af + B/f$, blue: AS with smoothed $\beta = Af + Bf^{-c}$. (For interpretation of the references to colour in this figure legend, the reader is referred to the web version of this article.)

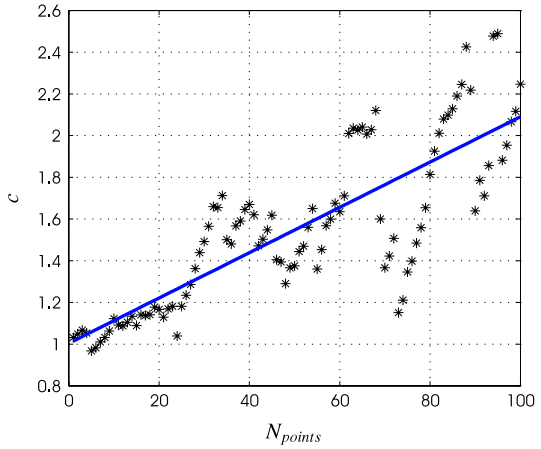

Fig. 9. Exponents c of $\beta(f) = Af + Bf^{-c}$ of the shear frame, case 1. Asterisk: exponents of the fit, line: line fitted to the exponents.

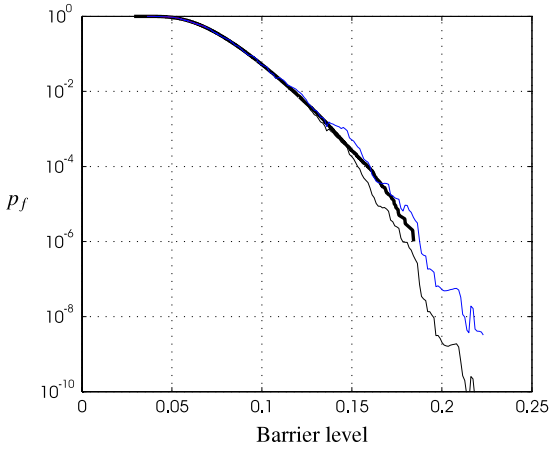

Fig. 10. Comparison of CDFs of the shear frame with Bouc–Wen nonlinearity, case 2. Bold black: Monte Carlo estimate, black: AS with $\beta = Af + B/f$, blue: AS with smoothed $\beta = Af + Bf^{-c}$. (For interpretation of the references to colour in this figure legend, the reader is referred to the web version of this article.)

3.3.2. Case 2: relative displacement of the last story

Fig. 10 shows the CDF of the shear frame for two different curves fitted to the data of maxima. Fig. 11 shows the change of

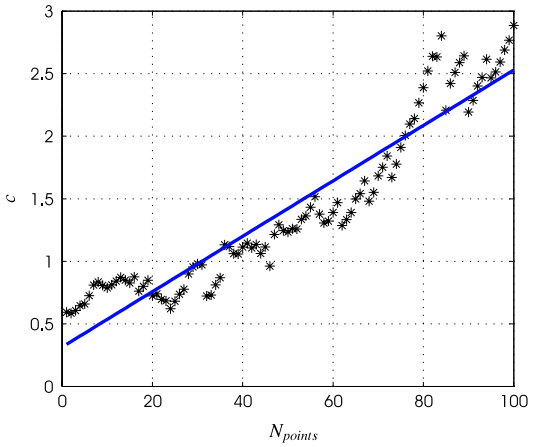

Fig. 11. Exponents c of the $\beta(f) = Af + Bf^{-c}$ of the shear frame, case 2. Asterisk: exponents of the fit, line: line fitted to the exponents.

the power of the second fit, as shown for the previous model in Fig. 6. Comparison of Figs. 9 and 11 with Figs. 4 and 6 shows that the probability distribution function (PDF) of the shear frame has more irregularity than the previous two cases, while the main difference of this model from the previous one, i.e. the SDOF Bouc–Wen oscillator, is the presence of many degrees of freedom, and hence interaction between them. In both cases of the nonlinear shear frame, both curves provide close estimations to the Monte Carlo simulation results down to a failure probability of 10^{-4}. However, the second curve seems to be more accurate in estimating lower probabilities.

4. Failure probability estimation of a nonlinear wind turbine

In order to assess the applicability of the method and reliability of its estimations for wind turbines, a reduced-order model of a wind turbine was developed and its failure probabilities were estimated with the proposed method. In the following sections the developed structural model, aerodynamic loads, wind field, and specifications of the wind turbine are explained in detail. Finally, the failure probabilities of the model are estimated using the proposed method.

4.1. Mechanical model

The motions of the blades relative to the hub and the motion of the tower in the mean wind direction are modeled by single-degree-of-freedom (SDOF) models. Only motions in the mean wind direction are considered, for which reason no gyroscopic forces are present, save the centripetal forces. Let $y_i(x,t)$, $i = 1, 2, 3$ denote the displacement fields of the blades relative to the hub, where $x \in [0, L]$ is measured from the hub and L is the length of the blades of Fig. 12. Further, $y_4(x,t)$ denotes the displacement of the tower in the same direction, where $x \in [0, h]$ is measured from the foundation and h is the height of the nacelle above the ground surface. Then, the indicated displacement fields may be written as

$$\left.\begin{aligned} y_i(x,t) &\simeq \Phi(x) q_i(t), \quad i = 1,2,3 \\ y_4(x,t) &\simeq \Phi_0(x) q_4(t), \end{aligned}\right\} \tag{22}$$

where $\Phi_0(x)$ is the part of the fundamental eigenmode of the wind turbine belonging to the tower and $\Phi(x)$ is the fundamental fixed base mode shape of the blade. The mode shapes are normalized to one at the nacelle and the blade tip, respectively, so the generalized coordinates $q_1(t), q_2(t), q_3(t)$ may be interpreted as

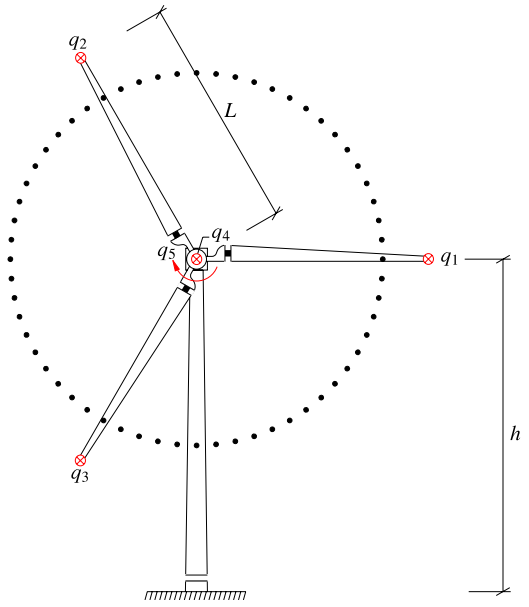

Fig. 12. Definition of degree of freedom section moments and pitch angles.

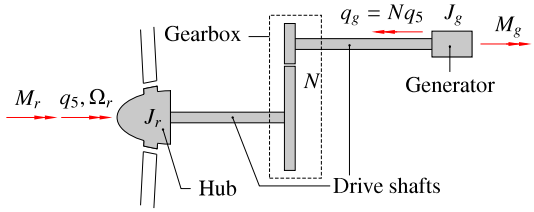

Fig. 13. Single-degree-of-freedom representation of the drive train.

the tip displacement of the blades relative to the hub, and $q_4(t)$ is the displacement of the nacelle. Note that a quasi-static deformation of the nacelle due to the mean rotor thrust will only affect $q_4(t)$. The blades are modeled as Bernoulli–Euler beams with bending stiffness $EI(x)$ around an axis orthogonal to the rotor plane, and mass per unit length $\mu(x)$. Similarly, the tower is modeled as a Bernoulli–Euler beam with bending stiffness $EI_0(x)$. The mass per unit length is formally written as

$$\bar{\mu}_0(x) = \mu_0(x) + M_0 \delta(x - h), \tag{23}$$

where $\mu_0(x)$ denotes the continuous mass distribution, M_0 is the mass of the nacelle and the hub, and $\delta(\cdot)$ is Dirac's delta function. The dynamic load per unit length on the tower in the mean wind direction is denoted $p_4(x,t)$. Correspondingly, the loads on the tree blades in the same direction are denoted $p_1(x,t)$, $p_2(x,t)$, and $p_3(x,t)$. The rigid body motion of the drive train is modeled as a single rotational degree of freedom q_5 by assuming infinite stiff drive shafts and no elastic deformation in the gear, whereby the following kinematic relation emerge for the angular rotation of the rotor of the generator:

$$q_g = Nq_5, \tag{24}$$

where N is the gear ratio; see Fig. 13. Furthermore, the mass moments of inertia of the gear wheels and the connected shafts are included in the mass moments of inertia J_r and J_g of the rotor and the generator rotor, respectively. Using Lagrange's equations [18], the following governing equations of the system may be obtained:

$$\mathbf{m}\ddot{\mathbf{q}}(t) + \mathbf{c}\dot{\mathbf{q}}(t) + \mathbf{k}\mathbf{q}(t) = \mathbf{f}(t) \tag{25}$$

$$\mathbf{m} = \begin{bmatrix} m_1 & 0 & 0 & m_2 & 0 \\ 0 & m_1 & 0 & m_2 & 0 \\ 0 & 0 & m_1 & m_2 & 0 \\ m_2 & m_2 & m_2 & m_0 & 0 \\ 0 & 0 & 0 & 0 & J \end{bmatrix}$$

$$\mathbf{k} = \begin{bmatrix} k & 0 & 0 & 0 & 0 \\ 0 & k & 0 & 0 & 0 \\ 0 & 0 & k & 0 & 0 \\ 0 & 0 & 0 & k_0 & 0 \\ 0 & 0 & 0 & 0 & 0 \end{bmatrix} \tag{26}$$

$$\left.\begin{aligned} m &= \int_0^L \mu(x)\mathrm{d}x \\ m_1 &= \int_0^L \mu(x)\Phi^2(x)\mathrm{d}x \\ m_2 &= \int_0^L \mu(x)\Phi(x)\mathrm{d}x \\ m_3 &= \int_0^L x\mu(x)\mathrm{d}x \\ m_4 &= \int_0^L x\mu(x)\Phi(x)\mathrm{d}x \\ m_5 &= \int_0^h x\mu_0(x)\Phi_0(x)\mathrm{d}x \\ m_0 &= \int_0^h \mu_0(x)\Phi_0^2(x)\mathrm{d}x + M_0 + 3m \\ J_r &= \int_0^L x^2\mu(x)\mathrm{d}x \end{aligned}\right\}, \tag{27}$$

where m is the mass of the blade, and m_0 and m_1 are the generalized masses related to the degrees of freedom $q_i(t)$, $i = 1, \ldots, 4$. m_2 is a coupling parameter in the mass matrix, and m_3, m_4, and m_5 will be used later in the calculation of the bending moments in the blade at the hub and in the lower foundation. J is the generalized mass moment of inertia related to the rigid-body degree of freedom $q_5(t)$, given as

$$J = J_r + N^2 J_g. \tag{28}$$

The damping matrix $\mathbf{c}$ merely includes structural damping. Aerodynamic damping is included later via the aerodynamic load. Then $\mathbf{c}$ may be written as

$$\mathbf{c} = \begin{bmatrix} 2\zeta\omega m_1 & 0 & 0 & 0 & 0 \\ 0 & 2\zeta\omega m_1 & 0 & 0 & 0 \\ 0 & 0 & 2\zeta\omega m_1 & 0 & 0 \\ 0 & 0 & 0 & 2\zeta_0\omega_0 m_0 & 0 \\ 0 & 0 & 0 & 0 & \eta M_{r,0}/\Omega_{r,0} \end{bmatrix} \tag{29}$$

$$\mathbf{q}(t) = \begin{bmatrix} q_1(t) \\ q_2(t) \\ q_3(t) \\ q_4(t) \\ q_5(t) \end{bmatrix} \qquad \mathbf{f}(t) = \begin{bmatrix} f_1(t) \\ f_2(t) \\ f_3(t) \\ f_4(t) \\ f_5(t) \end{bmatrix}, \tag{30}$$

where $\Omega_{r,0} = \dot{q}_{5,0}$ is the referential (nominal) rotational speed of the rotor. ω and ζ denote the eigenfrequency and damping ratio of the blades, when fixed to the hub. Correspondingly, ω_0 and ζ_0 denote the eigenfrequency and damping ratio of the lowest mode of the tower, which are assumed to be known. η is the loss factor of the transmission system due to friction in the gears and bearings, which typically is a few percent, and $M_{r,0} = P/\Omega_{r,0}$ is the referential rotor torque for $P = 5$MW nominal power output.

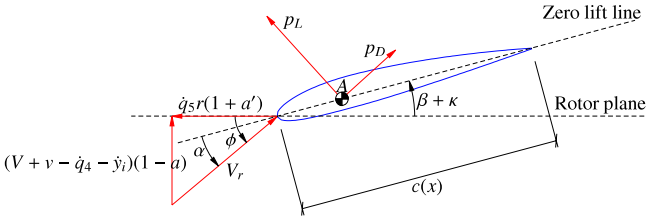

Fig. 14. Blade profile definition of velocities and forces.

The generalized stiffness coefficients of the blades and the tower are given as

$$\left.\begin{aligned} k &= \omega^2 m_1 \\ k_0 &= \omega_0^2 m_0 \end{aligned}\right\}. \tag{31}$$

k_0 is determined, so the generalized eigenvalue problem defined from (26) provides the prescribed angular lower eigenfrequency ω_0. The generalized external dynamic loads become

$$\left.\begin{aligned} f_i(t) &= \int_0^L \Phi(x)p_i(x,t)\mathrm{d}x, \quad i = 1,2,3 \\ f_4(t) &= \int_0^h \Phi_0(x)p_4(x,t)\mathrm{d}x + \sum_{i=1}^{3}\int_0^L \Phi(x)p_i(x,t)\mathrm{d}x \\ f_5(t) &= M_r - (1-\eta)NM_g \end{aligned}\right\}, \tag{32}$$

where M_r and M_g are the instantaneous rotor and generator torques, respectively, and an asynchronous slip variable generator is considered for which the generator torque under normal operation conditions is linearly dependent on the rotational speed $N\dot{q}_5(t)$. The relation may be given in the form

$$M_g(t) = M_{g,0}\frac{N\dot{q}_5(t) - \Omega_{g,00}}{\Omega_{g,0} - \Omega_{g,00}}, \tag{33}$$

where $M_{g,0} = M_{r,0}/N$ is the nominal generator torque, $\Omega_{g,0} = N\Omega_{r,0}$ is the nominal generator rotational speed, and $\Omega_{g,00}$ is the generator speed for the zero generator torque.

4.2. Load modeling

Only the aerodynamic load on the blades is considered, i.e. the wind load on the tower is ignored; $p_4(x,t) = 0$. Aerodynamic damping is included via a quasi-static effective angle of attack $\alpha(x,t)$, so changes of the angle of attack are instantly felt in the aerodynamic loads. This means that the time scale for adjustment of the non-stationary flow is assumed to be small compared to the fundamental eigenperiod of the blade. The wind loads are calculated by the Blade Element Momentum (BEM) method; see [19]. In this respect, the following parameters are defined:

$$\begin{aligned} V_r(x,t) &= \sqrt{(V+v-\dot{q}_4-\dot{y}_i)^2(1-a)^2 + \dot{q}_5^2 r^2(1+a')^2} \\ \phi(x,t) &= \arctan\left(\frac{(1-a)(V+v-\dot{q}_4-\dot{y}_i)}{(1+a')\dot{q}_5 r}\right) \\ \alpha(x,t) &= \phi(x,t) - \beta_i(t) - \kappa(x). \end{aligned} \tag{34}$$

V_r is the relative wind speed (see Fig. 14). V denotes the mean wind speed, and v is the turbulence contribution to the wind speed. The turbulence with a prescribed correlation structure is generated at 30 points on a circle with radius $0.8L$, as seen in Fig. 12. Next, the turbulence on a given blade is obtained by linear interpolation between the given points. The interpolated turbulence value is assumed common to all points on the blade. The mean wind speed V is assumed constant over the rotor area. a and a' are the axial and the tangential induction factors, respectively, which are calculated below by means of the BEM method, and $\dot{q}_4 + \dot{y}_i(x,t)$, where

Table 1
Structural parameters of the wind turbine model.

h	87.6 m	ζ_0	0.01
L	61.5 m	ζ	0.005
m	17,415 kg	ω	4.2 rad/s
m_0	404,520 kg	ω_0	2.0 rad/s
m_1	791 kg	η	0.05
m_2	1893 kg	ρ	1.25 kg/m^3
m_3	359,304 kg m	$\Omega_{r,0}$	1.27 rad/s
m_4	83,228 kg m	$M_{r,0}$	3946,018 N m
m_5	6100,058 kg m	υ	0.2
J_r	35,337,324 kg m^2	$\Omega_{g,00}$	73.7 rad/s
J_g	535 kg m^2	V_h	15 m/s
N	97	V_r	10.72 m/s
M_0	296,780 kg	V_o	25 m/s
k	14,120 N/m	V_i	5 m/s
k_0	1667,914 N/m		

$\dot{y}_i(x,t) = \Phi(x)\dot{q}_i(t)$ indicates the velocity of the cross-section of the abscissa x in the direction of the mean wind. This term is responsible for the aerodynamic damping of the blades and the turbine as a whole. ϕ is the so-called flow angle, and $\kappa = \kappa(x)$ denotes the pre-twist of the blade. The lift and drag force per unit of the blade $p_L(x,t)$ and $p_D(x,t)$ are given as

$$\left.\begin{aligned} p_L(x,t) &= \frac{1}{2}\rho V_r^2(x,t)C_L(\alpha)c(x) \\ p_D(x,t) &= \frac{1}{2}\rho V_r^2(x,t)C_D(\alpha)c(x) \end{aligned}\right\}, \tag{35}$$

where ρ is the density of air, $c(x)$ is the chord length, and $C_L(\alpha)$ and $C_D(\alpha)$ are the lift and drag coefficients. The load in the normal direction of the plane becomes

$$p_i(x,t) = \frac{1}{2}\rho V_r^2(x,t)C_N(\alpha)c(x), \tag{36}$$

where $C_N(\alpha)$ is the normal coefficient. $C_N(\alpha)$ and the corresponding tangential coefficient $C_T(\alpha)$ for the determination of the rotor torque are obtained from (see Fig. 14)

$$\begin{bmatrix} C_N \\ C_T \end{bmatrix} = \begin{bmatrix} \cos\phi & \sin\phi \\ \sin\phi & -\cos\phi \end{bmatrix} \begin{bmatrix} C_L \\ C_D \end{bmatrix}. \tag{37}$$

a and a' are then obtained as

$$a = \frac{1}{1+\frac{4F\sin^2\phi}{\sigma C_N}}, \qquad a' = \frac{1}{1+\frac{4F\sin\phi\cos\phi}{\sigma C_T}}, \tag{38}$$

where F is the Prandtl tip loss factor, given as

$$F = \frac{2}{\pi}\cos^{-1}\left(\exp\left(-\frac{B}{2}\frac{L-x}{x\sin\phi}\right)\right), \tag{39}$$

where $B = 3$ is the number of blades. The above procedure needs to be iterated until convergence of the induction factors has been achieved.

4.3. Wind modeling

Various wind speed distribution functions are used in the simulation of wind loads: log-normal, Gumbel, etc. Nevertheless, the IEC standard [20,21] recommends that the mean wind speed over a time period of 10 min at the hub height is Rayleigh distributed with the following PDF:

$$f_V(\mathrm{V}_h) = \frac{\pi \mathrm{V}_h}{2\mathrm{V}_a^2}\exp\left[-\pi\left(\frac{\mathrm{V}_h}{2\mathrm{V}_a}\right)^2\right], \tag{40}$$

where $\mathrm{V}_a = 0.2\mathrm{V}_{10}$ and V_h is the wind speed at the hub height. Next, it is assumed that the mean wind speed in terms of height obeys the following power profile, where υ is given in Table 1:

$$\mathrm{V}(z) = \mathrm{V}_h\left(\frac{z}{h}\right)^{\upsilon}. \tag{41}$$

In this work, it is assumed that the mean wind velocity V is constant over the rotor area. The governing equations of the system are usually represented in the state space form, so it is advantageous if the load is represented in the same form. Moreover, implementation and change of turbulence level with such loading is very easy and fast. A calibrated ARMA model might be represented in the state space format [22]; alternatively, a state space model for turbulence might be calibrated directly using the stochastic subspace modelling (SSM) method [23], which discards this transformation. The SSM method is even more attractive, since its model seems to be more accurate, stable, and with shorter memory (lower model order) than an ARMA model [23]. Accordingly, in this work, this method is used to calibrate a state space model for the turbulence. The SSM shows the way to find four matrices $\mathbf{A}_T$, $\mathbf{B}_T$, $\mathbf{C}_T$, and $\mathbf{D}_T$ of the state space model (48) such that the output of the model, $\mathbf{v}(j)$, simulates turbulence realizations while the input is only Gaussian distributed stochastic variables, e.g. $\Xi(j)$. The method finds these matrices through matching the cross-covariance function of the model output $\mathbf{v}(j)$ with the function prescribed for it, i.e. the cross-covariance function of the turbulence here. Provided that the auto spectral density of the turbulence is chosen, i.e. the double sided Kaimal auto-spectral density function (42),

$$\left.\begin{aligned} S_{vv}(\mathbf{z}_1,\mathbf{z}_2;\omega) &= \frac{1}{V_h}F\left(\frac{\omega}{V_h}\right) \\ F(k) &= \frac{\sigma_v^2}{\gamma}\frac{L}{(1+|Lk|)^{5/3}} \end{aligned}\right\}, \tag{42}$$

where σ_v is the standard deviation of the turbulence, L is the correlation length, and γ is a normalization parameter, given as

$$\left.\begin{aligned} \sigma_v &= 2.18\,V_* \\ L &= 5.25\,h \\ \gamma &= 3 \end{aligned}\right\}. \tag{43}$$

V_* is the friction velocity, given as $V_* = V_{10}k_t\kappa$, where V_{10} is the mean wind velocity at 10 m, $k_t = 0.17$ is a friction coefficient, and $\kappa = 0.40$ is von Karman's constant. The cross-spectral density might then be calculated using

$$S_{vv}(\mathbf{z}_1,\mathbf{z}_2;\omega) = \gamma_{vv}(\mathbf{z}_1,\mathbf{z}_2;\omega)S_{vv}^{\frac{1}{2}}(\mathbf{z}_1;\omega)S_{vv}^{\frac{1}{2}}(\mathbf{z}_2;\omega), \tag{44}$$

where $\gamma_{vv}(\mathbf{z}_1,\mathbf{z}_2;\omega)$ is the so-called coherence function. Among various possibilities for the turbulence coherence function, the following function, proposed by Shiotani and Iwayani [24], is used:

$$\gamma(\mathbf{z}_1,\mathbf{z}_2;\omega) = \exp\left(-\frac{|\omega|\sqrt{\mathbf{z}_1^2+\mathbf{z}_2^2}}{V_h}d_1\right) \times \exp\left(\mathrm{i}\frac{\mathrm{s}(\mathbf{z}_1,\mathbf{z}_2)\omega\sqrt{\mathbf{z}_1^2+\mathbf{z}_2^2}}{V_h}d_2\right). \tag{45}$$

The non-dimensional parameters d_1 and d_2 are given as $d_1 \simeq 1.5$ and $d_2 \simeq 1.3$ [24]. Next, the inverse Fourier transformation of the cross-spectral density provides the cross-covariance of the turbulence:

$$\kappa_{vv}(\mathbf{z}_1,\mathbf{z}_2;\tau) = \int_{-\infty}^{\infty} \mathrm{e}^{\mathrm{i}\omega t}\,S_{vv}(\mathbf{z}_1,\mathbf{z}_2;\omega)\,\mathrm{d}\tau. \tag{46}$$

A state space model (primarily) of the form (47) can be constructed with the SSM. The quadruple $(\mathbf{A}_T, \mathbf{K}_T, \mathbf{C}_T, \mathbf{R}_T)$ required for the

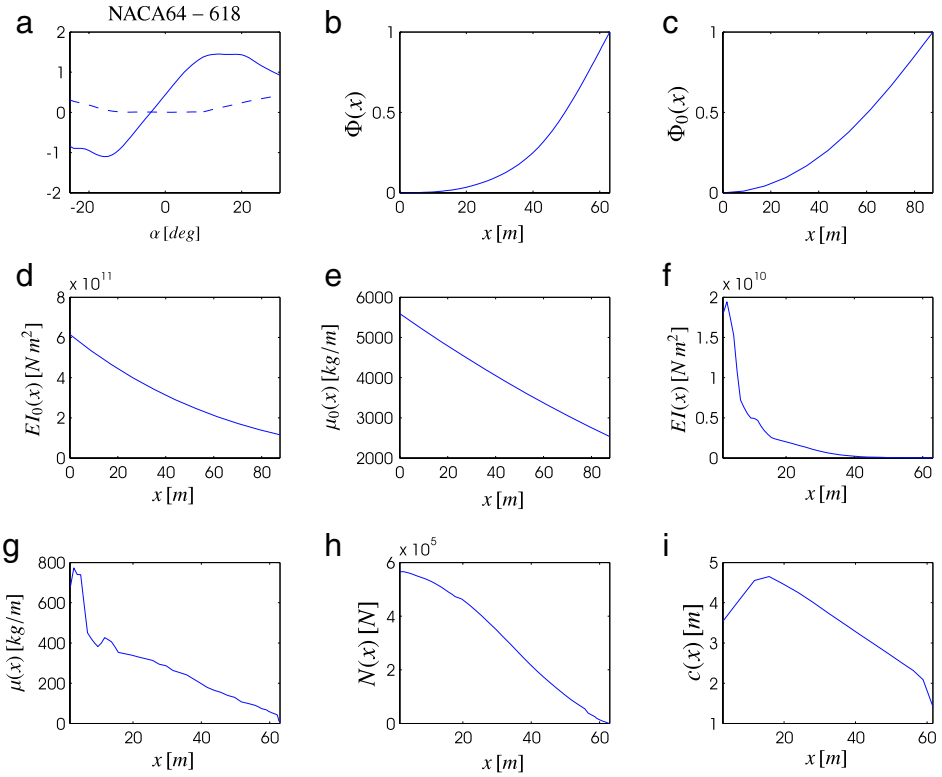

Fig. 15. Structural properties of the NREL 5 MW wind turbine. (a) —: lift coefficient of the NACA64-618, - - -: drag coefficient of the NACA64-618, (b) blade's mode shape, (c) tower's mode shape, (d) bending stiffness of the tower, (e) mass per unit length of the tower, (f) bending stiffness of the blade, (g) blade's mass per unit length, (h) blade's inertial load, (i) blade's cord length.

model is found by the SSM such that the cross-covariance function of (47) matches best to the cross-covariance function of the turbulence obtained from (46). Here, $\mathbf{x}(j+1)$ is an internal state vector at each discrete time step, $\mathbf{A}_T$ and $\mathbf{C}_T$ are system matrices, and $\mathbf{K}_T$ is the steady-state Kalman gain matrix. $\mathbf{e}(j)$ is a random excitation vector characterized with its covariance matrix, $E[\mathbf{e}(j)\mathbf{e}^T(j)] = \mathbf{R}_T$, and $\mathbf{v}(j)$ is the q-dimensional vector of turbulence realizations on the discretized nodes of the rotor plane.

$$\begin{aligned}\mathbf{x}(j+1) &= \mathbf{A}_T\mathbf{x}(j) + \mathbf{K}_T\mathbf{e}(j)\\ \mathbf{v}(j) &= \mathbf{C}_T\mathbf{x}(j) + \mathbf{e}(j).\end{aligned} \tag{47}$$

Next, (47) can be written in the form of (48), in which the $\boldsymbol{\Xi}(j) \sim N(0, \mathbf{I})$ are mutually independent unit intensity Gaussian white noise variables, and $\boldsymbol{\Phi}_T$ is a square matrix which satisfies $\mathbf{e}(j) = \boldsymbol{\Phi}_T\boldsymbol{\Xi}(j)$. $\boldsymbol{\Phi}_T$ can be obtained by any decomposition of the covariance matrix of the noise such that $\mathbf{R}_T = \boldsymbol{\Phi}_T\boldsymbol{\Phi}_T^T$, i.e. Cholesky decomposition. Then $\mathbf{B}_T = \mathbf{K}_T\boldsymbol{\Phi}_T$ and $\mathbf{D}_T = \boldsymbol{\Phi}_T$.

$$\begin{aligned}\mathbf{x}(j+1) &= \mathbf{A}_T\mathbf{x}(j) + \mathbf{B}_T\boldsymbol{\Xi}(j)\\ \mathbf{v}(j) &= \mathbf{C}_T\mathbf{x}(j) + \mathbf{D}_T\boldsymbol{\Xi}(j).\end{aligned} \tag{48}$$

The presented approach for turbulence modeling does not take into account the rotational sampling effect of the turbulence process. Therefore one needs to make an interpolation as the blades pass through different turbulence nodes in between two nodes.

4.4. Model specifications

The structural properties of the tower and the blades are adopted from the definitions of the NREL 5MW wind turbine [25,26], and are given in Table 1, along with the derived parameters entering the reduced model. The fundamental undamped fixed bay angular eigenfrequency, ω, and eigenmode, $\Phi(x)$, of the blades are determined by finite element (FE) analysis, in which the blade is discretized in 49 Bernoulli–Euler beam elements with piecewise constant bending stiffness EI and mass per unit length μ. The variation of EI and μ is shown in Fig. 15. The blade has seven different airfoil profiles from stem to tip [25]; nevertheless, in Fig. 15, the lift and drag coefficients of only the tip profile are shown as an example. The lift and drag coefficients for each profile are interpolated with two piecewise polynomials, each of order 9, in two different intervals of α. The two fitting intervals for the lift and drag coefficients are chosen so as to allow the best overall fit, i.e. the least sum of squared error (SSE), for all data points.

Similarly, the eigenmode $\Phi_0(x)$ of the tower is determined by FE analysis, in which the tower is discretized into ten Bernoulli–Euler

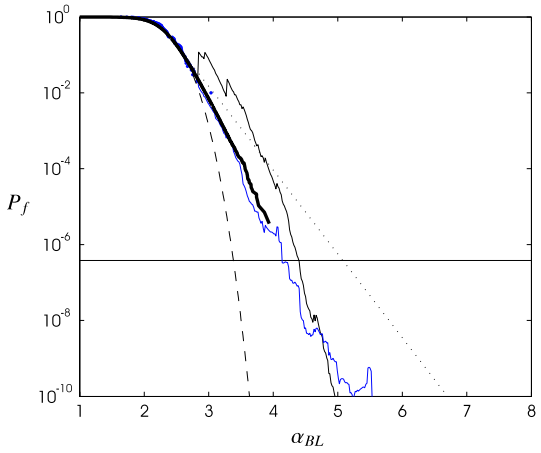

Fig. 16. Estimated failure probability of the wind turbine for a fixed-speed wind turbine. Dots: maxima of 100 epochs, —: 50-year recurrence period, bold black: Monte Carlo simulation, - -: three-parameter Weibull distribution, ···: Gumbel distribution, black: AS with $\beta = Af + B/f$, blue: AS with smoothed $\beta = Af + Bf^{-c}$. (For interpretation of the references to colour in this figure legend, the reader is referred to the web version of this article.)

Table 2
Blade aerodynamic properties.

Node (-)	Location	Element length (m)	Airfoil
1	2.8667	2.7333	Cylinder
2	5.6000	2.7333	Cylinder
3	8.3333	2.7333	Cylinder
4	11.7500	4.1000	DU40A17
5	15.8500	4.1000	DU35A17
6	19.9500	4.1000	DU35A17
7	24.0500	4.1000	DU30A17
8	28.1500	4.1000	DU25A17
9	32.2500	4.1000	DU25A17
10	36.3500	4.1000	DU21A17
11	40.4500	4.1000	DU21A17
12	44.5500	4.1000	NACA64A17
13	48.6500	4.1000	NACA64A17
14	52.7500	4.1000	NACA64A17
15	56.1667	2.7333	NACA64A17
16	58.9000	2.7333	NACA64A17
17	61.6333	2.7333	NACA64A17

beam elements, with piecewise constant bending stiffness and mass per unit length. The mass of the nacelle and the blades $M_0 + 3m$ is attached as a point mass at the free end. The variation of the bending stiffness and the mass per unit length is shown in Fig. 15. The rated wind speed of the model, i.e. the wind speed at which the nominal power is produced, is $V_r = 10.72$ m/s, as indicated in Table 1. For values other than this value, the rotor speed is set to its nominal value. The turbulence is generated in 31 nodes on the rotor plane, as shown in Fig. 12: there is one node on the hub and 30 nodes on the perimeter of rotor plane at $0.8L$ distance from the hub. The turbulence value between the nodes are interpolated from these nodes. The aerodynamic properties of the blades are given in Table 2.

4.5. Failure probability estimation

Failure probability estimation of the represented wind turbine is a highly nonlinear problem due to the presence of the nonlinearity in the aerodynamic load modeling described in 4.2. Moreover, even with a very coarse time integration increment such as $\Delta t = 0.2$ s, 600 s of modeling assuming 200 s of transient response needs 4000 discretized time samples, i.e. $t_s = 200$ s and $t \in [0, t_{end}]$, where $t_{end} = 800$ s. However, since the wind field is simulated on 31 spatially coherent nodes, the total number of stochastic variables, i.e. the dimension of the problem, becomes 124,000. The failure event in this case is defined as the magnitude of the tower tip deflection exceeding a certain barrier level $q_4^{BL} = \mu_{q_4} + \alpha_{BL}\sigma_{q_4}$, i.e. $F(q_4^{BL}) = \{\exists\, t \in [t_s, t_{end}]; |q_4(t)| \geq q_4^{BL}\}$. The mean value and standard deviation of the tower tip deflection are $\mu_{q_4} = 0.23$ m and $\sigma_{q_4} = 0.03$ m, respectively, for the developed model. The simultaneous presence of strong nonlinearities, high dimensions, and multiple excitations in this problem create a difficult case for failure probability estimation that faces critical difficulties for any of the grey-box methods. The failure probability of this system is estimated using the proposed asymptotic scheme, and the results are compared with those of the well-known peak over threshold (POT) method, based on fitting extreme value distributions to the maxima of 100 simulated epochs .

4.5.1. Peak over threshold (POT)

The so-called peak over threshold (POT) method has been used frequently in the wind engineering industry for estimation of the reliability of wind turbines [27]. It can be shown that if the parent distribution of the outcrossing event is one of the extreme value distributions, then outcrossing above a sufficiently large level follows a generalized Pareto (GP) distribution [28]. The most

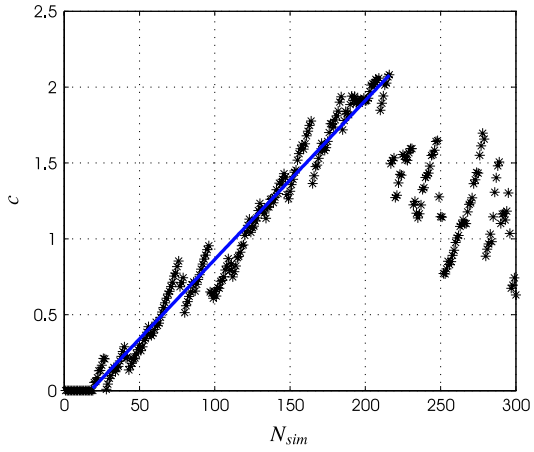

Fig. 17. Exponents c of $\beta(f) = Af + Bf^{-c}$ of the wind turbine. Asterisk: exponents of the fit, line: line fitted to the exponents.

controversial part of the method is the selection of the type of distribution which should be fitted to the data. This selection has high impact on the further analysis which is to be made based on such extrapolations. For instance, it is reported by some authors that incorporation of the Gumbel distribution results in very low safety levels for structures subjected to wind load rather than to gravity load, [27,29]. On the other hand, it is known that extrapolations based on a Weibull distribution will always lead to lower values for design loads [30], for which reason a Weibull distribution might be a proper candidate to be used instead. From a practical point of view, the Gumbel distribution is among the most popular distributions for the wind speed [31,32]. Simiu et al. [33] analyzed 100 wind records from different stations and fitted the distribution to the dynamic wind pressure, as an alternative to the wind speed, and concluded that the Weibull distribution fits the dynamic pressure of the wind better than the Gumbel distribution. It cannot be said for certain which distribution should be used since Weibull, Gumbel, and log-normal distributions have all been used by different authors [34,35]. Therefore, in agreement with wind turbine code of practice IEC 61400-1, both the three-parameter Weibull and Gumbel distributions were chosen in this context, and were fitted to the data. 100 epochs with a duration of 600 s were simulated and the candidate distributions were fitted to the extracted maxima. The data and the fits for the wind turbine model normalized by the mean value and standard deviation of the tower tip deflection are shown in Fig. 16.

4.5.2. Proposed method

Failure probability estimations of the proposed method are also shown in Fig. 16 with the black and blue curves as defined in previous numerical examples. As was already observed for the shear frame case, the power of the fitted curve might have various values, determined only by the behavior of the model. The powers of the fitted curves and the regression lines fitted to them for this model are shown in Fig. 17. Based on the scheme in which the points of the power of the fitting are scattered, points which seem to have a linear correlation are chosen and a line is fitted to them in the least square sense. These points provide enough information for estimation of the failure probabilities down to 10^{-10}. For this model, the power growth shows good correlation with the line fitted to it. However, it is observed that the black curve related to the original fit has a considerable jump in rather high failure probability area, i.e. the AS & MC region in Fig. 2, which shows that the estimations of this curve might lack some accuracy in this case. The results of the Monte Carlo simulation with 4×10^5 samples are shown in Fig. 16 by a solid black line. Comparison of this curve with

the other curves reveal that the second fit gives results that are very close to those of the Monte Carlo simulations.

5. Conclusions

The new asymptotic sampling scheme introduced in this paper has some advantages over previous schemes. First, it discards the optimization needed for calibrating the f factor, which decreases the computational cost of the algorithm. Second, it provides all of the failure probabilities of the system, down to the smallest. Modifications of the asymptotic expansion of the failure probability estimation are proposed which enhance the estimation results. The low computational cost, very low memory requirements, and capability of handling high-dimensional highly nonlinear problems make the proposed algorithm a good candidate for application in real large-scale problems. As an instance, the failure probabilities of a reduced-order model of a wind turbine exposed to a spatially correlated turbulent wind field has been estimated with success. This is an example of a problem which cannot be handled either by standard Monte Carlo simulation, due to excessively high computational time, or by most of the controlled Monte Carlo methods available in the literature, due to the simultaneous presence of model complexity, strong nonlinearities, and very high dimensions.

Acknowledgment

The Danish Energy Authority is acknowledged for support under grant EFP07-II, Estimation of Extreme Responses and Failure Probability of Wind Turbines under Normal Operation by Controlled Monte Carlo Simulation.

References

[1] Schuëller GI, Pradlwarter HJ. Benchmark study on reliability estimation in higher dimensions of structural systems an overview. Structural Safety 2007; 29:167–82.
[2] Schuëller GI, Pradlwarter HJ. Uncertain linear systems in dynamics: retrospective and recent developments by stochastic approaches. Engineering Structures 2009;31:2507–17.
[3] Au SK, Beck JL. Important sampling in high dimensions. Structural Safety 2003; 25:139–63.
[4] Katafygiotis LS, Zuev KM. Geometric insight into the challenges of solving high-dimensional reliability problems. Probabilistic Engineering Mechanics 2008;23:208–18.
[5] Valdebenito MA, Pradlwarter HJ, Schuëller GI. The role of the design point for calculating failure probabilities in view of dimensionality and structural nonlinearities. Structural Safety 2010;32:101–11.
[6] Schuëller GI, Pradlwarter HJ, Koutsourelakis PS. A critical appraisal of reliability estimation procedures for high dimensions. Probabilist Engineering Mechanics 2004;19(4):463–74.
[7] Pradlwarter HJ, Schuëller GI. Local domain Monte Carlo simulation. Structural Safety 2010;32:275–80.
[8] Macke M, Bucher C. Importance sampling for randomly excited dynamical systems. Journal of Sound and Vibration 2003;268:269–90.
[9] Au SK, Lam HF, Ng CT. Reliability analysis of single-degree-of-freedom elastoplastic systems. I: critical excitations. Journal of Engineering Mechanics 2007;133(10):1072–80.
[10] Pradlwarter HJ, Schuëller GI, Koutsourelakis PS, Charmpis 1,DC. Application of line sampling simulation method to reliability benchmark problems. Structural Safety 2007;29:208–21.
[11] Schuëller GI. In: Frangopol Dan, editor. Computational stochastic dynamics some lessons learned. Taylor & Francis; 2008 (Chapter 1).
[12] Au SK, Beck JL. Estimation of small failure probability in high dimensions by subset simulation. Probabilistic Engineering Mechanics 2001;16:263–77.
[13] Ching J, Beck JL, Au SK. Hybrid subset simulation method for reliability estimation of dynamical systems subject to stochastic excitation. Probabilistic Engineering Mechanics 2005;20:199–214.
[14] Bucher C. Computational analysis of randomness in structural mechanics. 1 edition CRC Press; 2009. April 2.
[15] Bucher C. Asymptotic sampling for high-dimensional reliability analysis. Probabilistic Engineering Mechanics 2009;24:504–10.
[16] Breitung KW. Asymptotic approximations for multinormal integrals. Journal of Engineering Mechanics 1984;110(3):357–66.
[17] Breitung KW. Asymptotic approximations for probability integrals. Probabilistic Engineering Mechanics 1989;4(4):187–90.
[18] Meirovitch L. Fundamentals of vibration. McGraw-Hill; 2001.
[19] Hansen MLO. Aerodynamics of wind turbines. Earthscan Publications Ltd.; 2001.
[20] IEC, Technical Committee 88. Amendment to the IEC 61400-1:2005 standard. International Electrotechnical Commission. IEC Technical Committee 88. Wind Turbines; 2009.
[21] IEC 61400-1 International Standard. Wind turbines Part 1: Design requirements. third ed. Reference number IEC 61400-1:2005(E). 2005.
[22] Akaik H. Markovian representation of stochastic processes and its application to the analysis of autoregressive moving average processes. Annals of the Institute of Statistical Mathematics 1974;26(1):363–87.
[23] Sichani MT, Pedersen BJ, Nielsen SRK. Stochastic subspace modelling of turbulence. World Academy of Science, Engineering and Technology. Proceedings 2010;58:1140–8.
[24] Shiotani M, Iwayani Y. Correlation of wind velocities in relation to the gust loadings. In: Proceedings of the 3rd conference on wind effects on buildings and structures. 1971.
[25] Jonkman J, Butterfield S, Musial W, Scott G. Definition of a 5-MW reference wind turbine for offshore system development. National Renewable Energy Laborator; 2009.
[26] Kooijman HJT, Lindenburg C, Winkelaar D, van der Hooft EL. Aero-elastic modelling of the DOWEC 6 MW pre-design in PHATAS. Energy research center of the Netherlands. DOWEC 10046_009, ECN-CX–01-135; September 2003.
[27] Simiu E, Heckert NA. Extreme wind distribution tails: a Peaks over Threshold approach. Journal of the Structural Engineering 1996;122(5):539–47.
[28] Naess A, Clausen PH. Combination of the peaks-over-threshold and bootstrapping methods for extreme value prediction. Structural Safety 2001;23: 315–30.
[29] Minciarellia F, Gioffrèc M, Grigoriud M, Simiu E. Estimates of extreme wind effects and wind load factors: influence of knowledge uncertainties. Probabilistic Engineering Mechanics 2001;16:331–40.
[30] Harris I. Generalised Pareto methods for wind extremes. useful tool or mathematical mirage? Journal of Wind Engineering and Industrial Aerodynamics 2005;93:341–60.
[31] Ellingwood BR, Galambos TV, MacGregor JG, Cornell CA. Development of a probability based load criterion for American National Standard A58. NIST Special Publication 577. National Bureau of Standards. Washington(DC): 1980.
[32] Cook NJ. Towards better estimates of extreme winds. International Journal of Wind Engineering and Industrial Aerodynamics 1982;9:295–323.
[33] Simiu E, Heckertb NA, Fillibenb JJ, Johnson SK. Extreme wind load estimates based on the Gumbel distribution of dynamic pressures: an assessment. Structural Safety 2001;23:221–9.
[34] Freudenreich K, Argyriadis K. The load level of modern wind turbines according to IEC 61400-1. Journal of Physics: Conference Series 2007;75: 012075.
[35] Naess A, Gaidai O. Estimation of extreme values from sampled time series. Structural Safety 2001;23:221–9.

APPENDIX F
First Passage Probability Estimation of Wind Turbines by Markov Chain Monte Carlo

The paper presented in this appendix is submitted to *Structure and Infrastructure Engineering*.

Structure and Infrastructure Engineering, Vol. 00, No. 00, Month 2011, 1–21

First Passage Probability Estimation of Wind Turbines by Markov Chain Monte Carlo

M.T. Sichani[a]* and S.R.K. Nielsen[a]

[a] *Department of Civil Engineering, Aalborg University, 9000 Aalborg, Denmark*;
(*Received 1 April 2011*)

Markov Chain Monte Carlo simulation has received considerable attention within the past decade as reportedly being one of the most powerful techniques for first passage probability estimation of dynamic systems. A very popular method in this direction is the Subset Simulation (SS) which is capable of estimating probability of rare events with low computation cost. The idea of the method is to break a rare event into a sequence of more probable events which are easy to be estimated based on the conditional simulation techniques. Recently two algorithms have been proposed in order to increase efficiency of the method by modifying the conditional sampler. In this paper applicability of the original SS is compared to the recently introduced modifications of the method on a wind turbine model. The model incorporates a PID pitch controller which aims at keeping the rotational speed of the wind turbine rotor equal to its nominal value. Finally Monte Carlo simulations are performed which allow assessment of the accuracy of the first passage probability estimation by SS methods.

Keywords: MCMC; subset simulation; wind turbine; pitch controller.

1. Introduction

In order to estimate the return period of the wind turbines, required by wind turbine design codes, it is necessary to estimate the low first passage probabilities, alternatively called failure probability, of these systems IEC (2005a). For this aim the IEC standard recommends fitting one of the extreme value distributions i.e. reversed Weibull or the Gumbel distribution to the peaks extracted from six epoches of 10min. duration, of the wind turbine data IEC (2005b). Unfortunately the choice of Extreme Value Distribution (EVD) combined with the part of the data used to find EVD parameters result in considerably different extrapolated design values. Therefore there is a high uncertainty in

*Corresponding author. Email: mts@civil.aau.dk

ISSN: 1573-2479 print/ISSN 1744-8980 online
© 2011 Taylor & Francis
DOI: 10.1080/1573247YYxxxxxxxx
http://www.informaworld.com

the design values extrapolated from these fits Harris (2005), Freudenreich and Argyriadis (2007).

Alternative to extreme value curve fitting and extrapolation, simulation techniques may be used for estimating these return periods. The natural choice for this purpose is the Standard Monte Carlo (SMC) simulation. Considering the design value, i.e. the threshold level for which the probability of the first passage is given, corresponding to the first passage probability of the order 10^{-7}, 10^8 simulations are required to estimate the barrier level corresponding to this probability with coefficient of variation of approximately 0.3. This is far beyond reach of the available computers' power in practice even on a modern machine. The Variance Reduction Monte Carlo (VRMC) methods are an alternative choice which are able to produce estimations similar to SMC but with less variance in their estimates compared to SMC. This readily results in lower computation effort if the same variance in estimations, as those of SMC, are desired Schueller and Pradlwarter (2009). The conditional Monte Carlo simulation using Markov Chains has recently received considerable attention in different fields of probabilistic systems' modeling and analysis Kelly and Smith (2009) i.e. risk-based life-cycle management Yuan *et al.* (2009).

The Subset Simulation (SS), introduced by Au and Beck Au and Beck (2001), for estimation of small probabilities of high dimensional systems is reportedly one of the most powerful techniques in the field of structural dynamics. Ching et al. Ching *et al.* (2005) introduced the splitting concept into the original SS which resulted in a hybrid subset simulation. The spherical subset simulation (S3) is introduced in Katafygiotis and Cheung (2007) which transforms the excitations into a unit hyper sphere allowing to concentrate the sampling density of the simulation around the directions in which the so-called seeds or important directions for the Markov Chains are concentrated. A new scheme that combines the method with Importance Sampling (IS) and also the reliability sensitivity analysis with SS have been addressed in Song *et al.* (2009). The recent proposals in this field have focused their attention on increasing efficiency of the method by modifying its sampling scheme Santoso *et al.* (2010), Zuev and Katafygiotis (2011).

It is interesting to determine applicability of SS techniques, as a powerful representative of VRMC methods, on the wind turbine systems specifically with an active controller. Presence of an active pitch controller is a new feature of this model which, to the best knowledge of authors, has not been considered in previous studies on the VRMC methods. This increases motivation for this study to analyze the effect of the controller on the statistical behavior of the structures. An advantage of SS over other VRMC methods such as IS is that the it can handle high dimensional and complicated problems within reasonable effort Schueller and Pradlwarter (2007). In this paper we start by a brief explanation of each method followed by a primary application assessment of the chosen SS schemes on a linear SDOF oscillator. This serves as a simple test to check the applicability of the methods regarding the dimensions of the problem. It should be noted that in view of reliability analysis the term *dimension* refers to the number of basic random variables, i.e. the actual random variables of the system transformed into iid standard normally distributed variables, of the model. This here refers to the iid Gaussian random variables that enter the turbulence filter to generate the wind field c.f. figure 1. Next the wind turbine model is described in brief and the applicable methods are used for estimating its small failure\first passage probabilities.

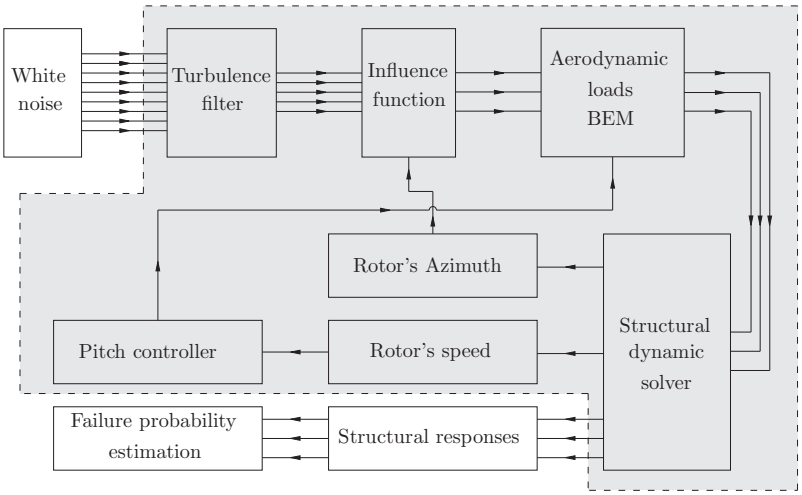

Figure 1. Flowchart of the wind turbine model

2. Reliability of wind turbines

Wind turbines have rather complicated models which does not allow extraction of their statistical characteristics within a reasonable effort with SMC, c.f. figure 1. Here a reduced order model of a 5MW reference wind turbine is used with the specifications adopted from the NREL reference wind turbine Sichani *et al.* (2011a,b), Jonkman *et al.* (2009). The developed model consists of the essential parts of a real 5MW wind turbine and hence may indicate the use of the methods when applied on a full scale wind turbine. The simplifications of the model are made in order to allow SMC simulations possible within a reasonable computation time yet covering the important aspects of the problems encountered in practice.

The main problem of these systems is their high dimensions coupled with nonlinearities Valdebenito *et al.* (2010). This makes the rare event simulation of the system a difficult task Katafygiotis and Zuev (2008). The coupling is due to presence of several interconnected model components, i.e. structural module, load calculation module and the rotational speed controller, while strong nonlinearities exist in some of the i.e. in load calculation module and the controller. Moreover the high computational cost for evaluation of the Limit State Function (LSF) requires prohibitively high computation time if many simulations are needed. Therefore a method which can handle these problems and is able to estimate the rare events of this system within reasonable effort could be of great interest in this area.

3. Subset simulation

Assume the LSF is defined as $G(\mathbf{X})$ where $\mathbf{X}$ consists of the random variables of the problem. The barrier level b_j which corresponds to a sample of $\mathbf{X}$, i.e. $\mathbf{x}_j$, is then given by $b_j = G(\mathbf{x}_j)$. In view of structural dynamics $\mathbf{X}$ can be recognized as the stochastic excitation within a given time duration and b as the maximum of the magnitude of the response to the given excitation c.f. 4.1. The strategy of the SS is to obtain samples of b which have low probability of occurrence, starting by that which can be accuractely estimated with low number of simulations e.g. $b^{(1)}$. Next, this barrier level will be increased gradually

until the highest(required) barrier level or probability is estimated with desired accuracy. This is done by defining intermediate probability levels $p_f = p_f^{(m)} < p_f^{(m-1)} < \cdots < p_f^{(1)}$ corresponding to the intermediate barrier levels $b = b^{(m)} > b^{(m-1)} > \cdots > b^{(1)}$. Using this property taken from the fact that first passage probability can not increase as the barrier level increases, the required first passage probability p_f can be written as

$$p_f(b^{(2)}|b^{(1)}) = \frac{p_f\big(b^{(2)} \bigcap b^{(1)}\big)}{p_f\big(b^{(1)}\big)} = \frac{p_f\big(b^{(2)}\big)}{p_f\big(b^{(1)}\big)} \tag{1}$$

$p_f\big(b^{(2)}|b^{(1)}\big)$ is the conditional probability of exceeding $b^{(2)}$ on the condition that $b^{(1)}$ is exceeded. Using (1) the final first passage probability, i.e. the lowest first passage probability required, may be written as the following product

$$p_f(b) = p_f\big(b^{(1)}\big) \prod_{i=1}^{m-1} p_f\big(b^{(i+1)}|b^{(i)}\big) \tag{2}$$

The SS method aims at estimating each of the m terms on the right hand side of (2) by some type of Monte Carlo simulation. Therefore it is beneficial to let the barrier level be chosen after the simulation of each stage is performed and fix the intermediate first passage probabilities associated with them. All the terms in the product are chosen large enough so that they can be estimated with low number of samples i.e. $p_0 = 0.1$ in conjunction with (3).

$$\left.\begin{aligned} p_f\big(b^{(1)}\big) &= p_0 \\ p_f\big(b^{(i+1)}|b^{(i)}\big) &= p_0 \quad , \quad i = 1, \cdots m-1 \end{aligned}\right\} \tag{3}$$

$b^{(1)}$, with its probability $p_f\big(b^{(1)}\big) = p_0$, is determined by performing SMC with low number of samples, i.e. $N_{sim} = 500$, as the $(p_0 \times N_{sim})^{\text{th}}$ barrier level when all simulated barrier levels are sorted in descending order. The conditional probability terms on the right hand side of (1) can not be estimated by SMC and need a technique which is capable of generating samples conditioned on the previous samples. For this reason those samples of $\mathbf{X}^{(1)}$ which correspond to the barrier levels higher than $b^{(1)}$, the so-called seeds, are saved for simulating the next generation of excitation. This consists of $N_{seed} = p_0 \times N_{sim}$ seeds to be kept in memory. Au and Beck Au and Beck (2001) proposed using a modified Metropolis Hastings algorithm for generation of the conditional samples which is explained in 3.3. In the next section the original Metropolis Hastings algorithm is described which is the basis for the conditional sampling scheme. In the following sections the proposed modifications are explained with emphasis on their difference with the original algorithm.

3.1 *Metropolis-Hastings algorithm*

Let $x(k)$ denote the samples of a discrete stochastic load process $X(k)$ at the instants of time $k = 1, \cdots, N$ - in the reliability analysis these refer to the basic random variables used to generate the loads -. The random variables $X(k)$ are assumed to be mutual independent and identical distributed with the Probability Density Function(PDF) $\pi\big(x(k)\big)$.

$X(k)$ is assembled in the random vector $\mathbf{X}$ with the Joint Probability Density Function(JPDF) $\pi(\mathbf{x})$. Due to the iid components $\pi(\mathbf{x})$ becomes as indicated in (4). It should be noted that the original Metropolis Hastings (MH) algorithm does not require iid components of the random variables $X(k)$ and only needs their JPDF to be known. In our context since we refer to the basic random variables the iid is also considered. Correspondingly the samples are stored in the vector $\mathbf{x}$. Let $\mathbf{X}^{(i)}$ and $\mathbf{X}^{(i+1)}$ denote stochastic vectors representing (or transformed into) the load process, when changing from barrier level $b^{(i)}$ to barrier level $b^{(i+1)}$. Both of these vectors are identical distributed, but not independent. The transition kernel, or alternatively called the *proposal distribution*, that $\mathbf{X}^{(i)} = \mathbf{x}$ moves to $\mathbf{X}^{(i+1)}$ is shown by $p(\mathbf{X}^{(i+1)}|\mathbf{X}^{(i)})$. Due to the independence and identical distribution of the components within $\mathbf{X}^{(i+1)}$ and $\mathbf{X}^{(i)}$, respectively, this may be written as

$$\left.\begin{aligned} \pi(\mathbf{x}^{(i)}) &= \prod_{k=1}^{N} \pi\big(x^{(i)}(k)\big) \\ p(\mathbf{x}^{(i+1)}|\mathbf{x}^{i}) &= \prod_{k=1}^{N} p\big(x^{(i+1)}(k)|x^{(i)}(k)\big) \end{aligned}\right\} \tag{4}$$

where $\pi(\cdot)$ and $p(\cdot)$ are the one dimensional PDFs of the discrete components $X(k)$. Consider "N_{sim}" samples $\{\mathbf{x}_1^{(i)}, \cdots, \mathbf{x}_{N_{sim}}^{(i)}\}$ of $\mathbf{X}^{(i)}$ from the i^{th} simulation level. The transition kernel that $\mathbf{X}^{(i)} = \mathbf{x}_j^{(i)}$ moves to a state in $\mathbf{X}^{(i+1)}$, e.g. $p(\mathbf{X}^{(i+1)}|\mathbf{X}^{(i)} = \mathbf{x}_j^{(i)})$, can be chosen with the mean value $\mathbf{x}_j^{(i)}$, but can otherwise be arbitrarily chosen Santoso *et al.* (2010). For instance a uniform or Gaussian distribution with an arbitrary standard deviation, such as the sample standard deviation of the seeds Au *et al.* (2010), and its mean value at the value of $x_j^{(i)}(k)$ for $k = 1, \cdots, N$. Initially a candidate $\boldsymbol{\xi}_j$ for $\mathbf{x}_j^{(i+1)}, j = 1, \cdots, N_{sim}$ is drawn from $p(\cdot|\mathbf{x}_j^{(i)})$. In order to ensure that samples of $\mathbf{X}_j^{(i+1)}$ generated by MH will also be distributed with distribution $\pi(\cdot)$, it is necessary that the so-called "reversibility condition", which states that $\pi(\boldsymbol{\xi}_j)\, p(\mathbf{x}_j^{(i)}|\boldsymbol{\xi}_j) = \pi(\mathbf{x}_j^{(i)})\, p(\boldsymbol{\xi}_j|\mathbf{x}_j^{(i)})$, be satisfied for all samples of $\mathbf{x}_j^{(i)}$ and $\boldsymbol{\xi}_j$, Chib and Greenberg (1995), Santoso *et al.* (2010). For this reason (5) is used as the probability of accepting candidate samples.

$$a(\mathbf{x}_j^{(i)}, \boldsymbol{\xi}_j) = \min\left\{1, \frac{\pi(\boldsymbol{\xi}_j)\, p(\mathbf{x}_j^{(i)}|\boldsymbol{\xi}_j)}{\pi(\mathbf{x}_j^{(i)})\, p(\boldsymbol{\xi}_j|\mathbf{x}_j^{(i)})}\right\} \tag{5}$$

Next, $\boldsymbol{\xi}_j$ is accepted as the next sample, e.g. $\mathbf{x}_j^{(i+1)} = \boldsymbol{\xi}_j$, with probability

$$\mathbf{x}_j^{(i+1)} = \begin{cases} \boldsymbol{\xi}_j & \text{w.p. } a(\mathbf{x}_j^{(i)}, \boldsymbol{\xi}_j) \\ \mathbf{x}_j^{(i)} & \text{w.p. } 1 - a(\mathbf{x}_j^{(i)}, \boldsymbol{\xi}_j) \end{cases} \tag{6}$$

where the term w.p. means "with probability". Therefore after generation of a candidate sample $\boldsymbol{\xi}_j$ a random number is drawn from a uniform distribution between 0 and 1 e.g. $\mathcal{U}(0,1)$. If this number is less than $a(\mathbf{x}_j^{(i)}, \boldsymbol{\xi}_j)$ of (5), $\boldsymbol{\xi}_j$ will be accepted as the next sample; else will be rejected and replaced by the seed $\mathbf{x}_j^{(i)}$. This procedure guarantees that the distribution of the samples will not be changed as barrier levels increase Hoff (2009). In case the proposal distribution is chosen to be symmetric, i.e. $p\big(\mathbf{B}|\mathbf{A}\big) = p\big(\mathbf{A}|\mathbf{B}\big)$, it is

called the *random walk Metropolis Hastings* and (5) reduces to

$$a(\mathbf{x}_j^{(i)}, \boldsymbol{\xi}_j) = \min\left\{1, \frac{\pi(\boldsymbol{\xi}_j)}{\pi(\mathbf{x}_j^{(i)})}\right\} \tag{7}$$

3.2 *Conditional probability estimation*

The method follows the procedure described in section 3 that started by a SMC and defining the first barrier level $b^{(1)}$. In the next step(s) N_{sim} candidate samples for $\mathbf{x}_j^{(i+1)}$, $j = 1, \cdots, N_{sim}$ will be generated using a conditional sampler, i.e. MH. The next generation of excitations are conditioned on a randomly chosen seed of the previous simulation. If $\boldsymbol{\xi}_j$ is accepted according to (5) or (7) and (6), the second accept\reject test will be performed as

$$\mathbf{x}_j^{(i+1)} = \begin{cases} \boldsymbol{\xi}_j & \text{if } \boldsymbol{\xi}_j \in \mathfrak{F}^{(i)} \\ \mathbf{x}_j^{(i)} & \text{if } \boldsymbol{\xi}_j \notin \mathfrak{F}^{(i)} \end{cases} \tag{8}$$

where $\mathfrak{F}^{(i)}$ denotes the failure domain of the i^{th} level e.g. $\mathfrak{F}^{(i)} = \{\boldsymbol{\xi}_j | G(\boldsymbol{\xi}_j) > b^{(i)}\}$. (8) means that $\boldsymbol{\xi}_j$ is accepted (after being accepted in the accept\reject test of the MH) only if it increases the barrier level to higher than $b^{(i)}$, else is rejected and replaced with its seed. This step provides the estimation for the conditional terms in (2) and will be repeated $m-1$ times, c.f. (2). The same strategy that was described in section 3 for choosing barrier levels and seeds will be used in all $m-1$ stages of the simulation. This results in

$$p_f^i = \frac{p_0^{i-1}}{N_{sim}} \sum_{j=1}^{N_{sim}} I_{\mathfrak{F}^{(i)}}(\mathbf{x}_j^{(i)}) \quad , \quad i = 1, \cdots, m \tag{9}$$

p_f^i represents the minimum failure\first passage probability calculated in the i^{th} step of the simulation. p_0^{i-1} means p_0 raised to power "$i-1$". $I_{\mathfrak{F}^{(i)}}(\mathbf{x}_j^{(i)})$ is the indicator function which will be one if the response to $\mathbf{x}_j^{(i)}$ lies in the i^{th} intermediate failure domain and is zero otherwise.

3.3 *Modified Metropolis-Hastings algorithm*

The MH algorithm as presented in 3.1 breaks down in high dimensional problems. This is since the probability of moving from $\mathbf{x}_j^{(i)}$ to $\boldsymbol{\xi}_j$, defined as (5), decreases exponentially as the number of basic variables - dimension of the problem - increases Au and Beck (2001). Therefore the Markov chains do not move so frequently from their current state to the next state and get stocked where they are. This problem can be solved by taking advantage of independency between candidate coordinates(components) and breaking the N-dimensional JPDFs $\pi(\mathbf{x}_j^{(i)})$ and $p\big(.|\mathbf{x}_j^{(i)}\big)$ into their corresponding N independent one dimensional PDFs $\pi(x_j^{(i)}(k))$ and $p\big(.|x_j^{(i)}(k)\big)$ respectively. Accordingly the probability of

accepting the next state for each sample is defined independently as

$$a\big(x_j^{(i)}(k),\xi_j(k)\big) = \min\left\{1,\frac{\pi\big(\xi_j(k)\big)\,p\big(x_j^{(i)}(k)|\xi_j(k)\big)}{\pi\big(x_j^{(i)}(k)\big)\,p\big(\xi_j(k)|x_j^{(i)}(k)\big)}\right\}\Bigg\} \tag{10}$$

which in case of symmetry proposal distribution $p\big(B\,|A\big) = p\big(A\,|B\big)$ reduces to

$$a\big(x_j^{(i)}(k),\zeta_j(k)\big) = \min\left\{1,\frac{\pi\big(\zeta_j(k)\big)}{\pi\big(x_j^{(i)}(k)\big)}\right\} \tag{11}$$

Next, the accept\reject test will be performed for each component of each realization. So for $k = 1,\cdots,N$

$$x_j^{(i+1)}(k) = \begin{cases}\xi_j(k) & \text{w.p. } a\big(x_j^{(i)}(k),\xi_j(k)\big)\\ x_j^{(i)}(k) & \text{w.p. } 1-a\big(x_j^{(i)}(k),\xi_j(k)\big)\end{cases} \tag{12}$$

This process will be repeated for $j = 1,\cdots,N_{sim}$ times to generate the next set of excitations i.e. $\mathbf{X}^{(i+1)} = \{\mathbf{x}_1^{(i+1)},\cdots,\mathbf{x}_{N_{sim}}^{(i+1)}\}$. This modification is proposed in Au and Beck (2001) and is called the *Modified Metropolis-Hastings* (MMH). Hereafter when this sampling scheme is used for the SS, it is invoked by the term SS-MMH.

3.4 *Modified Metropolis Hastings with Reduced Chain Correlation*

The Modified Metropolis-Hastings with Reduced chain Correlation(MMHRC) is recently proposed Santoso *et al.* (2010) which aims in reducing the correlation between the Markov chains in the MMH. In view of the sample generation MMHRC follows the original MH algorithm based on (5), (6) and (7), i.e. the N-dimensional JPDF is used. However every time the generated $\boldsymbol{\xi}_j$ is rejected according to (6), a new sample is generated conditioned on the same seed. This process is repeated as many times as needed to let the generated candidate be accepted by (6). Clearly this modification takes more time for sample generation compared to MMH. SS-MMHRC shows good performance for low to medium dimensional problems i.e. $N \leq 100$ Santoso *et al.* (2010). However on the numerical simulation performed in this study, c.f. 4.1, the Markov chains generated by MMHRC have high tendency to stay in the initial state, i.e. $a(\mathbf{x}_j^{(i)},\boldsymbol{\xi}_j) \approx 0$. This means that the barrier level is rarely increased. This is due to the high dimensions of the problem $N = 1501$ which is the same problem that causes breaking down of the original MH algorithm in high dimensions Au and Beck (2001).

3.5 *Modified Metropolis Hastings with Delayed Rejection*

Following the idea of Tierney and Mira (1999) the so-called Modified Metropolis-Hastings with Delayed Rejection (MMHDR) Zuev and Katafygiotis (2011) is proposed. Here the MMH approach is followed for generation of the conditional samples. Although in case a candidate sample does not belong to the failure region, i.e. $\boldsymbol{\xi}_j \notin \mathfrak{F}^{(i)}$ in (8), it will

not be rejected and will be given a second chance. In such a case the components of the candidate $\boldsymbol{\xi}_j$, e.g. $\xi_j(k)$, are divided into two non-overlapping sets. Set $T = \{k \,|\, x_j^{(i)}(k) = \xi_j(k)\}$ which consists of the set of coordinates which have evolved to new states and its complementary set $\overline{T}$ which includes the rest of the components. Next the coordinates which belong to T will be given another chance to evolve to a new state $\boldsymbol{\xi}^{(2)}$. The proposal density of moving to $\xi_j^{(2)}(k)$, e.g. $q(.|x_j^{(i)}(k), \xi_j(k))$, can in general be chosen different from the proposal density of moving from $x_j^{(i)}(k)$ to $\xi_j(k)$, e.g. $p(.|x_j^{(i)}(k))$. It should be noted that the candidate samples for $\boldsymbol{\xi}_j^{(2)}$ are again generated around the original seed $x_j^{(i)}(k)$ and not $\xi_j(k)$ i.e. $q(.|x_j^{(i)}(k), \xi_j(k)) = q(.|x_j^{(i)}(k))$, Katafygiotis and Cheung (2007). The probability of accepting the new samples conditioned on the two previous samples is defined as Tierney and Mira (1999)

$$\left.\begin{aligned} a^*\big(x_j^{(i)}(k), \xi_j(k), \xi_j^{(2)}(k)\big) = \\ \min\left\{1, \frac{\pi\big(\xi_j^{(2)}(k)\big)\, p\big(\xi_j(k)|\xi_j^{(2)}(k)\big)}{\pi\big(x_j^{(i)}(k)\big)\, p\big(\xi_j(k)|x_j^{(i)}(k)\big)} \times \right. \\ \left. \frac{q\big(x_j^{(i)}(k)|\xi_j^{(2)}(k), \xi_j(k)\big)\, a\big(\xi_j^{(2)}(k), \xi_j(k)\big)}{q\big(\xi_j^{(2)}(k)|x_j^{(i)}(k), \xi_j(k)\big)\, a\big(x_j^{(i)}(k), \xi_j(k)\big)} \right\} \end{aligned}\right. \tag{13}$$

where $a\big(\xi_j(k), \xi_j^{(2)}(k)\big)$ determines the probability of moving from $\xi_j(k)$ to $\xi_j^{(2)}(k)$ in the same manner as defined in (10). In case that both transition kernels are chosen symmetry (13) reduces to

$$\left.\begin{aligned} a^*\big(x_j^{(i)}(k), \xi_j(k), \xi_j^{(2)}(k)\big) = \min\left\{1, \right. \\ \left. \frac{p\big(\xi_j(k)|\xi_j^{(2)}(k)\big)\ \min\big\{\pi\big(\xi^{(2)}(k)\big), \pi\big(\xi(k)\big)\big\}}{p\big(\xi_j(k)|x_j^{(i)}(k)\big)\ \min\Big\{\pi\big(x_j^{(i)}(k)\big), \pi\big(\xi(k)\big)\Big\}} \right\} \end{aligned}\right. \tag{14}$$

where in (14) the equality $a \times \min\{1, b/a\} = b \times \min\{1, a/b\}$ is used which is true for any positive pair $\{a, b\}$.

4. Numerical simulations

4.1 *Linear SDOF oscillator*

The purpose of this simulation is to test applicability of the introduced SS schemes and chose the applicable algorithm(s) to be implemented on the wind turbine model. 500 initial samples, e.g. $N_{sim} = 500$, are chosen for all of the simulations on the SDOF oscillator. The addressed methods are applied on a SDOF linear oscillator presented in Au and Beck (2001) with its equation of motion

$$\ddot{y}(t) + 2\zeta\omega\dot{y}(t) + \omega^2 y(t) = x(t) \tag{15}$$

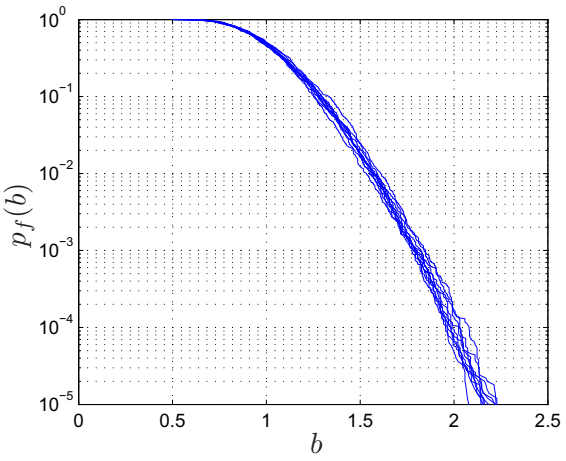

Figure 2. Estimations of the first passage probability of the SDOF oscillator with SS-MMH

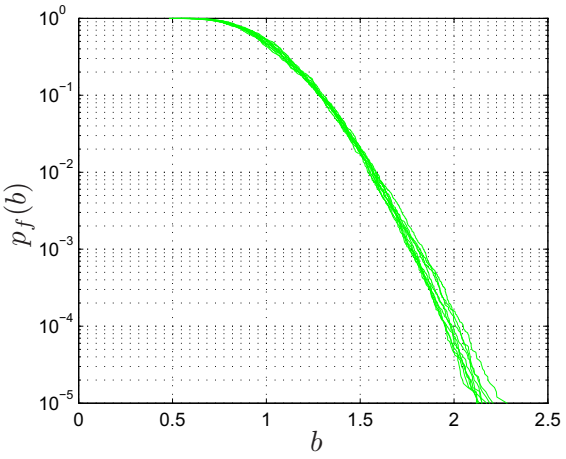

Figure 3. Estimations of the first passage probability of the SDOF oscillator with SS-MMHDR

where $\zeta = 0.02, \omega = 2.5\pi\, rad/s$. (15) is solved at discrete time steps $t_k = k\Delta t$, $k = 1, \cdots, N$. The time resolution is set to $\Delta t = 0.02$ which results in $N = 1501$. The excitation is assumed to be Gaussian white noise with unit spectral intensity $S_0 = 1$. Variance of the response process is $\sigma_X^2 = \pi/2\zeta\omega^3 = 0.4026$. The failure event is defined as the first passage of the maximum of the magnitude of the response of the oscillator from the barrier level "b", i.e. $P_f(b) = \text{Prob}\big(\max_{t\in[0,T]} |y(t)| > b\big)$ with $T = 30[s]$. This probability is estimated using SS-MMH, SS-MMHRC and SS-MMHDR. The proposal distributions are chosen uniform distributions with their spread equal to the standard deviation of the previous samples and centered around the initial sample's seed i.e. $p_k\big(.|x_j^{(i)}(k)\big) = q_k\big(.|x_j^{(i)}(k), \zeta_j(k)\big) = \mathcal{U}\Big(x_j^{(i)}(k) - \sigma_{x_j^{(i)}(k)}, x_j^{(i)}(k) + \sigma_{x_j^{(i)}(k)}\Big)$. The SS-MMHRC breaks down after the first (SMC) stage due to the mentioned reason. Ten estimations of the SS-MMH and SS-MMHDR are shown in figures 2 and 3 respectively. It should be noted that MMHDR algorithm makes a re-calculation whenever evaluation of the LSF rejects a candidate sample. This is not a minor computation effort since it requires the major part of the calculation, i.e. dynamic analysis, to be repeated.

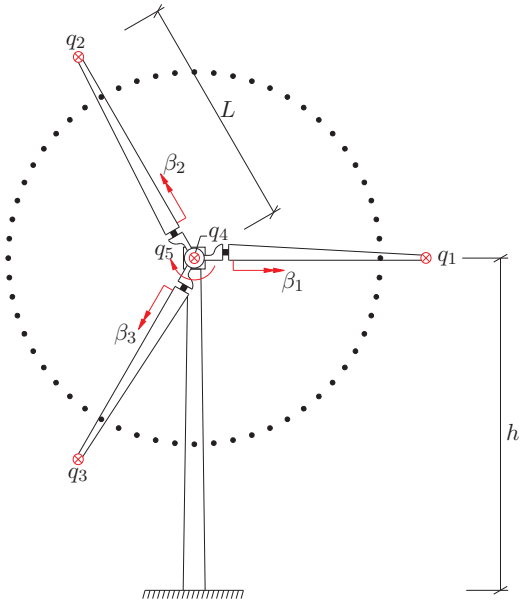

Figure 4. Definition of degrees of freedom and pitch angles

4.2 *Fixed speed Wind turbine*

The wind turbine model used in this study consists of four major modules e.g. the turbulence generator, Aerodynamic load calculation, structural dynamics and pitch controller. The spatially correlated turbulent wind field is generated using a state space model Sichani *et al.* (2010). The motions of the blades relative to the hub and the motion of the tower in the mean wind direction are modeled using modal model by one mode shape. Only motions in the mean wind direction is considered for which reason no gyroscopic forces are present, save the centripetal forces. Let $y_i(x,t), i = 1,2,3$ denote the displacement fields of the blades relative to the hub, where $x \in [0, L]$ is measured from the hub and L is the length of the blades, c.f. figure 4. Further $y_4(x,t)$ denotes the displacement of the tower in the same direction, where $x \in [0, h]$ is measured from the foundation and h is the height of the nacelle above the ground surface. Then, the indicated displacement fields may be written as

$$\left.\begin{array}{ll} y_i(x,t) \simeq \Phi(x) q_i(t) & , \quad i = 1,2,3 \\ y_4(x,t) \simeq \Phi_0(x) q_4(t) & \end{array}\right\} \tag{16}$$

$\Phi_0(x)$ is the part of the fundamental eigenmode of the wind turbine belonging to the tower and $\Phi(x)$ is the fundamental fixed base mode shape of the blade. The mode shapes are normalized to one at the nacelle and the blade tip, respectively, so the generalized coordinates $q_1(t), q_2(t), q_3(t)$ may be interpreted as the tip displacement of the blades relative to the hub, and $q_4(t)$ is the displacement of the nacelle. The blades are modeled as Bernoulli-Euler beams with the bending stiffness $EI(x)$ around an axis orthogonal to the rotor plane, and the mass per unit length $\mu(x)$. Similarly, the tower is modeled as a Bernoulli-Euler beam with the bending stiffness $EI_0(x)$. The mass per unit length is formally written as

$$\bar{\mu}_0(x) = \mu_0(x) + M_0 \delta(x - h) \tag{17}$$

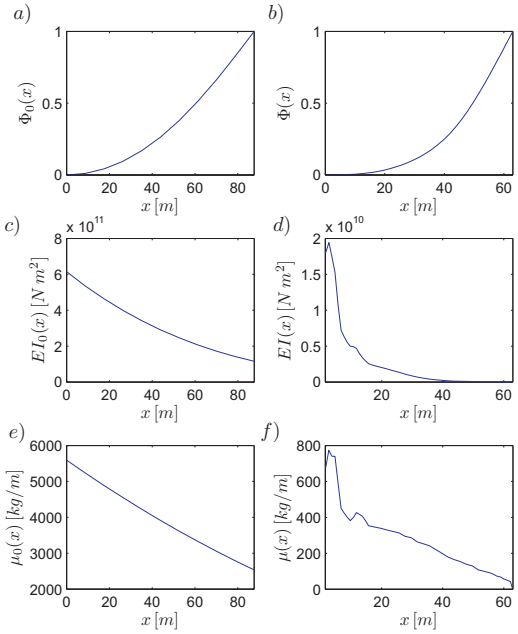

Figure 5. Structural properties of the NREL 5MW wind turbine. a) Tower's mode shape, b) Blade's mode shape, c) Bending stiffness of the tower, d) Bending stiffness of the blade, e) Tower's mass per unit length, f) Blade's mass per unit length

$\mu_0(x)$ denotes the continuous mass distribution, M_0 is the mass of the nacelle and the hub; $\delta(\cdot)$ is Dirac's delta function. The dynamic load per unit length on the tower in the mean wind direction is denoted $p_4(x,t)$. Correspondingly, the load on the three blades in the same direction are denoted $p_1(x,t), p_2(x,t)$ and $p_3(x,t)$. The rigid body motion of the drive train is modeled as a single rotational degree of freedom q_5 by assuming infinite stiff drive shafts and no elastic deformation in the gear, whereby the kinematic relation for the angular rotation of the rotor of the generator emerges as $q_g = Nq_5$. N is the gear ratio between high and low speed shafts. Furthermore, the mass moment of inertia of the gear wheels and the connected shafts are included into the mass moment of inertia J_r and J_g of the rotor and the generator rotor, respectively. Using Lagrange's equations the following governing equations of the system may be obtained

$$\mathbf{m}\ddot{\mathbf{q}}(t) + \mathbf{c}\dot{\mathbf{q}}(t) + \mathbf{k}\mathbf{q}(t) = \mathbf{f}(t) \tag{18}$$

where

$$\mathbf{m} = \begin{bmatrix} m_1 & 0 & 0 & m_2 & 0 \\ 0 & m_1 & 0 & m_2 & 0 \\ 0 & 0 & m_1 & m_2 & 0 \\ m_2 & m_2 & m_2 & m_0 & 0 \\ 0 & 0 & 0 & 0 & J \end{bmatrix} \tag{19}$$

$$\mathbf{k} = \begin{bmatrix} k & 0 & 0 & 0 & 0 \\ 0 & k & 0 & 0 & 0 \\ 0 & 0 & k & 0 & 0 \\ 0 & 0 & 0 & k_0 & 0 \\ 0 & 0 & 0 & 0 & 0 \end{bmatrix} \tag{20}$$

where

$$\left.\begin{aligned} m &= \int_0^L \mu(x)dx \\ m_1 &= \int_0^L \mu(x)\Phi^2(x)dx \\ m_2 &= \int_0^L \mu(x)\Phi(x)dx \\ m_3 &= \int_0^L x\mu(x)dx \\ m_4 &= \int_0^L x\mu(x)\Phi(x)dx \\ m_5 &= \int_0^h x\mu_0(x)\Phi_0(x)dx \\ m_0 &= \int_0^h \mu_0(x)\Phi_0^2(x)dx + M_0 + 3m \\ J_r &= \int_0^L x^2\mu(x)dx \end{aligned}\right\} \tag{21}$$

J is the generalized mass moment of inertia related to the rigid body degree-of-freedom $q_5(t)$ given as $J = J_r + N^2 J_g$. $\mathbf{q}(t)$ and $\mathbf{f}(t)$ represent the generalized (modal) displacements and the loads vectors respectively. The damping matrix $\mathbf{c}$ merely includes structural damping. Aerodynamic damping is included later via the aerodynamic load. Then $\mathbf{c}$ may be written as a diagonal matrix with its first three diagonal elements, e.g. blades' structural damping, equal to $2\zeta\omega m_1$, the tower's structural damping $2\zeta_0\omega_0 m_0$ and the energy loss in the gearbox modeled by the term $\eta M_{r,0}/\Omega_{r,0}$. $\Omega_{r,0} = \dot{q}_{5,0}$ is the referential (nominal) rotational speed of the rotor. ω and ζ denote the eigenfrequency and damping ratio of the blades, when fixed to the hub. Correspondingly, ω_0 and ζ_0 denote the eigenfrequency and damping ratio of the lowest mode of the tower, which are assumed to be known. η is the loss factor of the transmission system due to friction in gears and bearings, which typically is a few percent and $M_{r,0} = P/\Omega_{r,0}$ is the referential rotor torque for $P = 5$MW nominal power output. The generalized stiffness coefficients of the blades and the tower are given as $k = \omega^2 m_1$ and $k_0 = \omega_0^2 m_0$. The generalized external dynamic loads become

$$\left.\begin{aligned} f_i(t) &= \int_0^L \Phi(x)p_i(x,t)dx \quad , \quad i = 1,2,3 \\ f_4(t) &= \int_0^h \Phi_0(x)p_4(x,t)dx + \sum_{i=1}^{3}\int_0^L \Phi(x)p_i(x,t)dx \\ f_5(t) &= M_r - (1-\eta)NM_g \end{aligned}\right\} \tag{22}$$

where M_r and M_g are the instantaneous rotor and generator torques respectively. Asynchronous slip variable generator is considered for which the generator torque under normal operation conditions is linearly dependent on the rotational speed $N\dot{q}_5(t)$. The relation may be given in the form

$$M_g(t) = M_{g,0}\frac{N\dot{q}_5(t) - \Omega_{g,00}}{\Omega_{g,0} - \Omega_{g,00}} \tag{23}$$

where $M_{g,0} = M_{r,0}/N$ is the nominal generator torque, $\Omega_{g,0} = N\Omega_{r,0}$ is the nominal generator rotational speed and $\Omega_{g,00}$ is the generator speed for the zero generator torque.

In the *fixed speed wind turbine* the rotational speed of the rotor is set equal to its nominal value $\omega_{r,0}$.

4.3 *wind model*

The turbulent wind field is modeled using a state space formulation which results in a state space model of the form of (24) where $\mathbf{v}(j) = [v_1(j), \cdots, v_m(j)]$ represents the vector of turbulence in all of the nodes where realizations are simulated. $\mathbf{\Xi}(j) \sim \mathcal{N}(0, \mathbf{I})$ are mutually independent identically distributed Gaussian white noise variables, i.e. basic random variables, and $\mathbf{x}(j+1)$ is a temporary state vector which defines the order of the model.

$$\begin{aligned} \mathbf{x}(j+1) &= \mathbf{A}_T \mathbf{x}(j) + \mathbf{B}_T \mathbf{\Xi}(j) \\ \mathbf{v}(j) &= \mathbf{C}_T \mathbf{x}(j) + \mathbf{D}_T \mathbf{\Xi}(j) \end{aligned} \tag{24}$$

Calibration of the quadruple $(\mathbf{A}_T, \mathbf{K}_T, \mathbf{C}_T, \mathbf{D}_T)$ is out of scope of this work and is described in detail in Sichani *et al.* (2010). Here the idea is to calibrate the stated quadruple such that the cross-covariance function of (24) matches best to the cross-covariance function of the turbulence. In this study the Kaimal power spectral density function with exponentially decaying coherence function is assumed for the turbulence Sichani *et al.* (2011a). The presented approach for turbulence modeling does not take into account the rotational sampling effect of the turbulence process. Therefore it is needed to make an interpolation as the blades pass through different turbulence nodes in between two nodes which is done by the so-called *influence function* c.f. figure 1.

4.4 *Variable speed wind turbine*

In this case a controller is in charge of keeping the rotational speed of the rotor around its rated speed $\Omega_{r,0}$. The controller does this by changing the pitch angles of the blades, denoted as $\beta_1(t), \beta_2(t)$ and $\beta_3(t)$. These are controlled by 1st order filter equations assembled in the vector relation (25)

$$\dot{\boldsymbol{\beta}}(t) = -\frac{1}{\tau}\Big(\boldsymbol{\beta}(t) - \boldsymbol{\beta}_0(\mathbf{q}, \dot{\mathbf{q}}, t)\Big) \tag{25}$$

$$\boldsymbol{\beta}(t) = \begin{bmatrix} \beta_1(t) \\ \beta_2(t) \\ \beta_3(t) \end{bmatrix} \quad , \quad \boldsymbol{\beta}_0(\mathbf{q}, \dot{\mathbf{q}}, t) = \begin{bmatrix} \beta_{1,0}(\mathbf{q}, \dot{\mathbf{q}}, t) \\ \beta_{2,0}(\mathbf{q}, \dot{\mathbf{q}}, t) \\ \beta_{3,0}(\mathbf{q}, \dot{\mathbf{q}}, t) \end{bmatrix} \tag{26}$$

τ is a constant specifying the time-delay of the pitch actuators. $\beta_{j,0}(\mathbf{q}, \dot{\mathbf{q}}, t)$ denotes the pitch control demand. From various available techniques for controller types, the PID controller is chosen in this work. The control command is then expressed as

$$\boldsymbol{\beta}_{j,0}(\mathbf{q}, \dot{\mathbf{q}}, t) = G\bigg(e(t) + \frac{1}{\tau_i}\int_0^t e(t)d\tau + \tau_d \frac{d}{dt}e(t)\bigg) \tag{27}$$

where $j = 1, 2, 3$ is the blade counter. $e(t)$ is the error signal defined as

$$e(t) = \dot{q}_5(t) - \dot{q}_{5,0} \tag{28}$$

as seen the control demand is identical for all blades. G is the controller gain, τ_i is the integral control time constant and τ_d is the differentiator time constant. There exist several techniques for designing the indicated controller i.e. by means of the Ziegler-Nichols empirical tuning formula, Ogata (2009). In practice a pure differentiator is rarely used due to its noise amplification effect, therefore it is usually replaced by a first order low-pass filter, Xue *et al.* (2008). In the present work the controller gains are tuned manually with the gains indicated in table 1. The equations of motion (18) and the control equations (25) may be combined into the state vector equations

$$\dot{\mathbf{z}}(t) = \mathbf{A}\mathbf{z}(t) + \mathbf{B}\mathbf{f}\big(\mathbf{v}(t), \mathbf{z}(t)\big) + \mathbf{B}_0(t) \tag{29}$$

$$\mathbf{z}(t) = \begin{bmatrix} \mathbf{q}(t) \\ \dot{\mathbf{q}}(t) \\ \boldsymbol{\beta}(t) \end{bmatrix} \tag{30}$$

$$\left.\begin{aligned} \mathbf{A} &= \begin{bmatrix} \mathbf{0} & \mathbf{I} & \mathbf{0} \\ -\mathbf{m}^{-1}\mathbf{k} & -\mathbf{m}^{-1}\mathbf{c} & \mathbf{0} \\ \frac{1}{\tau}\mathbf{b}_1 & \frac{1}{\tau}\mathbf{b}_2 & -\frac{1}{\tau}\mathbf{I} \end{bmatrix} \\ \mathbf{B} &= \begin{bmatrix} \mathbf{0} \\ \mathbf{m}^{-1} \\ \mathbf{b}_3 \end{bmatrix} \\ \mathbf{B}_0(t) &= \begin{bmatrix} \mathbf{0} \\ \mathbf{0} \\ \mathbf{b}_0(t) \end{bmatrix} \end{aligned}\right\} \tag{31}$$

where $\mathbf{b}_0(t), \mathbf{b}_1, \mathbf{b}_2$ and $\mathbf{b}_3$ are given as

$$\mathbf{b}_0(t) = -\frac{G\,\Omega_{r,0}}{\tau}\left(1 + \frac{t}{\tau_i}\right)\begin{bmatrix} 1 \\ 1 \\ 1 \end{bmatrix} \tag{32}$$

$$\left.\begin{aligned} \mathbf{b}_1 &= \tfrac{G}{\tau_i}\begin{bmatrix} 0\,0\,0\,0\,1 \\ 0\,0\,0\,0\,1 \\ 0\,0\,0\,0\,1 \end{bmatrix} \\ \mathbf{b}_2 &= \tau_i\Big(1 - \eta\tfrac{\tau_d}{J}\tfrac{M_{r,0}}{\Omega_{r,0}}\Big)\mathbf{b}_1 \\ \mathbf{b}_3 &= \tfrac{\tau_d}{J}\mathbf{b}_2 \end{aligned}\right\} \tag{33}$$

Table 1. Structural parameters of the wind turbine model

h	87.6	m	ζ_0	0.01	
L	61.5	m	ζ	0.005	
m	17415	kg	ω	4.2	rad/s
m_0	404520	kg	ω_0	2.0	rad/s
m_1	791	kg	k	14120	N/m
m_2	1893	kg	k_0	1667914	N/m
m_3	359304	kg m	$\Omega_{r,0}$	1.27	rad/s
m_4	83228	kg m	$\Omega_{g,00}$	73.7	m/s
m_5	6100058	kg m	V_r	15	m/s
J_r	35337324	kg m^2	V_o	25	m/s
J_g	535	kg m^2	V_i	5	m/s
N	97		τ	0.2	s
M_0	296780	kg	τ_i	5	s
$M_{r,0}$	3946018	N m	τ_d	0	s
η	0.05				

Table 2. Subset simulation parameters

N_{sim}	p_0	m	CPU time [s]	Memory [GB]
500	0.1	6	1.5×10^4	1.2
500	0.5	15	3.4×10^4	6.0
1000	0.1	6	3.0×10^4	2.4
2000	0.1	6	6.0×10^4	4.8
3000	0.1	6	8.5×10^4	7.2

4.5 *Rare event estimation of the wind turbine*

The time duration for simulation is chosen 800[*sec*] where the first 200s are discarded to take into account the effect of the transient phase of the system response. The rest simulates a 10min. interval which is prescribed in design codes for extraction of probabilistic behavior of the turbines IEC (2005b). The resolution of the time integrator is set to $\Delta t = 0.2s$. Turbulent wind field is simulated on 31 nodes, one on the hub and others at $0.8L$ radial distance from hub on an equi-distance angular grid. The mean wind is set to $V_r = 15[m/s]$ and the cut-in and cut-out speeds are set to $V_i = 5[m/s]$ and $V_o = 25[m/s]$ respectively. The limit state function is defined as the first passage of the magnitude of the tower displacement from the threshold (barrier) level b i.e. $p_f(b) = \text{Prob}\left(\max_{t\in[0,T]} |z_4(t)| \geq b\right)$ with $T = 600[s]$ of simulation. Discarding the transient simulation time, the LSF is defined as a function of 93000 stochastic variables. Failure probability of the model is estimated by SS with parameters indicated in table 2 and SMC with 4.95×10^5 samples. A practical issue is the very high number of the basic random variables, e.g. the iid Gassian random numbers which will pass through the turbulence filter, needed to be stored in the memory for the next stage of the simulation. These consists of seeds for two consecutive simulation levels which contains $2N_{seed}$ sets of basic random variables requiring approximately 12MB of disc space for only one simulation. Therefore a simulation with 500 initial samples and $p_0 = 0.1$ requires approximately 1.2GB memory (or disc space) to save $2N_{seed} = 100$ seeds for two simulation levels. The proposal distributions are chosen uniform centered at the sample seed and with spread equal to 2 times standard deviation of the seeds of the previous level.

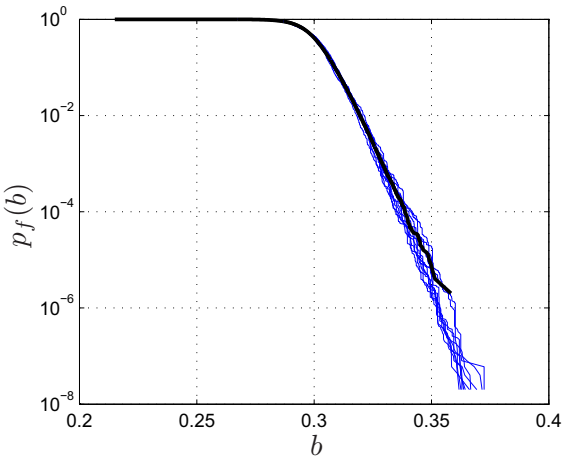

Figure 6. First passage probability estimation SS-MMH. Fixed speed wind turbine; 6 stages with $p_0 = 0.1$ Thick black: Standard Monte Carlo, Thin blue: Subset simulation with MMH sampling scheme

Figures 4.5 and 4.5 show estimates of the first passage probability of the fixed speed wind turbine with SS-MMH and SS-MMHDR respectively. In both figures number of samples is $N_{sim} = 500$ and probability increment is set to $p_0 = 0.1$. Each figure shows 10 estimates of the first passage probability with SS together with the SMC results. The figures show that both methods are successful in increasing barrier levels and their estimates are close to that of the SMC. However SS-MMHDR results suffer from small over estimation of the first passage probability at high barrier levels. Figures 4.5 and 4.5 show the estimates of the first passage probability of the variable speed wind turbine. The figures show that presence of the controller has considerable effect on first passage probability estimation. The controller not only changes the range of barrier levels but also makes the estimation of the first passage probability a more difficult task. As seen in figures 4.5 and 4.5 both methods have rather poor estimates of the first passage probabilities of order 10^{-7} for the variable speed wind turbine case.

For the fixed speed wind turbine the value $p_0 = 0.1$ is shown to be a good choice and both methods overcome the difficulties faced by high dimensions of the model. However the variable speed model has difficulties in estimating very low probabilities c.f. figures 4.5 and 4.5. In order to give more chance of uniform distribution of the seeds in the failure region of the problem, the intermediate failure probability has been increased by setting $p_0 = 0.5$. This clearly requires increasing the number of the simulation stages, e.g. m in (2) and (3), for estimation of the same failure probability. Here 15 stages of simulation have been used which allows estimation of the failure probabilities down to 1.2×10^{-7}.

Moreover it is interesting to assess the efficiency of the method by increasing the initial sample number compared to decreasing the intermediate threshold levels since they both end up in increasing the number of seeds and the computation cost. Therefore in the next steps N_{sim} has been changed from 500 to 1000, 2000 and 3000 while keeping $p_0 = 0.1$. Figures 4.5 and 4.5 show estimated first passage probabilities for the fixed and the variable speed cases respectively by SS-MMH with different configurations. It is seen that increasing number of samples has similar effects as decreasing the intermediate threshold level. However the recorded computation time, c.f. table2, on a 2.80GHz Intel i7 CPU with 8GB memory is in favor of choosing less initial samples, N_{sim}, with bigger probability increments, p_0, but with more simulation stages, m. Figures 4.5 and 4.5 are the counterparts of figures 4.5 and 4.5 but the SS-MMHDR method is used here. It is

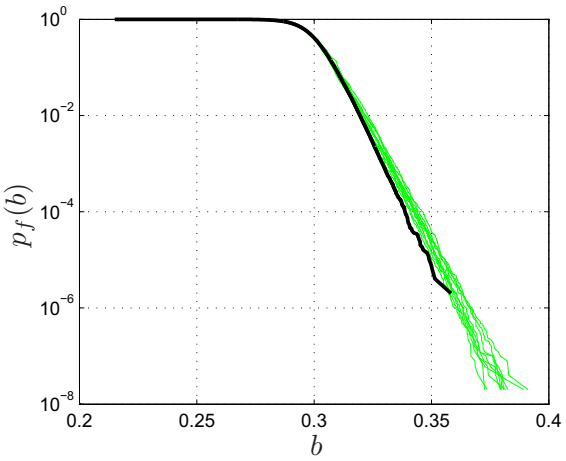

Figure 7. First passage probability estimation SS-MMHDR. Fixed speed wind turbine; 6 stages with $p_0 = 0.1$ Thick black: Standard Monte Carlo, Thin green: Subset simulation with MMHDR sampling scheme

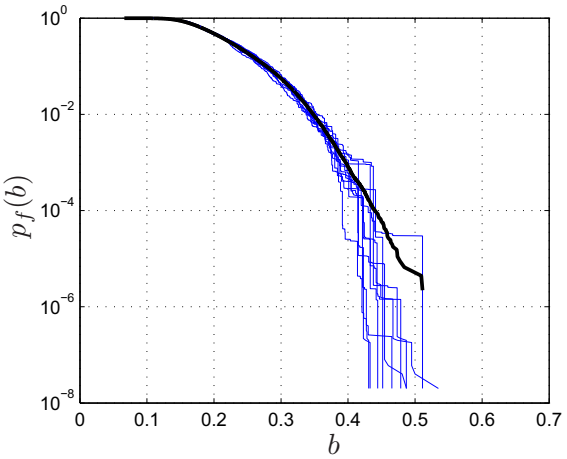

Figure 8. First passage probability estimation SS-MMH. Variable speed wind turbine; 6 stages with $p_0 = 0.1$ Thick black: Standard Monte Carlo, Thin blue: Subset simulation with MMH sampling scheme

seen that increasing number choosing bigger p_0 with more simulation stages increases the over estimation of the probability in the fixed wind turbine case. Although on the variable speed case the conclusion is the same as the SS-MMH method.

5. Conclusions

The low first passage probability of a reduced order wind turbine model is estimated based on the Makov Chain Monte Carlo. A well-known method for this aim, e.g. SS-MMH, with two of the most recent modifications to the original algorithm have been implemented and compared to the original method on a linear SDOF oscillator. The results show that in high dimensions the chains constructed by SS-MMHRC algorithm do not move to the next state often, and tend to stay in their initial state. However

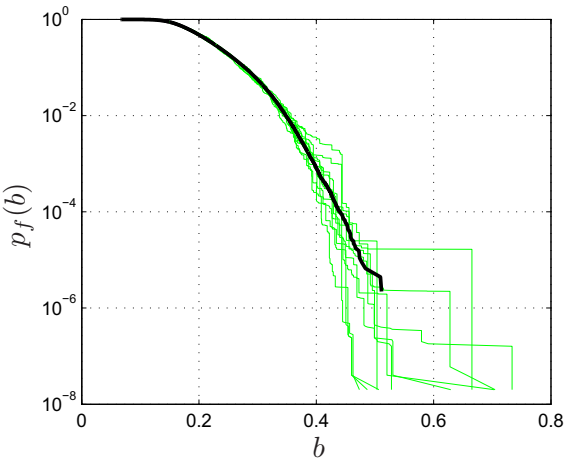

Figure 9. First passage probability estimation SS-MMHDR. Variable speed wind turbine; 6 stages with $p_0 = 0.1$ Thick black: Standard Monte Carlo, Thin green: Subset simulation with MMHDR sampling scheme

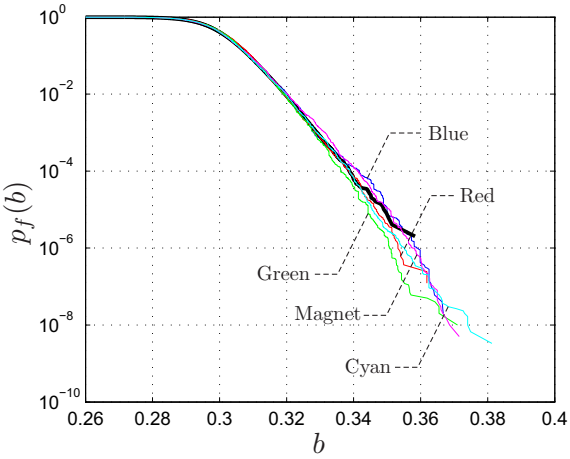

Figure 10. First passage probability estimation SS-MMH. Fixed speed wind turbine. blue: 6 stages with 500 samples and $p_0 = 0.1$; red : 15 stages with 500 samples and $p_0 = 0.5$; green: 6 stages with 1000 samples and $p_0 = 0.1$; magnet: 6 stages with 2000 samples and $p_0 = 0.1$; cyan: 6 stages with 3000 samples and $p_0 = 0.1$

the SS-MMH and the SS-MMHDR are both successful in moving to the next states and increase the barrier levels.

The estimated first passage probability of the fixed speed wind turbine is in good agreement with SMC with all different simulation configurations with SS-MMH. On the other hand SS-MMHDR results have small over estimations in their predictions. Estimations of the first passage probability of the variable speed wind turbine is also presented. This is a high dimensional nonlinear first passage estimation of a dynamic system incorporating a controller; which to the best knowledge of authors is the first time being reported in the literature on VRMC methods. It is seen that presence of a controller has considerable effect on first passage probability estimation. The controller not only changes the range of barrier levels but also makes the estimation of the first passage probability a more difficult task. The SS estimations of the first passage probability of the variable speed wind turbine underestimate the failure probability of the high barrier

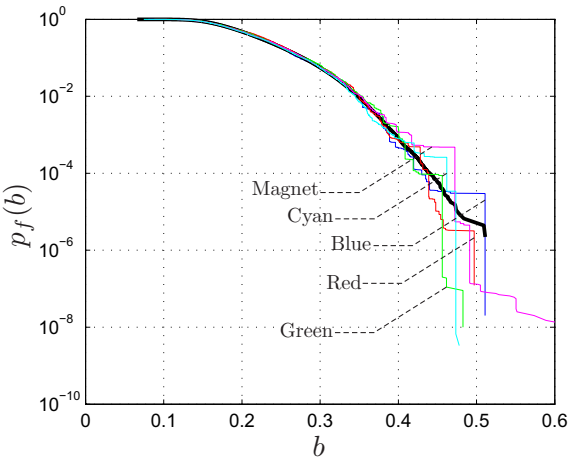

Figure 11. First passage probability estimation SS-MMH. Variable speed wind turbine. blue: 6 stages with 500 samples and $p_0 = 0.1$; red : 15 stages with 500 samples and $p_0 = 0.5$; green: 6 stages with 1000 samples and $p_0 = 0.1$; magnet: 6 stages with 2000 samples and $p_0 = 0.1$; cyan: 6 stages with 3000 samples and $p_0 = 0.1$

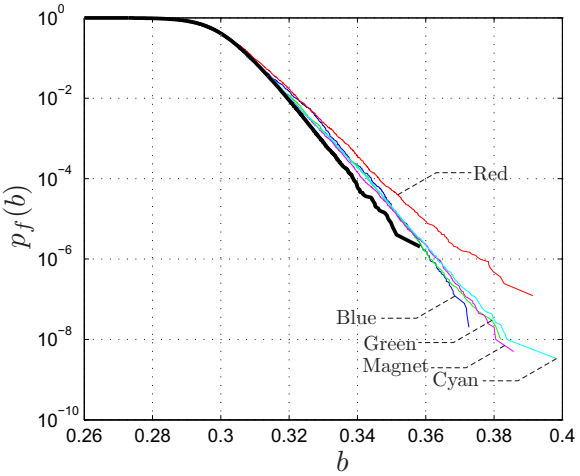

Figure 12. First passage probability estimation SS-MMHDR. Fixed speed wind turbine. blue: 6 stages with 500 samples and $p_0 = 0.1$; red : 15 stages with 500 samples and $p_0 = 0.5$; green: 6 stages with 1000 samples and $p_0 = 0.1$; magnet: 6 stages with 2000 samples and $p_0 = 0.1$; cyan: 6 stages with 3000 samples and $p_0 = 0.1$

levels i.e. of order 10^{-7}.

5.1 *Acknowledgements*

The Danish Energy Authority is acknowledged for support under the grant EFP07-II, Estimation of Extreme Responses and Failure Probability of Wind Turbines under Normal Operation by Controlled Monte Carlo Simulation.

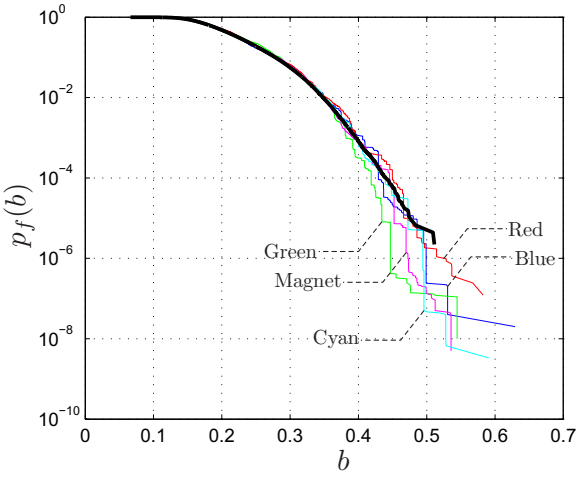

Figure 13. First passage probability estimation SS-MMHDR. Variable speed wind turbine. blue: 6 stages with 500 samples and $p_0 = 0.1$; red : 15 stages with 500 samples and $p_0 = 0.5$; green: 6 stages with 1000 samples and $p_0 = 0.1$; magnet: 6 stages with 2000 samples and $p_0 = 0.1$; cyan: 6 stages with 3000 samples and $p_0 = 0.1$

References

Au, S.K. and Beck, J.L., 2001. Estimation of small failure probabilities in high dimensions by subset simulation. *Probabilistic Engineering Mechanics*, 16 (4), 263 – 277.

Au, S., Cao, Z., and Wang, Y., 2010. Implementing advanced Monte Carlo simulation under spreadsheet environment. *Structural Safety*, 32 (5), 281 – 292 Probabilistic Methods for Modeling, Simulation and Optimization of Engineering Structures under Uncertainty in honor of Jim Beck's 60th Birthday.

Chib, S. and Greenberg, E., 1995. Understanding the Metropolis-Hastings Algorithm. *The American Statistician*, 49 (4), 327–335.

Ching, J., Beck, J., and Au, S., 2005. Hybrid Subset Simulation method for reliability estimation of dynamical systems subject to stochastic excitation. *Probabilistic Engineering Mechanics*, 20 (3), 199 – 214.

Freudenreich, K. and Argyriadis, K., 2007. The Load Level of Modern Wind Turbines according to IEC 61400-1. *Journal of Physics: Conference Series*, 75 (012075).

Harris, I., 2005. Generalised Pareto methods for wind extremes. Useful tool or mathematical mirage?. *Journal of Wind Engineering and Industrial Aerodynamics*, 93 (5), 341 – 360.

Hoff, P., 2009. *A First Course in Bayesian Statistical Methods*. 2nd Springer.

IEC, 2005a. *Amendment to the IEC 61400-1:2005 standard*. International Electrotechnical Commission.

IEC, 2005b. *IEC 61400-1 (2005) International Standard, Wind turbines - Part 1: Design requirements*. third International Electrotechnical Commission.

Jonkman, J., *et al.*, Definition of a 5-MW reference wind turbine for offshore system development. , 2009. , Technical report, National Renewable Energy Laboratory.

Katafygiotis, L. and Cheung, S., 2007. Application of spherical subset simulation method and auxiliary domain method on a benchmark reliability study. *Structural Safety*, 29 (3), 194 – 207 A Benchmark Study on Reliability in High Dimensions.

Katafygiotis, L. and Zuev, K., 2008. Geometric insight into the challenges of solving high-dimensional reliability problems. *Probabilistic Engineering Mechanics*, 23 (2-3), 208

– 218 5th International Conference on Computational Stochastic Mechanics.

Kelly, D.L. and Smith, C.L., 2009. Bayesian inference in probabilistic risk assessment– The current state of the art. *Reliability Engineering & System Safety*, 94 (2), 628 – 643.

Ogata, K., 2009. *Modern Control Engineering*. 5 Prentice Hall; 5 edition.

Santoso, A., Phoon, K., and Quek, S., 2010. Modified Metropolis-Hastings algorithm with reduced chain correlation for efficient subset simulation. *Probabilistic Engineering Mechanics*, In Press, Corrected Proof, –.

Schueller, G.I. and Pradlwarter, H.J., 2009. Uncertainty analysis of complex structural systems. *International Journal for Numerical Methods in Engineering*, 80, 881–913.

Schueller, G. and Pradlwarter, H., 2007. Benchmark study on reliability estimation in higher dimensions of structural systems - An overview. *Structural Safety*, 29 (3), 167 – 182 A Benchmark Study on Reliability in High Dimensions.

Sichani, M., Nielsen, S., and C.Bucher, 2011a. Efficient Estimation of First Passage Probability of High Dimensional Non-linear Systems. *submitted to Probabilistic Engineering Mechanics*.

Sichani, M., Nielsen, S., and Naess, A., 2011b. Failure Probability Estimation of Wind Turbines by Enhanced Monte Carlo. *submitted to Engineering Mechanics, ASCE*.

Sichani, M., Pedersen, B., and Nielsen, S., 2010. Stochastic subspace modelling of turbulence. *World Academy of Science, Engineering and Technology*, 58, 1140 – 1148.

Song, S., Lu, Z., and Qiao, H., 2009. Subset simulation for structural reliability sensitivity analysis. *Reliability Engineering & System Safety*, 94 (2), 658 – 665.

Tierney, L. and Mira, A., 1999. Some adaptive Monte Carlo methods for Bayesian inference. *Statistics in Medicine*, 18, 2507 – 2515.

Valdebenito, M., Pradlwarter, H., and Schueller, G., 2010. The role of the design point for calculating failure probabilities in view of dimensionality and structural nonlinearities. *Structural Safety*, 32 (2), 101 – 111.

Xue, D., Chen, Y., and Atherton, D., 2008. *Linear Feedback Control: Analysis and Design with MATLAB*. Society for Industrial and Applied Mathematics (SIAM).

Yuan, X.X., Mao, D., and Pandey, M., 2009. A Bayesian approach to modeling and predicting pitting flaws in steam generator tubes. *Reliability Engineering & System Safety*, 94 (11), 1838 – 1847.

Zuev, K. and Katafygiotis, L., 2011. Modified Metropolis-Hastings algorithm with delayed rejection. *Probabilistic Engineering Mechanics*, 26 (3), 405 – 412.

APPENDIX G
Failure Probability Estimation of Wind Turbines by Enhanced Monte Carlo

The paper presented in this appendix is accepted for publication in *Journal of Engineering Mechanics ASCE*.

ASCE
AMERICAN SOCIETY OF CIVIL ENGINEERS

Title: Failure Probability Estimation of Wind Turbines by Enhanced Monte Carlo

Author: M. T. Sichani, S. R. K. Nielsen, A. Naess

Publication: Journal of Engineering Mechanics

Publisher: American Society of Civil Engineers

Date: 09/05/2011

Copyright © 2011, ASCE. All rights reserved.

Permissions Request

As an ASCE author, you are permitted to reuse you own content for another ASCE or non-ASCE publication.

Please add the full credit line "With permission from ASCE" to your source citation. Please print this page for your records.

Type of use: Dissertation/Thesis

Portion: full article

Format: electronic

Use of this content will make up more than 25% of the new work: no

Author of this ASCE work or ASCE will publish the new work: yes

Failure Probability Estimation of Wind Turbines by Enhanced Monte Carlo

M.T. Sichani[1], S.R.K. Nielsen[2], A. Naess, F.ASCE[3]

ABSTRACT

This paper deals with the estimation of the failure probability of wind turbines required by codes of practice for designing them. The Standard Monte Carlo (SMC) simulations might be used for this reason conceptually as an alternative to the popular Peaks Over Threshold (POT) method. However, estimation of very low failure probabilities with SMC simulation easily leads to unacceptably high computational costs. In this study an Enhanced Monte Carlo (EMC) method is proposed that overcomes this obstacle. The method has advantages over both POT and SMC in terms of low computational cost and accuracy. The method is applied to a low order numerical model of a 5 MW wind turbine with a pitch controller exposed to a turbulent inflow. Two cases of the wind turbine model are investigated. In the first case the rotor is running with a constant rotational speed. In the second case the variable rotational speed is controlled by the pitch controller. This provides a fair framework for comparison of the behavior and failure event of the wind turbine with focus on the effect of the pitch controller. The Enhanced Monte Carlo method is then applied to the model and the failure probabilities of the model are estimated down to the values related to the required 50 year's return period of the wind turbine.

Keywords: Wind turbine; pitch controller; reliability analysis; return period.

[1]PhD fellow, Aalborg University, Department of Civil Engineering, Sohngaardsholsvej 57, 9000 Aalborg, Denmark. (corresponding author) E-mail: mts@civil.aau.dk, Phone: +45 9940 8570

[2]Professor, Aalborg University, Department of Civil Engineering, Sohngaardsholsvej 57, 9000 Aalborg, Denmark. E-mail: srkn@civil.aau.dk, Phone: +45 9940 8451

[3]Professor, Centre for Ships and Ocean Structures & Department of Mathematical Sciences, Norwegian University of Science and Technology, NO-7491 Trondheim, Norway. E-mail: arvidn@math.ntnu.no

Introduction

Design codes for wind turbines are based on a return period (expected first-passage time) of $T_r = 50$ years, (IEC 2005a). This requires estimation of the design values of the wind turbine models related to the failure probability of the order 10^{-7}. According to the IEC61400-1 standard (IEC 2005b), the design value r of a stochastic response process $R(t)$, $t \in [0, \infty)$ (deformation, bending moment, stress, etc.) is obtained by extrapolation of the failure probability of the design value, r, in a reference epoch T to the return period T_r. Presuming independent failure events in adjacent reference epochs, the exceedance probability of the design value is given as

$$P\Big(R_{max}(T_r) > r\Big) \simeq \frac{T_r}{T} P\Big(R_{max}(T) > r\Big), \tag{1}$$

where $R_{max}(T)$ and $R_{max}(T_r)$ denote the maximum values in intervals T and T_r, respectively. With $T_r = 50$ years and $T = 600$s, Eq. (1) provides the relation

$$P\Big(R_{max}(T) > r\Big) \lesssim \frac{T}{T_r} = 3.8 \times 10^{-7} \tag{2}$$

The design value "r" is obtained as the solution to Eq. (2). It is out of the question to determine "r" by SMC due to the indicated low failure probability. The suggested approach in the IEC61400-1 standard is to use a Weibull or a Gumbel distribution (Harris 2004; Cook and Harris 2004) as the distribution function $F_{R_{max}(T)}(r) = 1 - P\Big(R_{max}(T) > r\Big)$ for R_{max}. This provides the following two alternative distributions:

$$\left.\begin{aligned} F_{R_{max}(T)}(r) &= 1 - \exp\left(-\left(\frac{r - r_0}{r_1}\right)^{r_2}\right) \\ F_{R_{max}(T)}(r) &= \exp\left(-\exp\left(\frac{r - r_0}{r_1}\right)\right) \end{aligned}\right\} \tag{3}$$

where r_0, r_1 and $r_2 > 0$ are locations, scale and shape parameters, which are estimated from the available sample. Many other choices of the distributions have been suggested such as reversed Weibull, log-normal (Harris 2005; Simiu et al. 2001; Freudenreich and Argyriadis 2007) etc., combined by the well-known Peaks-Over-Threshold (POT) method. Due to the inherent uncertainties in the fitting type, these methods do not yield accurate estimates of the low failure probabilities, i.e. it is not clear which extreme value distribution should be used in different situations. Clearly, it is beneficial to use a robust technique for estimating these failure probabilities which has the robustness of the SMC but with lower computation cost. In this regard there exist possibilities for efficient estimation of these low failure probabilities such as Importance Sampling (IS) (Macke and Bucher 2003), Line Sampling (LS) (Schuëller 2008), local domain

Monte Carlo (Pradlwarter and Schuëller 2010) etc. which might all be called Variance Reduction Monte Carlo (VRMC) methods.

The critical problem that renders most of the available methods inapplicable in practice is their high vulnerability in analysis of high dimensional nonlinear systems (Sichani et al. 2011; Valdebenito et al. 2010). It should be noted that dimensionality in the context of the VRMC methods refers to the number of basic stochastic variables in the normal space, (Katafygiotis and Zuev 2008), i.e. discrete approximations of the white noise entering turbulence filter in this study. Next the aerodynamic loads are calculated based on the turbulent wind field. These are governed by a highly nonlinear relationship which is solved by iteration. These steps not only increases the complexity of the problem but also prohibit the development of a straight forward input-output relationship for the system. Therefore the calculation of the required a-priori data for these methods, e.g. the gradient of the Limit State Function (LSF) required by local domain Monte Carlo (Pradlwarter and Schuëller 2010), requires a high computational effort which is out of budget in practical applications.

Additionally to the above mentioned problems, methods such as IS or LS make it possible to calculate the failure probability of a predefined barrier level very accurately. However this might suffice in reliability assessment problems, it does not in design problems where the barrier level for a predefined failure probability, e.g. the value of r in Eq. (2), is required to be estimated. The use of these methods in such cases is conditional on coupling them with an additional optimization. The drawback is that the optimization requires estimation of failure probability for several barrier levels which urges tuning the whole set of a-priori system information, i.e. control functions (critical excitations) in IS (Macke and Bucher 2003) or important directions in LS (Schuëller 2008), each time the barrier level is changed. This necessitates repetition of the majority of the computation procedures and causes significant reduction of efficiency of the method. Based on the mentioned discussions it is concluded that a high computational load will be demanded in such cases, especially for nonlinear systems, which demotivates the use of these methods as also pointed out by other researchers (Pradlwarter et al. 2007).

Therefore it is motivating to use more general methods for such systems which can cross over these problems without losing much accuracy or efficiency. Recently, the new so-called Enhanced Monte Carlo (EMC) method has been proposed by Naess et al. (Naess and Gaidai 2008b), which has been successfully applied for extreme response prediction and reliability analysis of structures (Naess and Gaidai 2008a; Naess et al. 2009). The method is further elaborated regarding the statistical dependencies of the extreme value samples of the system response (Naess and Gaidai 2009). An advantage of this method is its closeness to the POT, although it is a more general approach. In the present paper the performance of the method on a nonlinear model embedding a controller is investigated. The presence of the controller adds a secondary nonlinearity to the model and makes tracing the system's behavior even more difficult. This problem

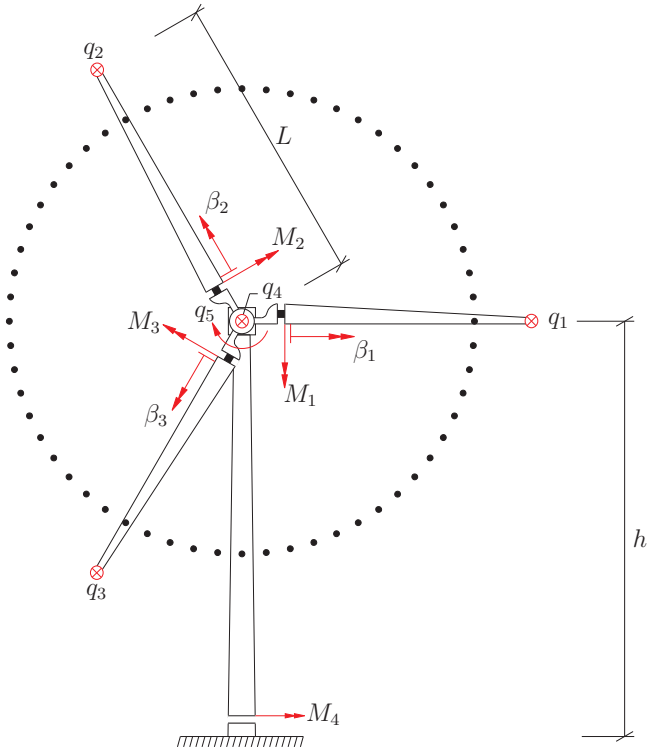

FIG. 1. Definition of degrees of freedom section moments and pitch angles.

has specific motivations for the wind turbines since it addresses a practical issue on demand by codes of practice.

Wind turbine model

In order to test the applicability of the proposed method on fixed and variable speed wind turbines a reduced order model of a 5 MW reference wind turbine is developed. The specifications of the wind turbine structure are adopted from the NREL reference wind turbine (Jonkman et al. 2009). It is attempted to cover the principal behavior of the wind turbine therefore the model consists of structure, pitch controller, aerodynamic loads and wind modules which are explained in detail in the following sections.

Mechanical Model

The motions of the blades relative to the hub and only the motion of the tower in the mean wind direction are modeled by single degree-of-freedom systems. Let $y_i(x,t), i = 1,2,3$ denote the displacement fields of the blades relative to the hub, where $x \in [0, L]$ is measured from the hub and L is the length of the blades of Fig. 1. Further $y_4(x,t)$ denotes the displacement of the tower in the same

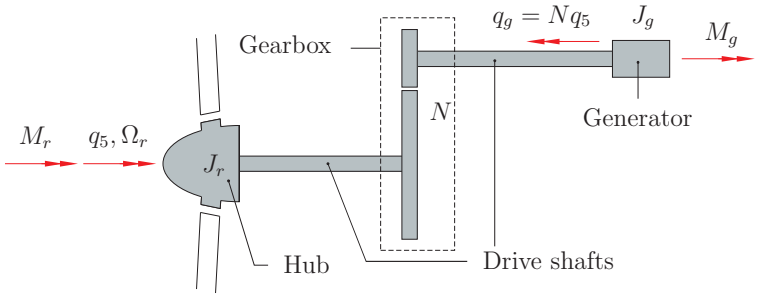

FIG. 2. Single degree of freedom representation of drive train.

direction, where $x \in [0, h]$ is measured from the foundation and h is the height of the nacelle above the ground surface. Then, the indicated displacement fields may written

$$\left.\begin{array}{rcll} y_i(x,t) & \simeq & \Phi(x)q_i(t) \quad , & i = 1,2,3 \\ y_4(x,t) & \simeq & \Phi_0(x)q_4(t)\,. & \end{array}\right\} \tag{4}$$

$\Phi_0(x)$ is the part of the fundamental eigenmode of the wind turbine belonging to the tower and $\Phi(x)$ is the fundamental fixed base mode shape of the blade. The blades and the tower are modeled as Bernoulli-Euler beams (Sichani et al. 2011). The dynamic load per unit length on the tower in the mean wind direction is denoted $p_4(x,t)$. Correspondingly, the load on the three blades in the same direction are denoted $p_1(x,t), p_2(x,t)$ and $p_3(x,t)$. The rigid body motion of the drive train is modeled as a single rotational degree of freedom q_5 by assuming infinite stiff drive shafts and no elastic deformation in the gear, whereby the following kinematic relation emerge for the angular rotation of the rotor of the generator

$$q_g = Nq_5 \tag{5}$$

where N is the gear ratio, cf. Fig. 2. Furthermore, the mass moment of inertia of the gear wheels and the connected shafts are included into the mass moment of inertia J_r and J_g of the rotor and the generator rotor, respectively. Using Euler-Lagrange's equations (Meirovitch 2001), the following governing equations of the system may be obtained

$$\mathbf{m}\ddot{\mathbf{q}}(t) + \mathbf{c}\dot{\mathbf{q}}(t) + \mathbf{k}\mathbf{q}(t) = \mathbf{f}(t) \tag{6}$$

$$\left.\begin{array}{rcl} \mathbf{m} = \begin{bmatrix} m_1 & 0 & 0 & m_2 & 0 \\ 0 & m_1 & 0 & m_2 & 0 \\ 0 & 0 & m_1 & m_2 & 0 \\ m_2 & m_2 & m_2 & m_0 & 0 \\ 0 & 0 & 0 & 0 & J \end{bmatrix} & , & \mathbf{k} = \begin{bmatrix} k & 0 & 0 & 0 & 0 \\ 0 & k & 0 & 0 & 0 \\ 0 & 0 & k & 0 & 0 \\ 0 & 0 & 0 & k_0 & 0 \\ 0 & 0 & 0 & 0 & 0 \end{bmatrix} \end{array}\right\} \tag{7}$$

$$\left.\begin{array}{lllllll} m & = & \int_0^L \mu(x)dx & & m_4 & = & \int_0^L x\mu(x)\Phi(x)dx \\ m_1 & = & \int_0^L \mu(x)\Phi^2(x)dx & & m_5 & = & \int_0^h x\mu_0(x)\Phi_0(x)dx \\ m_2 & = & \int_0^L \mu(x)\Phi(x)dx & & m_0 & = & \int_0^h \mu_0(x)\Phi_0^2(x)dx + M_0 + 3m \\ m_3 & = & \int_0^L x\mu(x)dx & & J_r & = & \int_0^L x^2\mu(x)dx \end{array}\right\} \quad (8)$$

J is the generalized mass moment of inertia related to the rigid body degree-of-freedom $q_5(t)$ given as

$$J = J_r + N^2 J_g \quad (9)$$

The damping matrix $\mathbf{c}$ merely includes structural damping. Aerodynamic damping is included later via the aerodynamic load. Then $\mathbf{c}$ may be written as

$$\mathbf{c} = \text{diag}(2\zeta\omega m_1, 2\zeta\omega m_1, 2\zeta\omega m_1, 2\zeta_0\omega_0 m_0, \eta M_{r,0}/\Omega_{r,0}) \quad (10)$$

$$\mathbf{q}(t) = \begin{bmatrix} q_1(t) \\ \vdots \\ q_5(t) \end{bmatrix} \quad , \quad \mathbf{f}(t) = \begin{bmatrix} f_1(t) \\ \vdots \\ f_5(t) \end{bmatrix} \quad (11)$$

where $\Omega_{r,0} = \dot{q}_{5,0}$ is the referential (nominal) rotational speed of the rotor. ω and ζ denote the eigenfrequency and damping ratio of the blades, when fixed to the hub. Correspondingly, ω_0 and ζ_0 denote the eigenfrequency and damping ratio of the lowest mode of the tower, which are assumed to be known. η is the loss factor of the transmission system due to friction in gears and bearings, which typically is a few percent and $M_{r,0} = P/\Omega_{r,0}$ is the referential rotor torque for $P = 5$MW nominal power output. The generalized stiffness coefficients of the blades and the tower are given as

$$k = \omega^2 m_1 \quad , \quad k_0 = \omega_0^2 m_0 \quad (12)$$

k_0 is determined, so the generalized eigenvalue problem defined from Eq. (7) provides the prescribed angular lower eigenfrequency ω_0. The generalized external dynamic loads become

$$\left.\begin{array}{lll} f_i(t) & = & \int_0^L \Phi(x)p_i(x,t)dx \quad , \quad i = 1,2,3 \\ f_4(t) & = & \int_0^h \Phi_0(x)p_4(x,t)dx + \\ & & \sum_{i=1}^{3} \int_0^L \Phi(x)p_i(x,t)dx \\ f_5(t) & = & M_r - (1+\eta)NM_g \end{array}\right\} \quad (13)$$

where M_r and M_g are the instantaneous rotor and generator torques respectively and asynchronous slip variable generator is considered for which the generator torque under normal operation conditions is linearly dependent on the rotational speed $N\dot{q}_5(t)$. The relation may be given on the form

$$M_g(t) = M_{g,0}\frac{N\dot{q}_5(t) - \Omega_{g,00}}{\Omega_{g,0} - \Omega_{g,00}} \quad (14)$$

where $M_{g,0} = M_{r,0}/N$ is the nominal generator torque, $\Omega_{g,0} = N\Omega_{r,0}$ is the nominal generator rotational speed and $\Omega_{g,00}$ is the generator speed for the zero generator torque.

Controller model

$\beta_1(t), \beta_2(t)$ and $\beta_3(t)$ denote the pitch angles of the blades, see Fig. 1. These are controlled by the 1st order filter equations assembled in the vector relation

$$\dot{\boldsymbol{\beta}}(t) = -\frac{1}{\tau}\Big(\boldsymbol{\beta}(t) - \boldsymbol{\beta}_0(\mathbf{q}, \dot{\mathbf{q}}, t)\Big) \tag{15}$$

$$\boldsymbol{\beta}(t) = \begin{bmatrix} \beta_1(t) \\ \beta_2(t) \\ \beta_3(t) \end{bmatrix} \quad , \quad \boldsymbol{\beta}_0(\mathbf{q}, \dot{\mathbf{q}}, t) = \begin{bmatrix} \beta_{1,0}(\mathbf{q}, \dot{\mathbf{q}}, t) \\ \beta_{2,0}(\mathbf{q}, \dot{\mathbf{q}}, t) \\ \beta_{3,0}(\mathbf{q}, \dot{\mathbf{q}}, t) \end{bmatrix} \tag{16}$$

τ is a constant specifying the time-delay of the pitch actuators. $\beta_{j,0}(\mathbf{q}, \dot{\mathbf{q}}, t)$ denotes the pitch control demand. From various available techniques for controller design, the PID controller, due to its wide range of applications in industry and its simplicity, (Ogata 2009), is chosen in this work. The control command is then expressed as

$$\begin{aligned} \boldsymbol{\beta}_{j,0}(\mathbf{q}, \dot{\mathbf{q}}, t) &= G\bigg(e(t) + \frac{1}{\tau_i}\int_0^t e(t)d\tau + \tau_d \frac{d}{dt}e(t)\bigg) \\ &= G\bigg(\dot{q}_5(t) - \Omega_{r,0} + \frac{1}{\tau_i}\Big(q_5(t) - t\Omega_{r,0}\Big) \\ &\quad + \frac{\tau_d}{J}\Big(f_5(t) - \eta\frac{M_{r,0}}{\Omega_{r,0}}\dot{q}_5(t)\Big)\bigg) \quad , \quad j = 1, 2, 3 \end{aligned} \tag{17}$$

where $e(t)$ is the error signal defined as

$$e(t) = \dot{q}_5(t) - \dot{q}_{5,0} \tag{18}$$

as seen the control demand is identical for all blades. G is the controller gain which is chosen inverse proportional to the partial derivative $\frac{\partial M_r}{\partial \boldsymbol{\beta}}$, τ_i is the integral control time constant and τ_d is the differentiator time constant which is chosen as a fraction of τ_i. There exist several techniques for designing the indicated controller i.e. by means of the Ziegler-Nichols empirical tuning formula, (Ogata 2009). In practice a pure differentiator is rarely used due to its noise amplification effect, therefore it is usually replaced by a first order low-pass filter, (Xue et al. 2008). In the present work the controller gains are tuned manually with the gains indicated in table 1. The equations of motion (6) and the control equations (15) may be combined into the state vector equations

$$\dot{\mathbf{z}}(t) = \mathbf{A}\mathbf{z}(t) + \mathbf{B}\mathbf{f}\big(\mathbf{v}(t), \mathbf{z}(t)\big) + \mathbf{B}_0(t) \tag{19}$$

$$\mathbf{z}(t) = \begin{bmatrix} \mathbf{q}(t) \\ \dot{\mathbf{q}}(t) \\ \boldsymbol{\beta}(t) \end{bmatrix} \quad , \quad \mathbf{A} = \begin{bmatrix} \mathbf{0} & \mathbf{I} & \mathbf{0} \\ -\mathbf{m}^{-1}\mathbf{k} & -\mathbf{m}^{-1}\mathbf{c} & \mathbf{0} \\ \frac{1}{\tau}\mathbf{b}_1 & \frac{1}{\tau}\mathbf{b}_2 & -\frac{1}{\tau}\mathbf{I} \end{bmatrix} \tag{20}$$

$$\mathbf{B} = \begin{bmatrix} \mathbf{0} \\ \mathbf{m}^{-1} \\ \mathbf{b}_3 \end{bmatrix} \quad , \quad \mathbf{B}_0(t) = \begin{bmatrix} \mathbf{0} \\ \mathbf{0} \\ \mathbf{b}_0(t) \end{bmatrix} \tag{21}$$

where $\mathbf{b}_0(t), \mathbf{b}_1, \mathbf{b}_2$ and $\mathbf{b}_3$ are given as

$$\mathbf{b}_0(t) = -\frac{G\,\Omega_{r,0}}{\tau}\left(1+\frac{t}{\tau_i}\right)\begin{bmatrix}1\\1\\1\end{bmatrix} \quad , \quad \mathbf{b}_1 = \frac{G}{\tau_i}\begin{bmatrix}0&0&0&0&1\\0&0&0&0&1\\0&0&0&0&1\end{bmatrix} \tag{22}$$

$$\mathbf{b}_2 = \tau_i\Big(1-\eta\tfrac{\tau_d}{J}\tfrac{M_{r,0}}{\Omega_{r,0}}\Big)\mathbf{b}_1 \quad , \quad \mathbf{b}_3 = \tfrac{\tau_d}{J}\mathbf{b}_2 \tag{23}$$

Aerodynamic Load model

Only the aerodynamic load on the blades is considered, i.e. wind load on the tower is ignored; $p_4(x,t) = 0$. Aerodynamic damping is included via a quasi-static effective angle of attack $\alpha(x,t)$ so changes of the angle of attack is instantly felt in the aerodynamic loads. The wind loads are calculated by the BEM method, (Hansen 2007). The turbulence with a prescribed correlation structure is generated in 30 points on a circle with radius $0.8L$ as seen in Fig. 1 and one on the hub. The mean wind speed V is assumed constant over the rotor area. This results in neglecting the effect of the shear effects. Nevertheless the dynamic part of the solution - versus the quasi-static part caused by the shear loads - which is of interest for the extreme value events of the wind turbine will be captured by the model. Therefore this assumption is made in favor of the numerical efficiency of the algorithm. A state space model for turbulence is calibrated using the SSM method, (Sichani et al. 2010; Sichani et al. 2011). The method is based on matching the cross-covariance function of the turbulence process with its prescribed function. This approach for turbulence modeling, like the spectral methods, does not take into account the rotational sampling effect of the turbulence process and just generates the turbulence at fixed grid points. Therefore it is needed to make an interpolation as the blades pass through different turbulence nodes in between two nodes which is done in the following way. At a certain instant of time the portion of a given blade is defined by the center angle $q_5(t)$ placed in the sector delimited by the center angles θ_i and θ_{i+1} representing the turbulence components $v_i(t)$ and $v_{i+1}(t)$ c.f. Fig.. Then, the turbulence $v(t)$ on the blade is obtained by linear interpolation as follow

$$v(t) = v_i(t) + \frac{v_{i+1}(t) - v_i(t)}{\theta_{i+1} - \theta_i}(q_5(t) - \theta_i) \tag{24}$$

Model specifications

Structural properties of the tower and the blades are adopted from the definitions of the NREL 5MW wind turbine (Jonkman et al. 2009; Kooijman et al. 2003), and have been indicated in table 1 along which the derived parameters entering the reduced model and the control parameters. The rated wind speed of the model i.e. the wind speed at which the nominal power is produced is $V_r = 10.72$m/s as indicated in table 1. For values higher than this value the pitch controller is

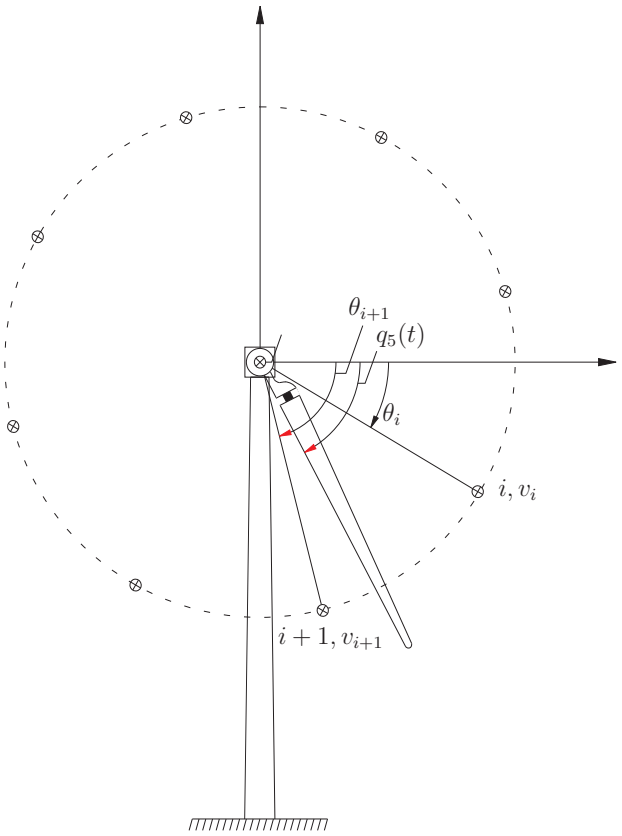

FIG. 3. Interpolation of turbulence.

turned on which decreases the rotor speed to its nominal value. Modal responses of the first blade and the tower are shown in Figs. 4.a and 4.b. As seen, the blade response relative to the hub is broad banded. This is due to the significant aerodynamic damping of the blade. The variable rotational speed of the rotor and the pitch command of the controller - which is the same for all three blades - are then shown in Figs. 4.c and 4.d.

Fixed versus variable speed model

Simulations show that the controller changes the system behavior significantly. Therefore a more detailed study with the aim of analyzing controller's effect is performed in this section. The two cases of operation referred to as *fixed speed* and *variable speed* will be considered. In the first case the rotational speed of the rotor is set to the nominal rotor speed $\Omega_{r,0}$ while in the second case the controller is in charge of keeping the speed around the nominal speed. According to the coupling between the rotor torque and the normal load, presence of the the pitch controller will affect the vibration level of the wind turbine. For further illustration a simulation of the wind turbine is carried out within 600 seconds.

TABLE 1. Structural and control parameters of the wind turbine model.

Parameter	Value	Dimension	Parameter	Value	Dimension
h	87.6	m	ω	4.2	rad/s
L	61.5	m	ω_0	2.0	rad/s
m	17415	kg	τ	0.2	s
m_0	404520	kg	τ_i	5	s
m_1	791	kg	τ_d	0	s
m_2	1893	kg	G	0.1	rad
m_3	359304	kg m	η	0.05	
m_4	83228	kg m	ρ	1.25	kg/m^3
m_5	6100058	kg m	$\Omega_{r,0}$	1.27	rad/s
J_r	35337324	kg m^2	V_h	15	m/s
J_g	535	kg m^2	$M_{r,0}$	3946018	N m
N	97		υ	0.2	
M_0	296780	kg	V_o	25	m/s
k	14120	N/m	V_i	5	m/s
k_0	1667914	N/m	$\Omega_{g,00}$	73.7	rad/s
ζ	0.005		V_r	15	m/s
ζ_0	0.01				

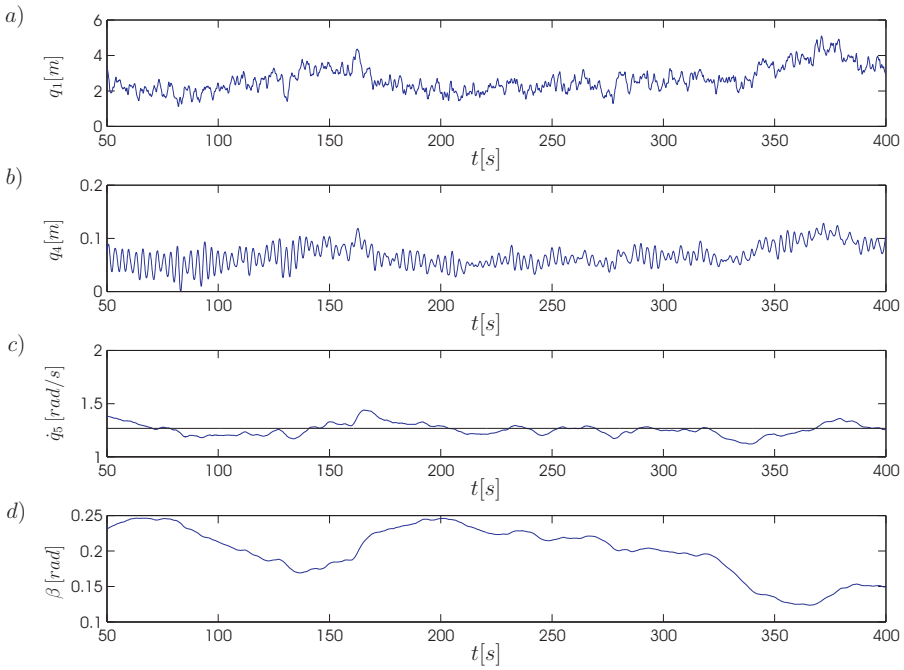

FIG. 4. Modal responses of each DOF of the wind turbine.

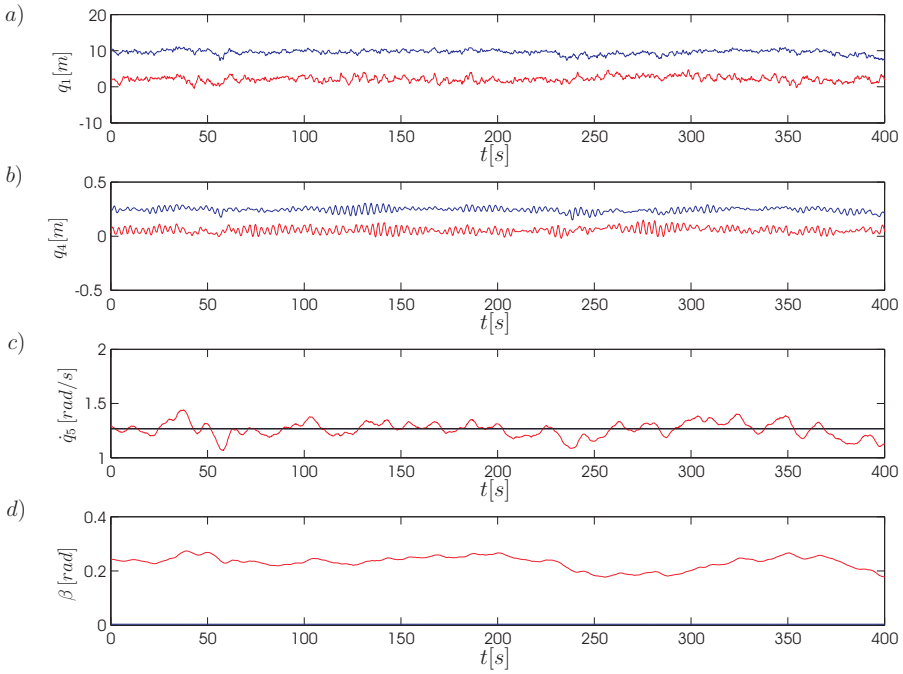

FIG. 5. Modal responses of each DOF of the wind turbine. blue: fixed speed; red: variable speed

The same wind field realization is used for both fixed and variable speed models. As seen in Fig. 5 the vibration amplitude of the variable speed case during normal operation is lower than the fixed speed case. However this is not guaranteed and the opposite also happens. As a counter example the responses to a specific realization of the wind field - the realization at hub hight is shown in Fig. 6 - are shown in Fig. 7. As seen in this figure, in extreme conditions, i.e. $t \in [100, 200]s$, the vibration level of the variable speed model exceeds its value for the fixed speed model. Results of the next section show that this case is dominant in the extreme conditions. This analysis is provided in order to illustrate the effect of the pitch controller which may be either increment or decrement of the safety margin of the system in extreme conditions.

Enhanced Monte Carlo

In the Enhanced Monte Carlo method the first step is to estimate the so-called Average Conditional Exceedance Rate (ACER) functions of each of the time series available. To fix ideas, let $X_1, \ldots, X_{N_p}$ denote a time series of data allocated to the discrete times $t_1, \ldots, t_{N_p}$. Our goal now is to accurately determine the distribution function of the extreme value $M_{N_p} = \max\{X_j\,; j = 1, \ldots, N_p\}$. Specifically, we want to estimate $P(\eta) = \text{Prob}(M_{N_p} \leq \eta)$ accurately for large values of η.

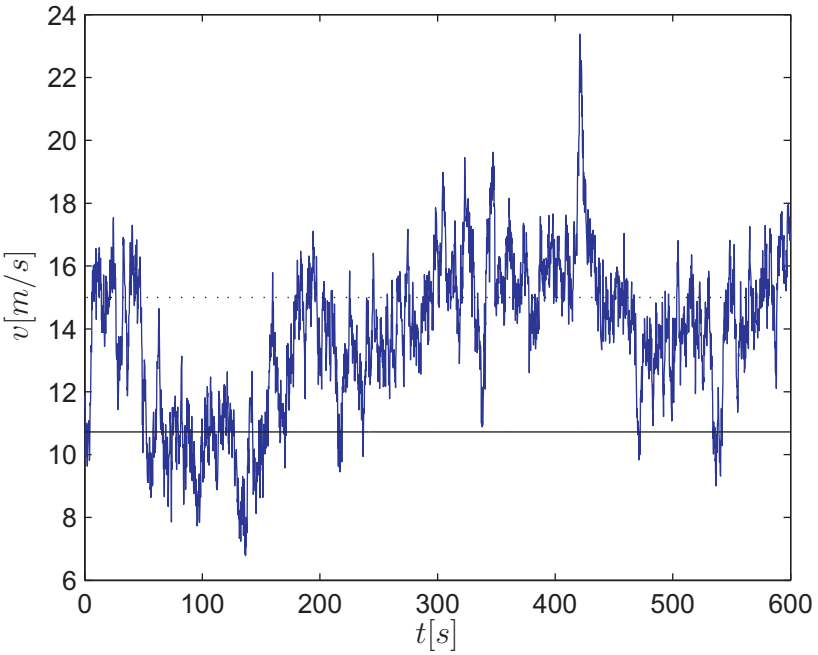

FIG. 6. Turbulent wind realization at the hub hight. ...: Mean wind speed; —: rated rotor speed

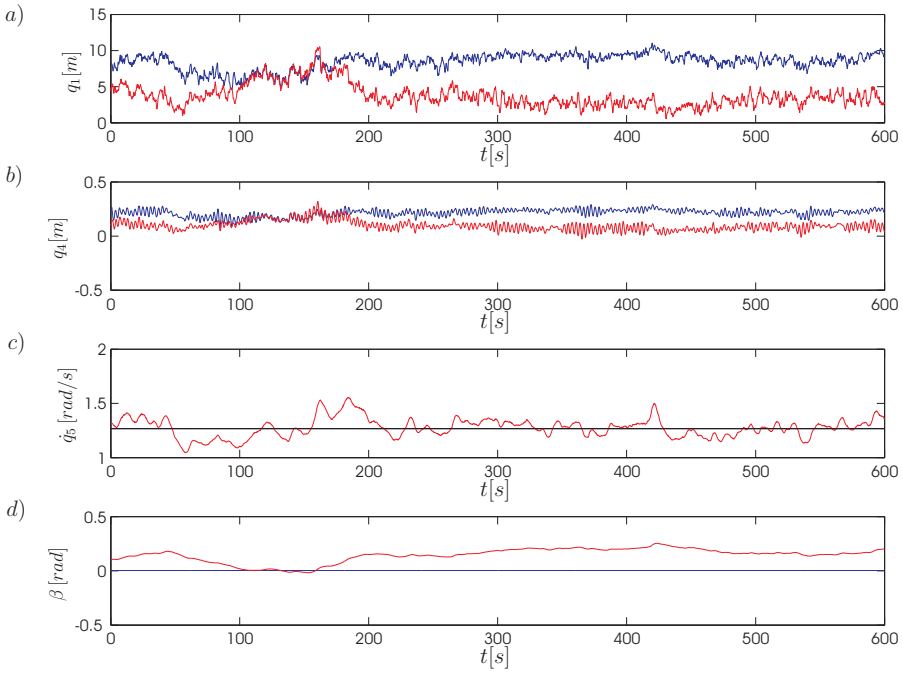

FIG. 7. Modal responses of the wind turbine to stochastic wind field. blue: fixed speed; red: variable speed

From the definition of M_{N_p}, it follows that,

$$P(\eta) = \text{Prob}(M_{N_p} \leq \eta) = \text{Prob}\{X_1 \leq \eta, \ldots, X_{N_p} \leq \eta\} \tag{25}$$

This equation is of no use in general for estimating $P(\eta)$ directly from the data. However, by introducing a cascade of conditioning approximations $P_k(\eta)$ of $P(\eta)$, where $P_k(\eta) \to P(\eta)$ as k increases, this problem can be solved in practice in a very efficient manner (Naess and Gaidai 2009; Naess et al. 2010). It can be shown that for $N_p >> 1$ and $k = 1, 2, \ldots$

$$P_k(\eta) \approx \exp\Big(- \sum_{j=k}^{N_p} \alpha_{kj}(\eta) \Big) , \tag{26}$$

where

$$\alpha_{kj}(\eta) = \text{Prob}\{X_j > \eta \,|\, X_{j-1} \leq \eta, \ldots, X_{j-k+1} \leq \eta\} \tag{27}$$

For the empirical estimation of the requisite quantities in the $P_k(\eta)$, it is expedient to introduce the concept of average conditional exceedance rates (ACER) as follows,

$$\varepsilon_k(\eta) = \frac{1}{N_p - k + 1} \sum_{j=k}^{N_p} \alpha_{kj}(\eta) \,, \; k = 1, 2, \ldots \tag{28}$$

The empirical estimation of the ACER function $\varepsilon_k(\eta)$ proceeds by counting the relative number of exceedances conditional on the requisite number of preceding non-exceedances, for the total data time series. This counting process is expressed by introducing the following random functions,

$$\begin{aligned} P_{kj}(\eta) &= \mathbf{1}\{X_j > \eta, X_{j-1} \leq \eta, \ldots, X_{j-k+1} \leq \eta\} \,, \\ Q_{kj}(\eta) &= \mathbf{1}\{X_{j-1} \leq \eta, \ldots, X_{j-k+1} \leq \eta\} \,, \\ & \qquad j = k, \ldots, N_p, \; k = 2, 3, \ldots \end{aligned} \tag{29}$$

where $\mathbf{1}\{\mathcal{A}\}$ denotes the indicator function of some event $\mathcal{A}$, that is, $\mathbf{1}\{\mathcal{A}\} = 1$ if $\mathcal{A}$ occurs, while $\mathbf{1}\{\mathcal{A}\} = 0$ otherwise. Then

$$\alpha_{kj}(\eta) = \frac{\text{E}[P_{kj}(\eta)]}{\text{E}[Q_{jk}(\eta)]} \,, \; j = k, \ldots, N_p, \; k = 2, \ldots \,, \tag{30}$$

where $\text{E}[\cdot]$ denotes the expectation operator. Assuming an ergodic process, then obviously $\varepsilon_k(\eta) = \alpha_{kk}(\eta) = \ldots = \alpha_{kN_p}(\eta)$, and it may be assumed that for the time series at hand

$$\varepsilon_k(\eta) = \lim_{N_p \to \infty} \frac{\sum_{j=k}^{N_p} p_{kj}(\eta)}{\sum_{j=k}^{N_p} q_{kj}(\eta)} \,, \tag{31}$$

where $p_{kj}(\eta)$ and $q_{kj}(\eta)$ are the realized values of $P_{kj}(\eta)$ and $Q_{kj}(\eta)$, respectively, for the observed time series.

The sample estimate of $\varepsilon_k(\eta)$ is,

$$\hat{\varepsilon}_k(\eta) = \frac{1}{R}\sum_{r=1}^{R} \hat{\varepsilon}_k^{(r)}(\eta)\,, \tag{32}$$

where R is the number of realizations (samples), and

$$\hat{\varepsilon}_k^{(r)}(\eta) = \frac{\sum_{j=k}^{N_p} p_{kj}^{(r)}(\eta)}{\sum_{j=k}^{N_p} q_{kj}^{(r)}(\eta)}\,, \tag{33}$$

where the index (r) refers to realization no. r. The empirical variance is calculated as,

$$\hat{s}_k(\eta)^2 = \frac{1}{R-1}\sum_{r=1}^{R} \Big(\hat{\varepsilon}_k^{(r)}(\eta) - \hat{\varepsilon}_k(\eta)\Big)^2\,. \tag{34}$$

The estimated mean value and standard deviation are then used to estimate the confidence intervals according to Eq. (35).

$$\tilde{CI}^{\pm}(\eta) = \hat{\varepsilon}_k(\eta) \pm 1.96\hat{s}_k(\eta)/\sqrt{R} \tag{35}$$

where the coefficient $1.96 = \Phi^{-1}\big((1+\mu_{CI})/2\big)$ where μ_{CI} denotes the confidence level e.g. 0.95 for 95% confidence intervals. Each of the empirical ACER functions is now used to achieve an optimal fit to a parametric function of the type,

$$\tilde{\varepsilon}_k(\eta) = q_k \exp\{-a_k(\eta - b_k)^{c_k}\} \tag{36}$$

for tail values of η, that is, for $\eta > \eta_0$, where η_0 denotes a suitably chosen tail marker. The class of parametric functions expressed by Eq. (36) reflects the basic underlying assumption that the correct asymptotic extreme value distribution is of the Gumbel type. This assumption is based on the observation that the statistical distributions that describe the response of the wind mills under study all belong to the domain of attraction of the Gumbel extreme value distribution. We believe that it is of some importance to have a method that captures the correct asymptotic behavior, otherwise the whole procedure runs the risk of being nothing but a curve fitting exercise without proper statistical justification.

Finding the values of the parameters (a_k, b_k, c_k, q_k) of the ACER function will be done by mean square optimization. This requires the specification of an initial guess as the starting point of the optimization process. As the starting point, a set of values for the parameter $d_k = \ln(q_k)$ is constructed. It is important to note that according to Eq. (36) $d_k > \ln\big(\tilde{\varepsilon}_k(\eta)\big)$ which must be satisfied in order to ensure convergence of the optimization algorithm.

There are several procedures that can be suggested for the optimization process. Here we shall describe one such approach. First, the set of d values is constructed as a vector of geometrically spaced values in the range of $[d_{min}, d_{max}]$ with the base β_d as $d_{n+1} = d_n + \beta_d(d_n - d_{n-1})$ which results in Eq. (37), where

N_d is the total number of grid points of d. The range of d values is defined as $d_{min} = \ln\left[\tilde{\varepsilon}_k(\eta_0/1.02)\right]$ and $d_{max} = 1.5 + \ln\left(\tilde{\varepsilon}_k(\eta_0)\right)$.

$$\begin{aligned} d_{n+1} &= d_1 + \frac{1-\beta_d^{n-1}}{1-\beta_d^{N_d-1}}\Delta_d\,, \quad n = 1, \ldots, N_d - 1 \\ \Delta_d &= d_{max} - d_{min} \end{aligned} \tag{37}$$

For each value of d, optimization is performed to find the other parameters related to it, that is, (a, b, c). The objective function of the optimization is defined as a weighted error of the fit. The weights are then defined as a function of the ACER functions and their confidence intervals as

$$w(\eta) = \left[\ln\left(\frac{\tilde{C}I^{+}(\eta)}{\tilde{C}I^{-}(\eta)}\right)\right]^{-p} \tag{38}$$

where p is a user defined power which controls the weight of the different points of the data for fitting i.e. 0.5 or 1. Finally the defined weights may be normalized to have their sum be equal to 1, but this does not affect the result of the optimization. In order to make an initial guess for the parameters (a, b, c) a further smoothing is then performed on the ACER functions by replacing the original data with the data extrapolated from a 3rd order polynomial fitted to the natural logarithm of the ACER functions e.g. $\tilde{\varepsilon}_k^{fit}(\eta)$ where $\tilde{\varepsilon}_k^{fit}(\eta) = \exp\left(d - \sum_{i=0}^{3} a_i \eta^i\right) \approx \tilde{\varepsilon}_k(\eta)$. Then the following procedure is used,

$$\left.\begin{aligned} Y_{init}(\eta) &= \ln\left(d - \sum_{i=0}^{3} a_i \eta^i\right) \\ b &= \frac{\eta_{min}\eta_{max} - \eta_{mid}^2}{\eta_{min} + \eta_{max} - 2\eta_{mid}} \\ c &= \frac{1}{2}\frac{Y_{init}(\eta_{max}) - Y_{init}(\eta_{min})}{\ln\left(\frac{\eta_{max}-\eta_{mid}}{\eta_{mid}-\eta_{min}}\right)} \\ a &= \frac{\exp\left(Y_{init}(\eta_{min})\right)}{(\eta_{min} - b)^c} \end{aligned}\right\} \tag{39}$$

where

$$\eta_{mid} = Y_{init}^{-1}\left[\frac{Y_{init}(\eta_{max}) + Y_{init}(\eta_{min})}{2}\right] \tag{40}$$

In case estimated parameters are such that $b \geq \eta_{min}$ or $c < 0$ the following initial

estimates are proposed

$$\left.\begin{aligned} b &= \eta_{min} - 0.05(\eta_{max} - \eta_{min}) \\ c &= 2 \\ a &= \frac{\exp\Big(Y_{init}(\eta_{min})\Big)}{(\eta_{mid} - b)^c} \end{aligned}\right\} \tag{41}$$

In the next step the objective function is defined as

$$\begin{aligned} \mathfrak{F}(b,a,c) &= \min_{\eta} ||\mathbf{F}||_2^2 \\ \mathbf{F} &= [f(\eta_{min},b,a,c) \ \cdots \ f(\eta_{max},b,a,c)] \end{aligned} \tag{42}$$

where $f(\eta_i,b,a,c) = w(\eta_i)\Big[-a(\eta_i-b)^c + d - \ln\big(\tilde{\varepsilon}_k(\eta_i)\big)\Big]$.

In the next step an optimization is carried out with respect to all four parameters (a,b,c,d) i.e. $\mathbf{F} = [f(\eta_{min},a,b,c,d) \ \cdots \ f(\eta_{max},a,b,c,d)]$. The initial values for the optimization are estimated in exactly the same way as before until Eq. (41). Then, optimization is performed with various initial conditions - start points - to see if it will converge to the same values. The final values of the parameters (d,b,a,c) is chosen from the optimization results e.g. $\mathbf{s} = [a,b,c,d]$ and its fit denoted as $\tilde{\varepsilon}_k^{\mathbf{s}}(\eta)$.

Once the solution is found, the extra data in the tail are cut under the condition which defined the modified ACER function $\varepsilon_k^{\mathbf{s}}(\eta)$ as $\varepsilon_k^{\mathbf{s}}(\eta) = \{\tilde{\varepsilon}_k^{\mathbf{s}}(\eta) \,|\, \tilde{\varepsilon}_k^{\mathbf{s}}(\eta) > 1.96\tilde{s}_k(\eta)/(\delta_{max}\sqrt{R})\}$. The confidence intervals are *re-anchored* to the $\varepsilon_k^{\mathbf{s}}(\eta)$. Re-anchoring consists of moving the mean value of the estimates for the ACER function from the estimated values $\tilde{\varepsilon}_k(\eta)$ to the fitted values $\tilde{\varepsilon}_k^{\mathbf{s}}(\eta)$ using Eq. (43). Re-anchoring makes it possible then to obtain smooth estimates of the confidence intervals from the information extracted from the data points.

$$\tilde{CI}^{\mathbf{s}\pm}(\eta) = \varepsilon_k^{\mathbf{s}}(\eta) \pm 1.96\tilde{s}_k(\eta)/\sqrt{R} \tag{43}$$

In order to obtain the estimation of the confidence intervals of the fit analytical expressions for the confidence intervals are obtained by perturbing values of the optimum solution $\mathbf{s}$. $CI^{\mathbf{s}\pm}(\eta)$ are then defined as the curves with the least weighted mean square error MSE, defined as

$$\text{MSE} = \sum_{\eta} w^{\mathbf{s}}(\eta)\Big(\ln\big(\varepsilon_k(\eta,\mathbf{s}^{pert}(i))\big) - \ln\big(\varepsilon_k^{\mathbf{s}}(\eta)\big)\Big)^2 \tag{44}$$

Where the weights are modified as

$$w^{\mathbf{s}}(\eta) = \left[\ln\left(\frac{\varepsilon_k^{\mathbf{s}}(\eta) + 1.96\tilde{s}_k(\eta)/\sqrt{R}}{\varepsilon_k^{\mathbf{s}}(\eta) - 1.96\tilde{s}_k(\eta)/\sqrt{R}}\right)\right]^{-p} \tag{45}$$

This can be done either with a deterministic or a stochastic updating way. In the deterministic approach a grid of ng points perturbed $\pm 5\%$ around the mean $\mathbf{s}$ is generated. All of the possible combination of these values should be checked to see if they lie in the specified interval specified by the *re-anchored* confidence intervals, $\tilde{CI}^{\mathbf{s}\pm}(\eta)$. Next the values which lead to curves with minimum MSE are chosen as the $CI^{\mathbf{s}\pm}(\eta)$. This clearly involves high computation effort e.g. for $ng = 10$ this process requires 10^4 function evaluations which might not be desired. Therefore the second approach based on the stochastic updating and the Gibbs sampler may be taken into account.

In the stochastic approach the parameters (d, b, a, c) for the confidence intervals are obtained based on Bayesian updating based on the Gibbs sampling. This needs a distribution of specified spread around the initial guess i.e. $\mathbf{s}$. This requires a good candidate distribution for generating parameters (d, b, a, c) which is clearly not available from theory. Nevertheless it is observed that using a uniform distribution with $0.1CL$ - where CL denotes the confidence level i.e. 0.05 for 95% confidence interval - spread around $\mathbf{s}$ will result in fast convergence of the algorithm.

Fixed speed wind turbine

The failure event is defined as the tower tip exceeds a certain barrier level, $q_4 > r$. This is a highly nonlinear problem due to the nonlinearities which exist within modeling the aerodynamic loads. Moreover even with a very coarse time integration increment as $\Delta t = 0.2s$, $600s$ assuming $200s$ of transient response , i.e. $t \in [0, 800]$, on 31 spatially coherent nodes involves 124001 number of stochastic variables in calculations. This means that the limit state is a hyper surface of dimensions 124001 which makes estimation of the low failure probability of this problem very difficult.

ACER functions from 20 time series realizations of the tower tip deflection are simulated shown in Fig. 8. Clearly ACER functions for five different "k" values, c.f. Fig. 9, are converging to each other as the barrier level increases. This inculcates that using the proposed method on any of the ACER functions extracted from the time series should not make difference if the tail marker from where the data points are selected is chosen high enough. In this study the $\tilde{\varepsilon}_2(k)$ is chosen as the ACER function to use the maximum data available from the simulation. Standard Monte Carlo (SMC) is also performed on the model using 240000 samples(epochs) and epochal peaks are extracted from it c.f. Fig. 8. As seen from the figure the extracted ACER functions show a shift which suggests that the response is not yet reached the stationary state. This may be surpassed by two approaches, either to continue simulation for a longer time or continue with the method using the epochal maximas. However the second approach takes more computational effort is still preferred since it guarantees that the extracted data points both for the SMC and the ACER method are from the same population. In this respect, 500 epochs are simulated and their maximas are extracted, the

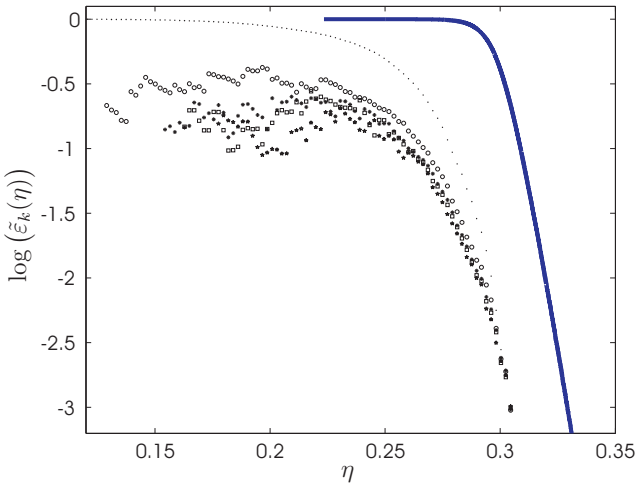

FIG. 8. ACER functions of the wind turbine; fixed speed. dots: ACER functions, Solid line: SMC

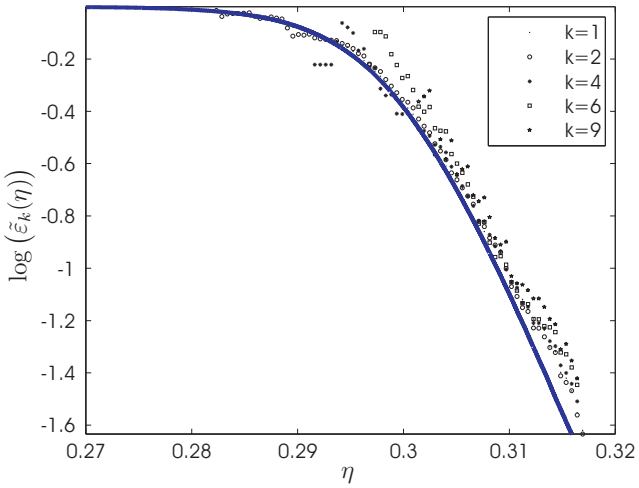

FIG. 9. ACER functions constructed based on the epochal maximas for the fixed speed wind turbine. dots: ACER functions, Solid line: SMC

ACER functions are then constructed based on these data and further analysis is performed on them c.f. Fig. 9 The figure shows that obviously these results belong to the same distribution family and analysis can be furthermore be followed based on them. Next the 95% confidence intervals of the data are estimated using (35) and are shown in Fig. 10. Fitting is then performed on the extracted ACER functions. It is observed that the tail marker location induce changes on the final predictions of the method and may result in non-trustable fits. Therefore the tail marker is chosen where the ACER functions for different values of k are already converged i.e. $\eta_0 \approx 0.29$. The estimated confidence intervals are then re-anchored

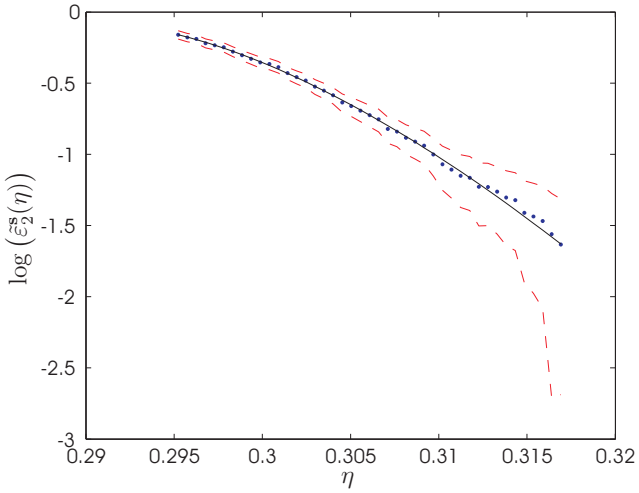

FIG. 10. Estimated ACER function and its 95% confidence intervals for the fixed speed wind turbine. ·: $\tilde{\varepsilon}_2(\eta)$, —: $\varepsilon_2^{\mathbf{s}}(\eta)$, − − −: $\tilde{CI}^{\pm}(\eta)$

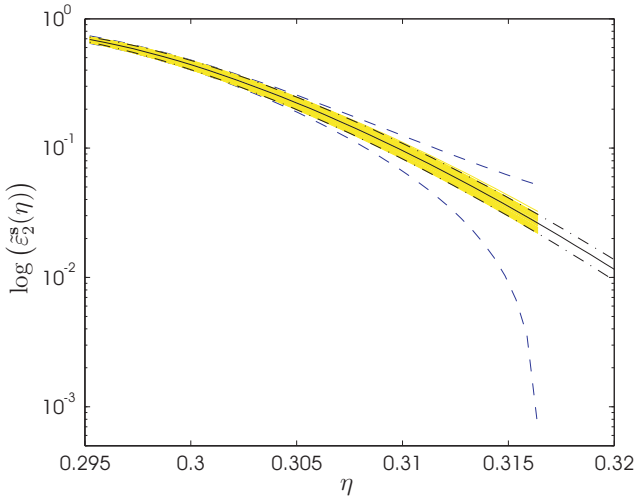

FIG. 11. Fitted ACER function and its 95% confidence intervals; fixed speed case. ——: $\varepsilon_2^{\mathbf{s}}(\eta)$, − − −: $\tilde{CI}^{\mathbf{s}\pm}(\eta)$, − · − · −: $CI^{\mathbf{s}\pm}(\eta)$

to the fitted curve shown in Fig. 11. The final fit together with its 95% confidence intervals together with the SMC results are shown in Fig. 12. The figure shows good agreement between the predictions and the SMC however at some points small errors can be seen which are not considerable. The method seems to be capable of capturing the general trend of the extreme values of the time series and worth being applied on the more complicated case, e.g. the pitch controlled variable speed wind turbine, which is presented in the next section.

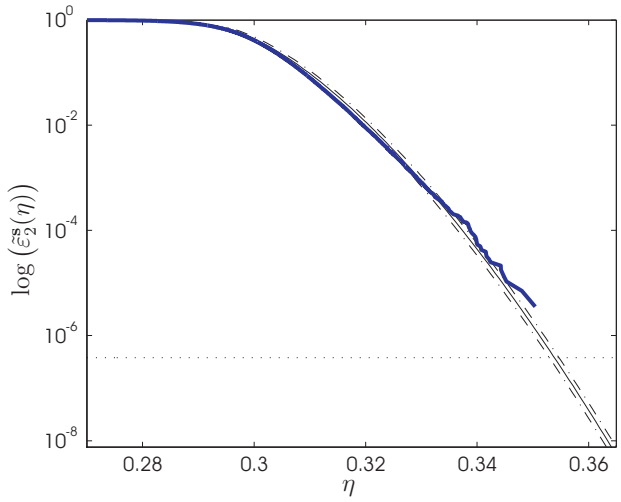

FIG. 12. Fitted ACER function and its 95% confidence intervals; fixed speed case. ——: $\varepsilon_2^{\mathbf{s}}(\eta)$, $- \cdot - \cdot -$: $CI^{\mathbf{s}\pm}(\eta)$, $\cdots$: 50 years return period

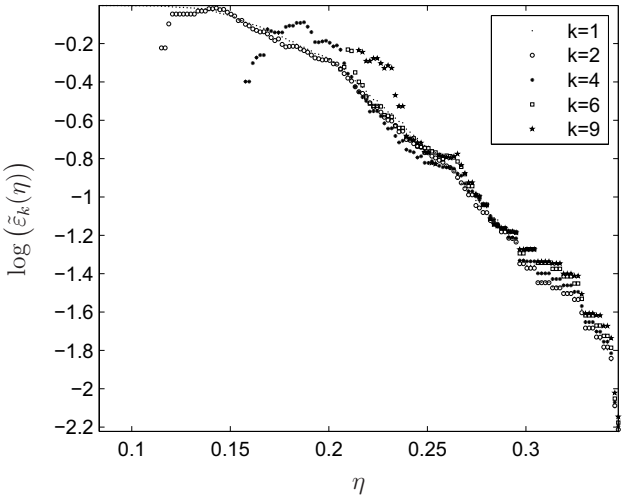

FIG. 13. ACER functions of the wind turbine; variable speed. dots: ACER functions, Solid line: SMC

Variable speed wind turbine

The second case simulates a variable speed wind turbine where the described PID controller is keeping the rotor speed in the vicinity of the nominal speed. This case is even more difficult to solve than the previous case since the controller introduces significant additional nonlinearity in the model. The failure probability of this case has been evaluated with the same method as the previous case. ACER functions are directly extracted from 500 epochal maxiams shown in Fig. 13. Estimated ACER functions together with the fitted function and the

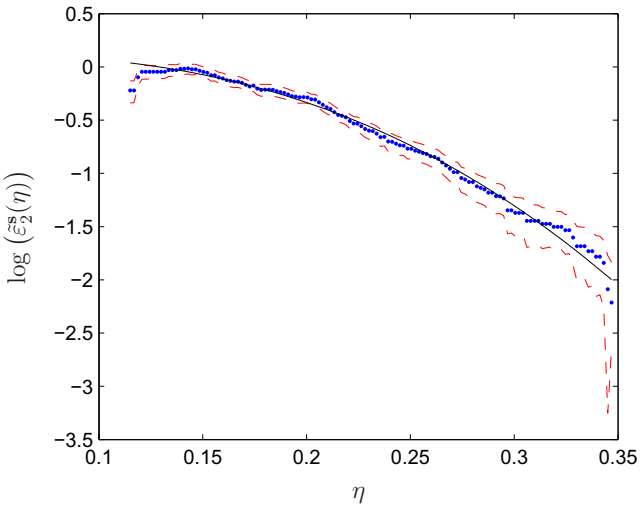

FIG. 14. Estimated ACER function and its 95% confidence intervals for the variable speed wind turbine. ·: $\tilde{\varepsilon}_2(\eta)$, —: $\varepsilon_2^{\mathrm{s}}(\eta)$, − − −: $\tilde{CI}^{\pm}(\eta)$

95% confidence intervals for this case are shown in Fig. 14. The figure shows that the fit matches very well within the range of the extracted data. Estimated confidence intervals of the fit are shown in Fig. 14

Confidence intervals of the fitted curve are estimated by after re-anchoring the estimated confidence intervals to the fit c.f. Fig. 15. The final fit versus SMC results together performed on 240000 samples are shown in Fig. 16. The figure shows that also in the case of the variable speed wind turbine where a controller acts on the turbine - by controlling the pitch of the blades - the EMC still performs quite good.

Conclusions

A simplified model of a 5MW wind turbine is developed and its failure probability is estimated by use of the EMC method. In order to evaluate the effect of controller on the structure a PID pitch controller is implemented in the model which is responsible to keep the rotor speed around its nominal value. The pitch controller decreases the load level in normal operational conditions nevertheless it may cause increase in the vibration level in extreme conditions as shown in the paper. This study shows that presence of a controller in a system effectively changes system behavior in extreme situations. However the conclusions made on the controller in this model can not be generalized to all models. This is since the type and tuning parameters of the controller also play an important role in the final behavior of the system. The EMC method proposed seems to be a good candidate for prediction of the extreme value distribution of both the fixed and variable speed wind turbine models; provided that sufficient number of simula-

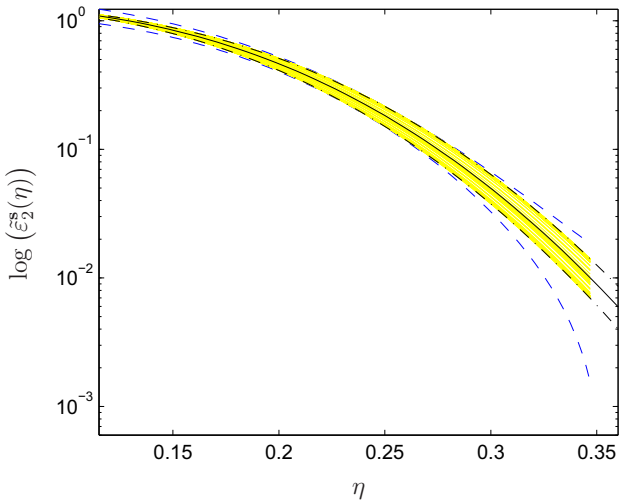

FIG. 15. Fitted ACER function and its 95% confidence intervals; variable speed case. ——: $\varepsilon_2^{\mathbf{s}}(\eta)$, − − −: $\tilde{CI}^{\mathbf{s}\pm}(\eta)$, − · − · −: $CI^{\mathbf{s}\pm}(\eta)$

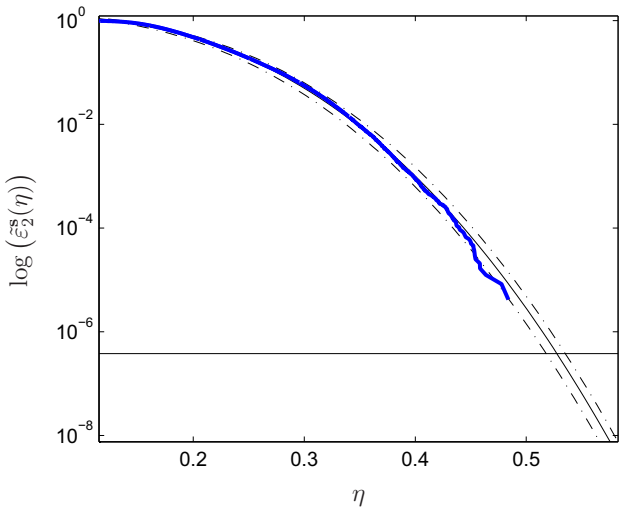

FIG. 16. Fitted ACER function and its 95% confidence intervals; variable speed case. ——: $\varepsilon_2^{\mathbf{s}}(\eta)$, − · − · −: $CI^{\mathbf{s}\pm}(\eta)$, · · ·: 50 years return period

tions are available. It is noted that for reliable results with the EMC method more simulations are required to be carried out compared to the problems with stationary responses, i.e. 500 instead of 20 for a stationary process. For low number of simulations highly uncertain results or difficulties with convergence of the optimization algorithm may be encountered. However, considering the difficulties stemming from the nonlinearities and high dimensions of the problem the method appears to be a good candidate compared to the SMC simulation.

Acknowledgements

The Danish Energy Authority is acknowledged for support under the grant EFP07-II, Estimation of Extreme Responses and Failure Probability of Wind Turbines under Normal Operation by Controlled Monte Carlo Simulation.

The financial support from the Research Council of Norway (NFR) through the Centre for Ships and Ocean Structures (CeSOS) at the Norwegian University of Science and Technology is also gratefully acknowledged.

REFERENCES

Cook, N. J. and Harris, R. I. (2004). "Exact and general FT1 penultimate distributions of extreme wind speeds drawn from tail-equivalent Weibull parents." *Structural Safety*, 26(4), 391 – 420.

Freudenreich, K. and Argyriadis, K. (2007). "The load level of modern wind turbines according to IEC 61400-1." *Journal of Physics: Conference Series*, 75(012075).

Hansen, M. (2007). *Aerodynamics of wind turbines*. Earthscan; 2nd edition.

Harris, I. (2005). "Generalised Pareto methods for wind extremes. Useful tool or mathematical mirage?." *Journal of Wind Engineering and Industrial Aerodynamics*, 93(5), 341 – 360.

Harris, R. I. (2004). "Extreme value analysis of epoch maxima–convergence, and choice of asymptote." *Journal of Wind Engineering and Industrial Aerodynamics*, 92(11), 897 – 918.

IEC (2005a). *Amendment to the IEC 61400-1:2005 standard*. International Electrotechnical Commission.

IEC (2005b). *IEC 61400-1 (2005) International Standard, Wind turbines - Part 1: Design requirements*. International Electrotechnical Commission, third edition.

Jonkman, J., Butterfield, S., Musial, W., and Scott, G. (2009). "Definition of a 5-MW reference wind turbine for offshore system development." *Report No. NREL/TP-500-38060*, National Renewable Energy Laboratory.

Katafygiotis, L. and Zuev, K. (2008). "Geometric insight into the challenges of solving high-dimensional reliability problems." *Probabilistic Engineering Mechanics*, 23(2-3), 208 – 218. 5th International Conference on Computational Stochastic Mechanics.

Kooijman, H., Lindenburg, C., Winkelaar, D., and van der Hooft, E. (2003). "Aero-elastic modelling of the dowec 6 MW pre-design in PHATAS." *Report No. DOWEC 10046_009, ECN-CX–01-135*, Energy research center of the Netherlands.

Macke, M. and Bucher, C. (2003). "Importance sampling for randomly excited dynamical systems." *Journal of Sound and Vibration*, 268(2), 269 – 290.

Meirovitch, L. (2001). *Fundamentals of Vibrations*. McGraw-Hill.

Naess, A. and Gaidai, O. (2008a). "A Monte Carlo approach to prediction of

extreme response statistics of drag dominated offshore structures." *J. Offshore Mech. Arct. Eng.*, 130(4), 041601 (6 pages).

Naess, A. and Gaidai, O. (2008b). "Monte Carlo methods for estimating the extreme response of dynamical systems." *Engineering Mechanics ASCE*, 134(8), 628–636.

Naess, A. and Gaidai, O. (2009). "Estimation of extreme values from sampled time series." *Structural Safety*, 31(4), 325 – 334.

Naess, A., Gaidai, O., and Batsevych, O. (2010). "Prediction of extreme response statistics of narrow-band random vibrations." *Engineering Mechanics ASCE*, 136(3), 290–298.

Naess, A., Leira, B., and Batsevych, O. (2009). "System reliability analysis by enhanced Monte Carlo simulation." *Structural Safety*, 31(5), 349 – 355.

Ogata, K. (2009). *Modern Control Engineering*. Prentice Hall; 5 edition, 5 edition.

Pradlwarter, H. and Schuëller, G. (2010). "Local domain Monte Carlo simulation." *Structural Safety*, 32(5), 275 – 280. Probabilistic Methods for Modeling, Simulation and Optimization of Engineering Structures under Uncertainty in honor of Jim Beck's 60th Birthday.

Pradlwarter, H., Schuëller, G., Koutsourelakis, P., and Charmpis, D. (2007). "Application of line sampling simulation method to reliability benchmark problems." *Structural Safety*, 29(3), 208 – 221. A Benchmark Study on Reliability in High Dimensions.

Schuëller, G. (2008). *Computational stochastic dynamics - some lessons learned*, chapter 1, 3–20. Computational Structural Dynamics and Earthquake Engineering Vol.2, Structures & Infrastructures Series. Taylor & Francis.

Sichani, M., Pedersen, B., and Nielsen, S. (2010). "Stochastic subspace modelling of turbulence." *World Academy of Science, Engineering and Technology*, 58, 1140–1148.

Sichani, M. T., Nielsen, S. R. K., and Bucher, C. (2011). "Efficient estimation of first passage probability of high dimensional non-linear systems." *Probabilistic Engineering Mechanics*, In Press, Accepted Manuscript, –.

Simiu, E., Heckert, N. A., Filliben, J. J., and Johnson, S. K. (2001). "Extreme wind load estimates based on the Gumbel distribution of dynamic pressures: an assessment." *Structural Safety*, 23(3), 221 – 229.

Valdebenito, M., Pradlwarter, H., and Schuëller, G. (2010). "The role of the design point for calculating failure probabilities in view of dimensionality and structural nonlinearities." *Structural Safety*, 32(2), 101 – 111.

Xue, D., Chen, Y., and Atherton, D. (2008). *Linear Feedback Control: Analysis and Design with MATLAB*. Society for Industrial and Applied Mathematics (SIAM).

APPENDIX H
Stochastic and chaotic sub- and superharmonic response of shallow cables due to chord elongations

The paper presented in this appendix is published in *Probabilistic Engineering Mechanics*, Volume 26, Issue 1, January 2011, Pages 44-53.

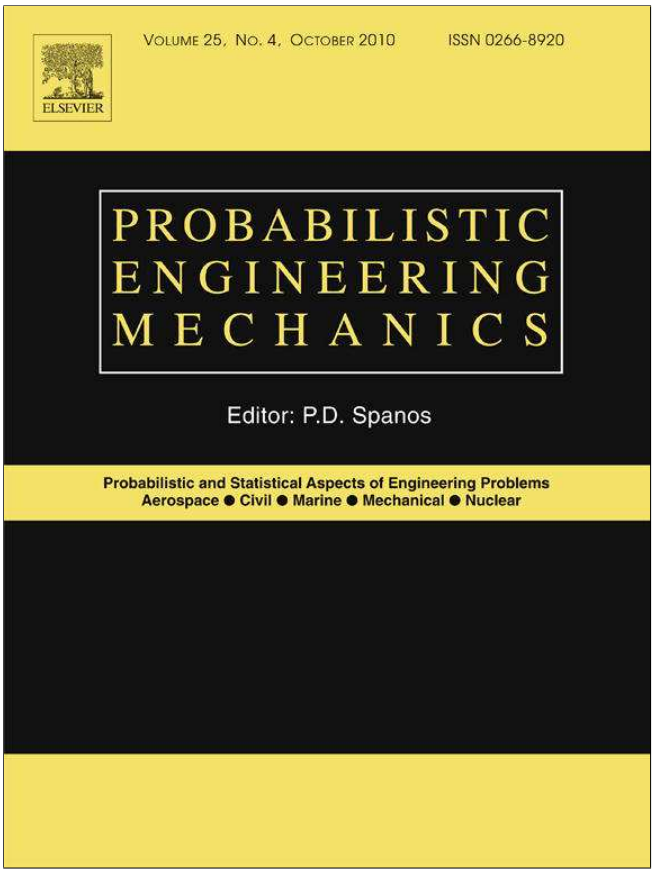

Probabilistic engineering mechanics

Order detail ID:	56237722	**Permission Status:**	**Granted**
Article Title:	Stochastic and chaotic sub- and superharmonic response of shallow cables due to chord elon gations	**Permission type:**	Republish or display content
		Type of use:	reuse in a thesis/dissertation
		Order License Id:	2742931263704
Author(s):	Nielsen, S.R.K.		
DOI:	10.1016/J.PROBENGMECH.2010.06.00	View details	
ISSN:	0266-8920		
Publication Type:	Journal		
Volume:	26		
Issue:	1		
Start page:	44		
Publisher:	ELSEVIER LTD.		

http://www.elsevier.com/copyright

Probabilistic Engineering Mechanics 26 (2011) 44–53

Contents lists available at ScienceDirect

Probabilistic Engineering Mechanics

journal homepage: www.elsevier.com/locate/probengmech

Stochastic and chaotic sub- and superharmonic response of shallow cables due to chord elongations☆

S.R.K. Nielsen, M.T. Sichani*

Department of Civil Engineering, Aalborg University, 9000 Aalborg, Denmark

ARTICLE INFO

Article history:
Received 31 December 2009
Received in revised form
28 April 2010
Accepted 21 June 2010
Available online 30 June 2010

Keywords:
Shallow cable
Stochastic chord length excitation
Chaotic vibrations
Subharmonic response
Superharmonic response
Monte Carlo simulation

ABSTRACT

The paper deals with the non-linear response of shallow cables driven by stochastically varying chord elongations caused by random vibrations of the supported structure. The chord elongation introduces parametric excitation in the linear stiffness terms of the modal coordinate equations, which are responsible for significant internal subharmonic and superharmonic resonances. Under harmonically varying support motions coupled ordered or chaotic in-plane and out-of-plane subharmonic and superharmonic periodic motions may take place. If the harmonically varying chord elongation is replaced by a zero-mean, stationary narrow-band random excitation with the same standard deviation and center frequency, qualitatively and quantitatively completely different modes of vibration are registered no matter how small the bandwidth of the excitation process is. Additionally, the stochastic excitation process tends to enhance chaotic behavior. Based on Monte Carlo simulation on a reduced non-linear two-degree-of freedom system the indicated effects have been investigated for stochastic subharmonic resonance of order 2:1, and stochastic superharmonic resonances of orders 1:2 and 2:3. By analyzing the responses for two chord elongation processes with almost identical auto-spectral density function, but completely different amplitudes, it is shown that the indicated qualitative and quantitative changes of the subharmonic resonance primarily are caused by the slowly varying phase of the stochastic excitation. The superharmonic stochastic responses are dominated by random jumps between a single mode in-plane and a coupled mode attractor, which are caused by the variation of the amplitude of the random excitation. Such jumps do not occur in the subharmonic response, because the single mode in-plane attractor is unstable.

© 2010 Elsevier Ltd. All rights reserved.

1. Introduction

Cables used as structural support elements of masts, towers and cable-stayed bridges are characterized by a sag-to-chord-length ratio below 0.01, which means that the natural frequencies for eigenvibrations in the plane of the equilibrium suspension and in the orthogonal direction, subsequently referred to as the in-plane and out-of-plane modes, are pairwise close. The slenderness and low inherent damping of the cables make them prone to vibrations, either induced as external loads on the cable from the wind or a combination of wind and rain, or via motions of the support points, [1,2]. Especially, the chord elongation caused by the difference between the components of the support point motions along the cable chord is of importance for the cable dynamics. The components of the support point motions in the orthogonal direction of the chord line of the static equilibrium suspension merely induce an external excitation of the modal equations of motion. In addition, the chord elongation also appears as a parametric excitation of the linear stiffness terms in the modal equations of motion. These parametric excitations are the primary cause for the internal resonances considered in this study.

Critical situations arise when the chord elongation is harmonically varying with an angular frequency ω_0 close to rational values of the frequency ratio ω_0/ω_1, where ω_1 is the fundamental out-of-plane angular eigenfrequency. Especially, coupled resonant vibrations of the in-plane and the out-of-plane modes may take place. For $\omega_0/\omega_1 \simeq 1$, harmonic resonance takes place driven by the additive load term of the in-plane mode. The out-of-plane mode is caused by internal resonance via the geometrical non-linear stiffness terms, and has a phase lead close to $\pi/2$ to the in-plane harmonic component, leading to a whirling motion around the chord line with an elliptical trajectory of the midpoint, [3]. Subharmonic and superharmonic resonances, synonymously known as internal resonances, imply that the resonant vibrations in the fundamental modes take place for rational frequency ratios ω_0/ω_1 significant larger and smaller than one, respectively. Especially important are the subharmonic resonance of order 2:1 and the superharmonic

☆ Dedicated to professor K. Sobczyk in honor of his seventieth birthday.

* Corresponding author. Tel.: +45 9940 8570; fax: +45 9814 8243.
E-mail addresses: soren.nielsen@civil.aau.dk (S.R.K. Nielsen), mts@civil.aau.dk (M.T. Sichani).

0266-8920/$ – see front matter © 2010 Elsevier Ltd. All rights reserved.
doi:10.1016/j.probengmech.2010.06.006

resonances of orders 1:2 and 2:3, corresponding to $\omega_0/\omega_1 \simeq 2$, $\omega_0/\omega_1 \simeq \frac{1}{2}$ and $\omega_0/\omega_1 \simeq \frac{2}{3}$. No stable subharmonic resonance of order 3:2 exists at realistic chord elongation amplitudes. The subharmonic resonance of order 2:1 and the superharmonic resonance of order 2:3 are caused by a combination of internal resonance due to the parametric excitation of the linear stiffness terms and the external excitation of the in-plane mode, [4,5]. The superharmonic resonance of order 1:2 is entirely caused by the parametric excitation of both modes, [4]. Due to the geometrical nonlinearities, the response may become chaotic under harmonic or internal resonances for sufficiently large amplitude of the chord elongation. The resonant response is enhanced at low structural damping of the cable, for which reason the chaotic behavior is more pronounced in this case than at higher damping.

In reality, the chord elongation is narrow-band stochastically varying, driven by the narrow-band random response of the supported structure. The bandwidth and the angular center-frequency of the auto-spectral density function of the chord elongation process may often be identified as the modal damping ratio and the angular eigenfrequency of one of the eigenmodes of the supported structure. It turns out that the subharmonic resonant response under stochastically varying chord elongation, qualitatively and quantitatively, is completely different from what is observed under a comparative harmonic excitation, even for extremely small bandwidths of the excitation. The superharmonic stochastic resonances are dominated by random jumps between a single mode in-plane attractor and a coupled mode attractor.

Chaotic behavior under stochastic excitation is defined as extreme sensitivity of the response on the initial conditions in a way that the response of two realizations of cable motion with close initial values, generated by the same arbitrary realization of the chord elongation process, deviate exponentially with time. The exponential growth rate is measured by the maximum Lyapunov exponent, which in this paper will be estimated by ergodic sampling by the algorithm of Wolf et al. [6]. A positive or negative Lyapunov exponent indicates chaotic or ordered behavior, respectively. It turns out that the tendency of chaotic behavior increases with increasing values of the bandwidth up to a certain value.

A narrow-band stochastic chord elongation differs from the comparative harmonic excitation in having a slowly varying amplitude and phase with time. It is the aim of the present study to investigate to what extent the indicated changes of the stochastic response are caused by the variation of the amplitude or by the phase. The solution approach is based on Monte Carlo simulation using two stochastic chord elongation models with almost identical auto-covariance functions. One is obtained by a linear filtration of Gaussian white noise through a narrow-band linear 2nd order filter, leading to realizations with slowly varying amplitudes and phases. The other model is based on a cosine transformation of a Wiener process, leading to realizations with the same constant amplitudes as the reference harmonic excitation, so the randomness is completely caused by a varying phase, see Wedig [7].

Deterministic superharmonic resonances of orders 2:3 and 1:n, $n = 2, 3, \ldots$ of a shallow cable were analyzed by Nielsen and Kirkegaard [4] based on analytical solutions to a reduced two-degree-of-freedom model. The effect of harmonic forced support motions has also been considered by Perkins, [8], who obtained analytical solutions for coupled in-plane and out-of-plane responses. The emphasis was on cables with relative large sag-to-chord length ratios to analyze 2:1 internal resonances close to the cross-over frequency of the fundamental in-plane eigenfrequency. Tien et al. [9] considered the analog subharmonic resonance of order 2:1 of a shallow arch under periodic excitation, based on an averaging procedure. Pinto de Costa et al. [10] studied

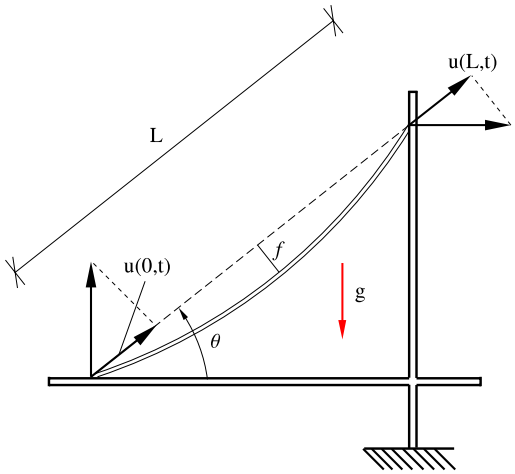

Fig. 1. Schematic view of a stay cable in a cable stayed bridge.

oscillations in the static equilibrium plane of bridge stay cables subjected to periodic motions of the bridge and/or towers using a Galerkin method. El-Attar et al. [11] evaluated the nonlinear cable response to multiple periodic support excitations with different phases using a 2DOF model. Rega and co-workers [3] performed a theoretical and experimental in-depth investigation on nonlinear multi-modal interactions and chaotic motion of the cable using a multi-mode model. An analysis of the harmonic resonance of the 2DOF model for a shallow cable exposed to a stochastically varying chord elongation was performed by Larsen and Nielsen [5]. It was shown that the whirling mode becomes unstable under stochastic chord elongation excitation. Instead, the cable jumps randomly between a coupled mode and a single in-plane mode attractor depending on the magnitude of the chord elongation process. A theory for determining the probability of occupying either of these modes of vibration was derived based on a continuous time two-state Markov chain model. The corresponding stochastic resonance of order 2:1 was investigated by Zhou et al. [12] based on analytical solutions for the deterministic ordered response, and the subharmonic stochastic response was analyzed by Monte Carlo simulations. It was found that the stochastic variations of the chord elongation enhanced the tendency to chaotic response relative to the comparable harmonic excitation, and that the coupled mode of vibration only exists for bandwidths below a certain critical value.

2. Theory

2.1. Mechanical model

Fig. 1 shows a stay cable in a cable stayed bridge, making the angle θ with the bridge deck. $u(0, t)$ and $u(L, t)$ denote the components of the support point motions at the bridge and the tower along the chord of the cable, where L denotes the chord length. Fig. 2 defines the parameters of the mechanical model of the cable. f is the sag at the midpoint, caused by the component $g\cos\theta$ of the acceleration of gravity in the orthogonal direction to the chord. The linear springs with the spring constants k_1 and k_2 model the flexibility of the bridge deck and the tower, respectively. The plane equilibrium state is maintained by a prestress force H along the chord line, which is assumed to be sufficiently large that a symmetric parabolic approximation may be used for the equilibrium suspension. Obviously, all components of the support point motions at the upper and lower support point along the axes of the indicated (x, y, z)-coordinate system induce dynamic displacement components $u(x, t)$, $v(x, t)$, $w(x, t)$

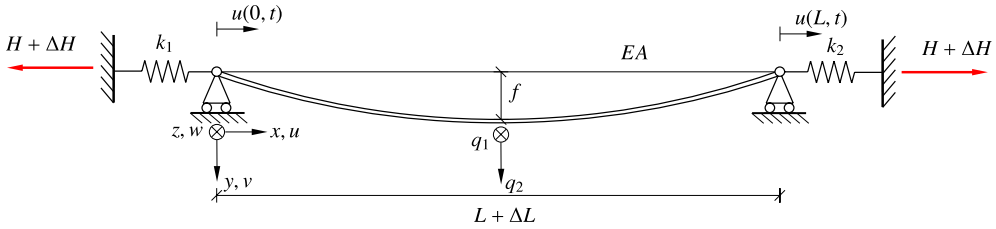

Fig. 2. Parameters in the mechanical model.

of a referential point of the cable. The components of the support point motions in the transverse direction of the chord merely induce an external (additive) load term of the modal equations of motion. These modal loads are important at harmonic resonance, where the excitation frequency is close to the fundamental angular eigenfrequencies. In the present investigation the focus is on sub—and superharmonic resonance, which is caused by harmonic excitations with frequencies significantly different from the fundamental eigenfrequencies. In this case the resonant response is caused by the chord elongation $\Delta L(t) = u(L,t) - u(0,t)$, which induces internal resonance via a parametric (multiplicative) excitation of the modal equations of motion. The remaining components of the support point motions have small influence on the qualitative and quantitative behavior of the cable response, and will be ignored in the following analysis. Conveniently, the chord elongation may be described by the following non-dimensional parameter

$$e(t) = \frac{EA}{H}\frac{\Delta L(t)}{L} \tag{1}$$

where E is the elasticity modulus and A is the cross-sectional area. Based on the parabolic equilibrium suspension the chord elongation $\Delta L(t)$ during quasi-static deformations can be written as [13]

$$\frac{\Delta L(t)}{L} = \left(\frac{16}{3}\frac{f^2}{L^2} + \frac{H}{EA}\right)\frac{\Delta H(t)}{H} = \frac{H}{EA}\left(\frac{1}{12}\lambda^2 + 1\right)\frac{\Delta H(t)}{H}. \tag{2}$$

$\Delta H(t)$ denotes the change of the chord force caused by the chord elongation $\Delta L(t)$, and λ^2 is the Irvine stiffness parameter [13]. The first term within the brackets represents the contribution from an inextensible deformation of the equilibrium suspension, whereas the second term specifies the contribution from the elastic deformation. It follows that the contribution from the deformation of the equilibrium suspension can be ignored in comparison to the elastic deformation if the Irvine parameter is significantly small, say $\lambda^2 < 0.5$. The upper bound for this inequality will be used to define shallowness quantitatively, and hence indicates the upper limit for application of the following theory. As a consequence, $e(t)$ defined in (1) becomes approximately equal to the fraction $H(t)/H$. Then, since negative chord forces are not allowed, $|e(t)|$ should be well below 1. Even though the excitation only affects the in-plane motion, stable out-of-plane displacements may be generated by non-linear couplings in both harmonic, subharmonic and superharmonic resonances in the fundamental modes. The in-plane and out-of-plane displacement components $v(x,t)$ and $w(x,t)$ are dominated by the fundamental eigenmodes. Then, the following single mode expansions of the in-plane and out-of-plane displacements turn out to be appropriate

$$v(x,t) \simeq \Phi_2(x)q_2(t), \qquad w(x,t) \simeq \Phi_1(x)q_1(t). \tag{3}$$

The eigenmodes $\Phi_1(x)$ and $\Phi_2(x)$ are normalized to 1 at the midpoint, so that the corresponding modal coordinates $q_1(t)$ and $q_2(t)$ are approximations to the actual displacements at this position. The related out-of-plane circular eigenfrequency ω_1 is slightly smaller than the in-plane eigenfrequency ω_2 due to the straining of the cable under symmetric in-plane eigenvibrations. These quantities have been specified in the Appendix. Retaining up to cubic non-linear terms in the equations of motion, the following highly reduced 2 degrees-of-freedom system may be formulated, Larsen and Nielsen [5]

$$\left.\begin{aligned} &\ddot{q}_1 + 2\zeta_1\omega_1\dot{q}_1 + \omega_1^2\left(1 + e(t)\right)q_1 \\ &\quad + \beta_1 q_1 q_2 + q_1\left(\gamma_1 q_1^2 + \gamma_2 q_2^2\right) = 0 \\ &\ddot{q}_2 + 2\zeta_2\omega_2\dot{q}_2 + \omega_2^2\left(1 + \alpha e(t)\right)q_2 + \beta_2 q_1^2 + \beta_3 q_2^2 \\ &\quad + q_2\left(\gamma_3 q_1^2 + \gamma_4 q_2^2\right) = -\eta e(t) \end{aligned}\right\} \tag{4}$$

ζ_1 and ζ_2 are the modal damping ratios, and α, β_1, β_2, β_3, γ_1, γ_2, γ_3, γ_4, η are parameters depending on the eigenmodes $\Phi_1(x)$ and $\Phi_2(x)$, which have been given in the Appendix along with the angular eigenfrequencies. As seen, the non-dimensional chord elongation $e(t)$ is exposing the system both to external and parametric excitation.

Based on simulations with a full non-linear finite difference model, it was demonstrated by Zhou et al. [12] that the indicated two degree-of-freedom model was adequate in predicting to a high degree of accuracy the qualitative, and even quantitative, dynamic responses and chaotic behavior of the cable as seen from the midpoint trajectories under stochastic excitation, as shown in Fig. 3, and from the Poincare-maps of the in-plane modal coordinate shown in Fig. 4. This accuracy is obtained because the anti-symmetric modes are not excited by the chord elongation, and because higher order symmetric modes are merely quasi-statically excited. Further, the influence of non-linearities of higher than cubic order is ignorable.

2.2. Chord elongation models

2.2.1. Harmonically varying chord elongations

The referential harmonically varying chord elongation is given as

$$e(t) = e_0\cos(\omega_0 t + w_0) \tag{5}$$

where ω_0 denotes the circular frequency, e_0 is the non-dimensional chord elongation amplitude defined by (1), and w_0 is a constant deterministic phase.

2.2.2. Stochastic chord elongations obtained by filtered white noise

One model for the stochastic chord elongation obtained by the filtration of a unit intensity white noise through a second order filter is given as

$$\ddot{e} + 2\mu\dot{e}\omega_0 + \omega_0^2 e = \sqrt{2\mu\omega_0^3}e_0 w(t) \tag{6}$$

where μ is the bandwidth (damping ratio) of the filter, and $w(\tau)$ is a zero mean unit intensity Gaussian white noise with the auto-covariance function

$$\kappa_{ww}(\tau) = E\left[w(t)w(t+\tau)\right] = \delta(\tau). \tag{7}$$

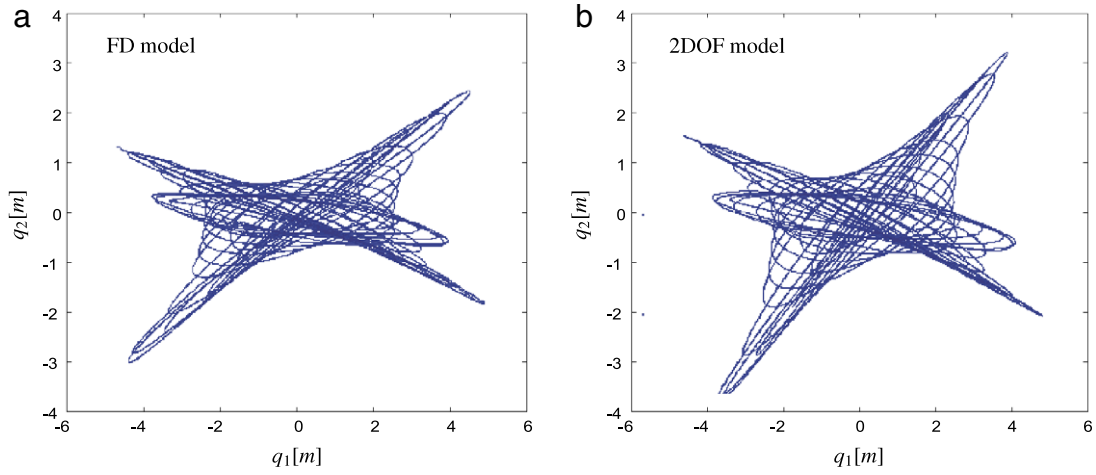

Fig. 3. Subharmonic stochastic resonance of order 2:1, filtered white noise, $e_0 = 0.3$, $\zeta_1 = \zeta_2 = 0.01$. (a) Non-linear finite difference model. (b) 2DOF model, [12].

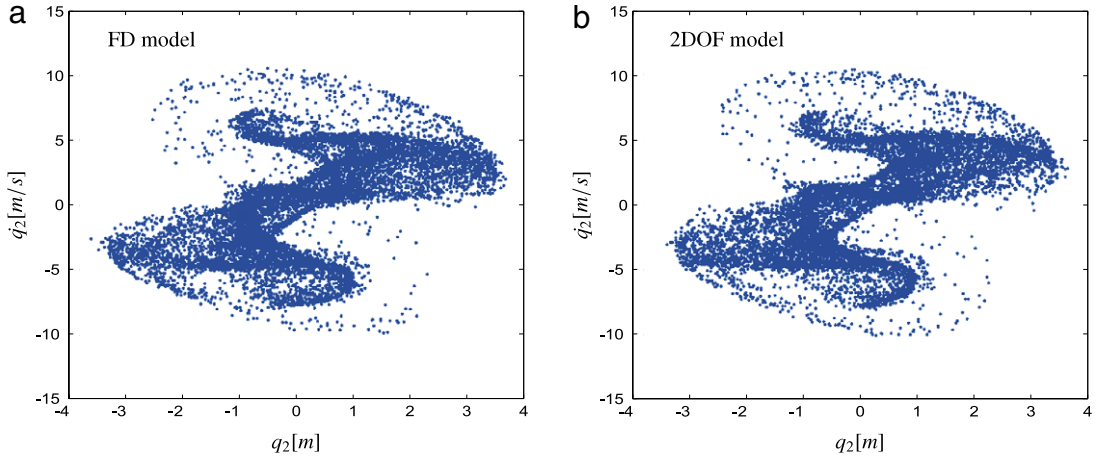

Fig. 4. Chaotic subharmonic resonance of order 2:1, harmonically varying chord elongation. Poincare-map of in-plane modal displacement and velocity, $\zeta_1 = \zeta_2 = 0.01$, $e_0 = 0.3\ \omega_0 = 2\omega_1$. (a) Nonlinear finite difference model. (b) 2DOF model, [12].

The auto-covariance function and the one-sided auto-spectral density function of the output process become:

$$\left.\begin{aligned}\kappa_{ee}(\tau) &= \frac{1}{2}e_0^2\,\mathrm{e}^{-\mu\omega_0|\tau|}\left(\cos(\omega_d\tau)+\frac{\mu}{\sqrt{1-\mu^2}}\sin(\omega_d|\tau|)\right)\\ \frac{\omega_0 S_e(\omega)}{e_0^2} &= \frac{2}{\pi}\,\frac{\mu}{\left(1-\frac{\omega^2}{\omega_0^2}\right)^2+4\mu^2\frac{\omega^2}{\omega_0^2}}\end{aligned}\right\} \quad (8)$$

$$\omega_d = \omega_0\sqrt{1-\mu^2}. \quad (9)$$

ω_d denotes the damped angular eigenfrequency of the filter.

2.2.3. Stochastic chord elongations by variable phase model

Alternatively, the chord elongation may be modelled as a cosine transformation of a Wiener process (Wedig [7])

$$e(t) = e_0\cos(\omega_0 t + W(t)) \quad (10)$$

$$W(t) = \sqrt{2\mu\omega_0}\int_0^t w(\tau)\mathrm{d}\tau \quad (11)$$

where $w(t)$ is a unit intensity white noise process as defined by (7). After a transient phase the auto-covariance function and the one-sided auto-spectral density function of (10) can be shown to be ([7])

$$\left.\begin{aligned}\kappa_{ee}(\tau) &= \frac{1}{2}e_0^2\,\mathrm{e}^{-\mu\omega_0|\tau|}\cos(\omega_0\tau)\\ \frac{\omega_0 S_e(\omega)}{e_0^2} &= \frac{1}{2\pi}\left(\frac{\mu}{\left(1+\frac{\omega}{\omega_0}\right)^2+\mu^2}+\frac{\mu}{\left(1-\frac{\omega}{\omega_0}\right)^2+\mu^2}\right)\end{aligned}\right\}. \quad (12)$$

The models (5), (6) and (10) all have zero mean, variance $\frac{1}{2}e_0^2$, and the dominating angular frequency ω_0. The amplitudes of (5) and (10) are both constant and equal to e_0, whereas the amplitude of (6) is slowly varying around e_0.

Despite the completely different realizations of (6) and (10) as shown in Fig. 5(a) and (b) the corresponding one-sided auto-spectral density functions (8) and (12) are almost identical as illustrated in Fig. 6. The main difference appears to be a frequency shift. The filtered white noise model has its peak value approximately at the angular frequency $\omega = (1-\mu^2)\omega_0$, whereas the random phase model has its peak value approximately at the angular frequency $\omega = (1+\mu^2)\omega_0$. Hence, the frequency shift amounts to $\Delta\omega = 2\mu^2\omega_0$. For $\mu < 0.1$, as used in Fig. 6, this discrepancy is considered acceptable. Obviously, higher order joint statistical moments of the two excitation models differ completely. In the numerical analysis the unit intensity white noise process is replaced by an equivalent broad-band Gaussian process with an auto-spectral density function, which is flat at the value $1/2\pi$ over all angular frequencies of importance.

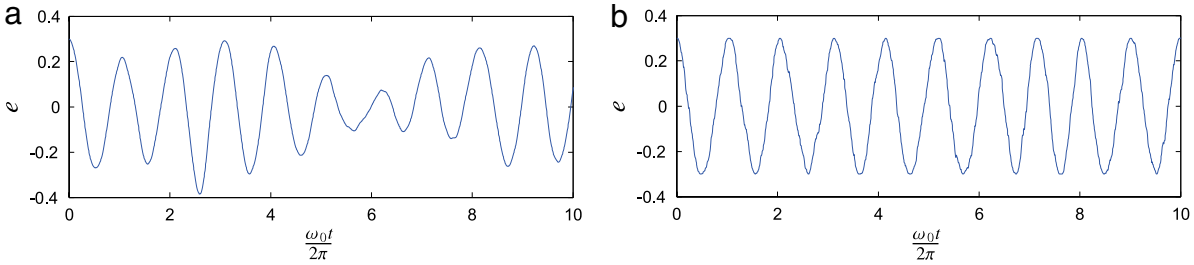

Fig. 5. (a) Filtered white noise process. (b) Variable phase process. $\mu = 0.01$, $e_0 = 0.3$.

Table 1
Data for stay cable.

EA	2.17×10^9 N
H	5.5×10^6 N
m	81.05 kg/m
L	260 m
θ_0	30.4°

3. Stochastic and chaotic analysis

The analysis will be performed for the longest stay in the cable stayed bridge across the Øresund between Sweden and Denmark, with data given in Table 1. The supports are assumed fixed, corresponding to $k_1 = k_2 = \infty$. Basically, the damping ratios of the cable are taken as $\zeta_1 = \zeta_2 = 0.002$. Additionally, the somewhat higher damping ratios $\zeta_1 = \zeta_2 = 0.01$ will be considered. These are supposed to model the case, where additional damping has been introduced via linear viscous dampers placed in the vicinity of the lower support point of the cable. The total weight of the cable is $W = 2.038 \times 10^5$ N. The sag-to-chord-length ratio is $\frac{f}{L} = 4.05 \times 10^{-3}$ and the Irvine stiffness parameter [13] becomes $\lambda^2 = 0.4140$. An amplitude $\Delta L_0 = 0.5$ m of the chord elongation corresponds to $e_0 = 0.759$, which is considered the maximum value for which the theory applies.

3.1. Subharmonic resonance of order 2:1

Fig. 7(a) shows the trajectory at the midpoint under subharmonic resonance of order 2:1 due to harmonically varying chord elongations. The damping ratios are $\zeta_1 = \zeta_2 = 0.01$, representing a cable with dampers. The response appears as a coupled periodic motion, where the in-plane modal coordinate is dominated by a small harmonic response at the angular frequency ω_0, and the out-of-plane coordinate by a resonance subharmonic motion at the angular frequency $\frac{1}{2}\omega_0$, resulting in the shown infinity sign like trajectory. It turns out that the in-plane single mode deterministic subharmonic attractor is unstable for arbitrary small excitation amplitudes, and the stable motion always appears as a coupled motion between the two modal coordinates. Fig. 7(b) show the corresponding trajectory during a comparable stochastic chord elongation obtained as filtered white noise with the bandwidth $\mu = 0.01$. The related time-series are shown in Fig. 8(a). As seen, the motion has changed dramatically qualitatively and quantitatively. Both modal coordinates are at subharmonic resonance, and the trajectories appear as ellipses with slowly varying semi-axes, rotating slowly around the chord line. Fig. 7(c) and Fig. 8(b) show the corresponding results at the smaller bandwidth $\mu = 0.001$. In this case the motion is still dominated by the deterministic attractor shown in Fig. 7(a), although the magnitude of the in-plane modal coordinate has increased significantly in magnitude. Finally, Fig. 7(c) shows the trajectory, when the bandwidth parameter is increased to $\mu = 0.05$. Now, the out-of-plane component has vanished totally, and the response of the in-plane modal coordinate is in subharmonic resonance.

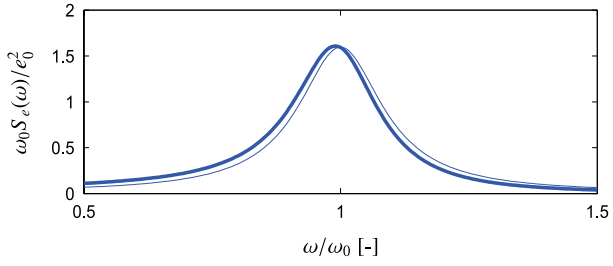

Fig. 6. One-sided auto-spectral density function for the two stochastic chord elongation processes, $\mu = 0.1$. Thick line: Filtered white noise process. Thin line: Variable phase process.

Fig. 9(a) and (b) show the variances $E[\sigma_{q_1}^2]$ and $E[\sigma_{q_2}^2]$ of the out-of-plane and the in-plane modal coordinates as a function of the bandwidth parameter μ for the two considered stochastic chord elongation models. The damping ratios are $\zeta_1 = \zeta_2 = 0.01$ and $\zeta_1 = \zeta_2 = 0.002$, respectively, where the latter represents a cable without dampers. As seen, $E[\sigma_{q_1}^2]$ decreases, and $E[\sigma_{q_2}^2]$ increases with μ. Especially, the out-of-plane response vanishes above a critical bandwidth value, which depends on the damping ratio and the parameter e_0. The existence of the critical bandwidth value explains the trajectory on Fig. 7(d). Further, it is seen that the variance estimates produced by the two models are in quite good agreement. Notice that the variance estimates for the stochastic chaotic response contain contributions from both the stochastic response and from the chaotic behavior. These components can hardly be separated, and hence their relative contribution cannot be quantified.

The stochastic chaotic behavior of the response subjected to the two alternative stochastic chord elongation processes has been investigated by comparing the estimated maximum Lyapunov exponent of the response using the same realization for the underlying unit intensity white noise process $w(t)$ in Eqs. (6) and (11). Fig. 10(a) and (b) show the estimated maximum Lyapunov exponent for high and low dampings as a function of μ and for discrete values of e_0. As seen, the stochastic response loses predictability above a critical bandwidth parameter. However, if e_0 is not too large, predictability is eventually recovered at sufficiently large bandwidth values. Generally, the tendency of chaotic behavior is more pronounced at low structural damping ratios than at high damping ratios. From Fig. 9(a) it is concluded that the stochastic response in Fig. 7(b) with $\mu = 0.01$ must be chaotic, whereas the stochastic responses in Fig. 7(c) and (d) with bandwidths $\mu = 0.001$ and $\mu = 0.05$ are ordered. The result for the referential harmonic chord elongation process is obtained in the limit as $\mu \to 0$. As seen, these are all negative. Hence, the response under harmonic varying chord elongation is predictable, at least for non-dimensional chord elongation amplitudes $e_0 \leq 0.3$.

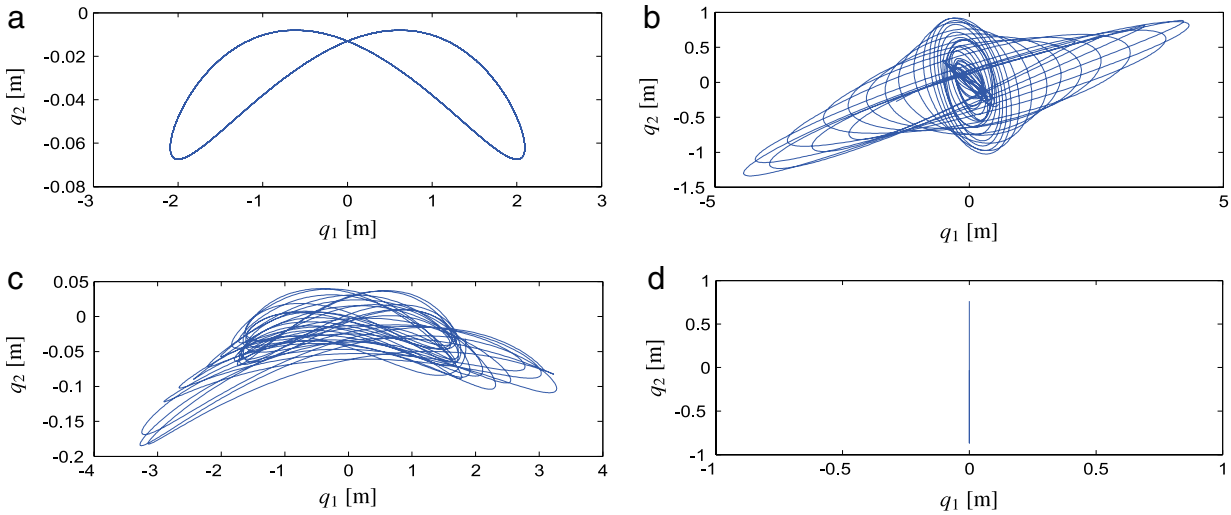

Fig. 7. Trajectory of the cable midpoint, subharmonic resonance of order 2:1, $e_0 = 0.1$, $\omega_0 = 2\omega_1$, $\zeta_1 = \zeta_2 = 0.01$. (a) Ordered response due to harmonically varying chord elongation. (b) Chaotic stochastic response, $\mu = 0.01$. (c) Ordered stochastic response, $\mu = 0.001$. (d) Ordered stochastic response, $\mu = 0.05$.

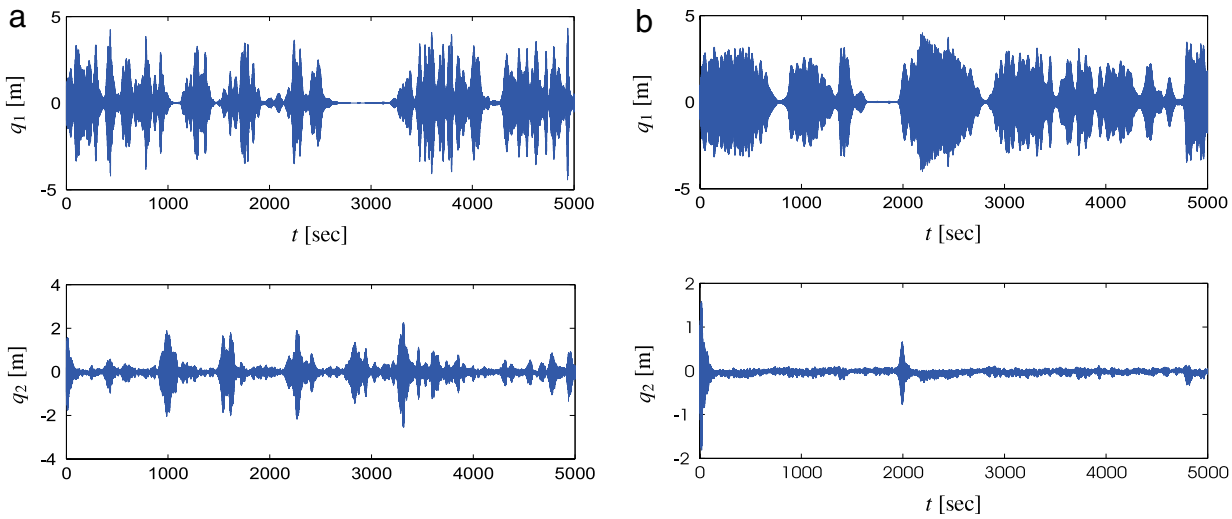

Fig. 8. Realizations of the cable midpoint, stochastic subharmonic resonance of order 2:1, $e_0 = 0.1$, $\omega_0 = 2\omega_1$, $\zeta_1 = \zeta_2 = 0.01$. (a) $\mu = 0.01$. (b) $\mu = 0.001$.

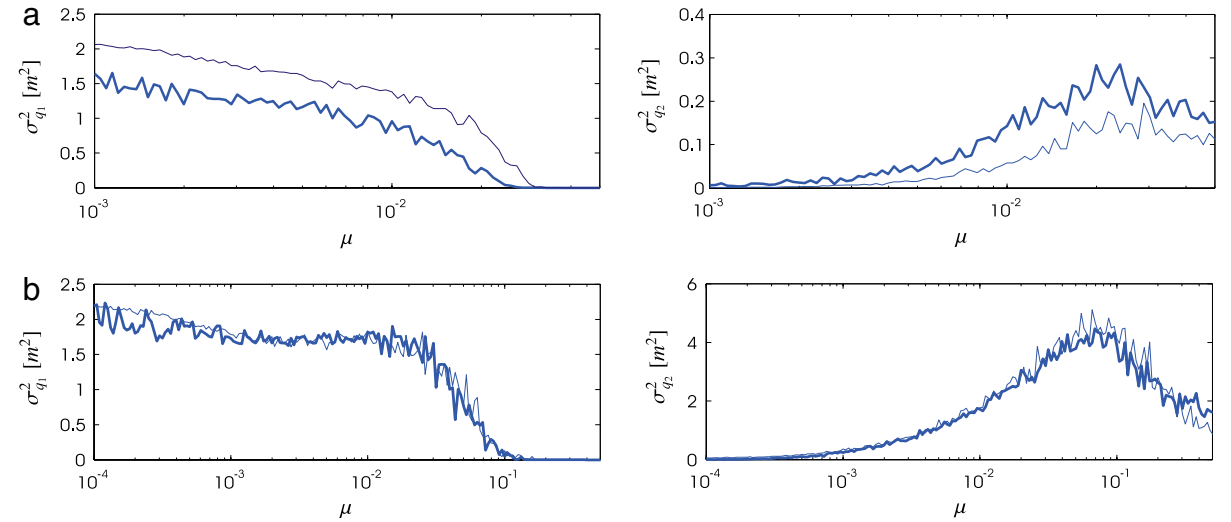

Fig. 9. Stochastic chaotic subharmonic resonance of order 2:1. Variation of variances with μ, $e_0 = 0.1$, $\omega_0 = 2\omega_1$. (a) $\zeta_1 = \zeta_2 = 0.01$. (b) $\zeta_1 = \zeta_2 = 0.002$. Thick line: Filtered white noise process. Thin line: Variable phase process.

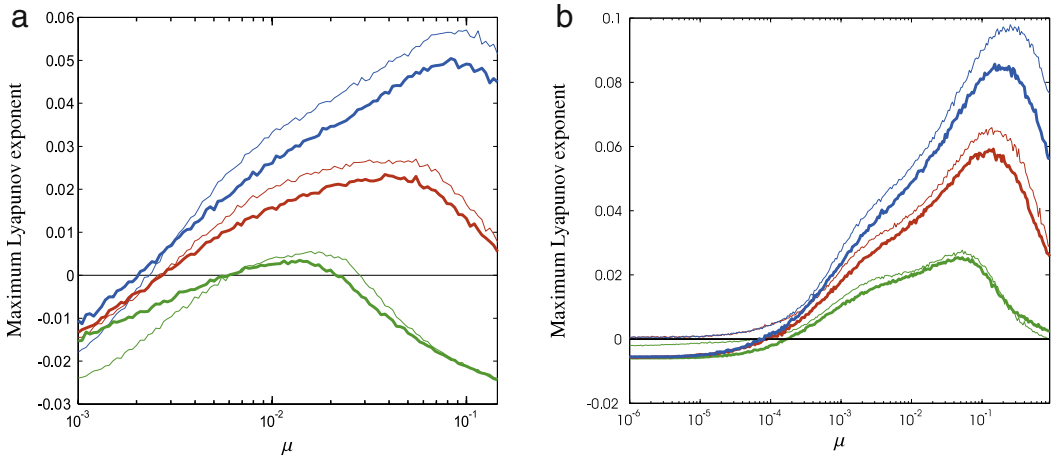

Fig. 10. Variation of maximum Lyapunov exponent with μ, $\omega_0 = 2\omega_1$. (a) $\zeta_1 = \zeta_2 = 0.01$, (b) $\zeta_1 = \zeta_2 = 0.002$. Bottom: $e_0 = 0.1$. Middle: $e_0 = 0.2$. Top: $e_0 = 0.3$. Thick line: Filtered white noise process. Thin line: Variable phase process.

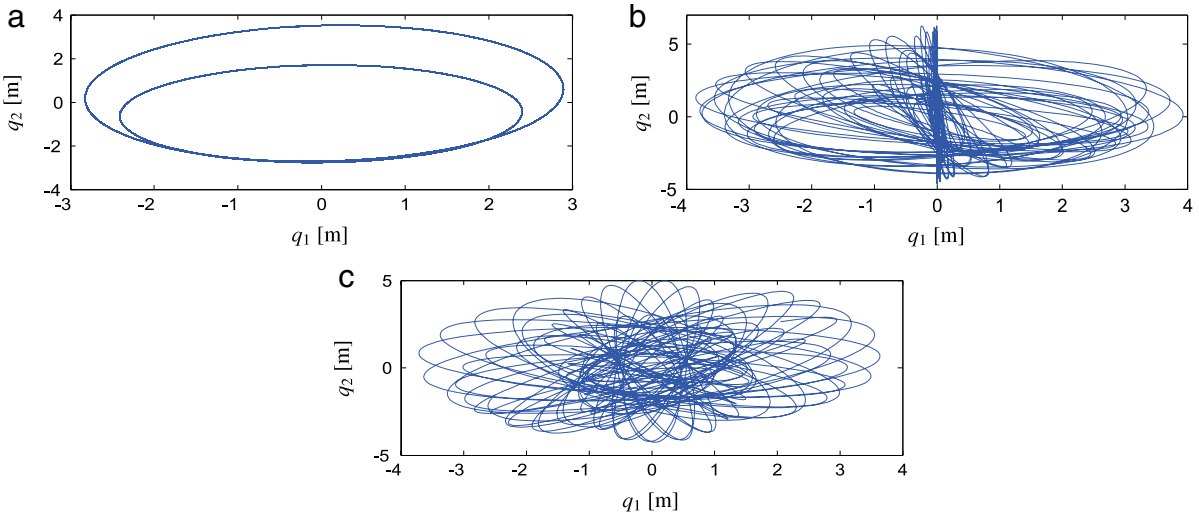

Fig. 11. Trajectory of the cable midpoint, ordered superharmonic resonance of order 1:2, $e_0 = 0.55$, $\omega_0 = 0.52\omega_1$, $\zeta_1 = \zeta_2 = 0.002$. (a) Harmonically varying chord elongation. (b) Stochastically varying chord elongation, filtered white noise, $\mu = 0.001$. (c) Stochastically varying chord elongation, variable phase process, $\mu = 0.001$.

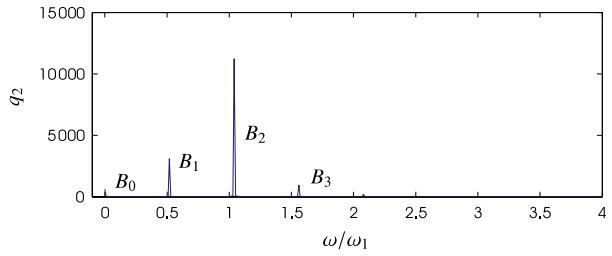

Fig. 12. Fourier transform of single mode in-plane modal coordinate, $e_0 = 0.3$, $\omega_0 = 0.52\omega_1$. Harmonically varying chord elongation.

The responses obtained by the two narrow-banded stochastic chord elongation models agree quite well. Hence, it may be concluded that the dramatic qualitative and quantitative changes of the subharmonic resonant response under stochastic excitation at realistic bandwidth parameters are caused by the 2nd order statistical moments of the excitation. Physically, the changes are due to the slowly varying phase of the excitation, which destroys the phase locking of the deterministic attractor. The amplitude variation has no influence on the response because the single mode in-plane subharmonic attractor is unstable for all amplitudes.

3.2. Superharmonic resonance of order 1:2

Fig. 11(a) shows the trajectory of the midpoint under coupled mode superharmonic resonance of order 1:2 due to harmonic varying chord elongations. The damping ratios are $\zeta_1 = \zeta_2 = 0.002$, representing a cable without dampers. Both modal coordinates are at superharmonic resonance. Additionally, another stable single mode in-plane subharmonic attractor exists. An FFT plot of the response in this attractor has been shown in Fig. 12, revealing a small harmonic amplitude B_1 at the angular frequency $\omega = \omega_0$, a significant superharmonic amplitude at the frequency $\omega = 2\omega_0$, and a small higher order harmonic amplitude B_3 at the angular frequency $\omega = 3\omega_0$. Fig. 11(b) shows the corresponding trajectory during comparable stochastic chord elongations obtained as filtered white noise with the bandwidth $\mu = 0.001$. In this case, random jumps between the two deterministic attractors take place. The single mode in-plane motion is visible in the trajectory as the vertical filled-in area in the vicinity of $q_1(t) = 0$. Fig. 11(c) shows the coupled mode trajectory during stochastic excitation with the variable phase model. No jumps to the single mode in-plane attractor take place. From this observation it is concluded that the jumps between the attractors are caused by the slow variation of the amplitude of the filtered white noise model.

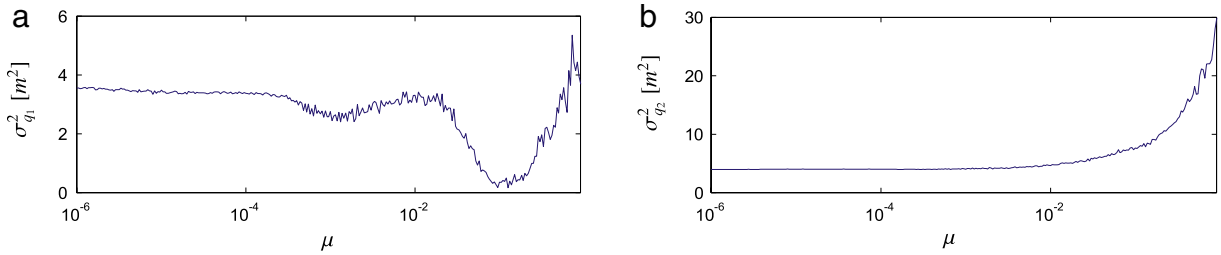

Fig. 13. Variation of variances of modal coordinates with μ, $e_0 = 0.55$. $\zeta_1 = \zeta_2 = 0.002$. Variable phase process.

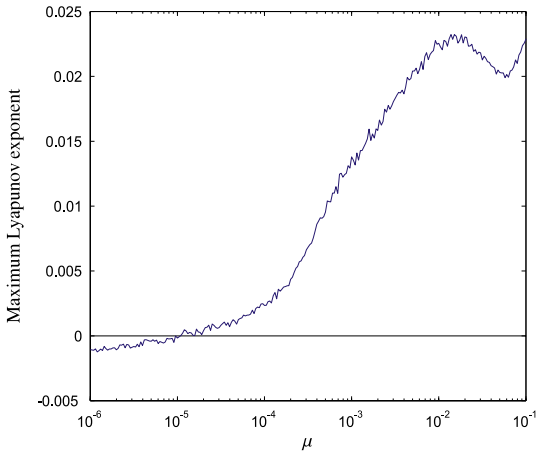

Fig. 14. Variation of maximum Lyapunov exponent with μ, $e_0 = 0.55$. $\zeta_1 = \zeta_2 = 0.002$. Variable phase process.

Because of the random jump between the two superharmonic attractors it is not possible with the applied ergodic sampling technique to obtain reliable estimates of the variance of the modal coordinates and the maximum Lyapunov exponent in the case of filtered white noise excitation. For this reason, these quantities will only be determined for the variable phase excitation. Fig. 13 shows the obtained variances as a function of the bandwidth parameter. The variances are approximately constant up to a certain bandwidth value, where the in-plane component starts to increase and the out-of-plane component to decrease in magnitude. The variance of the out-of-plane component attains a minimum at an unrealistic large bandwidth value, and increases monotonously beyond this minimum value. Fig. 14 shows the

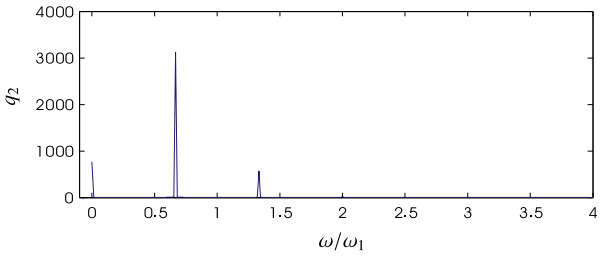

Fig. 16. Fourier transform of in-plane mode, $e_0 = 0.3$, $\omega_0 = \frac{2}{3}\omega_1$. Harmonic varying chord elongation.

variation of the estimated maximum Lyapunov exponent as a function of μ. As seen, the response is ordered as $\mu \to 0$, as displayed by the trajectory shown in Fig. 11(a). However, for any realistic bandwidth value the stochastic response is chaotic.

3.3. Superharmonic resonance of order 2:3

Fig. 15(a) shows the trajectory of the midpoint under coupled mode superharmonic resonance of order 2:3 due to harmonic varying chord elongations. Both modal coordinates are at superharmonic resonance. Additionally, another stable single mode in-plane attractor exists. The FFT plot of the response is shown in Fig. 16, revealing that the dominating component is the harmonic response amplitude at the angular frequency $\omega = \omega_0$. In particular, there is no superharmonic response component present. Fig. 15(b) shows the corresponding trajectory during comparable stochastic chord elongations obtained as filtered white noise with the bandwidth $\mu = 0.001$. As seen, random jumps take place between the two attractors, as was the case for the superharmonic resonant case of the order 1:2. Fig. 15(c) shows the coupled mode trajectory dur-

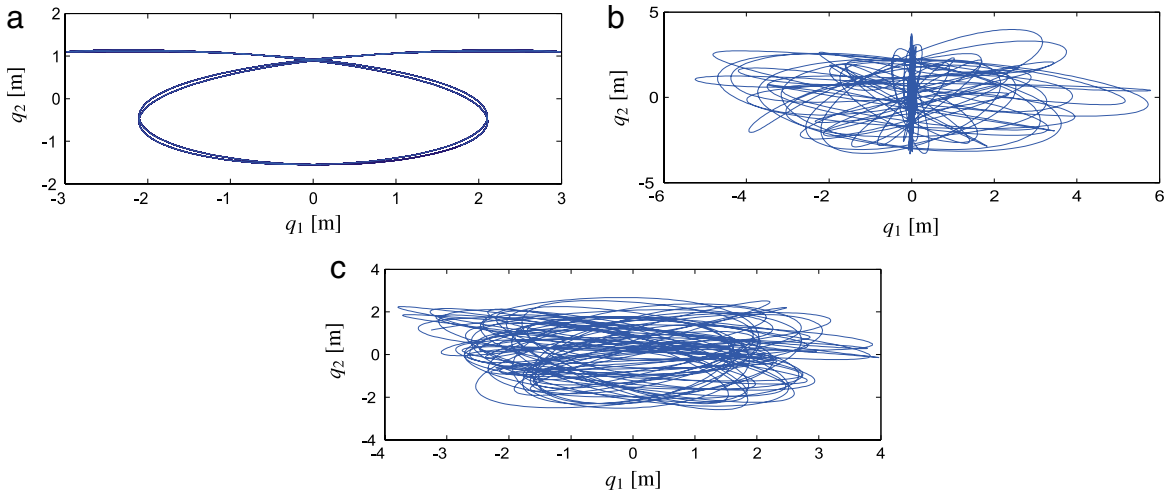

Fig. 15. Trajectory of the cable midpoint, ordered superharmonic resonance of order 2:3, $e_0 = 0.7$, $\omega_0 = \frac{2}{3}\omega_1$, $\zeta_1 = \zeta_2 = 0.002$. (a) Harmonic varying chord elongation. (b) Stochastic varying chord elongation, filtered white noise, $\mu = 0.001$. (c) Stochastic varying chord elongation, variable phase process, $\mu = 0.001$.

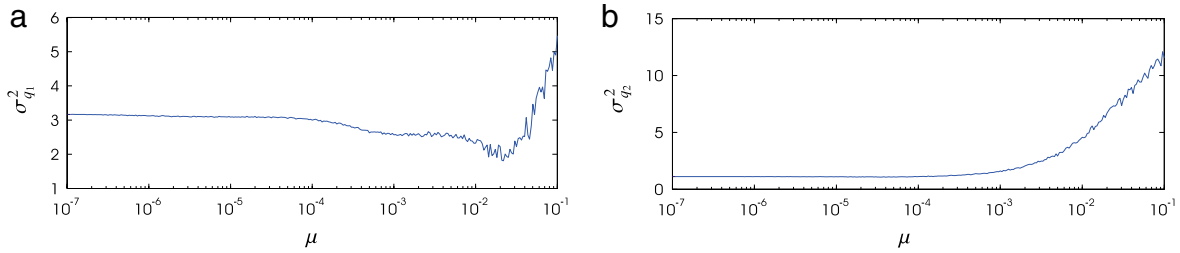

Fig. 17. Variation of variances of modal coordinates with μ, $e_0 = 0.7$, $\zeta_1 = \zeta_2 = 0.002$. Variable phase process.

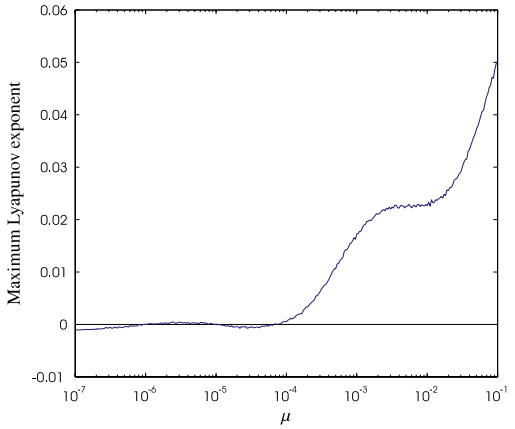

Fig. 18. Variation of maximum Lyapunov exponent with μ, $e_0 = 0.7$. $\zeta_1 = \zeta_2 = 0.002$. Variable phase process.

ing stochastic excitation with the variable phase model. No jumps to the single mode in-plane attractor take place, and it is concluded that the jumps between the attractors are caused by the slowly varying amplitude of the narrow-band stochastic chord elongation, whereas the variation of the phase is of no importance. Again, the variance of the modal coordinates and the maximum Lyapunov exponent will only be determined for the variable phase excitation.

Fig. 17 shows the obtained variances as a function of the bandwidth parameter. The variances are approximately constant up to a certain bandwidth value, where the in-plane component starts to increase and the out-of-plane component to decrease in magnitude. The variance of the out-of-plane component attains a minimum, and increases monotonously beyond this minimum value. Fig. 18 shows the variation of the estimated maximum Lyapunov exponent as a function of μ. As seen, the response is ordered as $\mu \to 0$. At finite, but unrealistic low bandwidth values, the stochastic response changes between ordered and chaotic behavior. However, for any realistic bandwidth value the stochastic response is always chaotic.

4. Conclusions

The stochastic response and chaotic behavior of a shallow cable have been analyzed by two comparable stochastic models for the chord elongation for the subharmonic resonance of order 2:1 and the superharmonic resonances of orders 1:2 and 2:3. One model is obtained by linear filtration of Gaussian white noise through a second order filter. The other model is based on a zero-time lag cosine transformation of a Wiener process. Both processes have almost identical auto-covariance functions, whereas higher order statistical moments are different.

The results for the stochastic subharmonic resonance of order 2:1 obtained by the two narrow-band stochastic chord elongation models agree quite well, from which it is concluded that the qualitative and quantitative changes of the stochastic subharmonic resonant response compared to the response obtained under harmonically varying chord elongation are caused by the 2nd order statistical moments of the excitation. Physically, the changes are due to the slowly varying phase of the excitation, which destroys the phase locking presumed by the deterministic attractor. The amplitude variation has no influence on the response because the single mode in-plane subharmonic attractor is unstable for all amplitudes. It is shown that a critical value of the bandwidth parameter exists above which the out-of-plane response vanishes, and the subharmonic resonant response takes place entirely in the in-plane modal coordinate. Based on a numerically determined maximum Lyapunov exponent stochastic it is demonstrated that the stochastic response loses predictability above a critical bandwidth parameter. If the variance of the chord elongation excitation is not too large, predictability is eventually recovered at sufficiently large bandwidth values. Further, the tendency of chaotic behavior is more pronounced at low structural damping than at high damping.

Two stable deterministic superharmonic resonance attractors of order 1:2 exist, which influence the stochastic superharmonic resonant response. One attractor is a coupled mode response, where both modal coordinates are at superharmonic resonance. The other attractor is a stable single mode in-plane subharmonic attractor. In the case of filtered white noise excitation a random jump between the two attractors takes place. These jumps do not take place for the variable phase excitation. Hence, the jumps are caused by the slowly varying amplitude of the narrow-band stochastic chord elongation, whereas the variation of the phase is of no importance. Variances and the chaotic behavior have only been analyzed for the random phase excitation. The variance of the components is approximately constant up to a certain bandwidth value, where the in-plane component starts to increase and the out-of-plane component to decrease in magnitude. The variance of the out-of-plane component attains a minimum at an unrealistic large bandwidth value, and increases monotonously beyond this minimum value. The stochastic response is ordered as $\mu \to 0$. However, for any realistic bandwidth value the stochastic response becomes chaotic.

The stable deterministic superharmonic resonance attractor of the order 2:3 consists of a coupled mode response. Additionally, a single mode in-plane harmonic varying attractor exists. In the case of filtered white noise excitation a random jump between the two attractors takes place. These jumps do not take place for the variable phase excitation. As for the superharmonic resonance of order 1:2, it is concluded that these jumps are caused by the slowly varying amplitude of the narrow-band stochastic chord elongation, whereas the variation of the phase is of no importance. Variances and the chaotic behavior have only been analyzed for the random phase excitation. The variance of the components is approximately constant up to a certain bandwidth value, where in-plane components start to increase and the out-of-plane component to decrease in magnitude. The variances are approximately constant up to a certain bandwidth value, where the in-plane component starts to increase and

the out-of-plane component to decrease in magnitude. The variance of the out-of-plane component attains a minimum, and increases monotonously beyond this minimum value. At finite, but unrealistic low bandwidth values, the stochastic response changes between ordered and chaotic behavior. However, for any realistic bandwidth value the stochastic response is always chaotic.

Appendix. Eigenfrequencies, eigenmodes and coefficients entering the reduced cable model

The eigenmodes $\Phi_1(x)$ and $\Phi_2(x)$ are given as (see Irvine [13])

$$\left.\begin{aligned}\Phi_1(x) &= \sin(\pi\xi)\\ \Phi_2(x) &= \frac{\cos\left[\frac{\Omega}{2}(1-\xi)\right]-\cos\frac{\Omega}{2}}{1-\cos\frac{\Omega}{2}}\end{aligned}\right\},\quad \xi=\frac{x}{L} \tag{13}$$

where Ω is the lowest positive solution to the transcendental equation

$$\tan\frac{\Omega}{2}=\frac{\Omega}{2}-\frac{4}{\lambda^2}\left(\frac{\Omega}{2}\right)^3 \tag{14}$$

λ^2 is the Irvine stiffness parameter, [13]

$$\lambda^2=64\frac{EA}{H}\frac{f^2}{L_eL} \tag{15}$$

L_e is an equivalent cable length which takes the flexibility of the supports into consideration defined as, [14]

$$L_e=L+\frac{AE}{k_1}+\frac{AE}{k_2}. \tag{16}$$

Then, the fundamental angular eigenfrequencies at fixed supports are given as

$$\left.\begin{aligned}\omega_1&=\pi\bar{\omega}\\ \omega_2&=\Omega\bar{\omega}\end{aligned}\right\} \tag{17}$$

where

$$\bar{\omega}=\frac{1}{L}\sqrt{\frac{H}{m}}. \tag{18}$$

From (13) the following parameters may be evaluated, [5]

$$\left.\begin{aligned}
a_1&=\int_0^1\Phi_1\,d\xi=\frac{2}{\pi}\\
b_1&=\int_0^1\Phi_1^2\,d\xi=\frac{1}{2}\\
c_1&=\int_0^1\left(\frac{d\Phi_1}{d\xi}\right)^2 d\xi=\frac{\pi^2}{2}\\
a_2&=\int_0^1\Phi_2\,d\xi=\frac{\sin\frac{\Omega}{2}-\frac{\Omega}{2}\cos\frac{\Omega}{2}}{\frac{\Omega}{2}\left(1-\cos\frac{\Omega}{2}\right)}\\
&\simeq\frac{2}{\pi}\left(1-\frac{4+2\pi-\pi^2}{4\pi}\Delta\Omega\right)\\
b_2&=\int_0^1\Phi_2^2\,d\xi=\frac{-3\sin\Omega+\Omega(2+\cos\Omega)}{2\Omega\left(1-\cos\frac{\Omega}{2}\right)^2}\\
&\simeq\frac{1}{2}\left(1-\frac{\pi-3}{\pi}\Delta\Omega\right)\\
c_2&=\int_0^1\left(\frac{d\Phi_2}{dx}\right)^2 d\xi=\frac{\Omega^2-\Omega\sin\Omega}{2\left(1-\cos\frac{\Omega}{2}\right)^2}\\
&\simeq\frac{\pi^2}{2}\left(1-\frac{\pi-3}{\pi}\Delta\Omega\right)
\end{aligned}\right\} \tag{19}$$

where the last expressions for a_2, b_2 and c_2 represent first order expansions in the parameter

$$\Delta\Omega=\Omega-\pi. \tag{20}$$

$\Delta\Omega$ is a non-dimensional measure of the difference $\omega_2-\omega_1$ between the fundamental in-plane and out-of-plane angular eigenfrequencies, cf. (17).

Then, the following results can be evaluated for the coefficients entering (4)

$$\left.\begin{aligned}
\alpha&=\frac{c_2}{c_2+\lambda^2a_2^2}\simeq\frac{\pi^3}{\pi^3+4\lambda^2}\\
\beta_1&=\frac{1}{8}\bar{\omega}^2\frac{\lambda^2}{f}a_2\frac{c_1}{b_1}\simeq\frac{\pi}{4}\bar{\omega}^2\frac{\lambda^2}{f}\left(1-\frac{4+2\pi-\pi^2}{4\pi}\Delta\Omega\right)\\
\beta_2&=\frac{1}{16}\bar{\omega}^2\frac{\lambda^2}{f}a_2\frac{c_1}{b_2}\simeq\frac{\pi}{8}\bar{\omega}^2\frac{\lambda^2}{f}\left(1-\frac{16-2\pi-\pi^2}{4\pi}\Delta\Omega\right)\\
\beta_3&=\frac{3}{16}\bar{\omega}^2\frac{\lambda^2}{f}a_2\frac{c_2}{b_2}\simeq\frac{3\pi}{8}\bar{\omega}^2\frac{\lambda^2}{f}\left(1-\frac{4+2\pi-\pi^2}{4\pi}\Delta\Omega\right)\\
\gamma_1&=\frac{1}{128}\bar{\omega}^2\frac{\lambda^2}{f^2}\frac{c_1}{b_1}c_1=\frac{\pi^4}{256}\bar{\omega}^2\frac{\lambda^2}{f^2}\\
\gamma_2&=\frac{1}{128}\bar{\omega}^2\frac{\lambda^2}{f^2}\frac{c_1}{b_1}c_2\simeq\frac{\pi^4}{256}\bar{\omega}^2\frac{\lambda^2}{f^2}\left(1-\frac{\pi-3}{\pi}\Delta\Omega\right)\\
\gamma_3&=\frac{1}{128}\bar{\omega}^2\frac{\lambda^2}{f^2}\frac{c_2}{b_2}c_1\simeq\frac{\pi^4}{256}\bar{\omega}^2\frac{\lambda^2}{f^2}\\
\gamma_4&=\frac{1}{128}\bar{\omega}^2\frac{\lambda^2}{f^2}\frac{c_2}{b_2}c_2\simeq\frac{\pi^4}{256}\bar{\omega}^2\frac{\lambda^2}{f^2}\left(1-\frac{\pi-3}{\pi}\Delta\Omega\right)\\
\eta&=8\bar{\omega}^2\frac{a_2}{b_2}f\simeq\frac{32}{\pi}\bar{\omega}^2\left(1-\frac{16-2\pi-\pi^2}{4\pi}\Delta\Omega\right)f
\end{aligned}\right\}. \tag{21}$$

References

[1] Cao DQ, Tucker RW, Wang C. A stochastic approach to cable dynamics with moving rivulets. Journal of Sound and Vibration 2003;268:291–304.

[2] Geurts C, Wouwenvelder T, Van Staalduinen P. Numerical modelling of rain–wind-induced vibration: Erasmus bridge rotterdam. Structural Engineering International 1990;2:135–92.

[3] Rega G. Nonlinear vibrations of suspended cables—part II: deterministic phenomena. Applied Mechanics Reviews 2004;57:497–514.

[4] Nielsen SRK, Kirkegaard PH. Super and combinatorial harmonic response of flexible cables with small sag. Journal of Sound and Vibration 2002;251:79–102.

[5] Larsen JW, Nielsen SRK. Nonlinear stochastic response of a shallow cable. International Journal of Non-Linear Mechanics 2006;41:327–44.

[6] Wolf A, Swift JB, Swinney HL, Vastano JA. Determining the Lyapunov exponents from time series. Physica D 1985;16:285–317.

[7] Wedig W. Vom Chaos zur Ordnung. Gamm-Mitteilungen Heft 2 1989;3–31.

[8] Perkins NC. Modal interaction in the nonlinear response of elastic cables under parametric/external excitation. International Journal of Non-Linear Mechanics 1992;27:233–50.

[9] Tien W-M, Sri Namachchivaya N, Bajaj AK. Non-linear dynamics of a shallow arch under periodic excitation. I. 1:2 internal resonance. International Journal of Non-Linear Mechanics 1994;29(3):349–66.

[10] Pinto da Costa A, Martins JAC, Branco F, Lilien JL. Oscillations of bridge stay cables induced by periodic motion of deck and/or tower. ASCE Journal of Engineering Mechanics 1996;122:613–22.

[11] El-Attar M, Ghobarah A, Aziz TS. Non-linear cable response to multiple support periodic excitations. Engineering Structures 2000;22:1301–12.

[12] Zhou Q, Larsen JW, Nielsen SRK, Qu WL. Nonlinear stochastic analysis of subharmonic response of a shallow cable. Nonlinear Dynamics 2007;48:97–114.

[13] Irvine HM. Cable structures. Cambridge (MA): MIT Press; 1981.

[14] Krenk S. Mechanics and analysis of beams, columns and cables. 2nd ed. Springer Verlag; 2001.